

視網膜功能在積體電路上之實現與應用

學生：林俐如

指導教授：吳重雨

國立交通大學電機資訊學院電子工程系電子研究所

摘要

在這個論文裡，介紹了視網膜功能在積體電路上的實現與應用。論文的主體分為四個部分：(1) 對哺乳類動物視網膜完整的介紹；(2) 回顧以雙載子接面電晶體為基礎之仿視網膜影像偵測器；(3) 回顧以雙載子接面電晶體為基礎之仿視網膜運動偵測器；(4) 新的神經型態晶片設計方法，以及模仿兔子視網膜內開暫態神經節細胞組的實驗晶片設計與結果。

哺乳類動物視網膜由五種不同的細胞構成，而每一種細胞又各自有不同的分類。除了將影像世界的訊息轉變為神經訊號外，視網膜還負責 0.3% 的大腦視覺處理功能。在本研究之初，我們嘗試以工程的角度去瞭解視網膜的功能，而這樣的瞭解也啟發了本論文的研究。

在以雙載子接面電晶體為基礎之仿視網膜影像偵測器的部分，首先提出了一個新型態的矽視網膜晶片，該矽視網膜晶片實現了脊椎動物視網膜的部分功能。在這個矽視網膜晶片裡，每個基礎單元都只包含兩個分開的感光雙載子接面電晶體。脊椎動物視網膜內水平細胞的平滑功能，由感光雙載子接面電晶體共用基極處，光線引發過量載子的分佈與再分佈動作有效實現。因此，這個矽視網膜晶片架構非常簡單而緊密，可以用金氧半場效電晶體場效電晶體製程技術將它做得很小。實驗結果也顯示這個矽視網膜晶片能夠萃取出影像的邊緣與偵測運動影像。接著介紹一個改良過的簡單而緊密的矽視網膜晶片架構。在這個架構中，被採用 n 通道金氧半場效電晶體場效電晶體連結不同基礎單元中的雙載子接面電晶體基極，來取代原來雙載子接面電晶體共用基極的平滑網路，形成獨特而緊密

的架構，因此平滑網路的特性變得具有廣泛地可調性。此外，每個雙載子接面電晶體也包含一個額外的射極作為列開關，以此大幅降低基礎單元的面積並增加解析度。平滑網路的可調性與此晶片偵測動態影像的能力都經實驗證實，相信這個改良後的結構將非常適合用來實現超大型積體電路智慧型影像偵測器。在本章最後提出了一個低光電流金氧半場校電晶體視網膜焦平面感測器結構，該結構採用擬雙載子接面電晶體平滑網路與適應性施密特電流觸發器。這個結構非常簡單而緊密，而且可以工作在極低的電流範圍，而施密特電流觸發器的滯後作用可以根據產生的光電流適應性調整。量測結果顯示此視網膜焦平面感測器可以成功地應用在字元辨識掃描器的相關產品上。

在以雙載子接面電晶體為基礎之仿視網膜運動偵測器的部分，首先提出的是採用雙載子接面電晶體矽視網膜與跨越零點偵測器設計的二維速度與方向選擇性視覺感測晶片。在這個感測器當中，採用了以標記為基礎延遲與關連的演算法來偵測運動中影像的速度與方向。此外，此架構更採用二元的脈衝訊號作為關連訊號來增加速度與方向的選擇性。在此感測器中的每個偵測基本單元都有緊密的架構，其中包含了一個雙載子接面電晶體為基礎之仿視網膜單元、一個電流輸入的邊緣萃取器、兩個延遲路徑、跟四個關連器，經由實驗證明製作的感測器晶片運作無誤。接著提出一個可偵測任意運動的金氧半場效電晶體場效電晶體即時焦平面運動偵測器，此偵測器採用以關連器為基礎的新型演算法。在此設計當中，採用以雙載子接面電晶體為基礎之仿視網膜感光細胞與平滑網路來擷取影像，並提高影像的對比，同時採用以關連器為基礎的新型演算法來做訊號處理，以決定入射影像的速度與方向。運動速度與方向的計算誤差經由平均累積十六個取樣畫面後已大幅降低。實驗結果已成功證明此運動偵測器藉由調整影像擷取頻率，能偵測每秒一畫素到每秒 140,000 畫素的運動影像，而最小的可偵測位移為每採樣時間內移動 5 微米。也就是說，這個高性能新型運動偵測器能被應用在許多即時的運動偵測系統上。再下來提出了一個具有仿視網膜處理電路的角速度與方向選擇性的圓形運動偵測器的設計與分析，這個圓形運動偵測器採極性結構，並且對圓形運動的角速度與運動方向（順時針與逆時針）具有選擇性。這個感測器的設計依然採用以關連器為基礎的新型演算法，而每個相關的畫素都相隔 45° 角。在關連畫素當中插入更多畫素有助於提高角速度的選擇性。角速度選擇性同時與影像邊緣的數目與位置有關，角速度與邊緣的關係在論文當中有詳細的分

析，實驗的結果也與角速度與方向選擇性的分析結果互相印證。最後提出一個金氧半場效電晶體場效電晶體即時焦平面切變運動偵測器，採用以關連器為基礎的新型演算法來偵測局部運動向量，並採用以偽雙載子接面電晶體為基礎之仿視網膜處理電路來偵測並前處理影像。為了要偵測切變運動，偵測畫素安置在切變運動軌跡上，這個架構對選定的切變運動速度與方向具選擇性。切變運動選擇性以三種圖樣不同的運動速度加以驗證。

在本論文的最後部分，提出了一個新的設計方法用以設計金氧半場效電晶體場效電晶體神經型態晶片，並模擬了兔子視網膜的開暫態神經結細胞組。量測結果顯示，該金氧半場效電晶體場效電晶體神經型態晶片的運作方式與生物量測結果相符，因此成功地驗證了該晶片的仿生功能。經由實驗驗證，這個設計方法所設計的神經型態晶片能協助解尚未揭露的視網膜細胞行為與視覺語言，而且也可用以設計所有的視網膜神經結細胞組。此外，該研究結果也使得許多極具潛力的視網膜晶片應用，諸如運動偵測、電腦視覺、人工視網膜跟生醫元件方面變得更有可行性。



IMPLEMENTATIONS AND APPLICATIONS OF THE RETINAL FUNCTIONS ON INTEGRATED CIRCUITS

Student: Li-Ju Lin

Advisor: Chung-Yu Wu

**Department of Electronics Engineering and Institute of Electronics
College of Electrical Engineering and Computer Science
National Chiao Tung University**



ABSTRACT

In this thesis, implementations and applications of the retinal functions on integrated circuits are introduced. The main parts of this thesis include: (1) a complete introduction of the mammalian retina; (2) review of the BJT-based silicon retina image sensors; (3) review of the BJT-based silicon retina motion sensors; (4) a new design methodology used to implement CMOS neuromorphic chips and an experimental chip that imitates the ON brisk transient ganglion cell set of rabbits' retinas.

The mammalian retina is comprised of five different kinds of cells, for each kind can be divided into more types. Besides transducing the visual world into neural signals, these cells are in charge of 0.3% of the visual function of the brain. In the beginning of this research, we try to understand the retinal functions from the engineering point of view, thus inspiring the following research of the thesis.

For the BJT-based silicon retina image sensors, firstly a new silicon retina is

proposed to realize the functions of the vertebrate retina. In the proposed silicon retina, each basic cell consists of two separated bipolar phototransistors only. The smooth function of the horizontal cell in the vertebrate retina is efficiently achieved by the diffusion and redistribution of the photogenerated excess carriers in the common base region of the phototransistors. Thus, the structure of the new silicon retina is very simple and compact. It can be easily implemented in CMOS technologies with a small chip area. Experimental results show that the new silicon retina is capable of extracting the edge of the image and detecting the moving object. Then an improved BJT-based silicon retina with simple and compact structure is proposed and analyzed. In the proposed structure, the BJT smoothing network is implemented by placing enhancement n-channel MOSFET's among the bases of parasitic BJT's existing in a CMOS process to form a unique and compact structure. Thus, the smoothing characteristics can be tuned in a wide range. Moreover, an extra emitter is incorporated with each BJT at the pixel to act as the row switch. This reduces the cell area of the silicon retina and increases the resolution. The measurement results on the tunability of the smooth area in the smoothing network as well as the dynamic characteristics of the proposed silicon retina in detecting moving objects have been presented. It is believed that the improved structure is very suitable for the very large scale integration implementation of the retina and its application systems for CMOS smart sensors. Finally, a new structure of low-photocurrent CMOS retinal focal-plane sensor with pseudo-BJT smoothing network and adaptive current Schmitt trigger is proposed. The proposed structure is very simple and compact. Moreover, the proposed circuit could be operated for low-induced current levels (pA), and the current hysteresis of the proposed current Schmitt trigger could be adjusted adaptively according to the value of induced photocurrents. Measurement results show that the proposed new retinal focal-plane sensor has successfully been used in character recognition of scanner systems, such as pen scanners, etc.

For the BJT-based silicon retina motion sensors, firstly a 2-D velocity- and direction-selective visual motion sensor with BJT-based silicon retina and temporal zero-crossing detector is proposed and implemented. In the proposed sensor, a token-based delay-and-correlate computational algorithm is adopted to detect the selected speed and direction of moving object images. Moreover, binary pulsed signals are used as correlative signals to increase the velocity and direction selectivities. Each basic detection cell in the sensor has a compact architecture which

consists of one BJT-based silicon retina cell, one current-input edge extractor, two delay paths, and four correlators. The correct operations of the fabricated sensor chip have been verified through measurements. Then a CMOS real-time focal-plane motion sensor intended to detect the global motion, using BJT-based retinal smoothing network and the modified correlation-based algorithm, is proposed. In the proposed design, the BJT-based retinal photoreceptor and smoothing network are adopted to acquire image and enhance the contrast of an image while the modified correlation-based algorithm is used in signal processing to determine the velocity and direction of the incident image. The deviations of the calculated velocity and direction for different image patterns are greatly reduced by averaging the correlated output over 16 frame sampling periods. Experimental results have successfully confirmed that the proposed motion sensor can work with different incident images and detect a velocity between 1 pixel/sec and 140,000 pixels/sec via controlling the frame sampling period. The minimum detectable displacement in a frame sampling period is 5 μ m. Consequently, the proposed high-performance new motion sensor can be applied to many real-time motion detection systems. Later a CMOS angular velocity- and direction-selective rotation sensor with a retinal processing circuit is implemented and analyzed. The proposed rotation sensor has a polar structure and is selective of the angular velocity and direction (clockwise and counterclockwise) of the rotation of images. The correlation-based algorithm is adopted and each pixel in the rotation sensor is correlated with the pixel that is 45 $^{\circ}$ apart. The angular velocity-selectivity is enhanced by placing more than one pixel between two correlated pixels. The angular velocity-selectivity is related to both the number and the positions of the edges in an image. Detailed analysis characterizes angular velocity-selectivity for different edges. The experimental results successfully verified the analyzed characteristics of angular velocity- and direction-selectivity. Finally, a CMOS focal-plane shear motion sensor is designed and implemented. The adopted motion computation method is based on the modified correlation-based algorithms to detect the local motion vectors. The adopted pseudo BJT-based retinal processing circuit is to sense and preprocess the incident image. In order to detect shear motion, the arrangement of pixels is along the path of shear motion in the chip of shear motion sensor. This structure is selective to the preferred shear direction and velocity of the images. The shear motion selectivity is verified after tested by three patterns translating at different velocities.

In the last part of this thesis, a new design methodology is proposed to

implement CMOS neuromorphic chips which imitate the ON brisk transient ganglion cell set of rabbits' retinas. The measurement results on the fabricated CMOS neuromorphic chip are consistent with the biological measurement results. Thus the biological functions of the chip have been successfully verified. It can be used to understand more biological behaviors and visual language of retinas under different input optical images which have not yet been tested in biological experiments. Based on the results, the full ganglion cell sets of retina can be designed. Thus many potential applications of retinal chips on motion sensors, computer vision, retinal prosthesis, and biomedical devices are feasible.



誌謝

首先要感謝我的指導老師吳重雨教授多年來耐心的指導與鼓勵，使我能順利完成博士學業。猶記得在 1997 年的夏天，我開始跟隨吳重雨教授進行矽仿視網膜的研究，轉眼已經過了十年。在這十年當中，吳重雨教授教導給我的，除了積體電路設計與類神經網路的專業知識外，更重要的是使我學習到待人處事之方法及團隊合作的精神，也讓我學會了挑戰困難及解決問題的正確態度與方法。雖然這十年的研究生涯走得並不容易，但是使我獲益良多。我也要感謝吳重雨教授安排我到匈牙利國家科學院與美國加州大學柏克萊分校進行短期研究，使我更具有國際觀與研究能力。另外也要特別感謝充滿愛心，和藹可親的師母曾昭玲女士，常常給予我關懷與加油打氣。此外還要感謝實驗室中另外四位教授——吳介琮、吳錦川、柯明道及陳巍仁教授給我的許多指導與建議。尤其要特別柯明道教授與其研究群給我在靜電放電防護方面專業的協助，使我研究的過程更加順利。

在十年的求學過程中，三〇七實驗室在老師與同學們的共同努力之下逐漸的茁壯，至今三〇七實驗室無論是在規模、設備及研究成果上，均已受到各界肯定，在此要感謝歷年來的學長姐為實驗室的建立與運作所付出的心力。十年實在是相當漫長的一段時間，有太多的伙伴與戰友陪同我走過，難以一一詳列，只能在此由衷感謝所有曾經與我一同在實驗室奮鬥的伙伴們，也希望三〇七實驗室能越來越好。

感謝匈牙利國家科學院的 Prof. Roska、Dr. Zarandy 與 Dr. Rekeczky 在我訪問匈牙利國家科學院時親切的招待與指導，也感謝加州大柏克萊分校的 Prof. Werblin 與瑞士 Friedrich Miescher Institute 的 Dr. Roska、Dr. Bálya 與 Dr. Münch 在我訪問美國加州大學柏克萊分校時給我各方面的協助，因為有這些專家學者跨領域的交流討論，才使得這篇論文能有今日的成果。

我還要特別感謝國科會提供研究計劃經費；感謝國家晶片設計製作中心提供晶片設計及製作環境，使我能夠完成論文中積體電路設計之實驗印證。此外，還要特別感謝姜信欽學長的在研究上及其他許多方面的指引與幫忙；感謝歷任助理——李婷媛小姐及卓慧貞小姐在實驗室行政事務上的許多協助；感謝其他關心我的師長及親朋好友們。

我要致上我最深最深的感謝給予我的公公黃榮田先生、婆婆蘇嬰嬋女士、弟弟林皇杉先生、妹妹林俐君小姐、大姑黃筱薇小姐、大姑丈連德宏先生、小姑黃筱霓小姐，以及陪伴我的黃冠勳先生，跟兩個寶貝黃榆珊、黃榆琇。沒有你們無怨無悔、永無止境的付出、鼓勵、支持與照顧，我無法完成今日的成就。衷心感謝你們，也感謝上蒼賜予如此幸福和樂的家庭。

最後，謹以論文獻給我的父親林演辰先生、母親羅森妹女士。我做到了！

林 俐 如
誌於 風城交大
九十六年 盛夏

CONTENT

CHAPTER 1 INTRODUCTION	1
1.1 THE NEUROMORPHIC VISION CHIPS	1
1.1.1 Mead’s Silicon Retina	1
1.1.2 Ruedi’s Motion Detection Silicon Retina	2
1.1.3 Andreou and Boahen’s Silicon Retina	2
1.1.4 BJT-based Silicon Retina	3
1.2 THE RETINOMORPHIC CHIPS	4
1.3 RESEARCH MOTIVATION AND ORGANIZATION OF THIS THESIS	5
Fig. 1. 1-Fig. 1. 6	8
CHAPTER 2 THE MAMMALIAN RETINA	11
2.1 FUNDAMENTAL KNOWLEDGE OF THE MAMMALIAN RETINA	11
2.1.1 Photoreceptor	12
2.1.2 Horizontal Cell	12
2.1.3 Bipolar Cells	13
2.1.4 Amacrine Cells	13
2.1.5 Ganglion Cells	13
2.2 THE CLASSIFICATION OF GANGLION CELLS OF THE RABBITS’ RETINA	14
2.3 OPERATING PRINCIPLE – FROM THE ENGINEERING POINTS OF VIEW	15
Table 2. 1	18
Fig. 2. 1-Fig. 2. 5	19
CHAPTER 3 THE BJT-BASED SILICON RETINA CHIPS	
(I) – THE IMAGE SENSORS	23
3.1 A NEW STRUCTURE OF THE 2-D SILICON RETINA	23
3.1.1 Introduction	23

3.1.2 Cell Architecture and Operational Principle	24
3.1.3 2-D Silicon Retina Array Design and Experimental Results	28
3.1.4 Conclusion	33
3.2 AN IMPROVED BJT-BASED SILICON RETINA WITH TUNABLE IMAGE SMOOTHING CAPABILITY	34
3.2.1 Introduction	34
3.2.2 Analyses of the Proposed BJT-Based Silicon Retina	35
3.2.3 The 2-D Architecture of Silicon Retina	40
3.2.4 Experimental Results	41
3.2.5 Conclusion	43
3.3 A LOW-PHOTOCURRENT CMOS RETINAL FOCAL-PLANE SENSOR WITH A PSEUDO-BJT SMOOTHING NETWORK AND AN ADAPTIVE CURRENT SCHMITT TRIGGER FOR SCANNER APPLICATIONS	43
3.3.1 Introduction	43
3.3.2 Architecture and Circuit	45
3.3.3 Simulation Results	47
3.3.4 Measurement Results	49
3.3.5 Conclusion	50
Table 3.1 -Table 3.3. 3	51
Fig. 3.1. 1-Fig. 3.3. 16	56
CHAPTER 4 THE BJT-BASED SILICON RETINA CHIPS	
(II) – THE MOTION SENSORS	77
4.1 A 2-D VELOCITY- AND DIRECTION-SELECTIVE SENSOR WITH BJT-BASED SILICON RETINA AND TEMPORAL ZERO-CROSSING DETECTOR	78
4.1.1 Introduction	78
4.1.2 Motion Computation Algorithm	79
4.1.3 Hardware Implementation	79
4.1.4 Measurement Results	82

4.1.5 Conclusion	83
4.2 A CMOS FOCAL-PLANE MOTION SENSOR WITH BJT-BASED RETINAL SMOOTHING NETWORK AND MODIFIED CORRELATION-BASED ALGORITHM	84
4.2.1 Introduction	84
4.2.2 Motion Computation Method	85
4.2.3 Architecture and Circuit	90
4.2.4 Experimental Results	92
4.2.5 Conclusion	94
4.3 ANALYSIS AND DESIGN OF A CMOS ANGULAR VELOCITY- AND DIRECTION-SELECTIVE ROTATION SENSOR WITH RETINAL PROCESSING CIRCUIT	94
4.3.1 Introduction	95
4.3.2 Rotation Detection Method	96
4.3.3 Architecture and Circuit	104
4.3.4 Experimental Results	106
4.3.5 Conclusion	108
4.4 A CMOS FOCAL-PLANE RETINAL SENSOR DESIGNED FOR SHEAR MOTION DETECTION	109
4.4.1 Introduction	109
4.4.2 Circuit Implementation	111
4.4.3 Experimental Results	112
4.4.4 Conclusion	114
Table 4. 1-Table 4.4. 1	115
Fig. 4.1. 1-Fig. 4.4. 12	117
CHAPTER 5 A NEUROMORPHIC CHIP THAT IMITATES THE ON BRISK TRANSIENT GANGLION CELL SET IN THE RETINAS OF RABBITS	146
5.1 INTRODUCTION	146

5.2	RETINA MODEL	148
5.2.1	Neuromorphic Model of the Retinal Cell Set	148
5.2.2	Macromodel for Chip Implementation	150
5.3	CIRCUIT AND CHIP ARCHITECTURE	151
5.3.1	Photoreceptor and Horizontal Cell	152
5.3.2	ON and OFF Bipolar Cells	153
5.3.3	Amacrine and Ganglion Cells	154
5.3.4	Whole Chip Architecture	155
5.4	EXPERIMENTAL RESULTS	155
5.4.1	Neuromorphic Model Simulation	155
5.4.2	The Experimental Chip and Setup	156
5.4.3	The Measured Spatiotemporal Patterns	157
5.4.4	Temporal Domain Analyses	158
5.5	SUMMARY	159
Table 5. 1-Table 5. 2		161
Fig. 5. 1-Fig. 5.11		163
CHAPTER 6	CONCLUSIONS AND FUTURE WORKS	174
6.1	MAIN RESULTS OF THIS THESIS	174
6.2	FUTURE WORKS	175



TABLE CAPTIONS

CHAPTER 2

Table 2. 1. Ganglion cell types, defined by response to spot sizes and level of dendritic stratification [38]

CHAPTER 3

Table 3. 1 Summary of the results of CHAPTER 3

Table 3.1. 1. The Experimental Results of the Fabricated Rm Amplifier

Table 3.1. 2. The Device Parameters of the Parasitic PNP Transistor in 0.8 μ m DPDM CMOS Process

Table 3.1. 3. The Summary of the Measured Characteristics of the Proposed 2-D 32x32 Silicon Retina

Table 3.2. 1. The summary on the characteristics of the fabricated FPA chip of BJT-based silicon retina

Table 3.3. 1. Feature Comparisons Between PBJT-Based Silicon Retina and Typical CMOS Sensor



CHAPTER 4

Table 4. 1 Summary of the results of CHAPTER 4

Table 4.3. 1. The size of the transistors of the retinal processing circuits

Table 4.4. 1 The summary on the characteristics of the fabricated chip of shear motion sensor

CHAPTER 5

Table 5. 1 The transistors' sizes of circuits in Fig. 5.4(a)-(c)

Table 5. 2 (a) The bias condition to measure the spatiotemporal patterns of Fig. 5.9

FIGURE CAPTIONS

CHAPTER 1

Fig. 1. 1. The Mead's retina [3].

Fig. 1. 2. Ruedi's motion detection silicon retina [5].

Fig. 1. 3. The model the outer-plexiform layer of retina. Reprinted from [6].

Fig. 1. 4. Andreou and Boahen's silicon retina [6].

Fig. 1. 5. BJT-based silicon retina [7].

Fig. 1. 6. Inner retina synaptic interactions. ON and OFF BCs relay cone signals to GCs. and excite NAs and WAs. NAs inhibit BCs. WAs, and transient GCs; their inhibition onto Ws is shunting. WAs modulate NA presynaptic inhibition and spread their signals laterally through gap junctions. BCs also excite local interneurons that inhibit complementary BCs and NAs. Reprinted from [28].

CHAPTER 2

Fig. 2. 1. Schematic of the mammalian retina. Reprinted from [41].

Fig. 2. 2. The major cell types of a typical mammalian retina. From the top row to the bottom, photoreceptors, horizontal cells, bipolar cells, amacrine cells and ganglion cells. Reprinted from [60].

Fig. 2. 3. Bipolar cell types of the primate retina. Reprinted from [41].

Fig. 2. 4. Spiking patterns in each row (measured from four different members of the same cell class) for five different classes of ganglion cells. The numbers at the beginning of each row refer to the classification shown in Table 2. 1. The arrows in row 5 (cell type 7) point to the enhanced activity at the stimulus edge, a feature that is characteristic of this class [38].

Fig. 2. 5. A sketch of the processing structure of the CNN model of the mammalian rabbit retina [44].

CHAPTER 3

Fig. 3.1. 1. (a) The top view of the proposed silicon retina cell. (b) The cross-sectional view of the proposed silicon retina cell.

- Fig. 3.1. 2. The conceptual cross-sectional view of the outer PNP phototransistor array showing the photogenerated carriers.
- Fig. 3.1. 3. The equivalent circuit of the smooth network in the proposed silicon retina structure. In the equivalent circuit, R_N represents the N-well base spreading resistance.
- Fig. 3.1. 4. The normalized signal intensity versus position of the original signal, the smooth signal, and their difference.
- Fig. 3.1. 5. The conceptual diagram showing that when a moving object passes through the silicon retina cell on the dashed line, the cell senses a pulsed light image.
- Fig. 3.1. 6. (a) The 2-D structure of the proposed silicon retina where two decoders are used to decode the input address and then activate the control Lines of the cells, two R_m amplifiers are used to convert the cell currents into the voltages, and the output buffer amplifies the voltage difference to obtain the output voltage. (b) The basic cell of the 2-D silicon retina where two control lines row and row' are generated from the row decoder, and four switches are used to control the current flow.
- Fig. 3.1. 7. The circuit diagrams of (a) the CMOS wideband R_m amplifier and (b) the CMOS output buffer used in the silicon retina chip.
- Fig. 3.1. 8. (a) The chip photograph of the 2-D silicon retina and (b) the cell photograph of the 2-D silicon retina.
- Fig. 3.1. 9. (a) The measured emitter current $I_{e,inner}$ of the inner PNP phototransistors plotted in the 2-D diagram and (b) the measured emitter current $I_{e,outer}$ of the outer phototransistor array in the silicon retina chip.
- Fig. 3.1. 10. The curves of $y=5$ in Fig. 3.1. 9(a) and (b) for the measured $I_{e,inner}$ and the measured $I_{e,outer}$, respectively. The corresponding $I_{e,outer}$ from simulation is also plotted together for comparison.
- Fig. 3.1. 11. The simulated emitter current $I_{e,outer}$ of the 2-D silicon retina.
- Fig. 3.1. 12. (a) The measured output voltages of the 2-D silicon retina with a large light spot incident upon it, which are plotted in the 2-D diagram to show the edge detection characteristics. (b) The curves of $y=8$ in (a) are plotted to observe the edge detection capability clearly.
- Fig. 3.1. 13. The measured output images when a character image "T" is incident on the chip. (a) The output image of the inner array, (b) the output image of

the outer array. (c) the output image of the retina chip, (d) the output image of (c) with only positive pulses only.

Fig. 3.1. 14. The measured response of V_{out} in two of the 2-D silicon retina cells with a moving pattern passing across the chip.

Fig. 3.2. 1. The equivalent circuit of the proposed two-dimensional (2-D) BJT-based silicon retina.

Fig. 3.2. 2. The cross-sectional view of the BJT smoothing network, which contains one BJT and one enhancement nMOSFET in each pixel.

Fig. 3.2. 3. The large-signal equivalent circuit of the BJT smoothing network in Fig. 1 with device capacitances.

Fig. 3.2. 4. The basic cell circuit of the FPA of the proposed 2-D BJT-based silicon retina.

Fig. 3.2. 5. The complete architecture of the FPA chip of the proposed 2-D BJT-based silicon retina.

Fig. 3.2. 6. The chip photograph of the fabricated 64x64 FPA of BJT-based silicon retina.

Fig. 3.2. 7. The measured output responses of (a) isolated BJT array, (b) BJT smoothing network with $V_G = 3.75$ V, and (c) BJT smoothing network with $V_G = 4.0$ V in the fabricated FPA chip of BJT-based silicon retina exposed to an image. The mathematically found zero-crossing positions of the measured output responses of the BJT-based silicon retina are shown in (d) for (b), and (e) for (c). In (a), (b), and (c), the 256 gray levels are used to divide the current range of (a) 0-0.2 μ A, (b) 0-0.165 μ A, and (c) 0-0.12 μ A, respectively.

Fig. 3.2. 8. The normalized contour plots of the measurement emitter currents of the BJT smoothing network for an (a) original image under (b) darker background and (c) brighter background, where the contrast of input pattern is kept the same and the gate bias of nMOSFET's is 3.9 V.

Fig. 3.2. 9. The measured output (a) turn-on and (b) turn-off temporal responses of a single pixel in the improved 2-D BJT-based silicon retina under different incident flashlight patterns with the same intensity and different sizes.

Fig. 3.2. 10. The measured output responses of a single pixel in the 2-D BJT-based silicon retina under a moving light bar incident upon the chip.

Fig. 3.2. 1. The equivalent circuit of the proposed two-dimensional (2-D) BJT-based

silicon retina.

Fig. 3.2. 2. The cross-sectional view of the BJT smoothing network, which contains one BJT and one enhancement nMOSFET in each pixel.

Fig. 3.2. 3. The large-signal equivalent circuit of the BJT smoothing network in Fig. 1 with device capacitances.

Fig. 3.2. 4. The basic cell circuit of the FPA of the proposed 2-D BJT-based silicon retina.

Fig. 3.2. 5. The complete architecture of the FPA chip of the proposed 2-D BJT-based silicon retina.

Fig. 3.2. 6. The chip photograph of the fabricated 64x64 FPA of BJT-based silicon retina.

Fig. 3.2. 7. The measured output responses of (a) isolated BJT array, (b) BJT smoothing network with $V_G = 3.75$ V, and (c) BJT smoothing network with $V_G = 4.0$ V in the fabricated FPA chip of BJT-based silicon retina exposed to an image. The mathematically found zero-crossing positions of the measured output responses of the BJT-based silicon retina are shown in (d) for (b), and (e) for (c). In (a), (b), and (c), the 256 gray levels are used to divide the current range of (a) 0-0.2 μ A, (b) 0-0.165 μ A, and (c) 0-0.12 μ A, respectively.

Fig. 3.2. 8. The normalized contour plots of the measurement emitter currents of the BJT smoothing network for an (a) original image under (b) darker background and (c) brighter background, where the contrast of input pattern is kept the same and the gate bias of nMOSFET's is 3.9 V.

Fig. 3.2. 9. The measured output (a) turn-on and (b) turn-off temporal responses of a single pixel in the improved 2-D BJT-based silicon retina under different incident flashlight patterns with the same intensity and different sizes.

Fig. 3.2. 10. The measured output responses of a single pixel in the 2-D BJT-based silicon retina under a moving light bar incident upon the chip.

CHAPTER 4

Fig. 4.1. 1. The adopted token-based delay-and-correlate motion computation algorithm.

Fig. 4.1. 2. (a) The structure of BJT-based silicon retina with tunable image smoothing

capability which is proposed in [7], [124]. (b) The measured responses of the emitter current difference of a single cell in the BJT-based silicon retina [7] with a moving light bar incident upon the chip.

Fig. 4.1. 3. (a) The edge extractor which detects the temporal zero-crossings from the edge signals given by the BJT-based silicon retina and generate the edge pulse. (b) The circuit architecture which is used to realize the element D in Fig. 4.1. 1 for the generation of delayed edge pulse signals. (c) The circuit architecture of the correlators.

Fig. 4.1. 4. (a) The layout diagram of the basic detection cell, and (b) the photography of the 32×32 2-D velocity- and direction-selective sensing chip which is fabricated by using 0.6 μm N-well CMOS technology.

Fig. 4.1. 5. The oscilloscope traces of the various computational stages of one motion detection cell in the 2-D array. The emitter currents of the BJTs are read out by using off-array OP AMPs circuits with negative-feedback resistors to linearly convert them into voltages. The bias voltages are: $V_G=3V$, $V_B=1.2V$, $V_P=2V$, $V_F=0V$, $V_{pulse}=0.9V$, and $V_{dX}=V_{dY}=0.7V$.

Fig. 4.1. 6. The measured output waveforms at the four output terminals of the fabricated sensor chip when a bright spot moves in the 45° direction with the preferred speed. The bias voltages are: $V_G=3V$, $V_B=1.2V$, $V_P=2V$, $V_F=0.3V$, pulse width=10μs, and delay time=71μs.

Fig. 4.1. 7. The measured maximum variance of the delay time of one pixel among 8 fabricated chips.

Fig. 4.1. 8. The measurement of the direction-selective function of the fabricated sensor chip where the inter-pulse delay time at the four terminals are measured and plotted for different directional angles. The bias voltages in the measurement are $V_G=3V$, $V_B=1.2V$, $V_P=2V$, $V_F=0.3V$, and pulse width=25μs.

Fig. 4.2. 1. Conceptual structure of the motion computation method. R is the retinal processing circuit; CF and PF are registers used to store the current and previous sampled outputs of R , and C is the correlator. All the outputs of C are summed by the accumulator to obtain the correlation output.

Fig. 4.2. 2. The pattern of a stripe with a width of $4P$, moving to the right. d is the distance from an edge to the center of the nearest pixel in the direction of

motion. P is the distance between two adjacent photo sensors in two adjacent pixels, or the length of each pixel.

Fig. 4.2. 3. Architecture of the proposed focal-plane motion sensor.

Fig. 4.2. 4. Structure of a single pixel.

Fig. 4.2. 5. Structure of the BJT-based retinal processing circuit.

Fig. 4.2. 6. HSPICE simulation results, illustrating the output of the retinal processing circuit (a) with the background photocurrent's varying from 1 nA to 0.1 μ A; (b) with the image blurred, and (c) with normally distributed noise, with a standard deviation of 0.04 nA.

Fig. 4.2. 7. Photographs of the proposed motion sensor for (a) the whole fabricated chip and (b) a single pixel.

Fig. 4.2. 8. Photo response of the photo-BJT.

Fig. 4.2. 9. Four test patterns; (a) stripes (b) circles (c) soccer (d) Lena.

Fig. 4.2. 10. Calculated velocity for the four kinds of patterns; (a) calculated velocity; (b) velocity deviation ratio. The velocity of the moving image varies from 1 pixel/sec to 10 pixels/sec in the $-x$ direction; the sampling rate is 10 Hz.

Fig. 4.2. 11. Calculated velocity at different sampling rates; (a) calculated velocity; (b) velocity deviation ratio. The sampling rate is 140K Hz for $V_m=140,000$ pixels/sec and 1 Hz for $V_m=1$ pixel/sec. Motion is in the $-y$ direction.

Fig. 4.2. 12. Minimum detectable velocity; (a) calculated velocity; (b) velocity deviation ratio. The velocity of the moving image varies from 274.5 to 122 pixels/sec in the $-x$ direction; the sampling rate is 3.05K Hz.

Fig. 4.2. 13. Calculated direction as the image moves at two different velocities; (a) calculated direction; (b) direction deviation. The velocities of the moving image are 3,750 and 7,500 pixels/sec, respectively. The sampling rate is 75K Hz for both curves.

Fig. 4.3. 1. Conceptual structure of the adopted correlation-based algorithm for rotation detection. Each pixel is comprised of a retinal processing circuit PH , registers CF and PF , and correlator C . MLE aggregates the output of all correlators in a single circle to determine the global rotation.

Fig. 4.3. 2. (a) An edge, rotating from the $(i-1)$ th pixel P_{i-1} to the i th P_i pixels within $n\theta$ clock cycles. θ is the angle between two correlated pixels. ω is the angular velocity and T is the clock period. (b) The relationship between R

and ω , where R is defined as the ratio of the number of times when the output of MLE is at logic 0 in N clock cycles, to N .

Fig. 4.3. 3. Example of an image with four edges located in various positions, rotating clockwise. There are eight pixels, $P0$ to $P7$. The image has four edges $E1$, $E2$, $E3$, and $E4$ and the initial angles between these edges and their own front pixels are θ_s , $3\theta_s/4$, $\theta_s/2$ and $\theta_s/4$, respectively.

Fig. 4.3. 4. (a) Relationship between R and ω for an image with L edges located at various positions. (b) MATLAB simulation results with $L=2$. (c) MATLAB simulation results with $L=4$. Curves 1 and 2 refer to the extreme cases in which R is maximum and minimum at every ω , respectively. Curves 3 and 4 refer to the simulation results with random θ_{ep} for every edge.

Fig. 4.3. 5. (a) Structure modified to enhance the angular velocity-selectivity. A total of a pixels are placed within θ_s while the two pixels separated by θ_s are correlated. (b) Example of an edge's approaching the a th pixel P_a . The edge crosses P_a at the n th clock cycle. (c) Relationship between ω and R for the modified structure.

Fig. 4.3. 6. (a) Relationship between R and ω for the modified structure when the image has L edges at arbitrary positions. (b) MATLAB simulation results with $a=2$ and $L=16$. Curves 1 and 2 are the extreme cases in which R is maximum and minimum at every ω , respectively. Curves 3 and 4 are the simulation results with random θ_{ep} for every edge.

Fig. 4.3. 7. Angular velocity versus angle with the center of rotation shifted in the 0θ direction by 0 , $0.4r$, and $0.8r$, where r is the radius of the circle of pixels.

Fig. 4.3. 8. Architecture of the proposed rotation sensor, which includes 104 pixels in five concentric circles. The clockwise and the counterclockwise correlation results of all the pixels in a single circle are sent to MLE .

Fig. 4.3. 9. Pixel structure of the rotation sensor. Each pixel consists of a retinal processing circuit, two registers CF and PF , two correlators, and two P-channel MOSFETs M_{mlecc} and M_{mlec} , which are parts of MLE , implemented by NAND gates.

Fig. 4.3. 10. Structure of the retinal processing circuit. The retinal processing circuit includes an isolated photo-BJT $Q2$, a smoothing photo-BJT $Q1$, a

current-input CMOS Schmitt trigger and an inverter.

Fig. 4.3. 11. Structure of *MLE*, which is implemented by a NAND gate with a fan-in number equal to the number of pixels in a circle.

Fig. 4.3. 12. Photograph of (a) the whole chip and (b) a single pixel, of the rotation sensor.

Fig. 4.3. 13. (a) Pattern used to test rotation direction-selectivity. (b) Waveforms measured by the logic analyzer with the image rotated clockwise. (c) Waveforms measured by the logic analyzer with the image rotated counterclockwise. The waveforms, CW2 (CCW2), CW3 (CCW3), CW4 (CCW4) and CW5 (CCW5) are the clockwise (counterclockwise) outputs of *MLE* of second, third, fourth and fifth circles. The contrast of the pattern is 99% and the light source is a 5mW LASER. The clock rate is 10 Hz and the angular velocity is $2.5 \pi/\text{sec}$.

Fig. 4.3. 14. (a) Test pattern with θ_{ep} of 11.25° and 22.5° . (b) Test pattern with θ_{ep} of 0° , 5.125° , 11.25° and 16.375° . (c) Test pattern, Lena. (d) Angular velocity-selectivity with the four patterns in Figs. 13(a), 14(a), 14(b) and 14(c).

Fig. 4.3. 15. Relationship between R and ω at clock rates of 0.01, 0.1, 1, 10, and 160 Hz. Angular velocities when R is maximum are at 0.0025, 0.025, 0.25, 2.5 and $40 \pi/\text{sec}$.

Fig. 4.3. 16. Relationship between R and clock rate at angular velocities of 0.02, 0.2, 2, 50 and $206 \pi/\text{sec}$. Clock rates when R is maximum at are 0.08, 0.8, 8, 200 and 824 Hz.

Fig. 4.3. 17. Angular velocity-selectivity under an illumination of 0.91 and 366 lux at a wavelength of 550 nm.

Fig. 4.4. 1. Elementary flow components (EFCs).

Fig. 4.4. 2. The architecture of the proposed shear sensor.

Fig. 4.4. 3. The pixel structure of the shear sensor.

Fig. 4.4. 4. The schematic of the retinal processing circuit.

Fig. 4.4. 5. Photograph of (a) the whole chip, and (b) a single pixel, of the shear motion sensor.

Fig. 4.4. 6. (a) Calculated velocities over 11 frames when the shear pattern moves at 0.06 mm/sec, 0.09 mm/sec and 0.18 mm/sec; (b) Deviations between

calculated and actual velocities. The sampling rate is 3 Hz.

Fig. 4.4. 7. (a) Calculated velocities over 11 frames when the reversed-shear pattern moves at 0.06 mm/sec, 0.09 mm/sec and 0.18 mm/sec; (b) Deviations between calculated and actual velocities. The sampling rate is 3 Hz.

Fig. 4.4. 8. From (a) to (k) represents eleven frames of shear motion test patterns, while (k) to (a) represents reversed-shear test patterns.

Fig. 4.4. 9. Three patterns used to test if the translation is dismissed: (a) an edge (b) a car and (c) Lenna

Fig. 4.4. 10 (a) Calculated velocities when the test pattern shown in Fig. 4.4. 8 (a), an edge, moving to the right at different velocities; (b) Calculated velocity decrease to nearly zero as sampling frames increase. The image translates to the right at 0.27 mm/sec. The sampling rate is 3 Hz.

Fig. 4.4. 11. (a) Calculated velocities when the test pattern shown in Fig. 4.4. 8 (b), a car, moving to the right at different velocities; (b) Calculated velocity decrease to nearly zero as sampling frames increase. The image translates to the right at 0.27 mm/sec. The sampling rate is 3 Hz.

Fig. 4.4. 12. (a) Calculated velocities when the test pattern shown in Fig. 4.4. 8 (c), Lenna, moving to the right at different velocities; (b) Calculated velocity decrease to nearly zero as sampling frames increase. The image translates to the right at 0.27 mm/sec. The sampling rate is 3 Hz.

CHAPTER 5

Fig. 5. 1. (a) The neuromorphic model and (b) the RC equivalent circuit of the ON brisk transient ganglion cell set of rabbits' retinas. The parameter τ denotes the time constant in millisecond of the LPF. The parameter D denotes the space constant, which is defined by the laterally diffusing range in cell number in a 180-cell array.

Fig. 5.2. The macromodel of a single pixel of the implemented chip.

Fig. 5.3. The block diagram of a single pixel.

Fig. 5.4. (a) The circuit of the photoreceptor and horizontal cell (PH1, PH2, H); (b) The circuit of ON and OFF bipolar cells (ONBIP, OFFBIP); (c) The circuit of amacrine and ganglion cells (Ama, GC).

Fig. 5.5. (a) The whole chip architecture of the implemented chip, and (b) the

implementation of smoothing networks.

Fig. 5.6. The HSPICE simulated spatiotemporal patterns of the neuromorphic model of the ON brisk transient cell set in a 32x32 array for (a) photoreceptor, (b) horizontal cell, (c) ON bipolar cell, (d) OFF bipolar cell, (e) amacrine cell, and (f) ganglion cell. These patterns are recorded from the 17th row of the array. The x-axis is normalized time and the y-axis is the pixel location which denotes space. The stimulus is applied to the 15th to the 20th pixel at time point 1001 to 2000. The waveform at the right of each pattern is the spatial domain waveform(s) obtained at the time marked by the vertical arrow(s). The waveform at the bottom of each pattern is the temporal domain waveform obtained at the location marked by the horizontal arrow.

Fig. 5.7. Photographs of (a) the whole chip and (b) a single cell.

Fig. 5.8. The read-out circuit to translate the output current into voltage.

Fig. 5.9. The measured spatiotemporal patterns for (a) photoreceptor, (b) horizontal cell, (c) ON bipolar cell, (d) OFF bipolar cell, (e) amacrine cell, and (f) ganglion cell. These patterns are recorded from the 17th row of the array. The x-axis is normalized time and the y-axis is the pixel location which denotes space. The stimulus is applied to the 19th to the 23rd pixel at time point 1001 to 2000. The waveform at the right of each pattern is the spatial domain waveform(s) obtained at the time marked by the vertical arrow(s). The waveform at the bottom of each pattern is the temporal domain waveform obtained at the location marked by the horizontal arrow.

Fig. 5.10. The normalized waveforms of the electrical model and chip measurements of (a) the ON bipolar cell, (b) the OFF bipolar cell, (c) the amacrine cell, and (d) the ganglion cell. The light stimulus starts at time point 1001, and ends at time point 2000.

Fig. 5.11. (a) The relationship between the time constant τ_H and the controlling biases. The bias V_{NHP} is set as $V_{dd}-\Delta V$ and V_{PHP} is set as ΔV . (b) The relationship between the time constant τ_L and the controlling biases. The bias V_{NLP} is set as $V_{dd}-\Delta V$ and V_{PLP} is set as ΔV . The relationships are obtained by varying the value of ΔV .

CHAPTER 1

INTRODUCTION

1.1 THE NEUROMORPHIC VISION CHIPS

The neuromorphic vision chips have been studied for several decades since the first work was presented [1]. Biological information-processing systems operate on completely different principles from conventional image-processing systems. For many problems, particularly those in which the input data are ill-conditioned and the computation can be specified in a relative manner, biological solutions are many orders of magnitude more effective than those we have been able to implement using digital methods [1]. From a science perspective [4], analog VLSI technology can be viewed as a modeling tool [1] aimed at capturing the behavior of neurons, networks of neurons, or the complex mechanical-electrical-chemical information processing in biological systems. Computationally, analog VLSI models can be more effective compared to software simulations. More important, they are further constrained by fundamental physical limitations and scaling laws; this may direct the development of more realistic models. The constraints imposed by the technology are: power dissipation, physical extent of computing hardware, density of interconnects, gain, precision and noise limitations in the characteristics of the basic elements, signal dynamic range, and robust behavior and stability. Space limitations do not permit a discussion of this relationship between physics/technology and computation. Thus the neuromorphic vision chip design attracts the most attention and gives rise to the researches on silicon retinas.

The models for implementing silicon retinas are based on functions of cells located in the outer-plexiform layer of the retina. Moreover, the models are further simplified to facilitate hardware implementation. Even though the models are quite simplified, many successful works have been proposed [3], [5]-[7]. Various kinds of applications have also been developed using the designed chips, such as motion detection sensors [8]-[19], and high-performance image sensors [20]-[24]. The proposed silicon retinas are classified as following:

1.1.1 Mead's Silicon Retina [3]

Mead's silicon retina chip is among the first chip, which implemented the functions of biological cells on silicon. The model used by Mead's silicon retina

contains the following three functions:

- (1) The photoreceptor cells transduce light into electrical signals and take the logarithm of light intensity.
- (2) The horizontal cells form a resistive network that spatially and temporally averages the photoreceptor output.
- (3) The bipolar cell's output is proportional to the difference between the photoreceptor signal and the horizontal signal.

The schematic of a single pixel of the Mead's retina is shown in Fig. 1. 1. A single bias circuit associated with each node controls the strength of the six associated resistive connections. Each photoreceptor acts as a voltage input that drives the corresponding node of the resistive network through a conductance. A transconductance amplifier is used to implement a unidirectional conductance so the photoreceptor acts as an effective voltage source. The resistive network computes a spatially weighted average of photoreceptor inputs. The spatial scale of the weighting function is determined by the product of the lateral resistance and the conductance coupling the photoreceptors into the network [1].

1.1.2 Ruedi's Motion Detection Silicon Retina [5]

Ruedi's silicon retina detects edges of image, which is used for the subsequent stage of motion detection. The edge detection is performed by the circuits illustrated in Fig. 1. 2. A copy of the current flowing from an N-well to P-substrate photodiode is injected in a hexagonal resistive network performing a low-pass spatial and temporal filtering of the image. The space constant is controlled by the voltages V_r and V_g . The photocurrent is amplified 1.2 times and compared to the output current of the diffusion network to define an edge. A Schmitt trigger is used to avoid that the edge signal oscillates for a contrast near the threshold. The output goes high when a defined spatial gradient is present.

1.1.3 Andreou and Boahen's Silicon Retina [6]

Andreou and Boahen proposed a model of retina that is different from Mead's retina model. Their model of retina is used to model the outer-plexiform as illustrated in Fig. 1. 3. The photoreceptors are activated by light and produce activity in the horizontal cells through excitatory chemical synapses. The horizontal cells suppress the activity of the photoreceptors through inhibitory chemical synapses. The photoreceptor and horizontal cells are electrically coupled to their neighbors by electrical synapses. These allow ionic currents to flow from one cell to another, and

are characterized by a certain conductance per unit area. This is a simplified model of the complex ion-channel dynamics. The advantage of performing this complex operation at the focal plane is that the dynamic range is extended. Actually, this advantage comes from the local automatic gain control.

Based on the model, a current-mode circuit implementation of outer-plexiform retina is proposed as shown in Fig. 1. 5. The gap junctions are realized using resistance while the chemical synapses are implemented using nonlinear transconductance. Nodes in the top layer of resistive network correspond to photoreceptor R while those in the lower layer represent the horizontal cell H. The two layers are coupled vertically using the two transistor current controlled current conveyor circuit and laterally using resistive networks. A parasitic photo-BJT is used to transduce light into current. It sources current to the receptor nodes while M2 sinks current from those nodes; these opposing effects correspond to excitation and inhibition. M1 sources current (excites) the horizontal cells nodes. The bias current I_x at the source of device M1 set its transconductance. For subthreshold operation, the voltages encode photocurrents logarithmically, allowing a large optical dynamic range.

1.1.4 BJT-based Silicon Retina [7]

In the BJT-based silicon retina architecture, the Mead's silicon retina model is implemented in an advanced way. The structure of a BJT based 2D silicon retina is shown in Fig. 1. 5. Each cell consists of two PNP photo-BJTs in N-well CMOS technology. One isolated photo-BJT with open bases is used as a phototransistor to transduce light into photocurrent, which mimics the photoreceptor. Another PNP photo-BJT with its base connected with other similar BJTs through nMOSFETs mimics the smoothing function of horizontal cells. The nMOSFETs acting as adjustable resistors are used to form the smoothing network. This proposed silicon retina structure is compact and fully compatible with CMOS technology. Thus, it can be easily integrated with other integrated circuits to form a VLSI microsystem.

In many applications, input images often have wide-ranging variations of intensity or contrast. This requires an adjustable smoothing range. To achieve adjustable smoothing, the gate voltage of the nMOSFET in the smoothing network of Fig. 1. 5 are controllable. When the gate voltage is high, the nMOSFET device is operated in the strong-inversion region and has a small drain-source resistance. On the other hand, when the gate voltage is low, the nMOSFET device is operated in the subthreshold

region and the drain-source resistance is large. Therefore, the nMOSFETs provide a wide range of resistance values to achieve the wide-range adjustment of the smoothing range.

1.2 THE RETINOMORPHIC CHIPS

With increasing discoveries in neuroscience, it was found that the retina is much more than the outer-plexiform layer. It is constructed by 5 different cells, and each cell has several sub-types. These cells work together with complicated circuitries, and achieve 0.3% of the visual function of the brain [25]. Through decades of research on the simplified models of the retina, scientists have harvested fruitful results. Now we wonder what more the retina can do. The wondering leads to the research on the retinomorphonic chips [26]-[30]. The retinomorphonic chips are chips that imitate the function of biological retinas. Since the retina is the most powerful image sensor with preprocessor, finding the operating principles of the retina most likely inspires important breakthrough in nowadays' image sensor design.

In Yagi's model [30], the retinal responses are divided into two types. One is a sustained-type response in which cells respond continuously during illuminations, and the other is a transient-type response in which cells respond transiently when illumination is turned on or off [31], [32]. The sustained response is thought to be relevant to the perception of static images, and the transient response is thought to be relevant to the perception of moving objects. The design retinomorphonic chip has a multi-chip structure. The output of the chip emulating the sustained response has a Laplacian-Gaussian-like receptive field and, therefore, carries out a smoothing and a contrast-enhancement on the input images. The output of the chip emulating the transient response is obtained by subtracting consecutive image frames that are smoothed in advance by a resistive network.

In Boahen's model [26]-[29], the visual pathways range from small and sustained in the fovea, where fine details of an object stabilized by tracking are resolved, to large and transient in the periphery, where sudden motion in time surroundings is captured. Activity in each pathway is encoded by a pair of complementary channels, served by ON- and OFF- sustained or by ON- and OFF- transient channels. The ON channel signals increase in amplitude by increasing vesicle-release or spike-discharge rates; the OFF channel signals decrease in amplitude in a similar fashion [33]. The design retinomorphonic chip is divided into two parts: the inner and

the outer retina. The outer retina is the same as

Fig. 1. 4, while the model of the inner retina is shown in Fig. 1. 6. Briefly, BC inputs to the inner retina excite GCs, an electrically coupled network of wide-field amacrine cells (WAs), and narrow-field amacrine cells (NAs) that provide feedback inhibition on to the bipolar terminals (BTs) [34]. WA, which receives excitation from both ON and OFF BT and inhibition from both ON and OFF NA, modulates presynaptic feedback inhibition from NA to BT. A large membrane capacitance is used to model the NA's slow, sustained response, which leads to a less sustained response at the BT through presynaptic inhibition [35]. Push-pull inhibition is realized by a third set of amacrine cells in the model and is implemented by the ON-OFF BC circuit. These BT signals excite both sustained and transient GCs, but transient cells receive feedforward inhibition from NAs as well [36].

However, our detailed view of the operation of the mammalian retina changed dramatically by the discovery of the operation of the inner plexiform layer [36]-[42]. The mammalian retina extracts a set of 12 different “movies” from the visual scene and sends each movie to higher visual centers. These movies exist in physically distinct strata of the inner retina, embodied in the dendritic arborizations of a dozen different ganglion cell types. The dendritic arbors are stacked in discrete layers throughout the inner retina where they are synaptically contacted by excitatory and inhibitory connections from a variety of different cell types [40]. This led to the understanding of the roles of different amacrine cells, as well as the dual path in each channel. These channels have different responses to light input patterns from the visual world, which comprise the necessary visual information needed for the brain to analyze the visual world, thus they constitute visual language for the brain [39], [43]. This visual language is very complicated and much of it is still unknown or not understood by neuroscientists. Therefore, both the morphological and electrophysiological characteristics of the retina should be considered before designing a retinal chip.

1.3 RESEARCH MOTIVATION AND ORGANIZATION OF THIS THESIS

1.3.1 Research Motivation

The retina is a unique organ common to all organisms with the faculty of sight and is used to communicate with the visual world. It has superior performance in such

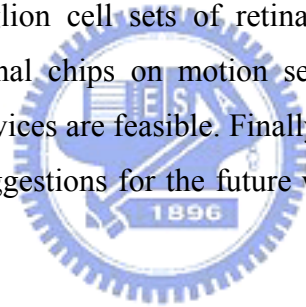
areas as visual perception image detection and preprocessing: for example, in covering a wide range (10^{10}) of light intensities; in responding to very low levels of contrast ($\sim 1\%$); and in integrating for short periods of times (~ 0.04 second) [25]. It is also a sophisticated feature preprocessor with continuous input and several parallel output channels. These interacting channels represent the visual scene. With decades of research on the BJT-based silicon retina, we have obtained fruitful results in intelligent visual sensors [7], [23], [46] and motion sensors [17]-[19], [47]. When go deep into the research of image processing systems, many bottlenecks are still left unsolved, such as real-time motion detection and classification, real-time image analysis and recognition, etc. With substantial progress on the discovery of biological visual system, we are likely to be inspired by nature.

The motivation of this thesis is to propose a new design methodology to mimic the retinal circuitries and functions on semiconductor integrated circuits. It is important to duplicate successfully the retinal functions, channels, and visual language on silicon chips because of the key advantages this might provide. First, it could help neuroscientists to understand retinal functions and visual language. Since biological experiments can only be performed on a very limited number of cells, it is very difficult to see the global spatiotemporal features of retinal cells using this method alone. Second, it could provide valuable clues concerning neural activities in the visual cortex and thus move a few more steps toward the discovery of the visual processing of the brain. Third and finally, duplication could enable important applications in the areas of intelligent visual sensor systems and retinal prostheses. Since the neuromorphic multilayer CNN model [43]-[45] shed light to understand the role of different circuits and layer parameters. It is feasible to implement the complete retinal circuitry with nowadays VLSI technology.

1.3.2 Thesis Organization

This thesis contains six chapters. Chapter 1 introduces the neuromorphic visual systems. Several successful vision chips are reviewed as a milestone of the research on silicon retinas. Moreover, going along with revealing the secrets of the retina, a new research trend on the retinomorphic chips are carried out. Since present retinomorphic chips don't imitate the detail functions and structures of the real retina, a new design methodology is proposed to fulfill complete imitation. Chapter 2 presents the mammalian retina from the engineering point of view. The cell type

classification, circuitry, and functions of retinal cells are described in detail. In this chapter, we try to analyze why the retinal cells are designed in this way to inspire new directions in vision processing systems design. Chapter 3 reviewed three BJT-based silicon retinas, from the dawn of our research on the neuromorphic vision chip design to the commercial application. Thus exhibits the potential of research on neuromorphic vision chips. Chapter 4 reviewed four motion sensors with BJT-based silicon retinas, such that further exhibits the advantages of neuromorphic vision chips in various kinds of applications. In Chapter 5, a new CMOS design is proposed to implement CMOS neuromorphic chips which imitate the ON brisk transient ganglion cell set of rabbits' retinas. The measurement results on the fabricated CMOS neuromorphic chip are consistent with the biological measurement results. Thus the biological functions of the chip have been successfully verified. It can be used to understand more biological behaviors and visual language of retinas under different input optical images which have not yet been tested in biological experiments. Based on the results, the full ganglion cell sets of retina can be designed. Thus many potential applications of retinal chips on motion sensors, computer vision, retinal prosthesis, and biomedical devices are feasible. Finally, the conclusion of this thesis is given in Chapter 6. Some suggestions for the future works are also addressed in this chapter.



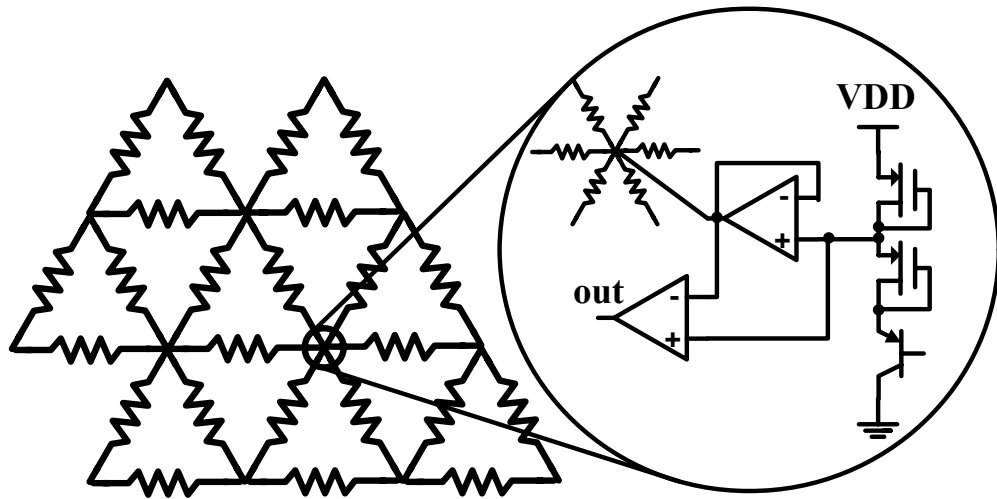


Fig. 1. 1. The Mead's retina [3].

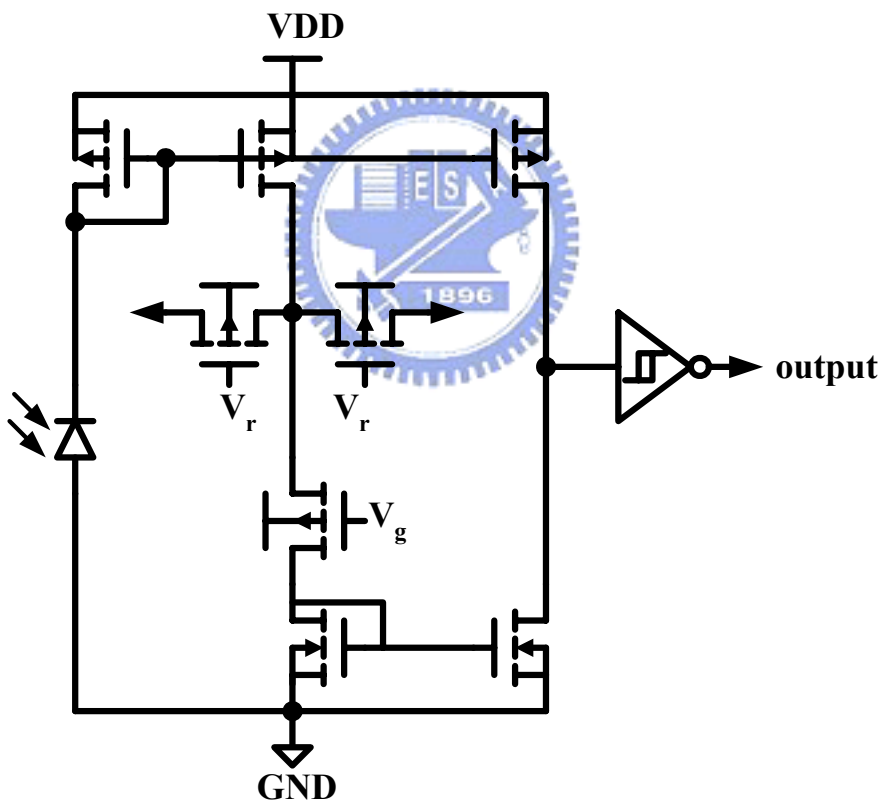


Fig. 1. 2. Ruedi's motion detection silicon retina [5].

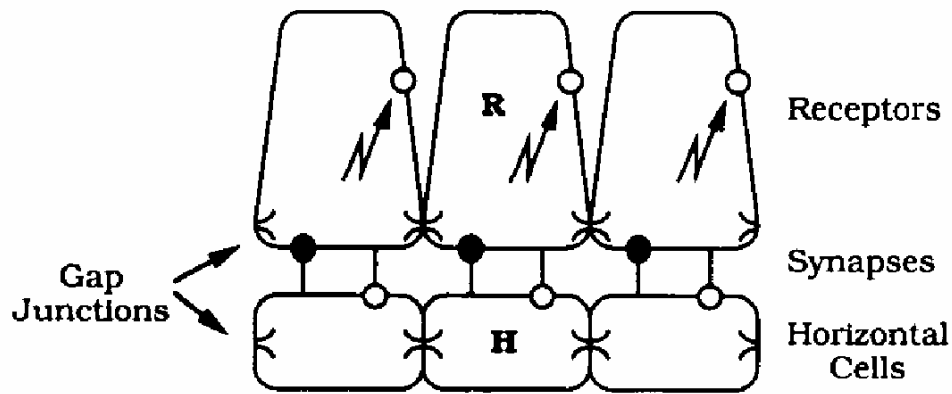


Fig. 1. 3. The model the outer-plexiform layer of retina. Reprinted from [6].

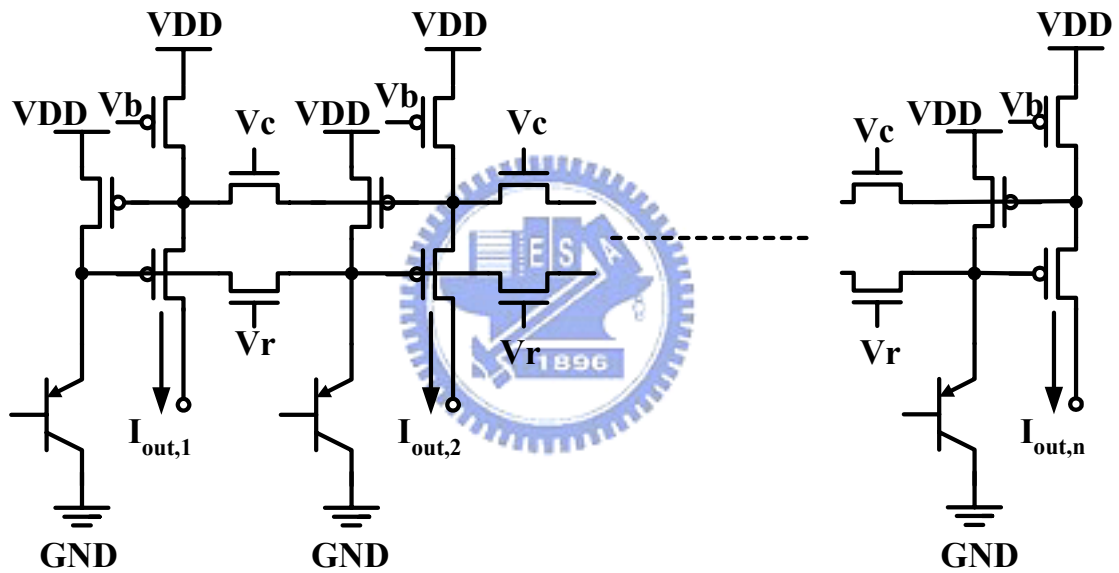


Fig. 1. 4. Andreou and Boahen's silicon retina [6].

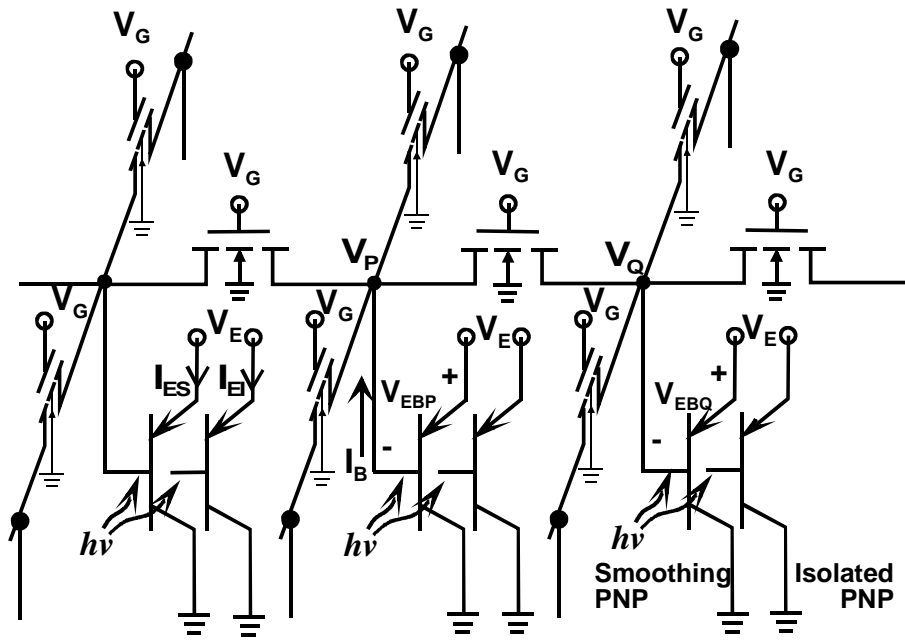


Fig. 1. 5. BJT-based silicon retina [7].

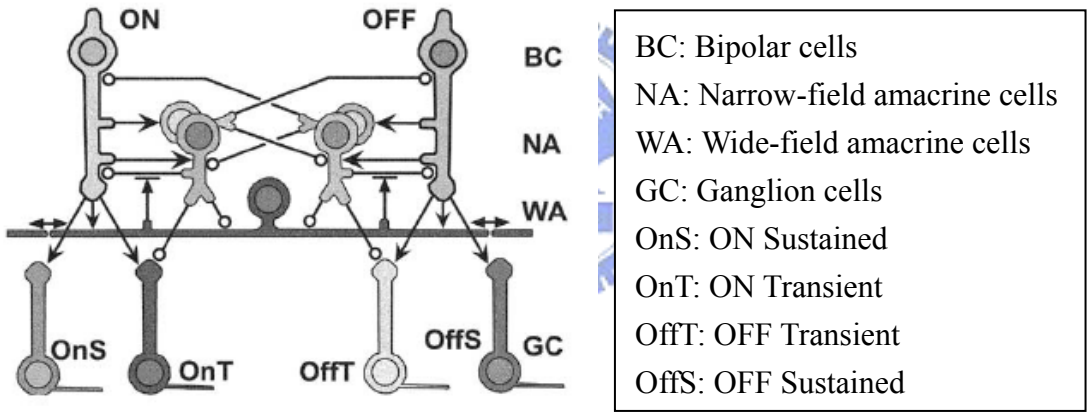


Fig. 1. 6. Inner retina synaptic interactions. ON and OFF BCs relay cone signals to GCs. and excite NAs and WAs. NAs inhibit BCs. WAs, and transient GCs; their inhibition onto Ws is shunting. WAs modulate NA presynaptic inhibition and spread their signals laterally through gap junctions. BCs also excite local interneurons that inhibit complementary BCs and NAs. Reprinted from [28].

CHAPTER 2

THE MAMMALIAN RETINA

2.1 FUNDAMENTAL KNOWLEDGE OF THE MAMMALIAN RETINA

The retina is a thin sheet of brain tissue (100 to 250 μ m thick) that grows out into the eye to provide neural processing for photoreceptor signals. It includes both photoreceptor and the first two to four stages of neural processing. Its output projects centrally over many axons, and analysis of these information channels occupies about half of the cerebral cortex [48], [49]. Moreover, it comprises about 75 discrete neuron types connected in specific, highly stereotyped patterns [25]. It sends different ‘images’ of the outside world to the brain — an image of contours (line drawing), a color image (watercolor painting) or an image of moving objects (movie). This is commonly referred to as parallel processing and starts as early as the first synapse of the retina, the cone pedicle. The schematic of the mammalian retina is shown in Fig. 2. 1 [41]. There are six classes of neuron in the mammalian retina: rods (1), cones (2), horizontal cells (3), bipolar cells (4), amacrine cells (5) and retinal ganglion cells (RGCs) (6). They have a laminar distribution (OS/IS, outer and inner segments of rods and cones; ONL, outer nuclear layer; OPL, outer plexiform layer; INL, inner nuclear layer; IPL, inner plexiform layer; GCL, ganglion cell layer; NFL, optic nerve fiber layer). Rods and cones together are labeled as photoreceptors.

At the synaptic terminals of rods and cones, the light-evoked signals are transferred onto bipolar and horizontal cells. Horizontal cells, of which there are between one and three types in mammalian retinas, provide lateral interactions in the outer plexiform layer. One type of rod bipolar cell and at least nine types of cone bipolar cell transfer the light signals into the inner plexiform layer (IPL), onto the dendrites of amacrine and ganglion cells. Cone bipolar cells fall into two main groups: ON and OFF bipolar cells. Amacrine cells are inhibitory interneurons, and there are as many as 50 morphological types [50]. Ganglion cell dendrites collect the signals of bipolar and amacrine cells and their axons transmit these signals to the visual center of the brain. At least 10–15 morphological types of ganglion cell are found in any mammalian retina [51]. The major cell types of a typical mammalian retina are shown in Fig. 2. 2 [60]. The cells are introduced below:

2.1.1 Photoreceptor

The photoreceptor mosaic is optimized to cover the full range of environmental light intensity (10^{10}) [25]. This design specification requires two types of detector with different sensitivities, the rod and the cone. The rod serves under starlight where photons are so sparse that over 0.2 second (the rod integration time), they cause only ~ 1 photoisomerization (R^*)/10,000 rods. Consequently, under starlight and for 3 log units brighter, a rod must give a binary response reporting over each integration time the occurrence of either 0 or $1R^*$. The rod continues to server at dawn as photons arrive more densely, providing more than one R^* /integration time. The rod sums these linearly up to $20R^*$ /integration time and then gradually saturates, with 100 R^* evoking a maximal photocurrent of $\sim 20\text{pA}$ [53].

The cone serves under full daylight, beginning when photon density reaches ~ 100 photons/receptor/integration time. The cone actually absorbs and transduces single photons, but because its gain is 50-fold lower than the rod's, it requires 100 R^* for the signal to rise above the continuous dark noise. By $1000R^*$ /integration time, when rods are nearly saturated, the cone responds strongly. The cone photocurrent saturates at $\sim 30\text{pA}$ (similar to the rod), but this occurs at much higher intensities up to $10^6 R^*$ /cone/integration time [54], [55]. Consequently, whereas the rod signal is at first binary and then graded, but always corrupted by photon noise, the cone signal is always graded and far less noisy. Thus, the so-called photoreceptors in silicon retinas are actually cones.

2.1.2 Horizontal Cell

Horizontal cell dendrites are inserted as lateral elements into the invaginating contacts of cone pedicles, and horizontal cell axon terminals form the lateral elements within rod spherules. It is assumed that horizontal cells release the inhibitory transmitter and provide feedback inhibition at the photoreceptor synaptic terminal. As horizontal cells summate light signals from several cones, such feedback would cause lateral inhibition, through which a cone's light response is reduced by the illumination of neighboring cones. This mechanism is thought to enhance the response to the edges of visual stimuli and to reduce the response to areas of uniform brightness. There is also evidence that light-dependent release of GABA from horizontal cells provides feed-forward inhibition of bipolar cell dendrites. Irrespective of their precise mode of action, horizontal cells sum light responses across a broad region, and subtract it from the local signal. Because horizontal cells are coupled through gap junctions, their

receptive fields can be much wider than their dendritic fields[41], [52].

2.1.3 Bipolar Cells

Bipolar cell types of the primate retina are shown in Fig. 2. 3 [42]. Their axons terminate at different levels in the IPL; those terminating in the outer half are putative OFF cone bipolar cells, and those terminating in the inner half are ON bipolar cells. The axons of OFF and ON cone bipolar cells terminate at different levels (strata) within the IPL: OFF in the outer half, ON in the inner half. However, superimposed on this ON/OFF dichotomy, further bipolar cell types have been described in Fig. 2. 3 and every mammalian retina that has been studied contains at least four types of OFF and four types of ON cone bipolar cell [56], [57]. We are just beginning to understand their functional roles²⁸. Axons that carry more transient OFF light signals terminate in the middle of the IPL; those that carry sustained OFF light signals are found in a more peripheral position [58], [59].

2.1.4 Amacrine Cells

There are twenty-nine types of amacrine cells. All retinal ganglion cells receive input from cone bipolar cells, but most direct synapses on the ganglion cells are from amacrine cells. The exact fraction varies among different functional types of ganglion cells, ranging from roughly 70% for alpha cells (large, movement-sensitive ganglion cells found in most mammals) to 50% for the midget ganglion cells located in the monkey central fovea. Amacrine cells also make inhibitory synapses on the axon terminals of bipolar cells, thus controlling their output to ganglion cells. In contrast to horizontal cells, which have a single broad role, amacrine cells have dedicated functions—they carry out narrow tasks concerned with shaping and control of ganglion cell responses. The different amacrine cells have distinct pre- and postsynaptic partners, contain a variety of neurotransmitters. Amacrine cells seem to account for correlated firing among ganglion cells. Shared input from a common amacrine cell will tend to make ganglion cells fire together [60].

2.1.5 Ganglion Cells

The retinal ganglion cells summarized signals of previous retinal cells, and then send neural spiking to the brain. They have been found to diverse in both stratification and physiological properties. There are at least 10–15 different morphological types of ganglion cell in any mammalian retina [42], [51]. The underlying belief is that cells with distinct morphologies have distinct physiological functions. It was thought that they represented feature detectors that react to specific light stimuli. Among them

were direction selective ganglion cells, which respond to light spots that move in a certain direction across their receptive field. In the primate retina, two types of concentrically organized receptive field have been found. One type showed no chromatic receptive field organization, whereas in the other type the centre and surround were chromatically selective [61]. The detailed classification of ganglion cells is described in section 2.2.

2.2 THE CLASSIFICATION OF GANGLION CELLS OF THE RABBITS' RETINA

The physiological classification of ganglion cells has been the most detailed in rabbit of any mammalian species. So the classification of ganglion cells of the rabbit is introduced here. Many neuroscientists have made classifications of ganglion cells. Although there are areas of disagreement all neuroscientists confirm this diversity. Morphologically, the retinal ganglion cells are divided into two types of concentrically organized receptive fields, one with a small, linearly summing receptive field center (X cell) and another with a large, non-linear responsive area (Y cell). In the cat, the correspondence between X-cells and β , and Y-cells and α was established long ago, as was the analogous match between P and M, midget and parasol cells in the monkey [60]. Physiologically, the retinal ganglion cells are divided into ON centre/OFF surround and OFF centre/ON surround cells [41].

In this thesis, the classification of [62], [63] is adopted. Here the ganglion cells are divided into with concentric receptive fields and with complex receptive fields. Concentric ganglion cells were those that had ON or OFF centers with antagonistic surrounds and were classified into different groups by extracellular recordings of their ON- or OFF-center response sign, excitatory receptive field center size, linearity of spatial summation, and brisk vs. sluggish and transient vs. sustained responses to step changes in light intensity [62]. Ganglion cells that had complex receptive field properties are ON-OFF and ON direction-selective cells, orientation-selective cells, local edge detectors, and uniformity detectors. Cells were first classified by their characteristic extracellular responses to manually controlled stimuli similar to those which have been used in previous in vivo studies [63]. The recorded cell types are presented in Table 2. 1 [38]. In [38], space-time patterns of concentric ganglion cells are reported. Spiking patterns of five different classes of ganglion cells are shown in Fig. 2. 4. We can see in Fig. 2. 4 that even for the same cell, the space-time patterns

vary in every record.

Based on the results of [38], a simple multi-layer cellular neural/non-linear network (CNN) model was built [44]. Fig. 2. 5 is a sketch of the processing structure of the CNN model of the mammalian rabbit retina. Each layer of a neuron-type is represented by a horizontal line. The vertical lines represent the connections between cell types. The third row contains the retina output cells, where the names are the neurobiologic names and their positive input is the bipolar layer, and their negative inputs are the amacrine FF layers. In chapter 5, the ON Brisk Transient ganglion cell is chosen to verify the design methodology proposed in this thesis.

2.3 OPERATING PRINCIPLE – FROM THE ENGINEERING

POINTS OF VIEW

The instantaneous dynamic range of the photoreceptors spans only about 1000:1, but the mean level around which this instantaneous range operates can move, facilitated by gain adjustments in the photoreceptors themselves, over a range of 10^6 to 1 or more, from twilight to bright sunlight. There is a range of intensities of about 10^3 :1 near twilight where the cone photoreceptors do not operate. In this range the visual message is conveyed through the rod system that hijacks the cone circuitry within the retina. Above this intensity range the cones predominate. The switch is obvious to us: it is the intensity at which we begin to see color.

Photoreceptor activity is passed to the next processing layer, the horizontal cells. These cells are strongly interconnected so they form a broad diffusion layer. Each horizontal cell receives input from a local population of photoreceptors, and because of the interconnections, the horizontal cell layer acts to diffuse the image, so the visual image appears to be quite blurred with a space constant of a few degrees. Diffusion within this layer generates some important qualities for the visual image. Horizontal cell activity at any point represents a local spatial (and temporal) average of neural activity.

The horizontal cells “feed back” with a sign-inverting phase to the cone photoreceptors to modify the representation generated by the transduction component of the photoreceptors. The range of neural activity in the feedback-enhanced image is reduced so that small incremental changes around the mean are well-represented, while changes far from the mean level are suppressed. The feedback of a blurred image has an effect similar to that used by early photographers to enhance the edges

of an image. They developed a positive transparency on top of a slightly blurred negative transparency. The negative feedback from horizontal cells to cones accomplishes a similar effect, edge-enhancing the resulting visual representation.

This interaction is “read out” by the bipolar cells. These representations have been enhanced in a variety of ways. They are gain adjusted to fit the ambient level of the original scene, and then mean adjusted by the horizontal cell network, and the features of the scene are edge-enhanced as a result of the interaction of the sharp and blurred images. Bipolar cells exist in two main varieties: those that represent (by activity coming out of the plane) the brightness of the image, and those that represent (by activity moving back into the plane) the darkness of the image. These two representations are useful because the visual system is best at identifying small changes in intensity above and below the mean level, and having two separate systems, each tuned to one of these representations appears to be an effective implementation of this phenomenon.

The nature of synaptic connections in the nervous system is such that it favors transmission of increases in activity (out of the plane) over decreases in activity (into the plane). Consequently, the signals leaving the two bipolar cell arrays are “rectified” in that the (out of the plane) activity is accentuated and the activity into the plane is lost. These two representations of the visual world are now presented to the next layer of processing for further enhancement of the visual representation. This is the region where the dozen movies of the visual world are generated. Each of the representations is “filtered” in space and time so that numerous representations, each with a different space or time constant, are generated.

Then different space-time components interact with each other to generate a further enhanced representation. These interrelationships between different space-time representations are implemented by a second set of interneurons, the amacrine cells in the inner retina. Unlike the horizontal cells discussed above that form a highly uniform interconnected system, there is great diversity in the amacrine cell population, and they are not strongly interconnected. Each seems to receive input from one or more space-time representations, delivered by the bipolar cells, and communicate by inhibiting one or more of the other space-time representations.

If we think of each space-time representation as an extracted “visual feature”, then the amacrine cells form a set of interactions between features. One way to think about this would be to imagine that each feature is broadcasting, via the amacrine

cells, to turn down its representation in other feature detectors, and simultaneously, all other feature detectors, via the amacrine cells are turning down their specific feature quality in adjacent features. This interaction represents a form of lateral inhibition, not in physical space but in the abstract space of the features themselves [40].



Table 2. 1. Ganglion cell types, defined by response to spot sizes and level of dendritic stratification [38]

Cell type ¹	Previous classification [62]	Response Polarity	Spiking response to small spots (100-200 μ m)	Spiking response to larger spots (600-1000 μ m)	Morphology
1 (22)	OFF Brisk Linear 1	OFF	Sustained ²	Sustained	Monostratified
2 (7)	OFF Brisk Linear 2	OFF	Sustained	Sustained	Monostratified, dye-coupled to amacrine cells ³
3 (36)	OFF Local Edge Detector	ON OFF for 50-200 μ m OFF for >200 μ m spots	Sustained	No response	Monostratified
4 (25)	OFF Brisk Transient	OFF	Transient	Transient	Monostratified
5 (16)	ON Brisk Transient Nonlinear	ON	Transient	Transient	Monostratified
6 (20)	ON Brisk Transient Linear	ON	Transient	Very small response or no response	Monostratified
7 (28)	ON Brisk Sustained Linear	ON	Sustained	Transient	Diffusively stratified
8 (6)	ON Sluggish	ON	Sustained	Sustained	monostratified
9 (10)	?	ON	Sustained	Sustained	Bi-stratified
10 (4)	ON Local Edge Detector	ON	Sustained	No response	?

¹ Numbers in brackets refer to the number of measured cells. (16 ON cells and 13 OFF cells were not classified.)

² The Response was defined Transient if at the end of a 1-s flash there was no response. Otherwise it was defined as Sustained. ON cells were tested with white spots; OFF cells with black spots.

³ This cell type had a little wider ramification than the other monostratified cell classes.

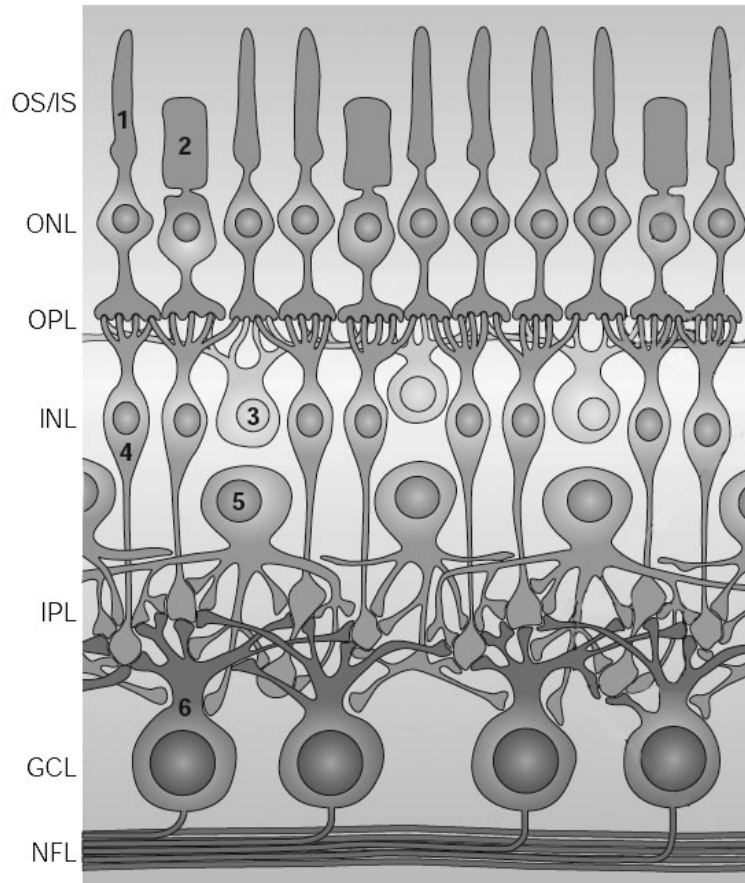


Fig. 2. 1. Schematic of the mammalian retina. Reprinted from [41].



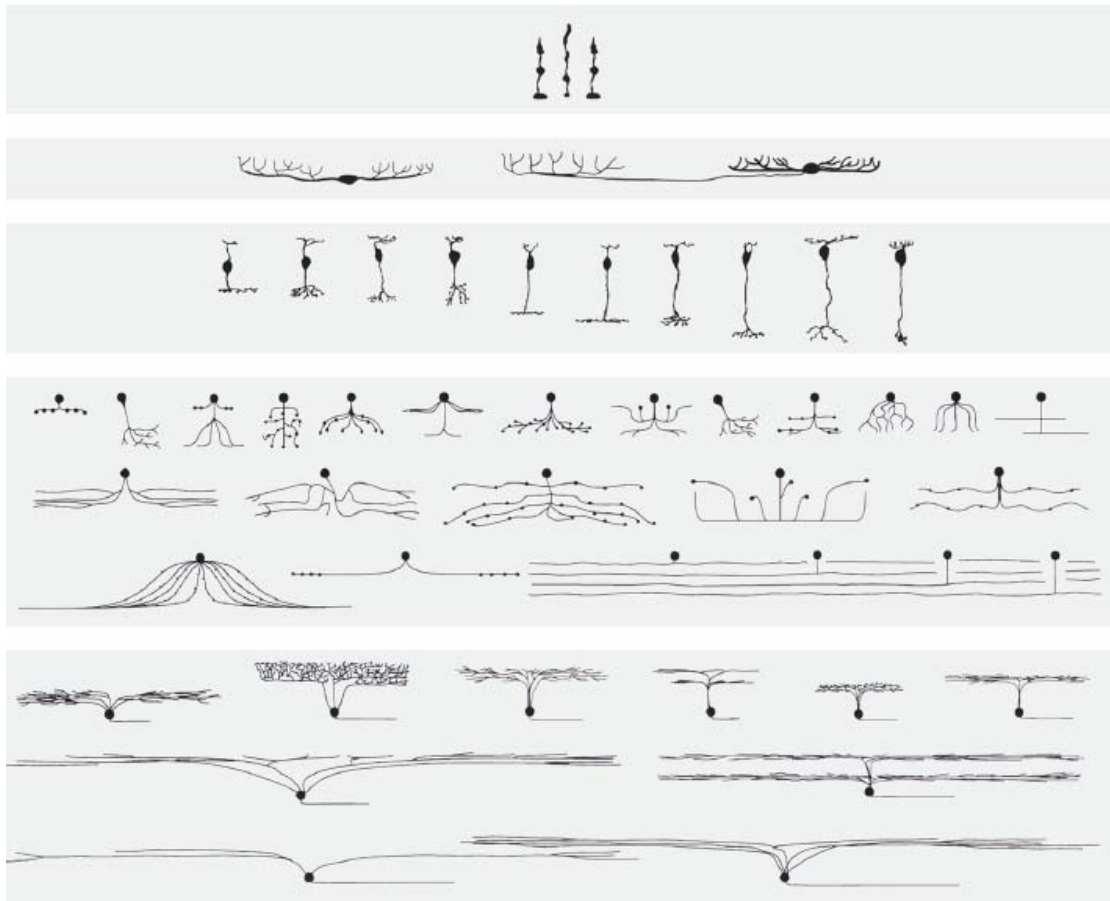


Fig. 2. 2. The major cell types of a typical mammalian retina. From the top row to the bottom, photoreceptors, horizontal cells, bipolar cells, amacrine cells and ganglion cells. Reprinted from [60].

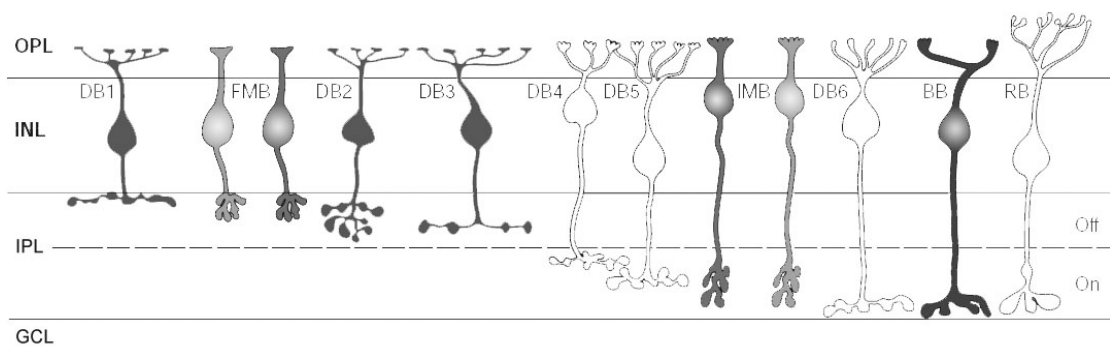


Fig. 2. 3. Bipolar cell types of the primate retina. Reprinted from [41].

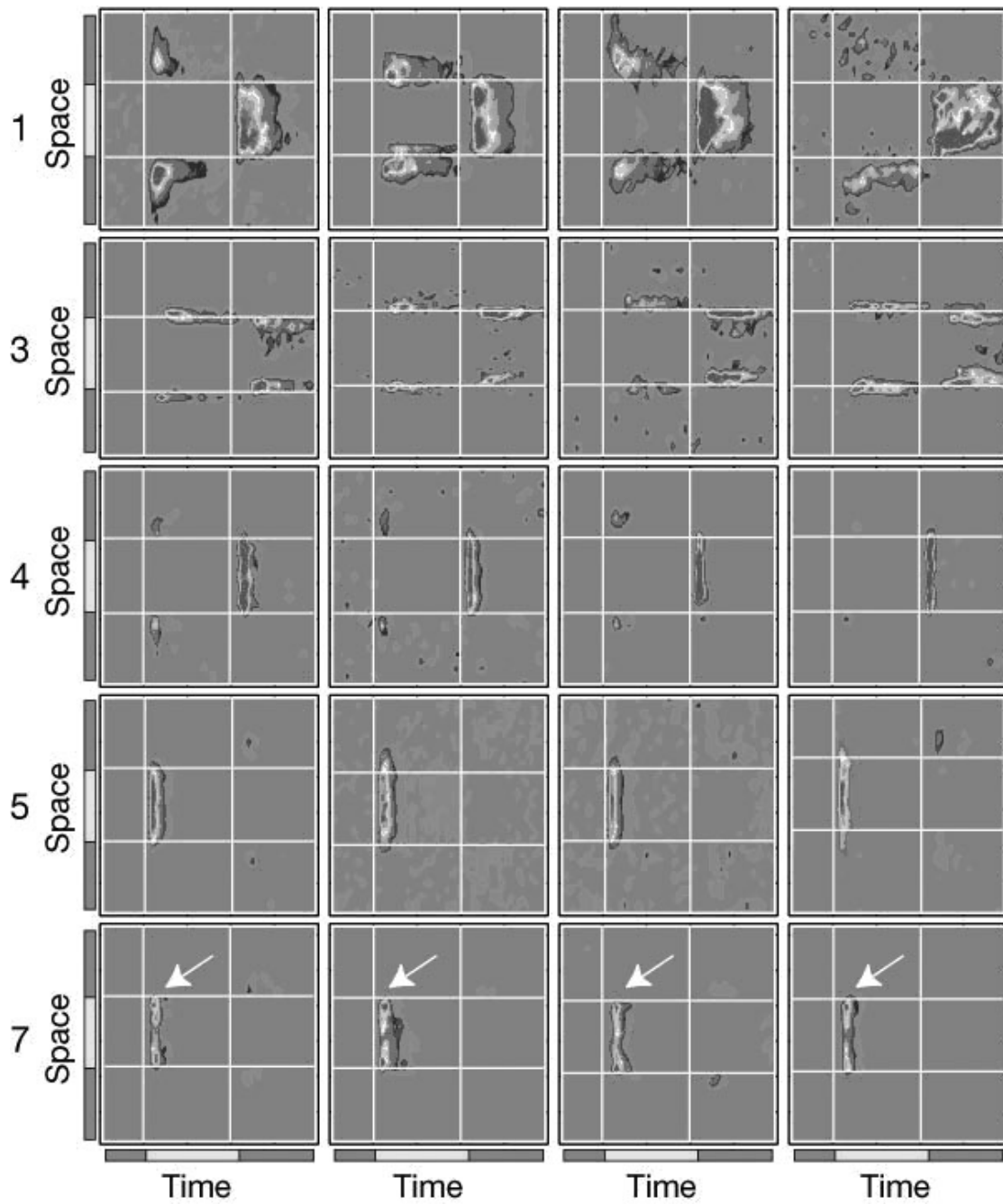


Fig. 2. 4. Spiking patterns in each row (measured from four different members of the same cell class) for five different classes of ganglion cells. The numbers at the beginning of each row refer to the classification shown in Table 2. 1. The arrows in row 5 (cell type 7) point to the enhanced activity at the stimulus edge, a feature that is characteristic of this class [38].

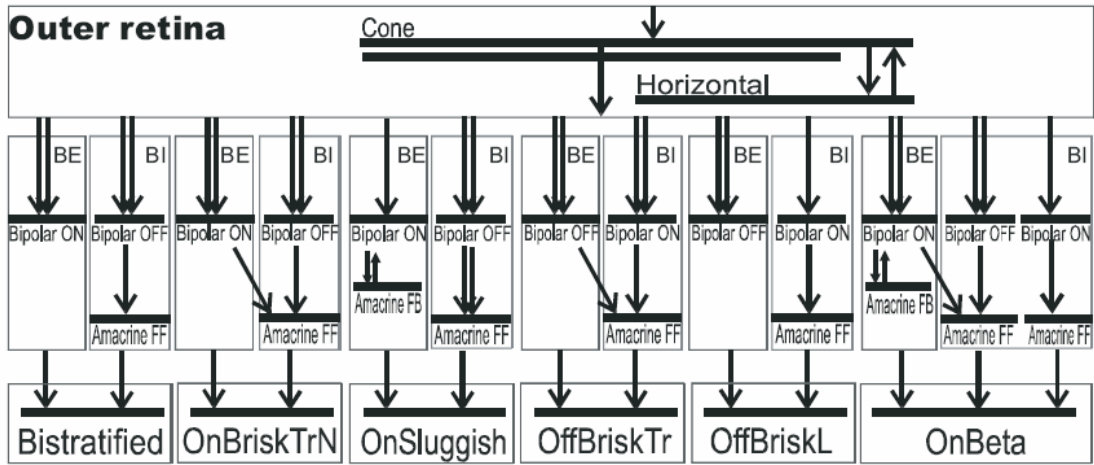


Fig. 2. 5. A sketch of the processing structure of the CNN model of the mammalian rabbit retina [44].



CHAPTER 3

THE BJT-BASED SILICON RETINA CHIPS (I) – THE IMAGE SENSORS

In digital image processing system, the inputs from a 2-D image sensor array are first scanned, quantized, and subsequently processed by the pipelined parallel algorithms or multiprocessors [64], [65] to obtain a fast throughput rate. In this processing system, the computational cost for machine vision implementation by large-scale digital processors is quite high, and the processing speed is still not fast enough for real-time applications.

The retina is the early processing element in the visual nervous system of the vertebrate [1], [66], [67]. It performs the early visual processing in a parallel manner to provide real-time information for the brain to perceive the images of the surrounding world [76]-[78]. Due to the superior processing capability of the retina, many efforts have been devoted to implement the functions of retina in the silicon integrated circuits (IC's) [2][3][20][21][24][68]. To implement the functions of the retina, analog circuits are superior to digital circuits because analog circuits have the advantages of compact structure to perform useful operations, small chip size, and low-power consumption [70], [79]-[83].

In this chapter, three retinal image sensors are presented. In section 3.1, a new structure of the 2-D silicon retina is introduced. This is the first BJT-based silicon retina, which is the pioneer of following research. In section 3.2, an improved BJT-based silicon retina with tunable image smoothing capability is proposed. This design improved the smoothing mechanism of the design of section 3.1. Thus the smoothing range can be tunable. In section 3.3, a low-photocurrent CMOS retinal focal-plane sensor with a pseudo-BJT smoothing network and an adaptive current schmitt trigger for scanner applications is presented. This is a technical application of the BJT silicon retina design. Summary of these three works are shown in Table 3. 1.

3.1 A NEW STRUCTURE OF THE 2-D SILICON RETINA

3.1.1 Introduction

To take advantages of the retina in image processing, the two retinal functions of edge extraction and moving object detection should be incorporated into the photosensing system. An interesting hardware implementation of retinal processing on

a physical semiconductor substrate has been presented by Mead et al. [67]. The main architecture of this implementation is a resistive network or mesh that receives the inputs from a set of photoreceptors and performs the smooth function. This resistive network is equivalent to the horizontal cell in the vertebrate retina. Recently, some important image processing architectures using the resistive mesh have been presented [68]-[72], [10]. To realize a large resistive mesh on a chip, several structures have been proposed [68]-[72], [10] to minimize the size of the resistive elements. However, the resistive network still requires large chip area and complicated wiring. This makes the VLSI implementation of the retina quite difficult.

A new concept is developed to implement the smooth function in a compact and efficient semiconductor structure that is fully compatible with both CMOS and BICMOS technologies and can be easily integrated with other integrated circuits to form a VLSI image processing system. The new structure consists of a phototransistor array with a common base region. When the light is incident upon the common open-base region, excess carriers are generated and diffused out. The result of the carrier diffusion and distribution makes the output emitter currents decay logarithmically with distance, just like that in the resistive network. This phenomenon, which has bothered the operation of the photosensing arrays in the CCD design [73], can be used to implement the smooth function of the vertebrate retina. Thus, the silicon retina can be realized in a compact structure without complex resistive network.

In each basic cell of the proposed silicon retina structure, one parasitic PNP (NPN) bipolar phototransistor in the common N- (P-) base region is used to sense the light and generate the smoothing photocurrent. The other parasitic bipolar phototransistor in a separate base region is used to sense the light and generate the instantaneous photocurrent. The new silicon retina structure has been analyzed and experimentally verified in both 1-D linear array [74] and 2-D array.

In Section 3.1.2, the structure and the operation of the new silicon retina are described. The important characteristics of edge detection and moving object detection are also discussed. The 2-D array design of the new silicon retina is described in Section 3.1.3, where the experimental results are also analyzed and discussed in detail. In Section 3.1.4, the conclusion is given.

3.1.2 Cell Architecture and Operational Principle

The proposed new CMOS retina structure contains many basic cells. Each basic

cell consists of an inner open-base parasitic PNP (NPN) phototransistor as the photoreceptor and an outer open-base parasitic PNP (NPN) phototransistor in the common N- (P-) well as the smooth unit. The cross-sectional view of the CMOS N-well retina cell is shown in Fig. 3.1. 1(a), and the layout diagram is shown in Fig. 3.1. 1(b). As shown in Fig. 3.1. 1(b), the inner open-base parasitic PNP transistor is surrounded by the V_{SS} -biased P-substrate so that it is isolated from the outer open-base parasitic PNP transistors. The outer PNP phototransistor shares the same base region (N-well) with all other outer PNP phototransistors in other cells. It is seen that a metal-defined light window is located in the open-base regions of the two PNP phototransistors. When an image light is incident upon the chip, only the semiconductor region under the window receives the light. The light generates carriers in the open-base region. This results in the photocurrent at the emitter. The depletion region of the collector junction has a greater efficiency in generating the carriers when the light is incident upon the silicon. Thus, the metal-defined window is put across the collector junctions of the two PNP phototransistors.

To make the phototransistors operated in the active region, the common P-substrate collector must be biased by a negative V_{SS} voltage, and their emitters are kept at the virtual ground. When the light is incident upon the cell, excess carriers are generated in both isolated inner N-well and surrounded outer N-well. These photogenerated carriers in the floating base region act as those injected by the external base current and generate an emitter current $I_{e,inner}$ in the inner cell. On the other hand, the smooth network consisting of many phototransistors in the surrounding common outer N-well also receives a nearly equal input photocurrent in the common N-well base region and produces a smooth current $I_{e,outer}$ at each emitter, which is one of the output nodes in the network. $I_{e,outer}$ is then subtracted by $I_{e,inner}$ with suitable weighting factors, and the difference is further converted into voltage for further processing. This output voltage has the similar response as the output of a vertebrate retina.

The smooth function of the new silicon retina cell is performed by the outer phototransistor array in the surrounding common N-well. Fig. 3.1. 2 shows the conceptual cross-sectional view of the outer phototransistor array. As shown in Fig. 3.1. 2, the outer phototransistor array acts as a multi-emitter PNP phototransistor. Because the collector is biased by the negative V_{SS} , and the emitters are kept at virtual ground, there is a reverse bias on the collector junction, and a large electric field is produced across the depletion region. When the light is incident upon the

phototransistor, the electron-hole pairs are photogenerated in the base region (common N-well) or the depletion region of the collector junction. Most photogenerated minority carriers (holes) diffuse toward the collector junction and are swept to the collector. On the other hand, the photogenerated electrons act as the injected electrons, similar to those injected by an external base current I_b . They diffuse out in the common base region and could reach the emitter junctions and make the junctions forward biased. Along the diffusion path, parts of them are recombined by the excess holes in the active base regions underneath the emitter junctions.

To explain the phenomenon more clearly, the 1-D linear phototransistor array as shown in Fig. 3.1. 2 is considered. If the light is incident upon the phototransistor no.0 only, the photogenerated electrons diffuse out to other dark phototransistors. Due to the effect of carrier recombination, the number of these diffused electrons reaching the base regions of the dark phototransistors located farther away from the no.0 phototransistor becomes smaller and so does the effective base current. Due to the smaller base current and the voltage drop on the series base spreading resistance, the resultant base-emitter voltages V_{be} in the dark phototransistors become smaller. Thus, the emitter currents of these phototransistors are smaller as their locations are farther away from the illuminated phototransistor. Generally, if the dark phototransistors are located not too far away from the illuminated phototransistor, the excess carrier density is high, and both spreading resistance and recombination effects are important. However, if the distance is comparable with the carrier diffusion length, the excess carrier density is low, and only the spreading resistance effect dominates.

To characterize the above mentioned phenomena and effects in the equivalent circuit, the 2-D smooth unit with the phototransistors array in the outer common N-well region as shown in Fig. 3.1. 2 may be represented by the equivalent network as shown in Fig. 3.1. 3. In Fig. 3.1. 3, the effective series resistors R_N are connected into the 2-D structure. They are nearly independent of the cell location if only the spreading resistance effect is considered. Generally, the distance among the cells affects the R_N value and thus the smooth function. If the cell distance is scaled down, R_N is smaller, and the smooth function is enhanced. The resultant smoothing curve is less sharp, and more cells are involved in the smoothing. The other effect of cell scaling is to increase the resolution and the settling time of the smooth network.

If the surface recombination effect is considered, extra current sources connected between the base of the phototransistor and the ground may be used. These currents

are slightly larger for those dark cells close to the light incident area and very small for those dark cells far away from the light incident area.

From the equivalent circuit shown in Fig. 3.1. 3, the base current I_b of the phototransistor can be expressed as

$$I_b \approx I_c / \beta \approx (I_s / \beta) \exp(qV_{be} / kT) \quad (1)$$

where I_s is the reverse saturation current of the phototransistor. V_{be} is the base-emitter voltage, β is the dc current gain, q is the electronic charge, k is the Boltzmann constant, and T is the absolute temperature. Taking the voltage drop on R_N into consideration, the ratio of the base currents at the node N and the adjacent node $N + 1$ can be written from (1) as

$$\begin{aligned} \frac{I_b(N+1)}{I_b(N)} &= \exp[qV_{be}(N+1)/kT - qV_{be}(n)/kT] \\ &= \exp(q\Delta V_{be} / kT) \\ &= \exp[qR_N I(N) / kT] \end{aligned} \quad (2)$$

where I is the current flowing through R_N , and the current gain β is assumed to be constant. From the above equation, the base currents of the two adjacent nodes have the exponential relationship and so do their corresponding emitter currents. This verifies the smooth function in the new silicon retina.

In the retina, the edge of an object is detected by the high contrast between surface of the object and background. The general principle of the edge detection can be understood by using the curves in Fig. 3.1. 4. In Fig. 3.1. 4, the original signal has a very large edge contrast. After smoothing, the smooth signal is obtained with a smooth edge. By subtracting both signals, an abrupt difference from negative to positive at the edge can be obtained. This difference signal can be easily detected.

In the proposed structure, the smooth signal of the input image can be obtained from the emitter current $I_{e,outer}$ of the outer phototransistor. At the same time, the emitter current $I_{e,inner}$ of the inner phototransistor represents the signal of the original image. The subtraction of these two current $I_{e,outer}$ and $I_{e,inner}$ results in a difference signal with a sharp change from negative to positive at the edge of the image. Thus, the edge signal of the image can be detected definitely.

When a moving object appears, the relationship of the object image and the silicon retina cell is shown in Fig. 3.1. 5. As the image of the moving object passes by one of the retina cells during the fixed period of time, the cell senses a light pulse with the

same period of time. Thus, the moving object detection of the silicon retina can be tested by measuring the cell pulse responses with a moving input image.

The large base-collector junction and multi-emitter junctions in the outer phototransistor array form a large distributed RC network where R is the spreading resistance of the base region, and C is either collector or emitter junction capacitance. This can also be understood from the lumped equivalent circuit of Fig. 3.1. 3. When the light is incident upon the outer area, the photogenerated base current diffuses out to reach a certain number of outer phototransistors. In these phototransistors, the emitter junction should be charged from its original bias $V_{be,dark}$ in the dark to a new value V_{be} , whereas, the collector junction should be charged from $|V_{ss}| - |V_{be,dark}|$ to $|V_{ss}| - |V_{be}|$. Thus, it takes time for the outer phototransistor network to reach the new steady state when the light is incident upon it. This time is called the settling time or the integration time of the smooth network. On the other hand, the isolated inner phototransistor has a quick response to the light. This means that at the instant when the light is incident upon the retina cell, $I_{e,outer}$ is still kept at the original value in the dark, but $I_{e,inner}$ is raised up to the new value. Thus, $I_{e,inner} - I_{e,outer}$ has a positive value. Since $I_{e,outer}$ gradually increases to its final stable value, which is close to $I_{e,inner}$, $I_{e,inner} - I_{e,outer}$ becomes less and less positive. Similarly, when the light is suddenly off, $I_{e,outer}$ is kept at its stable value while $I_{e,inner}$ is suddenly reduced to its dark value. Thus, $I_{e,inner} - I_{e,outer}$ is negative and gradually increases to its stable value in the dark. Measuring the positive and negative pulses of $I_{e,inner} - I_{e,outer}$ can easily sense the moving object passing by the measured cell. In this way, the moving object can be detected by the proposed silicon retina.

In the detection of a moving object using the proposed silicon retina, the sensitivity can be increased by using a high-gain output amplifier. The detection speed can be improved by decreasing the settling time or the integration time. As in the edge extraction, the resolution can be improved by using a scaled cell array.

3.1.3 2-D Silicon Retina Array Design and Experimental Results

The overall architecture of the 2-D silicon retina array is shown in Fig. 3.1. 6(a), and the structure of the basic cell circuitry in the 2-D array is shown in Fig. 3.1. 6(b). In Fig. 3.1. 6(a), two decoders and a multiplexer are used to control the output of the cell. The row decoder decodes the m row address bits and activates one of 2^m row control signals row and row'. The column decoder decodes the n column address bits to activate one of 2^n output channels in the multiplexer. Through the multiplexer, the

selected output channel sends out the inner and the outer emitter currents of the selected cell to the two tunable R_m amplifiers, and the input cell currents are converted into the voltages. Then, the two voltages are sent to the output differential amplifier with the gain A_v . The output voltage V_{out} of the differential amplifier can be expressed as

$$V_{out} = -R_m A_v (I_{e,outer} - I_{e,inner}) \quad (3)$$

where

$$R_m \cong \frac{1}{g_{mn3} + g_{mp3}}$$

$$A_v \cong \frac{g_{mp1}}{g_{mn1}} \left(1 + \frac{2g_{mp1}}{g_{dp1} + g_{dn1}} \right) \left(1 - \frac{g_{mpo2}}{g_{mpo1}} \right)$$

As shown in Fig. 3.1. 6(b), the basic cell contains a PNP phototransistor pair and four NMOS switches. In the chip layout, each cell has equal distance to its four nearest neighbors. The four switches in the cell are controlled by the row control signal row and its complement signal row'. When one row of the silicon retina cells is selected by the row address bits, the control signal row of this row is activated to high, whereas, row' is low. Thus, SW1 and SW2 are closed to connect the two emitters to the multiplexer. Through the multiplexer, they are further connected to the inputs of the R_m amplifiers, which are kept at virtual ground. Thus, the emitters are nearly grounded to send out $I_{e,outer}$ and $I_{e,inner}$. At the same time, SW3 and SW4 are open to prevent the emitter currents from flowing into the ground. Oppositely, when the row of the silicon retina cells isn't selected, the control signal row of this row is low, and row' is high. Then, SW1 and SW2 are open to prevent the emitter currents from reaching the multiplexer and the output amplifier. Meanwhile, SW3 and SW4 are closed to connect both emitters to ground so that the deselected emitter currents are bypassed to ground.

The circuit diagrams of the R_m amplifier and the output buffer are shown in Fig. 3.1. 7(a) and (b), respectively. The R_m amplifier in Fig. 3.1. 7(a) with the shunt-shunt feedback configuration offers a very low input impedance, a good linearity, and a high frequency bandwidth [75]. In Fig. 3.1. 7(a), the basic I-V conversion is achieved by the common-gate transistor MN1(MP1) and the current source device MP2(MN2). The transistors MN4 and MP4 form a source-follower output buffer to enhance the driving capability and decrease the output impedance. The transistors MN3 and MP3,

which offer a feedback path from the output stage, are used to reduce both input and output impedances. The transistors MNR and MPR are used to adjust the gain of the R_m amplifier. The output buffer in Fig. 3.1. 7(b) consists of a basic differential amplifier and a source-follower. The differential amplifier produces an output voltage that is proportional with $I_{e,inner} - I_{e,outer}$ whereas, the source-follower offers a large driving capability to drive the output pads. The typical measured characteristics of the fabricated R_m amplifier are listed in Table 3.1. 1.

In the structure of Fig. 3.1. 6(a), the output signal of each cell can be accessed by sending a set of address bits. The whole image frame can be obtained pixel-by-pixel by sending a sequence of address bits. If parallel outputs are preferred, the column decoder and the multiplexer can be omitted, and the i outputs can be obtained through n -output amplifiers. In this way, the whole image frame can be obtained row-by-row by sending a sequence of row address bits.

In this research, two experimental 32x32 silicon retina array chips have been designed and fabricated by using 0.8 μ m double-poly double-metal N-well CMOS process. One of the chips is designed with both R_m amplifier and output buffer as shown in Fig. 3.1. 6(a) to measure the full function of the silicon retina. The other is designed without R_m amplifiers and output buffer to measure the cell current directly. Both cell arrays have a fill factor of 0.33.

In the proposed silicon retina, there are four NMOS switches, two phototransistors, and five interconnection lines as shown in Fig. 3.1. 6(b). Generally, the NMOS switches are uncritical devices, and the minimum device dimension can be used. The phototransistor area can be reduced to the limit where the generated minimum photocurrent can be detected. The two major limitations on cell compaction are 1) the layout design rules, especially those for the N-well spacings and 2) the number of available interconnection levels to route the five cell signal lines compactly. In this experimental work, the cell is designed by using a relaxed design rule, and the cell area is 60 μ m x 60 μ m. Further cell area reduction can be done by pushing the cell layout to the minimum design rules.

To measure the performance of the new silicon retina cell array, a low-power He-Ne laser and several lens are used to generate a definite input image for test. Because of the serious scattering of the regular light source [74], it cannot be used to generate the input image. However, since the retina is made of semiconductor silicon, it will function well under regular light. In the test setup, the lens focuses the

low-power laser beam to a small light spot that is incident upon the silicon retina cells. In the measurement of the smooth characteristic of the outer phototransistor array, the laser light spot is incident upon the corner of the silicon retina array. Fig. 3.1. 9(a) shows the measured $I_{e,inner}$ of the inner phototransistor array in the 2-D plot, whereas. Fig. 3.1. 9(b) shows the measured $I_{e,outer}$ of the outer phototransistor array in the 2-D plot. As discussed above, $I_{e,inner}$ represents the local intensity of the input image, whereas, $I_{e,outer}$ represents the smoothed input image. Comparing Fig. 3.1. 9(a) with (b), it can be seen that the outer phototransistor array really smoothes the whole input image. To see the detail, the contents on the line $y=5$ in Fig. 3.1. 9(a) and (b) are selected to display in Fig. 3.1. 10 where the measured $I_{e,inner}$ is scaled down by a factor of 0.25 for easy comparison with $I_{e,outer}$. Since the light spot has some diffraction effects, its effective incident area covers twelve pixels of cells so that $I_{e,inner}$ in these cells is not zero as may be seen in. Comparing the curves of $I_{e,inner}$ and $I_{e,outer}$, the smooth effect of the outer phototransistor array can be verified. To analyze the function of the outer phototransistor array using the proposed equivalent circuit in Fig. 3, the device parameters of the PNP bipolar transistors are measured first.



Table 3.1. 2 shows the measured device parameters of the PNP transistor. Ideally, both inner and outer phototransistors have the same photogenerated current. Thus, the emitter current $I_{e,inner}$ of the inner phototransistor is used as the input current of the light-incident outer phototransistors in the simulation. Fig. 11 shows the 2-D graph for the SPICE simulated $I_{e,outer}$ of the outer phototransistor array with R_N in Fig. 3 equal to $2.8 \text{ k}\Omega$. To further investigate the measured data and the simulated data, the contents on the line $y=5$ in Fig. 11 for the simulated $I_{e,outer}$ are also plotted in Fig. 10 Fig. 3.1. 10 for comparison. The consistence between the simulated $I_{e,outer}$ curve and the measured $I_{e,outer}$ is good, which proves the suitability of the proposed equivalent circuit in Fig. 3.1. 3 in simulating the behavior of the outer phototransistor array as the smooth network.

In Fig. 3.1. 10, the simulated $I_{e,outer}$ curve is slightly sharper than the measured $I_{e,outer}$. The deviation near the corner may be caused by the edge effect of the smoothing array. On the other hand, the deviations for $x>3$ could be caused by the surface recombination effect mentioned in Section 3.1.2, which is not considered in the equivalent circuit of Fig. 3.1. 3. Due to the surface recombination effect, the measured $I_{e,outer}$ is smaller in those dark cells close to the light-incident cells. The surface recombination effect can be characterized by connecting suitable current sources between the base of the phototransistors and the ground. The use of these current sources decreases $I_{e,outer}$ so that it is more consistent with the measured values as shown in Fig. 3.1. 10.

To measure the edge-detection effect of the proposed silicon retina, the laser light spot is incident upon the chip. Fig. 3.1. 12(a) shows the 2-D plot of the measured output voltages V_{out} of each cell through the on-chip R_m amplifier and output buffer. As shown in Fig. 3.1. 12(a), a voltage change from positive to negative is obtained around the edge of the incident light spot. To observe the response clearly, the curves of $y = 8$ is shown in Fig. 3.1. 12 (b). In Fig. 3.1. 12 (b), a voltage change from positive to negative around the edge of the spot located at the vicinity of $x = 6$, can be seen clearly. By detecting the change, the edge-detection of the proposed silicon retina can be performed in the image processing system.

According to the measurement, the smooth network of the experimental chip takes about 3ms to settle down. To reading out the pixel signal, it takes about $1\mu\text{s}$ to settle down the decode switch introduced transients. Thus, the maximum readout operation

frequency is about 1MHz, and the equivalent frame rate is about 1kHz. The measured results of the fabricated CMOS retina chip are summarized in Table 3.1. 3. Generally, the scaled down cells could decrease the settling times in both smooth network and readout operation. Thus, the maximum operational frequency and the frame rate could be improved.

To further evaluate the performance of the proposed silicon retina, a simple image is used as the input to the fabricated retina, and the output characteristics are measured. Fig. 3.1. 13(a)-(c) show the inner image, the outer image, and the difference image, respectively, when a character “T” pattern is incident upon the silicon retina. In this test pattern, the light intensity decreases gradually from the left-up to right- bottom as showed in Fig. 3.1. 13(a). Under such nonuniform light intensity, the silicon retina still functions well in this measurement. In Fig. 3.1. 13(c), the edge of the pattern “T” stands out from the bright light. In Fig. 3.1. 13(d), only the positive pulses of the response in Fig. 3.1. 13(c) are chosen, and the resulting image becomes clearer. From the above results, it has been verified that the proposed silicon retina can perform the function of edge-detection.

The most important characteristic of the retina is to detect a moving image. As discussed in Section 3.1.2, the moving target detection can be performed by applying a moving image passing across the silicon retina. Fig. 3.1. 14 shows the measured output voltages of the cell (24, 18) and the cell (24, 26). At the moment when the front edge of the moving pattern passes across the measured cells, two successive positive voltage pulses, which are proportional to $I_{e,inner} - I_{e,outer}$ can be recorded on the scope trace as shown in Fig. 3.1. 14. Similarly, two negative voltage pulses, which are proportional to $I_{e,inner} - I_{e,outer}$, can be obtained when the back edge of the moving pattern leaves the measured cells. By detecting the pulses, the moving object can be detected. At the same time, some information about the moving object can also be obtained from the characteristics of the output voltage pulses.

3.1.4 Conclusion

A new structure of the silicon retina cell that contains only two isolated PNP phototransistors is proposed and analyzed. In this structure, the smooth network is implemented by the phototransistors in a common open-base region. Experimental results verify the retinal functions of both edge detection and moving image detection. The new structure has very simple interconnection and wiring. The layout is compact, and the resultant chip area is small. Thus, it is feasible to realize the new silicon retina

with the associated image processing neural network in VLSI. Further research on this new structure will focus on device characterizations and applications.

3.2 AN IMPROVED BJT-BASED SILICON RETINA WITH TUNABLE IMAGE SMOOTHING CAPABILITY

3.2.1 Introduction

Recently, a new silicon retina structure called the bipolar junction transistor (BJT) based silicon retina is proposed [74], [84]. In the BJT-based silicon retina, the function of the horizontal cells is realized by the BJT smoothing network. The BJT's in the BJT smoothing network are used not only as photoreceptors, but as the smoothing devices. The spatial smoothing function on the images is realized by both carrier transport effect and base resistance bias effect [85]-[87] of the BJT's in the same base region. The structure of the BJT smoothing network is simple and compact. Moreover, it is suitable for the very large scale integration (VLSI) implementation. As indicated in [88]-[92], the smoothing range of those images with wide-range variations on intensity or contrast is required to be adjustable. In the BJT smoothing network of [74] and [84], the extrinsic base resistance among the active bases of the BJT's can be designed to obtain different image smoothing ranges. However, it cannot be adjusted after fabrication. This limits the applications of the BJT-based silicon retina in smart sensors.

The BJT smoothing network with an enhancement-mode n-channel MOSFET inserted between the bases of two parasitic p-n-p BJT's existing in an n-well CMOS process is proposed here to increase the tunability of image smoothing ranges. It is shown that the inserted nMOSFET can be operated either in the strong-inversion region or subthreshold region to provide a wide range of resistance values to achieve the wide-range adjustment of smoothing ranges. As compared to the original BJT smoothing network [74], [84], the proposed BJT smoothing network has smaller chip area in realizing the same base resistance and higher tunability of image smoothing ranges.

In the focal-plane array (FPA) of the proposed BJT-based silicon retina, the access circuit of silicon retina cells is realized by using the multiemitter BJT's. Thus, the pixel area can be kept small. A 64x64 experimental chip has been designed and fabricated by using 0.5- μm n-well CMOS technology. The measurement results on both static and dynamic characteristics have verified the correct functions of the

proposed BJT-based silicon retina. In Section 3.2.2, the structure of the proposed BJT-based silicon retina is described and both static and dynamic operations are also analyzed. In Section 3.2.3, the FPA architecture of the silicon retina is presented. The experimental results of the 64x64 experimental chip are presented in Section 3.2.4. Finally, the conclusion is given.

3.2.2 Analyses of the Proposed BJT-Based Silicon Retina

The equivalent circuit of the proposed BJT-based silicon retina is shown in Fig. 3.2. 1 where I_{ES} is the emitter currents of the smoothing pnp BJT in the BJT smoothing network, I_{EI} is the emitter currents of accompanying isolated pnp BJT's, and V_{EB} is the emitter-base junction voltage of the BJT's. In this structure, each pixel has two parasitic vertical pnp BJT's existing in the CMOS process. The two BJT's (called isolated BJT and smoothing BJT) have an open base to serve as phototransistors. Moreover, an enhancement-mode nchannel MOSFET is inserted between the active bases of two smoothing BJT's to form the BJT smoothing network. Thus, the smoothing BJT can serve as phototransistor and smoothing device. The cross-sectional view of the two smoothing BJT's and one nMOSFET in the BJT smoothing network is shown in Fig. 3.2. 2. The tunable conjunction resistance in the BJT smoothing network is efficiently realized by the channel resistance of the inserted nMOSFET's with adjustable common gate bias. As shown in Fig. 3.2. 2, the n source/drain of the nMOSFET is placed on the boundary of the n-wells, which are base regions of the parasitic pnp BJT's in n-well CMOS technology. This makes the proposed BJT smoothing network quite compact.

The BJT smoothing network is used to realize the smoothing function of the horizontal cells in the retina, whereas the accompanied isolated BJT at each pixel is used to realize the photoreceptor cell in the retina. The role of the BJT smoothing network is to compute the spatially and temporally weighted average of images. When the light is incident upon one pixel, it is simultaneously incident upon the two floating bases of both smoothing BJT and isolated BJT. Thus, electron-hole pairs are generated in and nearby the depletion region of the two base-collector junctions. Due to the electric field in the depletion region, the generated electrons are swept into the base region, whereas the holes are swept into the collector. The electrons swept into the base region form a transversely flowing photocurrent in the BJT smoothing network. This gives rise to the forward bias of each base-emitter junction and the current on each emitter. Due to the nMOSFET channel resistance, there are voltage

drops in the base region of the BJT smoothing network when the photoinduced electron currents flow. This effect makes the forward bias voltages of base-emitter junctions different from one another and, thus, the magnitudes of emitter currents in the BJT smoothing network become a *weighted* distribution function of distance. The BJT smoothing network, therefore, can perform the required spatial smoothing.

The excitatory synapse between the photoreceptor and horizontal cell in the retina is implemented by letting photons simultaneously stimulate the floating bases of both BJT's at each pixel. According to the analog model [68] of the retina, the response of the bipolar cell in the retina is realized by subtracting the emitter current of the BJT in the smoothing network from that of the isolated BJT at the same pixel. Thus, the output current of the silicon retina in Fig. 3.2. 1 is $I_{EF}-I_{ES}$.

A. Static Characteristics

To model the static characteristics of the BJT smoothing network in Fig. 3.2. 1, where the bipolar phototransistors are operated in the active region, the Ebers-Moll equivalent circuit of the BJT is used. The resultant large-signal equivalent circuit of the BJT smoothing network is shown in Fig. 3.2. 3, where the diode D_P (D_Q) represents the emitter-base junction of the BJT, I_P (I_Q) represents its emitter current, α_F is the common-base forward short-circuit current gain, I_{hv} represents the photocurrent induced by photons, C_{BE} (C_{BC}) is the base-emitter (collector) capacitance of the BJT, C_G is the gate-source (drain) capacitance of the nMOSFET, and V_G (V_P , V_Q) is the gate (drain, source)-substrate voltage of the nMOSFET. If the nMOSFET in Fig. 3.2. 3 is operated in the subthreshold region, the current I_{PQ} flowing through the nMOSFET is the diffusion current. I_{PQ} can be expressed as [93]

$$I_{PQ} = \frac{W}{L} I_{D0} \exp\left(\frac{V_G}{nV_T}\right) \left[\exp\left(-\frac{V_Q}{V_T}\right) - \exp\left(-\frac{V_P}{V_T}\right) \right] \quad (1)$$

where W/L is the channel width-to-length ratio of the nMOSFET, I_{D0} and n are process-dependant parameters, and V_T is the thermal voltage. The emitter currents I_P and I_Q flowing through D_P and D_Q in Fig. 3.2. 2(a), respectively, can be expressed as

$$I_P = I_{E0} \exp\left[\frac{(V_E - V_P)}{V_T}\right] \quad (2)$$

$$I_Q = I_{E0} \exp\left[\frac{(V_E - V_Q)}{V_T}\right] \quad (3)$$

where I_{E0} is the emitter-base reverse saturation current of the BJT and V_E is the emitter voltage. Substituting (2) and (3) into (1) to cancel the terms of V_P and V_Q , we have

$$I_{PQ} = \frac{W}{L} \frac{I_{D0}}{I_{ES}} \exp\left[\frac{\frac{I}{n}V_G - V_E}{V_T}\right] (I_Q - I_P) \quad (4)$$

It can be seen from (4) that I_{PQ} is linearly proportional to $(I_Q - I_P)$ with a constant coefficient determined by V_G and V_E .

From the above analyses, it can be seen that the linear resistive network used to model the horizontal cells can be implemented by the proposed compact BJT smoothing network with subthreshold operated nMOSFET's. This is because the emitter-base junction of the BJT provides the nonlinear conductance to cancel the nonlinear conductance of the nMOSFET so that a linear resistive network is formed. This unique combination of the BJT and MOSFET makes the proposed BJT smoothing network simpler than those proposed in [20], [21], [24].

When $V_G - V_Q$ of the nMOSFET's in Fig. 3.2. 3 is greater than the threshold voltage, the current flowing through the nMOSFET is the drift current and the improved BJT smoothing network acts as a nonlinear network. It performs the spatially smoothing function through the base resistance bias effect of the BJT's [87]. As derived in [87], the emitter current $I_E(n)$ of the smoothing BJT at the n^{th} pixel in the one-dimensional (1-D) smoothing network under the single-point stimulus can be expressed as

$$\frac{I_E(n)}{I_E(0)} = \frac{\cos^2(z)}{\cos^2\left[z\left(1 - \frac{n}{N}\right)\right]} \quad (5)$$

$$z \tan z = \frac{RN}{2V_T} I_{hv}(0) \quad (6)$$

Where R is the sum of base resistance and effective channel resistance of the nMOSFET among the active bases of BJT's, N is the total BJT number in the 1-D network, $I_E(0)$ is the output emitter current at the stimulated pixel, and $I_{hv}(0)$ is the incident photocurrent. As seen from (5) and (6), the emitter current ratio in (5) and the smoothing function are adjustable if R is adjustable. Since the channel resistance of the nMOSFET is dominant in R , the inserted nMOSFET can be used to adjust R

through V_G in order to obtain different smoothing ranges.

Since the base potential difference between two adjacent BJT's in the BJT smoothing network is quite small, the inserted nMOSFET is operated in the linear region when V_G is large. Its channel resistance R_{DS} can be expressed as

$$R_{DS} = \left[\frac{W}{L} \mu_n C_{OX} (V_G - V_E + V_{EB} - V_{th}) \right]^{-1} \quad (7)$$

where W/L is the geometric ratio of the nMOSFET, μ_n is the effective electron mobility, C_{ox} is the gate oxide capacitance per unit area, and V_{th} is the threshold voltage under the reverse substrate bias $V_E - V_{EB}$. As may be seen from (7), R_{DS} is tunable by V_G . Thus, the smoothing characteristics of the BJT smoothing network can be adjusted by [87].

It can be seen from the above analyses that the proposed BJT smoothing network can meet the requirement of adjustable image smoothing from local to global, as indicated in [88]-[92]. Moreover, the proposed BJT smoothing network can perform wide-range smoothing functions with small chip area.

When the incident light intensity is increased, the emitter-base junction voltage V_{EB} of the BJT in the proposed BJT smoothing network is increased. If the MOSFET is in the subthreshold region, the effective channel resistance is decreased with the increasing light intensity. However, the effect of decreasing channel resistance can be completely compensated by the increasing base-emitter junction conductance. Thus, I_{PQ} in (4) remains unchanged, and so does the smoothing characteristics.

If the nMOSFET in the smoothing network is operated in the linear region, R_{DS} in (7) is decreased with light intensity increasing. The reduced R_{DS} in the proposed BJT smoothing network leads to more global smoothing and the low-contrast image becomes less visible. This problem also arises in the MOSFET resistive smoothing networks [20], [21], [24]. However, in the proposed BJT smoothing network, the above-mentioned effect can be compensated.

In the BJT smoothing network of [74] and [84] with an invariant intercell resistance, the smoothing is adaptive. Under brighter background or higher contrast, the BJT smoothing network can be automatically adjusted to achieve a more local smoothing range [87]. This unique performance, which is due to the nonlinear base resistance bias effect, also exists in the proposed BJT smoothing network. When the intensity of light incident on the proposed BJT smoothing network with the

nMOSFET's in the linear region is increased, the increase of the smoothing range due to the decreased R_{DS} can be compensated by the reduced smoothing range due to the base resistance bias effect. The resultant smooth area is still decreased due to the stronger base resistance bias effect.

B. Dynamic Characteristics

To characterize the temporally average function of the proposed BJT smoothing network, its large-signal equivalent circuit with device capacitances, as shown in Fig. 3.2. 3, is considered. This circuit structure is similar to the organization of the horizontal cells in the vertebrate retina, where the node capacitance $C_{BE}+C_{BC}+4C_G$ is equivalent to the membrane capacitance of horizontal cells, whereas the channel resistance R_{DS} of the nMOSFET is equivalent to the resistance of the gap junction between two horizontal cells.

When a flashlight is incident upon the silicon retina, it takes certain delay time to build up the emitter currents of both the isolated BJT and smoothing BJT due to BJT intrinsic turn-on delay and RC components at the base node. In the proposed BJT smoothing network, the delay time t_s is dominated by the RC effect in the equivalent circuit of Fig. 3.2. 3. Assume that under light illumination, the base node voltage V_Q at the incident pixel is decreased from V_{QS} to $V_{QS}-\Delta V_{QS}$. The delay time t_s can be approximately expressed as

$$t_s \approx \frac{(C_{BEQ} + C_{BCQ} + 4C_{GQ})\Delta V_{QS}}{I_{hvQ} + \alpha_F I_Q - 4I_{PQ} - I_Q} \quad (8)$$

where both capacitances and currents are nonlinear function of node voltages and $4I_{PQ}$ is the total current flowing into the base node from the four neighboring nodes, as shown in Fig. 3.2. 3. For the dark pixel in the smoothing network, ΔV_{QS} is smaller and $I_{hvQ} = 0$. Thus, its t_s is nearly the same as that at the incident pixel. Similarly, the delay time t_i to build up the emitter current of the isolated BJT incident by light can be approximately expressed as

$$t_i \approx \frac{(C_{BE} + C_{BC})\Delta V_i}{I_{hv} + \alpha_F I_{Ei} - I_{Ei}} \quad (9)$$

where I_{Ei} is the transient emitter current, ΔV_i is the change of base node voltage, and both capacitances and currents are nonlinear functions of node voltages. Comparing (9) to (8), it can be found that the isolated BJT has a smaller capacitance and a larger current. Thus, t_i is much smaller than t_s . Therefore, the output current $I_{EI}-I_{ES}$ of the

BJT-based silicon retina has a significant positive pulse when light is incident. Both peak value and pulsewidth are dependent on the size of flashlight. When the size of flashlight is larger, the current I_{PQ} in (8) is smaller due to the spatial smoothing function of the smoothing network. Thus, t_s is smaller, leading to a smaller pulsewidth.

When the light is turned off, the base node voltage is increased to the value in the off state. It is found that the charging current is mainly provided by the BJT itself. Thus, the turn-off times of both smoothing BJT and isolated BJT are nearly the same. Since the base node of the BJT in the BJT smoothing network has an extra capacitance $4C_{GQ}$ as in (8), the turn-off time is slightly larger. Thus, a smaller negative pulse is resulted when the flashlight is turned off.

3.2.3 The 2-D Architecture of Silicon Retina

In the design of the FPA of the proposed BJT-based silicon retina, compact row/column selection circuits are required to achieve small pixel area. Fig. 3.2. 4 shows the basic cell structure of the FPA of BJT-based silicon retina. Both isolated and smoothing BJT's at each pixel have extra emitters directly connected to the row line. Two pMOS devices are connected in series with the active emitters of BJT's to serve as the row switches $SW1$ and $SW2$ controlled by the row line. Through the switches, the emitter currents can be sent to smoothing and isolated column lines biased at V_E . In each cell, four nMOSFET's are connected from the smoothing BJT to the four neighbors to form the proposed 2-D BJT smoothing network. Equivalently, each cell has two nMOSFET's, as shown in Fig. 3.2. 4. All the gates of nMOSFET's are connected to the common gate line with the adjustable voltage V_G .

When the row line is selected through the row decoder, its voltage is set at GND . The extra emitters act as collectors of pnp BJT's and $SW1$ and $SW2$ are closed. Thus, the two emitter currents I_{EI} and I_{ES} of isolated and smoothing pnp BJT's at the selected pixel can be sent to the isolated and smoothing column lines, respectively. When the row line is deselected, its voltage is raised to the emitter voltage V_E . In this case, $SW1$ and $SW2$ are open and the normal emitters of pnp BJT's are disconnected from the column lines and become floating. However, the extra emitters connected to the row selection line are connected to V_E . With all the deselected emitters of BJT's connected to V_E , the BJT's in the smoothing network can be kept in the normal state so that the normal smoothing operation can be performed.

The complete FPA architecture of the proposed BJT-based silicon retina is shown

in Fig. 3.2. 5. As may be seen from Fig. 3.2. 5, each column line has two pMOS devices as the column switches controlled by the column decoder. When the column is selected, one pair of switches is closed to connect both isolated and smoothing column lines to the readout circuit. When the column is deselected, the other pair of switches is closed to connect both column lines to V_E . Thus, all emitters in the deselected columns can be biased at V_E .

As shown in Fig. 3.2. 5, the readout circuit is used at the output to sense both emitter currents I_{EI} and I_{ES} and convert them into voltages. The subtraction of the two voltages is then performed to obtain the output voltage V_O , which represents the response of the bipolar cell in the retina.

3.2.4 Experimental Results

An experimental chip of the proposed BJT-based silicon retina is designed and fabricated by using 0.5- μ m n-well double-poly double-metal CMOS technology. Fig. 3.2. 6 shows the chip photograph of the fabricated 64x64 FPA of the BJT-based silicon retina. In the quiescent state without image inputs, the power dissipation of the sensor array in the silicon retina is very small, being that of 64x64 open-base BJT's. Thus, the total quiescent power dissipation is determined by the peripheral circuit, which is about 45mW. In the illuminated state, the power dissipation of the sensor array is caused by the photocurrents of the BJT's, which depends on the image light intensity. The typical total active power dissipation of the silicon retina FPA in the illuminated state is about 3-30mW. The characteristics of the fabricated FPA chip of BJT-based silicon retina are summarized in Table 3.2. 1.

To verify the tunable smoothing function of the proposed BJT smoothing network, an image is projected on the experimental chip with the gate bias V_G of nMOSFET's tuned at different values. Fig. 3.2. 7 (a) shows the measured output responses of the isolated BJT's. These responses represent those of the photoreceptors in the retina. Fig. 3.2. 7(b) and (c) shows the measured output responses of the BJT's in the BJT smoothing network with V_G at 3.75 and 4.0 V, respectively. These responses represent those of the horizontal cells in the retina. Fig. 3.2. 7(d) and (e) shows the mathematically found zero crossing positions of the outputs of the BJT-based silicon retina. The zero-crossing points of the measured output signals of the BJT-based silicon retina can be used to identify the edges of objects[91], [92], and [94]. As shown in Fig. 3.2. 7(d) and (e), when the smooth area is smaller, the smaller variation of light intensity can be identified. In other words, the edges with smaller contrast can

be identified.

Fig. 3.2. 8 shows the measurement results on the unique adaptive characteristics of the proposed BJT-silicon retina, as mentioned in Section 3.2.2-A. It can be seen that the smooth area of the BJT smoothing network under brighter background, as shown in Fig. 3.2. 8(c), is smaller than that under darker background, as shown in Fig. 3.2. 8(b). Moreover, the effect of the decreasing channel resistance of nMOSFET's on the increase of smooth area does not appear in the measurement results, as predicted in Section 3.2.2-A.

Fig. 3.2. 9(a) and (b) shows the measured output temporal responses of a single pixel in the fabricated FPA chip of the BJT-based silicon retina under three flashlight spot patterns with nearly the same intensity, but different spot diameters. It can be seen in Fig. 3.2. 9(a) that the positive pulse is generated when the flashlight is incident. The pulse has higher peak for a smaller flash spot. This is consistent with the analyses in Section 3.2.2-B.

When the light is turned off, the measured output temporal responses of the fabricated silicon retina decays to the off state, as shown in Fig. 3.2. 9(b). The small negative pulse is not observed because the large off transition time of the flashlight allows both isolated and smoothing BJT turned off simultaneously. The peaks in Fig. 3.2. 9(b) are induced by the closing time of the mechanical shutter used in this measurement.

Fig. 3.2. 10 shows the measured output responses of a single pixel in the fabricated FPA chip of the BJT-based silicon retina with a moving light bar projected upon the chip. During the periods of T1 and T2, indicated in Fig. 3.2. 10, the light bar is not incident on the readout pixel. Therefore, there are very small output responses in the isolated BJT due to the diffracted light. However, the response of the BJT in the smoothing network is gradually increased as the light bar is approaching and decreased as the light bar is leaving. This is caused by the spatial smoothing function of the BJT smoothing network. When the light bar is projected upon the readout pixel, the isolated BJT has a larger response than the smoothing BJT. The difference of these two responses, as generated by the silicon retina shown in Fig. 3.2. 10, involve negative and positive pulses as the light bar is approaching and positive and negative pulses as the light bar is leaving. The zero-crossing points occur at t_1 and t_2 . These zero-crossing characteristics caused by the passing of the edge of object can be applied to the detection of velocity and direction of moving objects [95].

In the FPA chip of the BJT-based silicon retina, the current Gain β of BJT's is not completely matched due to process variations. One of the dominant factors for β mismatch is the base width. Since the parasitic p-n-p BJT's in n-well CMOS process has a wide base width, this leads to a low β of 4.8 and a low β mismatch. The measured global variations are 6% on the same wafer, 4% in the same chip, and 0.1% at the same pixel. In the FPA of BJT-based silicon retina, the current difference of two bipolar phototransistors is taken as the output signal. Using the output current difference to perform edge detection or moving object detection, only the pixels near the edge are involved. Under good local matching error of 0.1%, it is found that the detection capability is not affected by this small β variation. Moreover, under uniform light illumination, the 4% β variation across the chip in the BJT smoothing network can be smoothed so that the resultant zero-crossing error signals are quite small. They can be cleared out by zero-crossing detectors [96]. Thus, the β variation has negligible effects on the performance of the proposed BJT-based silicon retina.

3.2.5 Conclusion

A CMOS 64x64 FPA of BJT-based silicon retina with simple structure and tunable smoothing characteristics has been designed, analyzed, and fabricated by using 0.5 μ m n-well double-poly double-metal CMOS technology. In the proposed BJT-based silicon retina structure, nMOSFET's are merged among the BJT's in the BJT smoothing network to make the smooth area tunable through the adjustable channel resistance controlled by the gate voltage. Moreover, the multiemitter structure is used to simplify the row selection circuit. Both simulation results and experimental results of static and dynamic performance of the proposed structure have been presented. Further research will be conducted in the applications of the proposed BJT-based silicon retina to the detection of velocity and direction of moving objects [95].

3.3 A LOW-PHOTOCURRENT CMOS RETINAL FOCAL-PLANE SENSOR WITH A PSEUDO-BJT SMOOTHING NETWORK AND AN ADAPTIVE CURRENT SCHMITT TRIGGER FOR SCANNER APPLICATIONS

3.3.1 Introduction

Traditionally, real-time vision proceeds by acquiring images with CCD cameras or CMOS imagers by processing them in digital platforms. The traditional approach

to deal with vision tasks is to proceed according to two main steps: 1) acquisition of the image on a low-cost CCD camera and 2) software processing on digital platforms (DSP or PC). While the computational capabilities of digital platforms improve each year, they do not necessarily comply with low cost and portability. An attractive solution to this problem is to shift part of the computation into the sensor by dedicating some circuitry around photo-captor accomplished pixel-level processing. In this way, the CCD cameras or CMOS imagers are replaced with a more sophisticated device which is able to preprocess the acquired images and provide the next processing stages with limited requirements (computational power, low cost, portability, and low power consumption) [100]. Consequently, bio-inspired smart vision systems and applications become more and more attractive in research and development. The general approach in the design of these systems is to realize some processing as functions of neural vision systems of mammals in the photo-sensor array [7], [17], [84], [97], [98] so that they can perform major functions in image processing, such as photo-input sensing, edge detection, moving object detection, etc.

As proposed in [7], [17], [84], the BJT-based retinal sensor chip mimics parts of functions of the cells in the outer plexiform layer of the real retina. As in the real retina, the retinal sensor chip similar advantageous features, such as high noise immunity, edge enhancement, and high dynamic range. Therefore, the BJT-based retinal structure [7], [17], [84] has been proven that it is very compact and suitable for VLSI implementation.

However, the parasitic p⁺-n-well-p-substrate BJTs used in the BJT-based retinal sensor have a smaller current gain as the n-well CMOS technology scaling down to 0.25 μm or below [99]. Besides, the chip area of the parasitic BJT is large. To solve the problems mentioned above, a new circuit structure is developed and called the pseudo-BJT (PBJT) [99]. By incorporating a photodiode with the PBJT to form a photo-PBJT, the new PBJT-based retinal sensor with an adaptive current Schmitt trigger for noise removal is proposed. It has three advantages. First, the process-independent current gain could be precisely controlled by the geometric parameters of MOSFETs. Second, the chip area is less than that of the BJT-based retinal sensor. Third, the proposed circuit structure is compatible completely with advanced CMOS technology. Besides, the additional advantages of low operational photocurrent levels (pA) and robust noise immunity are proposed. This new PBJT-based retinal circuit is different from previous papers [7], [17], [84], [99],

[100]-[104]. Particularly, optical noise problems are more notable in recognition applied to characters, as mentioned in [105]. A new structure, the adaptive current Schmitt trigger, could be adjusted adaptively according to the value of induced photocurrents, which enhances noise immunity and eliminates disturbances. Since all MOS devices in the proposed retinal sensor circuit are operated in the subthreshold region, the power dissipation is very low. Thus, it is suitable for the front-end sensor applications of portable optical scanner systems like pen scanners [107]. Table 3.3. 1 shows the feature comparisons between PBJT-based retinal sensor and typical CMOS sensor. Proven by Table 3.3. 1, these superior features of retinal processing circuits to the conventional CMOS and CCD images are the same as mentioned in [26]. This new PBJT-based retinal sensor has excellent photosensitivity per photodiode area, optical dynamic range, noise immunity, continuous sensing, edge enhancement, and intelligent characteristic.

The detection of static and moving objects, such as a moving white bar, are tested and proved through HSPICE simulation. The area of this chip is $3000 \times 3030 \mu\text{m}^2$ and that of a single pixel is $70 \times 70 \mu\text{m}^2$ with a fill factor of 75%. It is with fully functional 32×32 implementations consuming less than $8.8 \mu\text{W}$ per pixel at 3.3 V. Measurement results successfully verified the correct functions and performance of the proposed new retinal sensor circuits in character recognition of scanner systems. This proposed retinal chip could recognize the size of characters capable of scanning, which is 8–14 points. The screen size is 32×32 pixels, and the scanner resolution is 169 dpi (14 pixels/mm). The illumination for all the following measurements is set at 0.87 normalized with fluorescent light at a wavelength of $550 \mu\text{m}$ (13.8 lux).

In Section 3.3.2, it describes the architecture and the proposed circuit. Section 3.3.3 presents simulation results of the proposed circuit. Section 3.3.4 displays measurement results. Section 3.3.5 gives conclusions and feature works.

3.3.2 Architecture and Circuit

Fig. 3.3. 1 shows the architecture of the proposed retinal focal-plane sensor, which consists of the 32×32 pixel array and the peripheral circuits. First, the pixel array is to detect the image with noise and function for noise removal. Next, the row and column decoder could select the desired pixel randomly. Finally, the data buffer is to convert the parallel data to serial data in order to reduce the output pins of the chip.

Fig. 3.3. 2 shows the conceptual dc output characteristics of the adaptive current Schmitt trigger. Current hysteresis (ΔI) is the quality of the current Schmitt trigger in

which the input threshold changes as a function of the input current level. Adding current hysteresis in the retinal sensor circuit could enhance the function of noise immunity. As the input starts positive and goes negative, the output does not change until it reaches the negative trip point. In the same way, the input starts negative and goes positive in direction, the output does not switch until it reaches the positive trip point. In the proposed pixel structure of a retinal focal-plane sensor, as shown in Fig. 3.3. 3, an isolated PNP pseudo-BJT is used as photoreceptor, a smoothing NPN pseudo-BJT with adjustable N-channel MOSFET resistors is used to form the retinal smoothing network, an adaptive current Schmitt trigger, and an inverter are included. The transistors Mp1, Mp2, and photodiode D₀ are as the PNP pseudo-BJT. The transistors Mn1, Mn2, and a photodiode D₀ are as the NPN pseudo-BJT with four adjustable N-channel MOS resistors Ms1-Ms4 as the smoothing network. The smoothing network is connected to its four neighbors, and the resistance of four MOS resistors is controlled by the gate voltage V_{smooth} (VF). The adaptive current Schmitt trigger comprises of Mp1, Mp2, Mn1, and Mn2, and hysteresis level adjustment Mpf1, Mpf2, Mnf1, and Mnf2. The current I_{iso} is the generated current of PNP pseudo-BJT whereas the current I_{smt} is that of NPN pseudo-BJT. In this proposed retinal sensor, it operates in the subthreshold region. Therefore, the circuit just consumes little power during in nonlighting mode. If the current I_{smt} is bigger than the current I_{iso}, at first, the V_{out} (Retina_out) goes too high and it turns on the MOS Mnf2 to draw the current ΔI/2. By the same token, the current I_{smt} is smaller than the current I_{iso} initially, the V_{out} (Retina_out) stays low level and it turns on the MOS Mpf2 to sink the current ΔI/2. The positive and negative trip points can be expressed as

$$I_{iso} - I_{smt} = \pm \frac{\Delta I}{2} \quad (1)$$

where ΔI is the current hysteresis. If the induced photocurrent is larger, the current of transistors Mn1 and Mp1 becomes also larger. Due to the function of current mirror Mn1-Mnf1 and Mp1-Mpf1, the current of Mnf1 and Mpf1 could be adjusted by the induced photocurrent. Hence, this proposed circuit could adjust the current ΔI adaptively without external controlling voltage. The transistors Mp and Mn are composed of an inverter to amplify the output of the adaptive current Schmitt trigger to VDD or GND so that the signal is converted from analog to binary. All the simulations of the proposed circuit are analyzed in Section 3.3.3.

3.3.3 Simulation Results

All simulation results are based upon the device parameters of 0.35 μ m 1P4M CMOS technology with 3.3-V power supply. The designed device dimensions and the controlling voltage of the pixel circuit in Fig. 3.3. 3 are listed in Table 3.3. 2. First, we simulate the current gain of NPN pseudo-BJT and PNP pseudo-BJT in the low-induced current level, respectively. The drain current equation in the subthreshold region can be expressed as [105]

$$I_{ds} = K_x \frac{W}{L} \left[1 - \exp\left(\frac{-V_{DS}}{vt}\right) \right] \exp\left[\frac{(V_{GS} - V_{th})}{nvt}\right] \quad (2)$$

Where K_x depends on process parameter, W/L is the geometric ratio of the MOS, V_{th} is the threshold voltage of MOS, vt is the thermal voltage and is given by Kt/q , and n is the subthreshold swing parameter. Based on (2), the current gain of pseudo-BJT can be written as

$$\beta = \frac{\frac{W}{L} \left[1 - \exp\left(\frac{-V_{DS1}}{vt}\right) \right]}{2 \frac{W}{L} \left[1 - \exp\left(\frac{-V_{DS2}}{vt}\right) \right]} \times \exp\left[\left(\frac{1}{n1} - \frac{1}{n2}\right) \left(\frac{V_{GS} - V_{th}}{vt}\right)\right] \quad (3)$$

By using (3), in Fig. 3.3. 4, it shows the beta value of NPN pseudo-BJT and PNP pseudo-BJT. Due to the parameter of V_{DS} for master and slave MOSFETs, in low-induced current levels, the current gain is bigger than the designed value. When the induced current becomes bigger, the parameter V_{DS} for master and slave MOSFETs are close to each other. Therefore, the current gain approaches to desired value as shown in Fig. 3.3. 4. In order to reduce the affect of subthreshold swing parameters, the slave MOSFETs must be structured by making parallel copies of the master MOSFET. Hence, the current gain would be independent of the subthreshold swing parameter. Next, it is applied in a one-dimensional (1-D) array to verify the function of smoothing, as shown in Fig. 3.3. 5(a) and (b), with 50 pixels is considered. The light is incident on the 20th to the 30th pixels. Finally, to verify the performance of circuits for low induced current levels, the induced photocurrent is simulated in 100 pA, and 10 pA, respectively. Compared to Fig. 3.3. 5(a) and (b), the main difference between them is the VF. If the incident lighting were larger, the photodiode of the retinal sensor would induce bigger currents. Therefore, the resistance of smoothing networks could be smaller because of the suitable scale of voltage variations in the

smoothing network. In other words, if it is in the dimming-illumination environment, the induced photocurrent is smaller. Therefore, it needs bigger resistance to function as expected. The MOS resistance in the subthreshold region can be expressed as

$$R_{ds} = \left[Kx \frac{W}{L} \exp \left[\frac{(VF - V_{th})}{nvt} \right] \right]^{-1} \quad (4)$$

As seen from (4), R_{ds} is tunable by VF . Thus, the smoothing characteristics of retinal sensors can be adjusted by VF . In these simulation results, as mentioned above, this proposed circuit could be operated in the dimming-illumination environment for low induced current levels (pA). In Fig. 3.3. 6, the dc output characteristics (a)–(d) of the adaptive current Schmitt trigger with fixed I_{smt} current is shown. This dc characteristic is to verify the function of adaptive current Schmitt trigger, which is to fix the I_{smt} current and to sweep the I_{iso} current. For the fixed smoothing current (a)–(d) in Fig. 3.3. 6, they are 10 pA, 20 pA, 30 pA, and 40 pA, respectively. Based on (1), the center point is the position of the smoothing current I_{smt} and the dc current output is symmetric, as shown in Fig. 3.3. 2. The values of ΔI are 2 pA, 3.5 pA, 5.5 pA, and 8.7 pA, respectively. Therefore, the simulation results show that current hysteresis could be adjusted adaptively according to the value of induced photocurrent.

Finally, we apply this retinal focal-plane sensor into two-dimensional (2-D) 32x32 pixel array, and simulate the incident static image to verify the detecting function of 2-D retinal focal-plane sensor. In Fig. 3.3. 7(a), the input pattern A with noise, which is a zero-mean random noise with a standard deviation of 60% of induced photocurrent, is shown. Fig. 3.3. 7(b) presents the 32x32 pixels output (Retina_out) of the 2-D retinal focal-plane sensor. Thus, good performance for detection on the 2-D retinal sensor is illustrated. Moreover, due to the pseudo-BJT smoothing network and adaptive current Schmitt trigger, these simulation results show robust noise immunity in this proposed circuit. In Fig. 3.3. 8, the SPICE simulated output voltages under input current waveforms corresponding to the photocurrents generated by moving image patterns of white bars with a minimum width of 500 m where the scanning speed is 100 mm/s, which is larger than the maximum specified speed of 40 mm/s for pen scanners. These simulation results have successfully confirmed the correct functions and performance of the proposed new

retinal sensor circuits in the character recognition of scanner systems.

3.3.4 Measurement Results

Fig. 3.3. 9(a) presents a photograph of the layout of the fabricated chip and Fig. 3.3. 9(b) displays the photograph of a single pixel. The area of this chip is $3000 \times 3030 \mu\text{m}^2$ and that of a single pixel is $70 \times 70 \mu\text{m}^2$ with a fill factor of 75% and with fully functional 32×32 implementations consuming less than $8.8 \mu\text{W}$ per pixel at 3.3 V. Fig. 3.3. 10 shows the oscilloscope traces of frame rates for fully serial readouts and serial output via the data buffer. The frame rate for character reorganization is 97.1 frames/s. Fig. 3.3. 11(a)–(f) display measurement results normalized with fluorescent lights at a wavelength of $550 \mu\text{m}$ (13.8 lux) of different illuminations for character “B,” which is in the range of 0.02–5.3. Fig. 3.3. 12(a) is the static graded image pattern with different contrasts (%) fully incident upon the retinal sensor. The contrast for whole black and complete white is 100%. In Fig. 3.3. 12(b), the contrast of image is enhanced and columns 6 and 26 are located in the contrast of 20%, as shown in Fig. 3.3. 12(a). Therefore, the minimum acceptable contrast is 20%. Fig. 3.3. 13(a)–(h) successfully show the smoothing function for noise removal at different control voltages, which range from $V_F = 0.85$ – 1.5 V. Fig. 3.3. 14(a) presents the incident image with random distributed noise with a standard deviation of 50% and Fig. 3.3. 14(b) is the measurement result at $V_F = 1.5$ V. Fig. 3.3. 15(a) shows the incident image blurred and Fig. 3.3. 15(b) is the measurement result at $V_F = 1.5$ V. The measurement results of Fig. 3.3. 14(b) and Fig. 3.3. 15(b) show that the proposed new retinal sensor circuits could restore unclear characters, as show in Fig. 3.3. 14(a) and Fig. 3.3. 15(a), into clear characters. Fig. 3.3. 16 shows the minimum black space versus the scanning speed for character patterns in 169 dpi. The minimum adjacent distance is expected to be increased with scanner speed, and this is observed. The measurement results for this proposed retinal chip could recognize the size of characters capable of scanning, which is 8–14 points. The screen size is 32×32 pixels, and the scanner resolution is 169 dpi (14 pixels/mm). The illumination for all of the following measurements is set at 0.87 normalized with fluorescent light at a wavelength of $550 \mu\text{m}$ (13.8 lux). These measurement results have successfully verified the correct functions and performance of the proposed new retinal sensor circuits in the character recognition of scanner systems. The characteristics of the fabricated PBJT-based retinal sensor for scanner applications are summarized in Table 3.3. 3.

3.3.5 Conclusion

This work presents a low-photocurrent CMOS retinal focal-plane sensor with a pseudo-BJT smoothing network and adaptive current Schmitt trigger. In this proposed architecture, the pixel structure is very simple and compact compared to the BJT-based retinal sensor. Due to the pseudo-BJT smoothing network and adaptive current Schmitt trigger, these measurement results show robust noise immunity in this proposed circuit. The minimum acceptable contrast is 20%. The screen size is 32x32 pixels and the scanner resolution is 169 dpi (14 pixels/mm). The area of this chip is $3000 \times 3030 \mu\text{m}^2$ and that of a single pixel is $70 \times 70 \mu\text{m}^2$ with a fill factor of 75% and with fully functional 32x32 implementations consuming less than $8.8 \mu\text{W}$ per pixel at 3.3 V. According to the measurement results above, this work has successfully verified the correct functions and performance of the proposed new retinal sensor circuits in character recognition of scanner systems. In future research, this fabricated chip will be adaptively adjusted according to desired applications, for example, applied in surveillance sensor systems or intelligent transportation systems, etc.

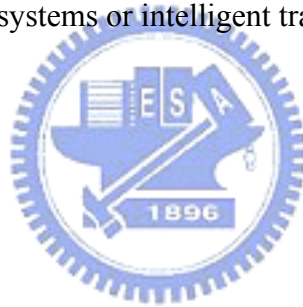


Table 3. 1 Summary of the results of CHAPTER 3

Section	3.1 [46]	3.2 [7]	3.3 [23]
Published year	1995	1999	2004
Technology	0.8 μ m 2P2M	0.5 μ m 2P2M	0.35 μ m 1P4M
Resolution	32 x 32	64 x 64	32 x 32
Pixel size	60 μ m x 60 μ m	45 μ m x 45 μ m	70 μ m x 70 μ m
Fill factor	0.33	0.49	0.75
Chip size		4mm x 4mm	3mm x 3.03mm
Power supply		3V, 5V	3.3V
Power dissipation		3mW ~ 30mW	9mW
Current gain of BJTs		4.8	20
Readout time of one pixel	1 μ s	16 μ s	10.4 μ s
Frame rate	1KHz	9.6 kHz	97.1Hz

Table 3.1. 1. The Experimental Results of the Fabricated Rm Amplifier

Control Voltage ($V_{CN}=V_{CP}$)	+2.5V ~ -0.9V
Transresistance (r_m)	919 Ohm ~ 1914 Ohm
Input Impedance (r_{in})	44.6 Ohm ~ 88.2 Ohm
Output Impedance (r_o)	2.34 Ohm ~ 44.6 Ohm
-3dB Frequency (f_{-3db})	246.3 MHz ~ 97.4 MHz

Table 3.1. 2. The Device Parameters of the Parasitic PNP Transistor in 0.8 μ m

DPDM CMOS Process

Parameters	parasitic PNP transistor	
BF	23.6	
BR	0.0024	
IS	9.23E-18	A
NF	1.03	
NR	1.03	
VAF	145	V
VAR	15.82	V
ISC	4.70E-12	A
ISE	4.56E-12	A
NC	2.89	
NE	4.46	
IKF	2.00E-04	A
IKR	3.00E-04	A
RB	469.5	Ohm
RBM	50	Ohm
RE	34	Ohm
RC	37.5	Ohm
IKB	1.04E-05	A
CJC	2.13E-14	F
CJE	6.50E-14	F
MJC	0.749	
MJE	0.525	
VJC	0.85	V
V3E	0.93	V

Table 3.1. 3. The Summary of the Measured Characteristics of the Proposed 2-D 32x32 Silicon Retina

Process	0.8 DPDM CMOS
Resolution	32x32
Cell Area	60 μ m \times 60 μ m
Fill Factor	0.33
Integration Time or Settling Time of the Smooth Network	3ms
Settling Time of the Pixel Readout Operation	1 μ s
Pixel Readout Speed	1MHz
Frame Rate	1KHz

Table 3.2. 1. The summary on the characteristics of the fabricated FPA chip of BJT-based silicon retina

Technology	0.5 μ m N-well CMOS Double Poly Double Metal
Resolution	64x64
Sampling geometry	Rectangular
Pixel size	45 μ m \times 45 μ m
Size of the bipolar phototransistors	3.3 μ m \times 2.2 μ m (emitter), 15 μ m \times 34 μ m (base)
W/L of the inserted nMOSFET among smoothing BJTs	3 μ m/6 μ m
Fill factor (size of the light window)	0.49 (29.5 μ m \times 34 μ m)
Chip size	4mm \times 4mm
Power supply	3V, 5V
Total quiescent power dissipation	45mW
Active power dissipation of the sensor array in the illuminated state	3mW ~ 30mW (Depending on image light intensity)
Current gain of BJTs	4.8
Settling time of the BJT smoothing network	1ms
Readout time of one pixel	16 μ s
Frame rate for column parallel readout	9.6 kHz

Table 3.3. 1. Feature Comparisons Between PBJT-Based Silicon Retina and Typical CMOS Sensor

Feature Comparisons	PBJT-based Silicon Retina	CMOS Sensor
Technology	TSMC 0.35 μ m 1P4M	TSMC 0.35 μ m 1P4M
Pixel size	70 μ m \times 70 μ m (fill factor 75%)	7 μ m \times 7 μ m (fill factor 30%)
Photosensitivity per photodiode area	120 μ A/cm ² -lux	6 μ A/cm ² -lux
Standby dark power consumption	~0	10mW
Operational pixel power consumption	8.8 μ W/pixel (Array size 32 \times 32)	0.32 μ W/pixel (Array size 352 \times 288)
Post processor	Simple (without noise removal operation)	Complex
Optical dynamic range	120dB	70dB
Noise immunity	Yes	None
Processing time	Real-time	Need integration time about 30ms
Timing diagram	The same	The same
Power supply	2.2V	3.3V
Scalable	Yes	Yes
Image output	Digital	Analog
Sensor characteristics	Intelligent	Regular

Table 3.3. 2. Designed Device Dimensions and the Controlling Voltages of the Pixel Circuit in Fig. 3.3. 3

Technology	0.35 μ m SILICIDE CMOS (SPQM)
Mp1(W/L)	1 μ m/1 μ m
Mp2(W/L)	20 μ m/1 μ m
Mpf1(W/L)	2 μ m/1 μ m
Mpf2(W/L)	2 μ m/1 μ m
Mn1(W/L)	1 μ m/1 μ m
Mn2(W/L)	20 μ m/1 μ m
Mnf1(W/L)	10 μ m/1 μ m
Mnf2(W/L)	10 μ m/1 μ m
Ms1=Ms2=Ms3=Ms4(W/L)	1 μ m/1 μ m
Mp(W/L)	0.4 μ m/0.35 μ m
Mn(W/L)	0.4 μ m/0.35 μ m
Vsmooth(VF)	Adjustable

Table 3.3. 3. Summary on the Characteristics of the Fabricated PBJT-Based Retinal Sensor for Scanner Applications

Technology	0.35 μ m SILICIDE CMOS (SPQM)
Resolution	32x32
Sampling geometry	Rectangular
Pixel size	70 μ m x 70 μ m
Fill factor (size of light window)	75%
Chip size	3000 μ m x 3030 μ m
Power supply	3.3V
Total DC power consumption	9mW
Current gain of PBJTs	20
Readout time of one pixel	10.4 μ s
Frame rate for total serial readout	97.1 frames/s
Scanner resolution	169 dpi
Size of characters capable of scanning	8-14

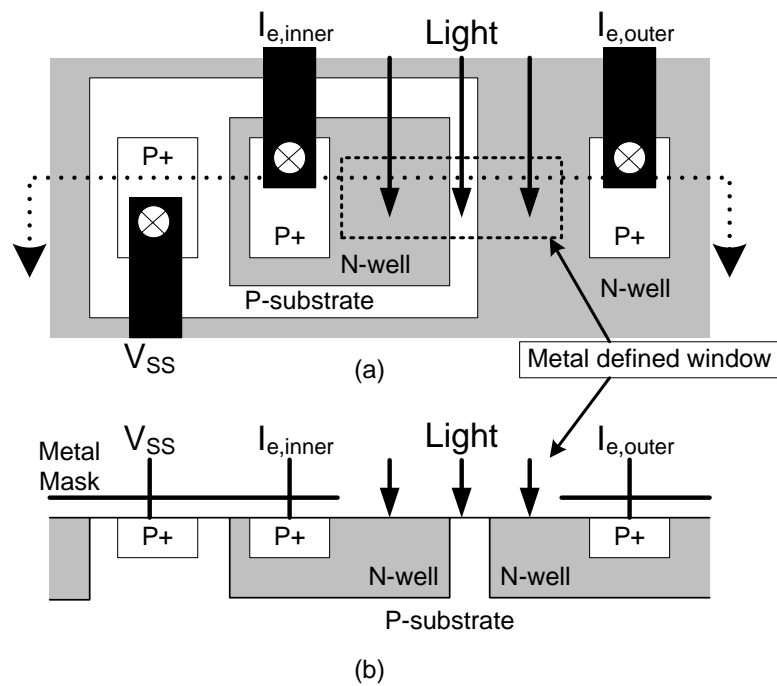


Fig. 3.1. 1. (a) The top view of the proposed silicon retina cell. (b) The cross-sectional view of the proposed silicon retina cell.

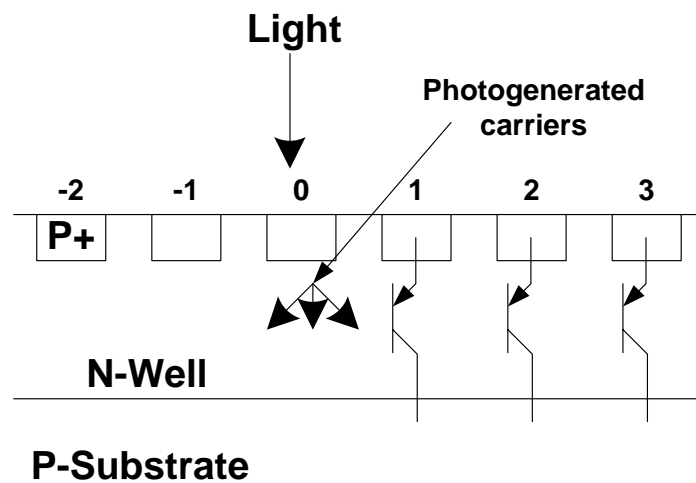
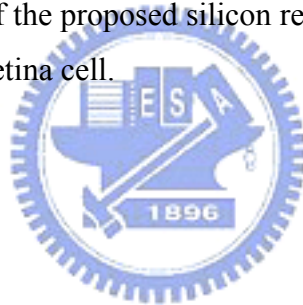


Fig. 3.1. 2. The conceptual cross-sectional view of the outer PNP phototransistor array showing the photogenerated carriers.

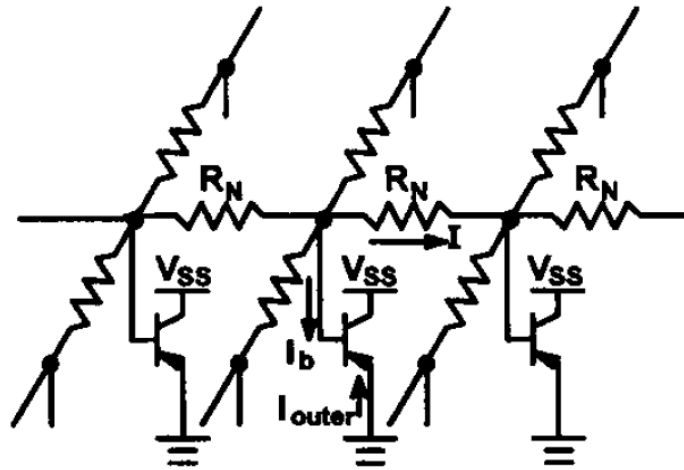


Fig. 3.1. 3. The equivalent circuit of the smooth network in the proposed silicon retina structure. In the equivalent circuit, R_N represents the N-well base spreading resistance.

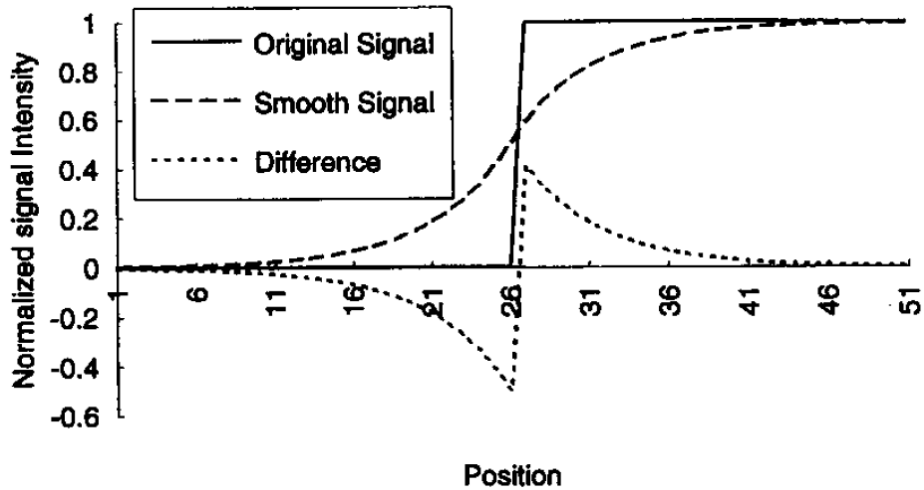


Fig. 3.1. 4. The normalized signal intensity versus position of the original signal, the smooth signal, and their difference.

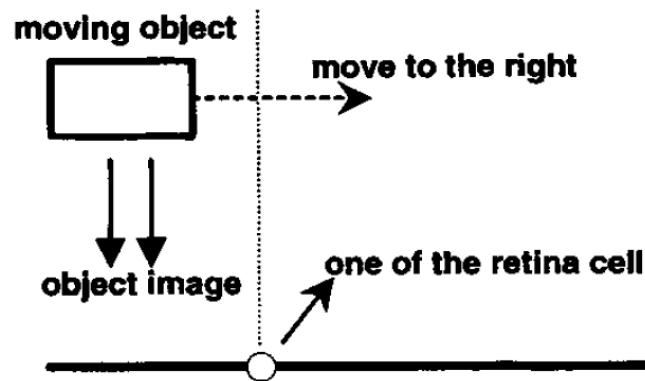
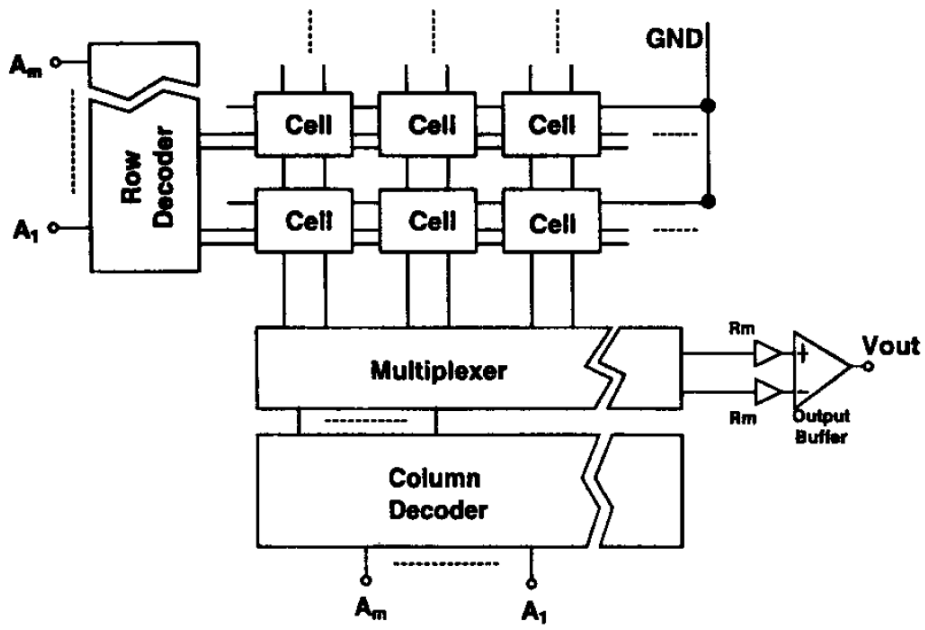
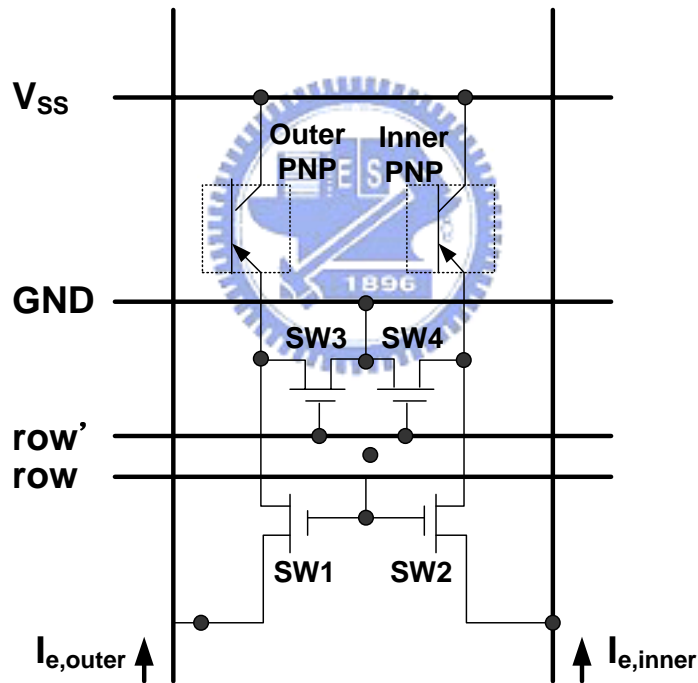


Fig. 3.1. 5. The conceptual diagram showing that when a moving object passes through the silicon retina cell on the dashed line, the cell senses a pulsed light image.

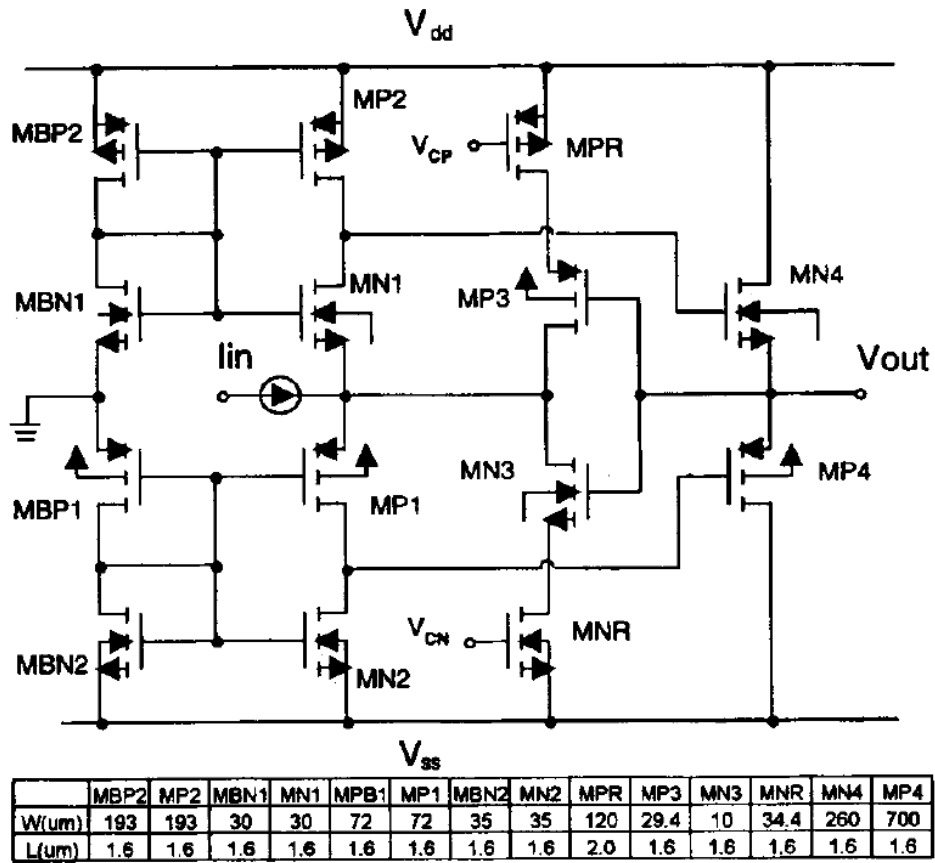


(a)

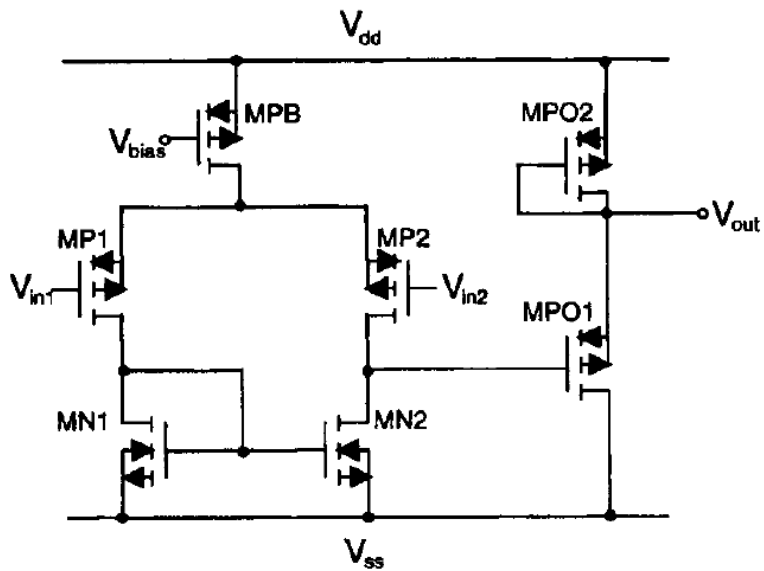


(b)

Fig. 3.1. 6. (a) The 2-D structure of the proposed silicon retina where two decoders are used to decode the input address and then activate the control Lines of the cells, two R_m amplifiers are used to convert the cell currents into the voltages, and the output buffer amplifies the voltage difference to obtain the output voltage. (b) The basic cell of the 2-D silicon retina where two control lines row and row' are generated from the row decoder, and four switches are used to control the current flow.

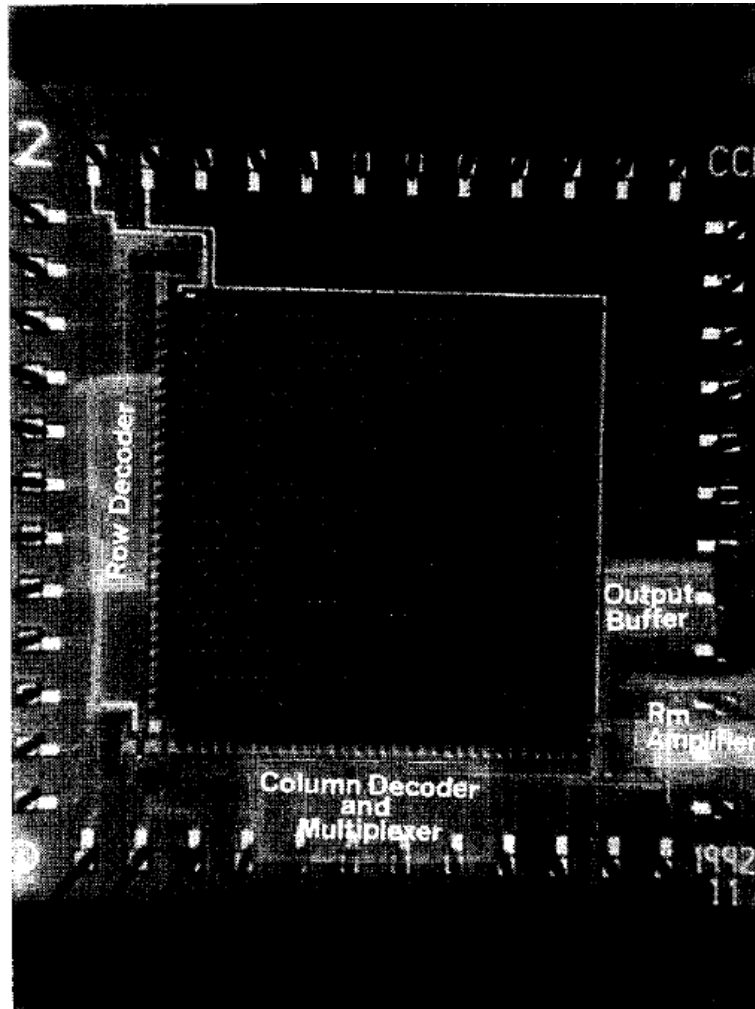


(a)

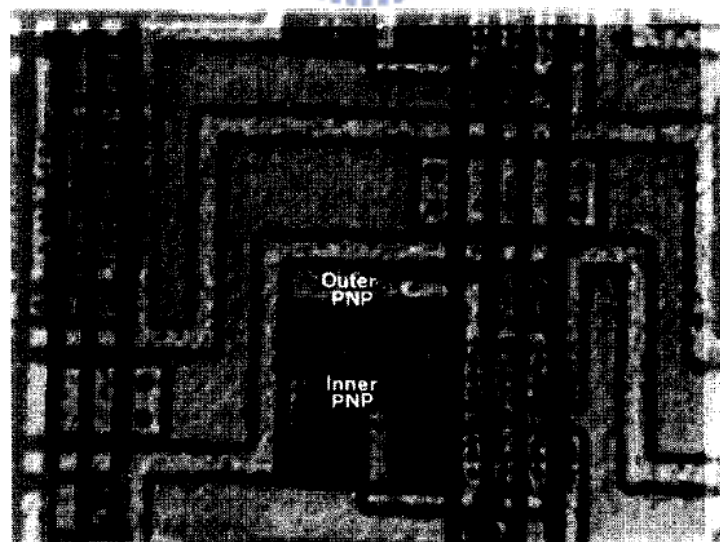


(b)

Fig. 3.1. 7. The circuit diagrams of (a) the CMOS wideband Rm amplifier and (b) the CMOS output buffer used in the silicon retina chip.

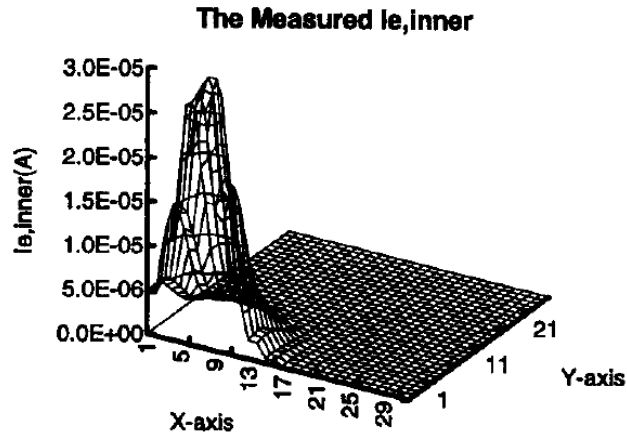


(a)

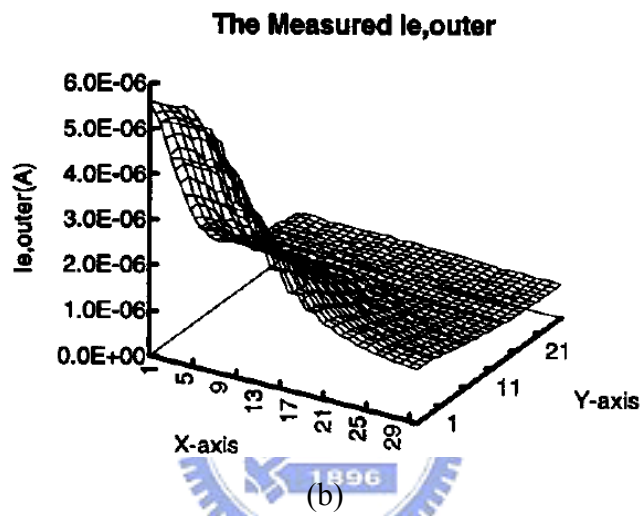


(b)

Fig. 3.1. 8. (a) The chip photograph of the 2-D silicon retina and (b) the cell photograph of the 2-D silicon retina.



(a)



(b)

Fig. 3.1. 9. (a) The measured emitter current $I_{e,inner}$ of the inner PNP phototransistors plotted in the 2-D diagram and (b) the measured emitter current $I_{e,outer}$ of the outer phototransistor array in the silicon retina chip.

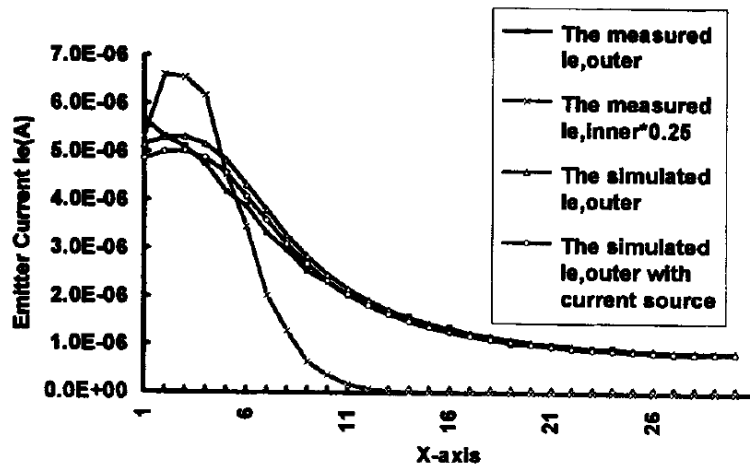


Fig. 3.1. 10. The curves of $y=5$ in Fig. 3.1. 9(a) and (b) for the measured $I_{e,inner}$ and the measured $I_{e,outer}$, respectively. The corresponding $I_{e,outer}$ from simulation is also plotted together for comparison.

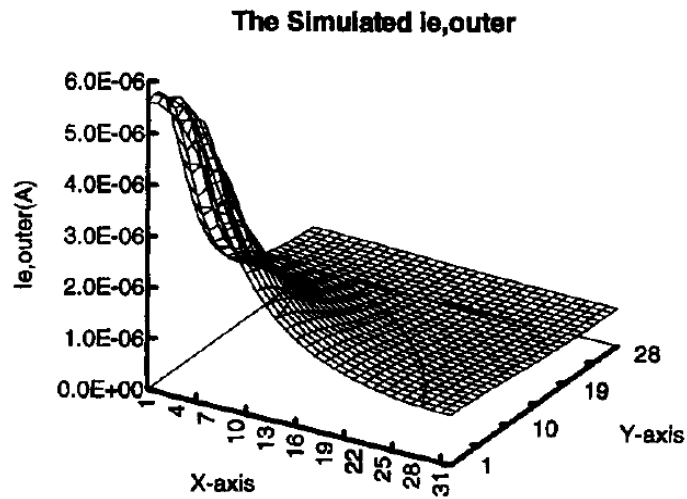


Fig. 3.1. 11. The simulated emitter current $I_{e,outer}$ of the 2-D silicon retina.

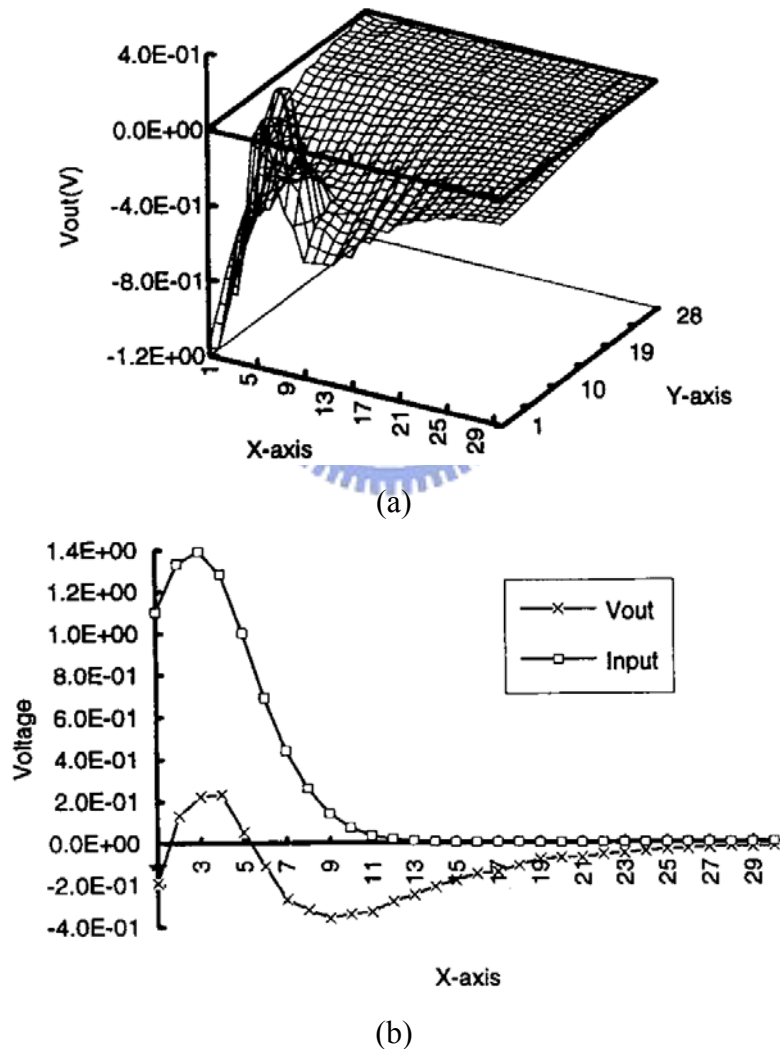


Fig. 3.1. 12. (a) The measured output voltages of the 2-D silicon retina with a large light spot incident upon it, which are plotted in the 2-D diagram to show the edge detection characteristics. (b) The curves of $y=8$ in (a) are plotted to observe the edge detection capability clearly.

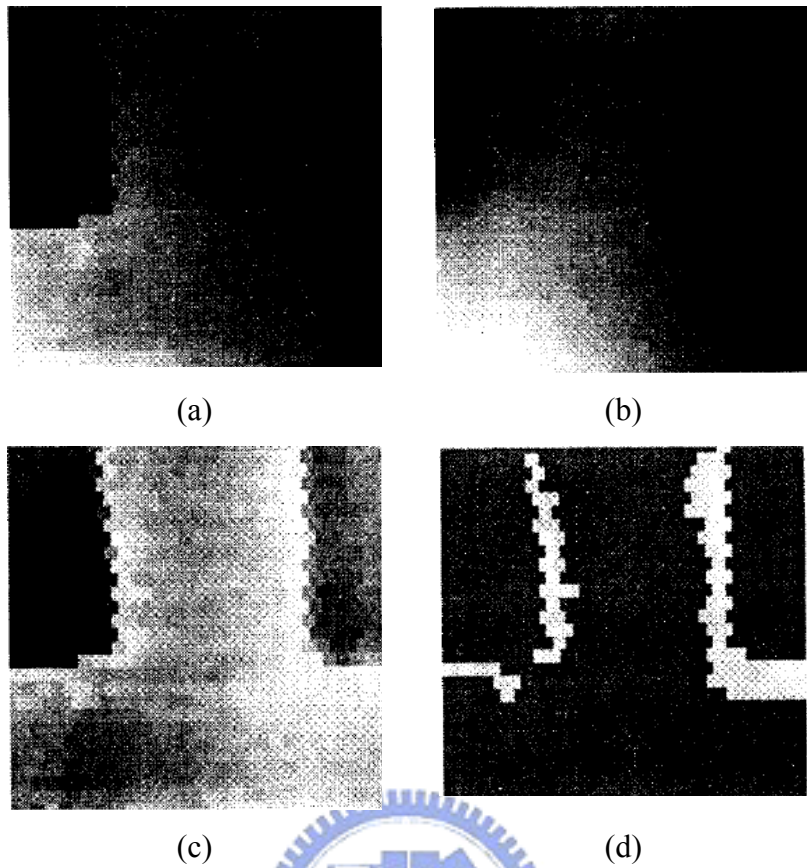


Fig. 3.1. 13. The measured output images when a character image “T” is incident on the chip. (a) The output image of the inner array, (b) the output image of the outer array. (c) the output image of the retina chip, (d) the output image of (c) with only positive pulses only.

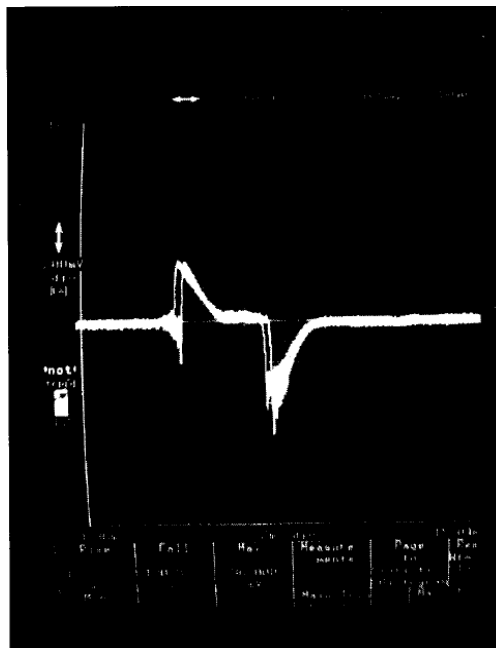


Fig. 3.1. 14. The measured response of V_{out} in two of the 2-D silicon retina cells with a moving pattern passing across the chip.

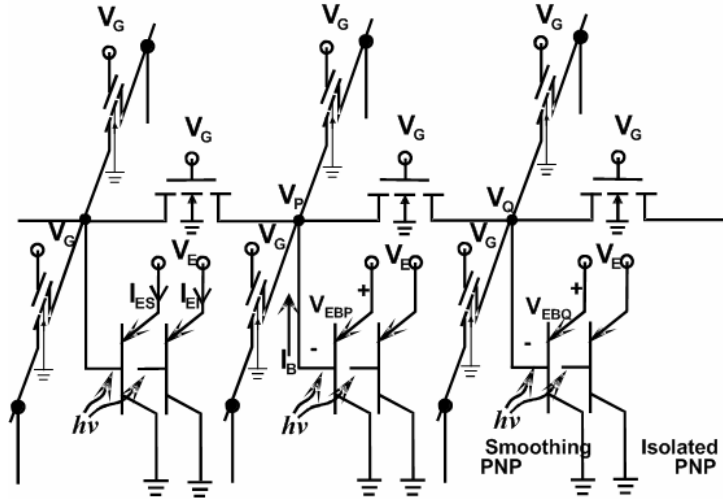


Fig. 3.2. 1. The equivalent circuit of the proposed two-dimensional (2-D) BJT-based silicon retina.

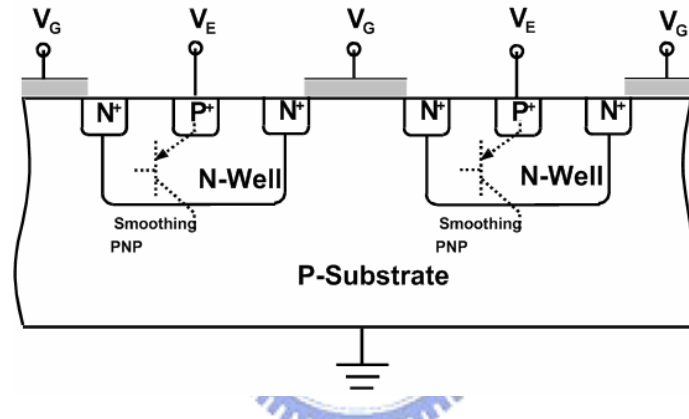


Fig. 3.2. 2. The cross-sectional view of the BJT smoothing network, which contains one BJT and one enhancement nMOSFET in each pixel.

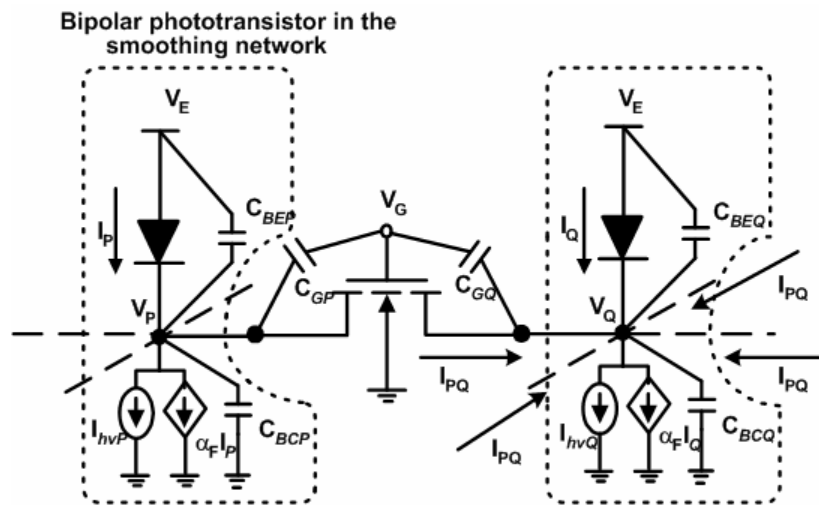


Fig. 3.2. 3. The large-signal equivalent circuit of the BJT smoothing network in Fig. 1 with device capacitances.

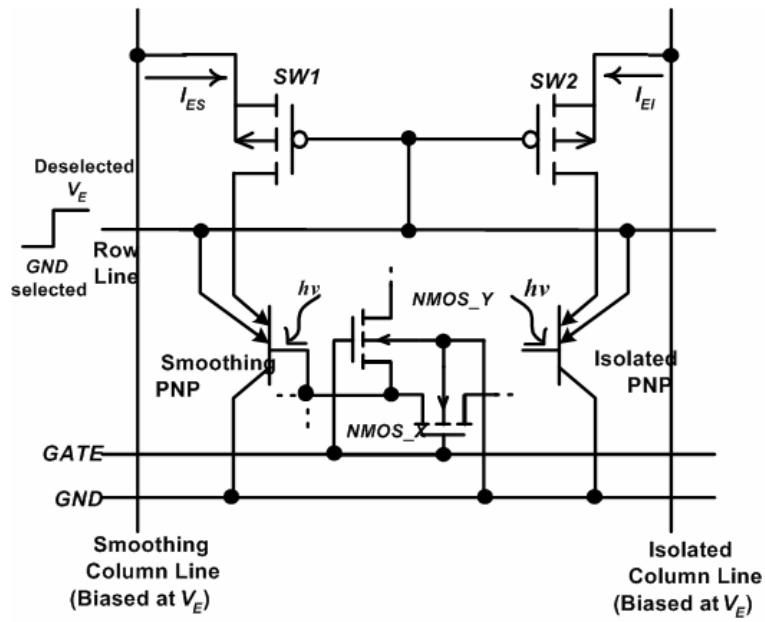


Fig. 3.2. 4. The basic cell circuit of the FPA of the proposed 2-D BJT-based silicon retina.

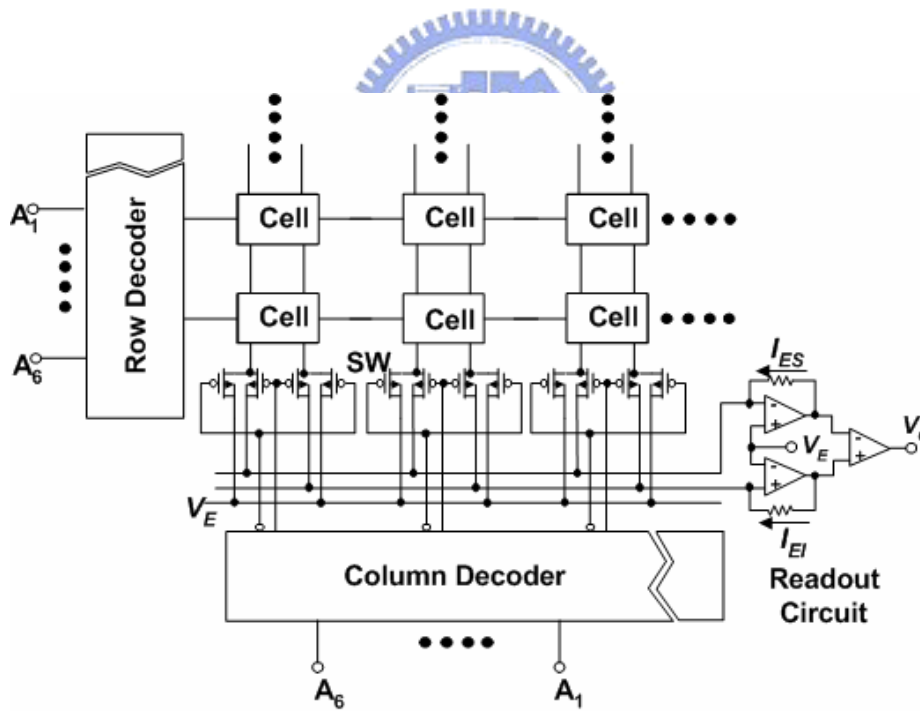


Fig. 3.2. 5. The complete architecture of the FPA chip of the proposed 2-D BJT-based silicon retina.

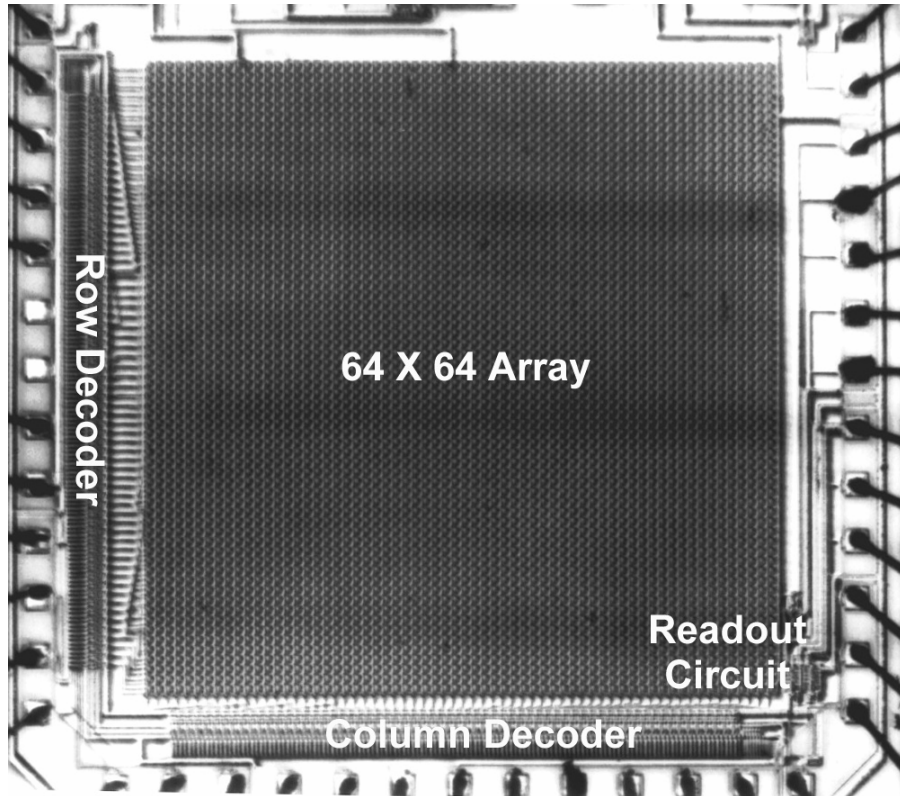


Fig. 3.2. 6. The chip photograph of the fabricated 64x64 FPA of BJT-based silicon retina.

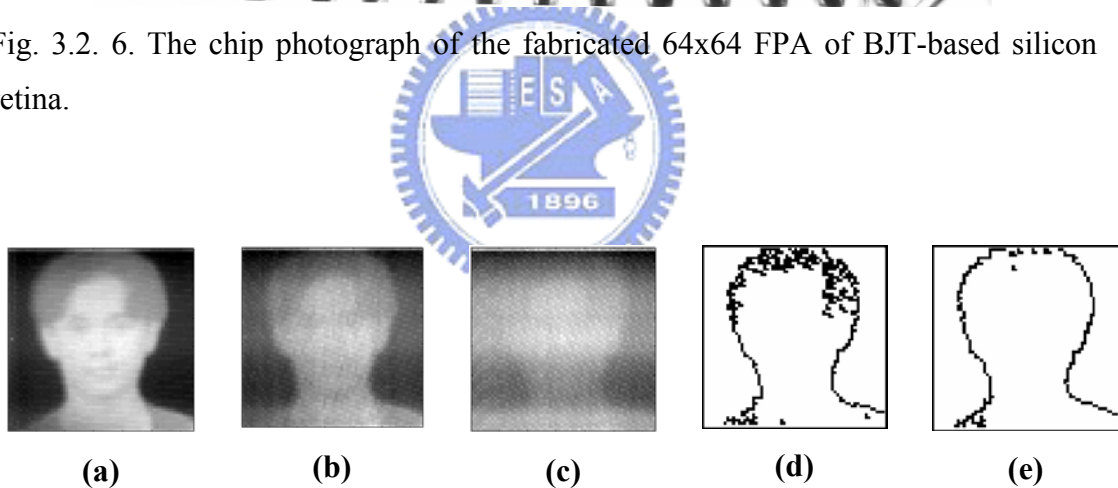
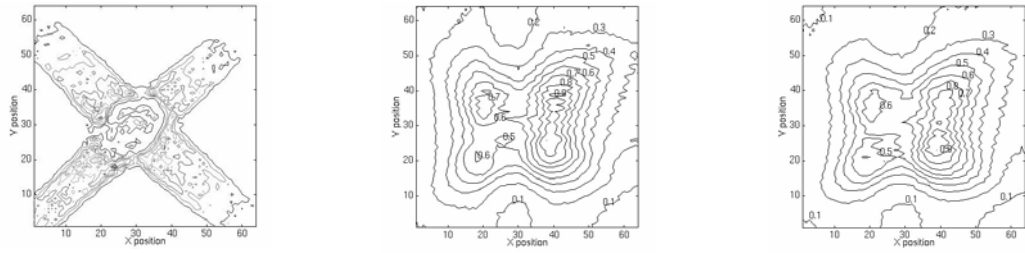
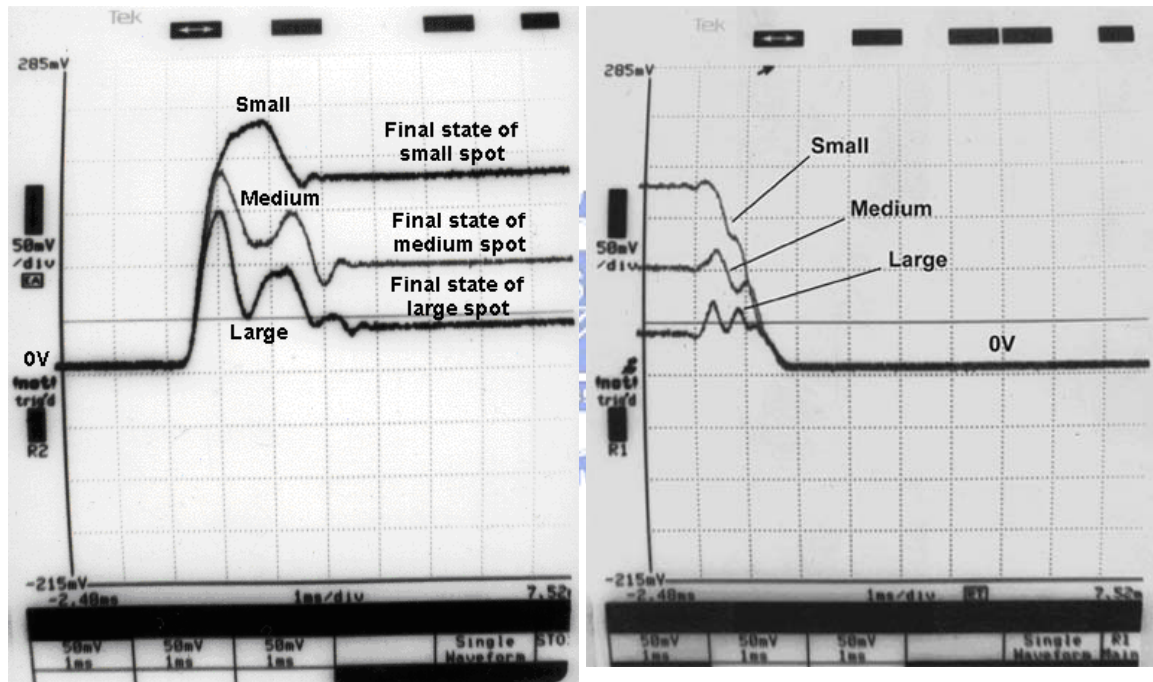


Fig. 3.2. 7. The measured output responses of (a) isolated BJT array, (b) BJT smoothing network with $V_G = 3.75$ V, and (c) BJT smoothing network with $V_G = 4.0$ V in the fabricated FPA chip of BJT-based silicon retina exposed to an image. The mathematically found zero-crossing positions of the measured output responses of the BJT-based silicon retina are shown in (d) for (b), and (e) for (c). In (a), (b), and (c), the 256 gray levels are used to divide the current range of (a) 0-0.2 μ A, (b) 0-0.165 μ A, and (c) 0-0.12 μ A, respectively.



(a) The original image (b) Darker background (c) Brighter background

Fig. 3.2. 8. The normalized contour plots of the measurement emitter currents of the BJT smoothing network for an (a) original image under (b) darker background and (c) brighter background, where the contrast of input pattern is kept the same and the gate bias of nMOSFET's is 3.9 V.



(a)

(b)

Fig. 3.2. 9. The measured output (a) turn-on and (b) turn-off temporal responses of a single pixel in the improved 2-D BJT-based silicon retina under different incident flashlight patterns with the same intensity and different sizes.

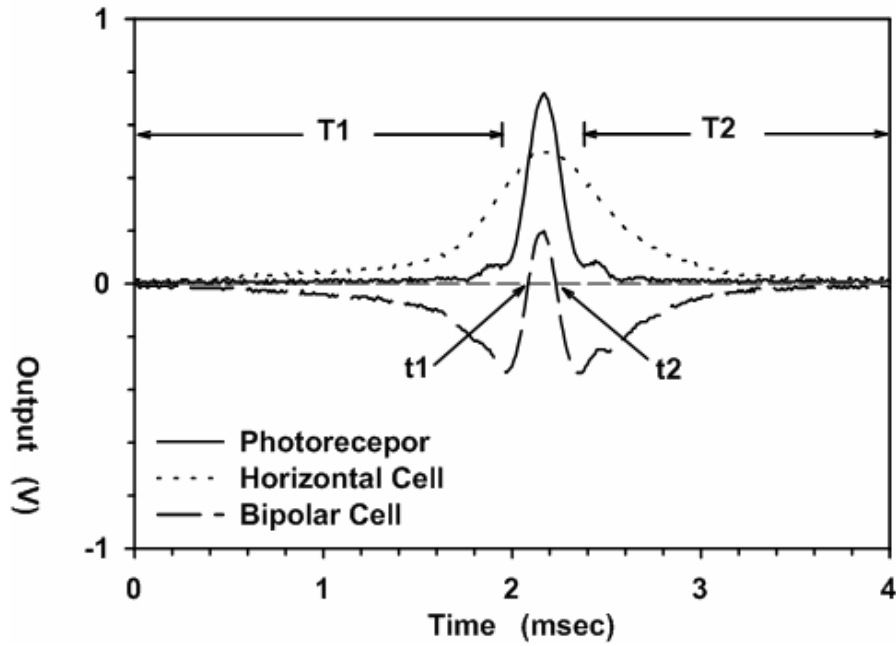


Fig. 3.2. 10. The measured output responses of a single pixel in the 2-D BJT-based silicon retina under a moving light bar incident upon the chip.

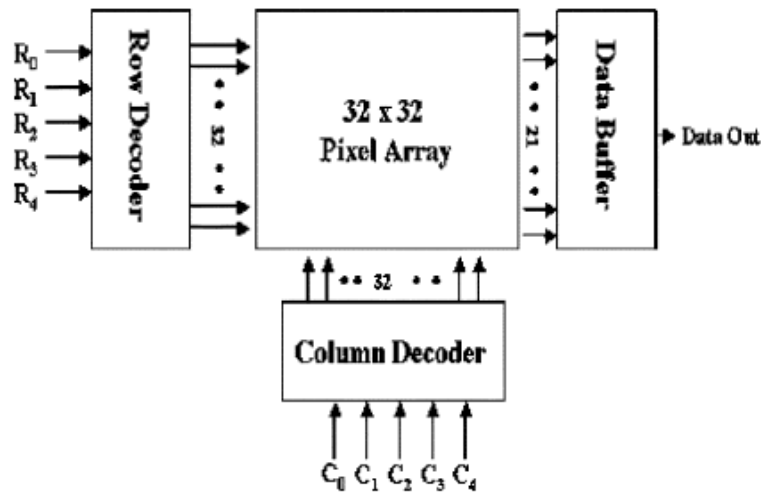


Fig. 3.3. 1. Architecture of the proposed retinal focal-plane sensor.

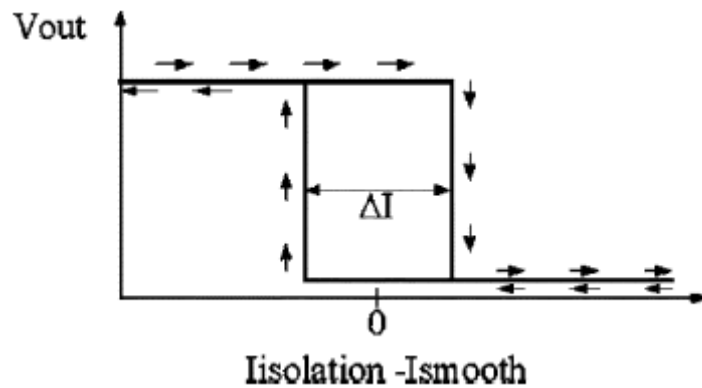


Fig. 3.3. 2. Concept of adaptive current Schmitt trigger of proposed retinal focal-plane sensor.

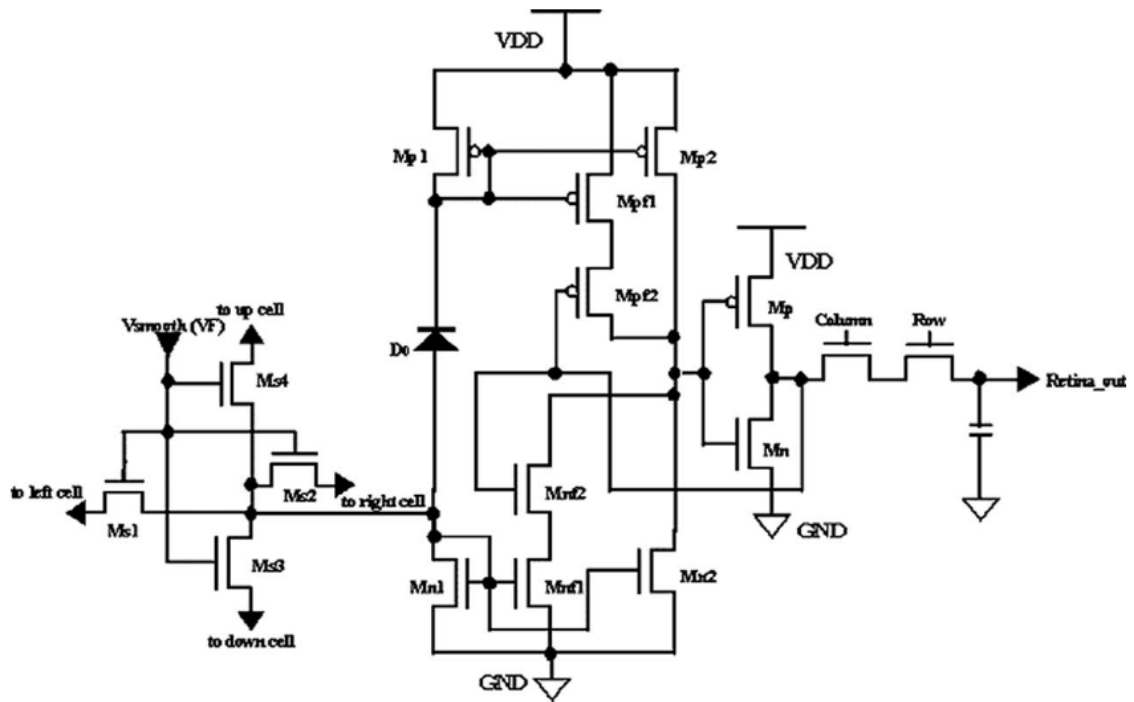
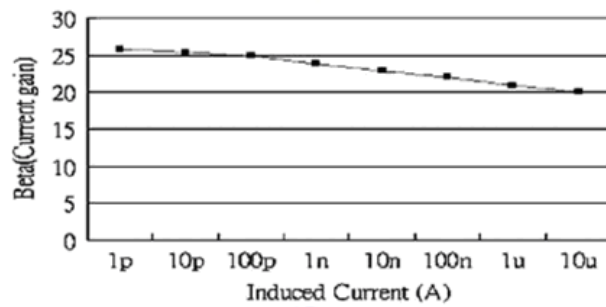
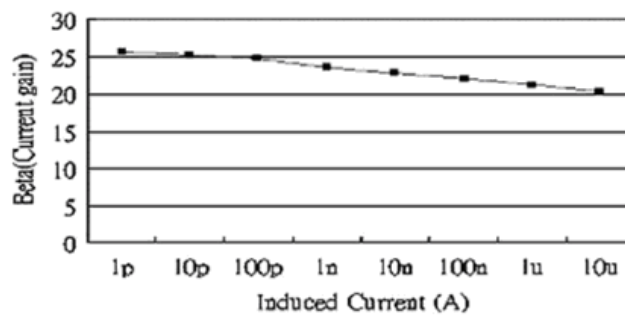


Fig. 3.3. 3. Pixel structure of the proposed retinal focal-plane sensor circuit.

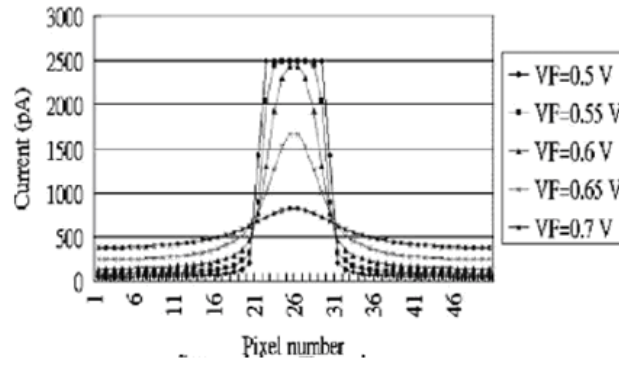


(a)

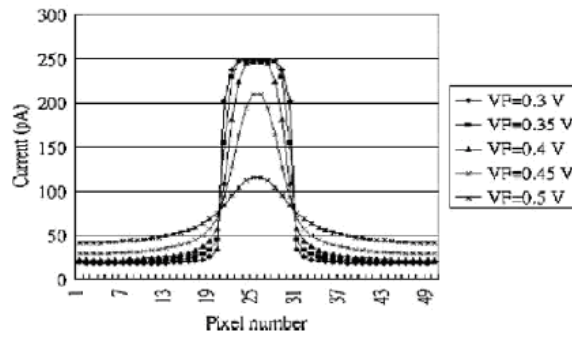


(b)

Fig. 3.3. 4. (a) Current gain of NPN pseudo-BJT. (b) Current gain of PNP pseudo-BJT.

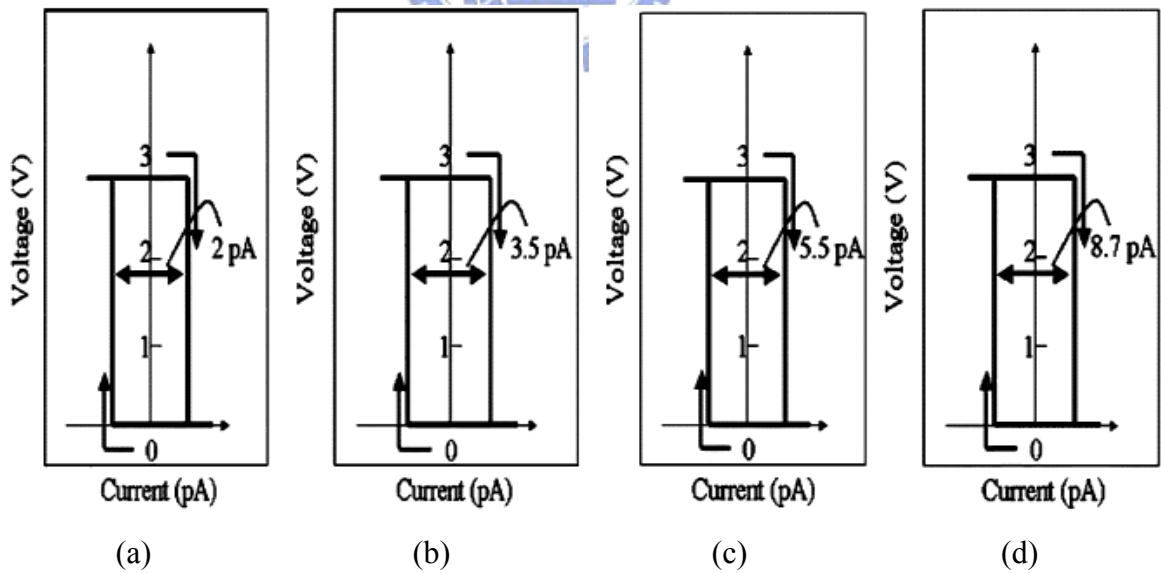


(a)



(b)

Fig. 3.3. 5. (a) Smoothing function for induced photocurrent 100 pA. (b) Smoothing function for induced photocurrent 10 pA.



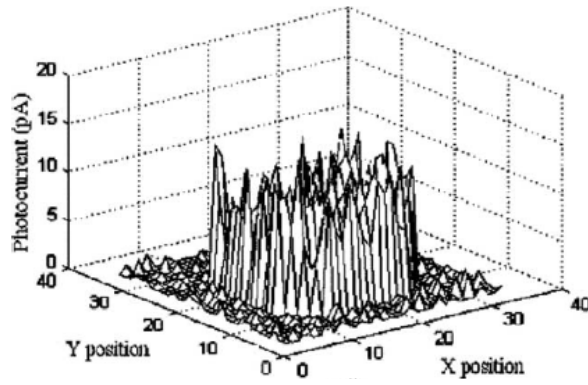
(a)

(b)

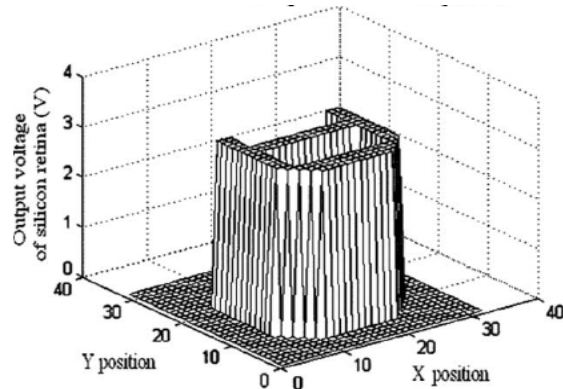
(c)

(d)

Fig. 3.3. 6. DC output characteristics (a)–(d) of adaptive current Schmitt trigger with fixed I_{smt} current 10 pA, 20 pA, 30 pA, and 40 pA, respectively.



(a)



(b)

Fig. 3.3. 7. (a) Input pattern A with a zero mean random noise that is with a standard deviation of 60% of induced current and the induced photocurrent 10pA. (b) 32x32 pixels output (Retina_out) of 2-D retinal focal-plane sensor for input pattern A.

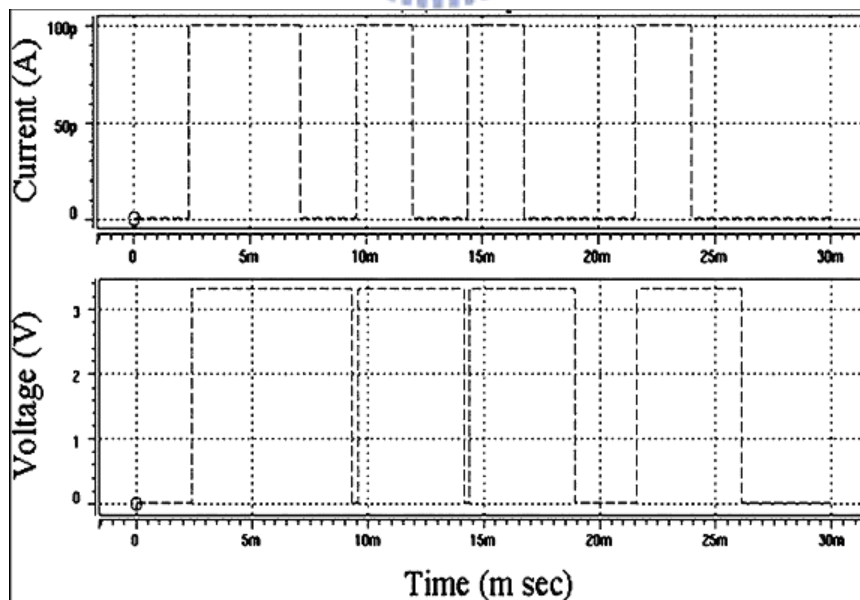
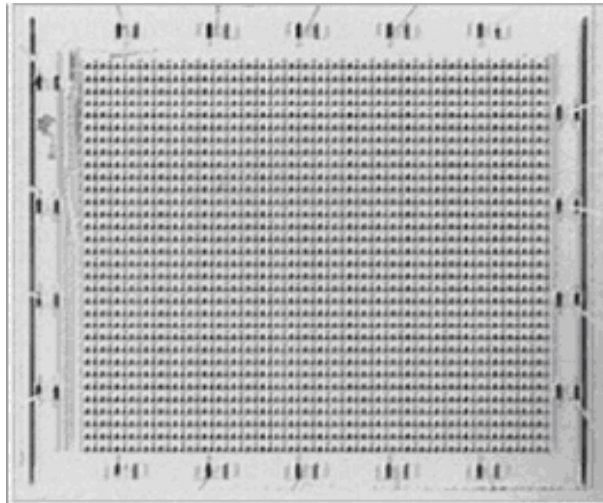
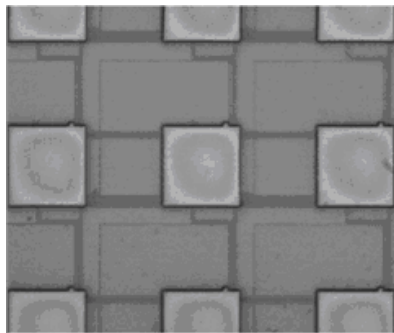


Fig. 3.3. 8. Output voltages under input current waveforms corresponding to the photocurrents generated by moving image patterns of white bars with minimum width of 500 μ m.



(a)



(b)

Fig. 3.3. 9. Photographs of the proposed retinal sensor for (a) the whole fabricated chip and (b) a single pixel.

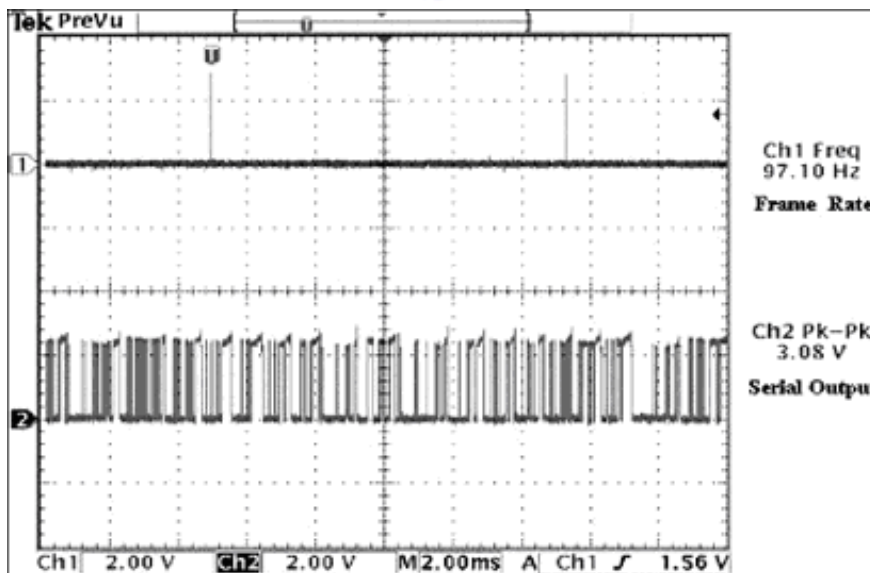


Fig. 3.3. 10. Measured waveforms for frame rate (97.1 frames/s) and serial output via data buffer.

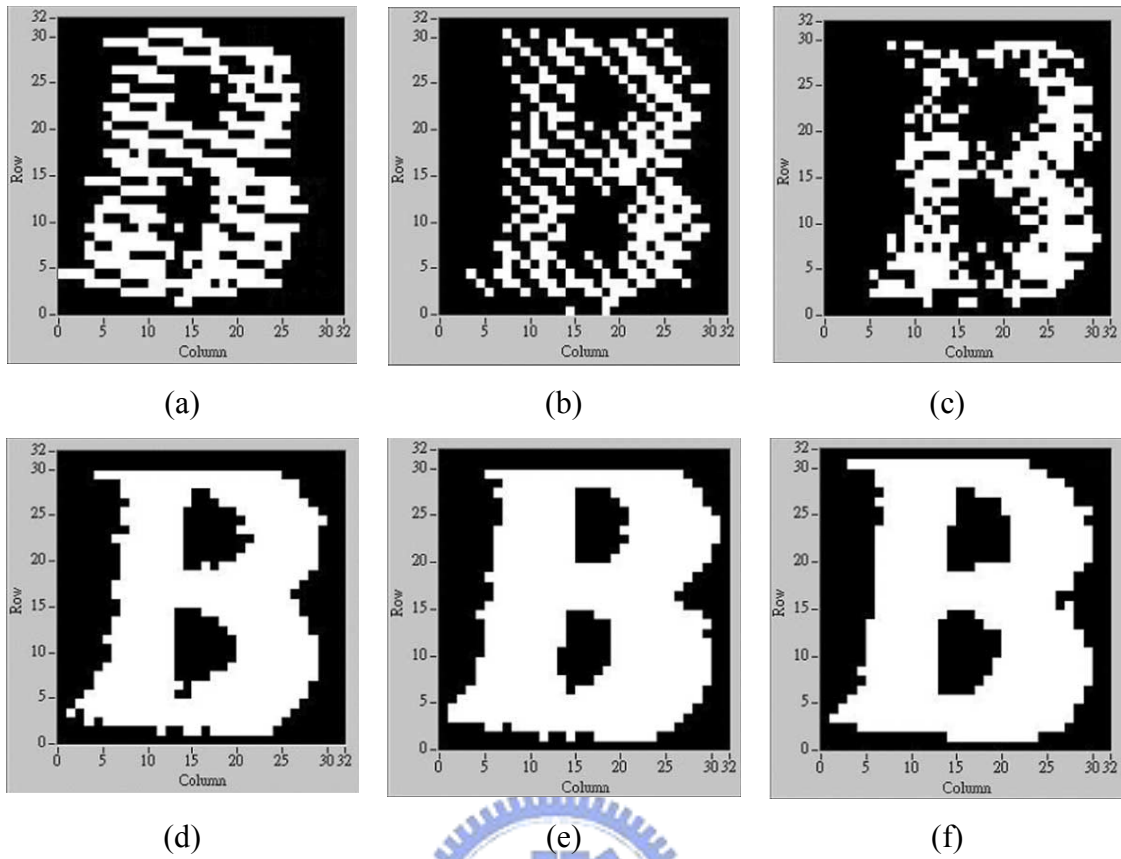
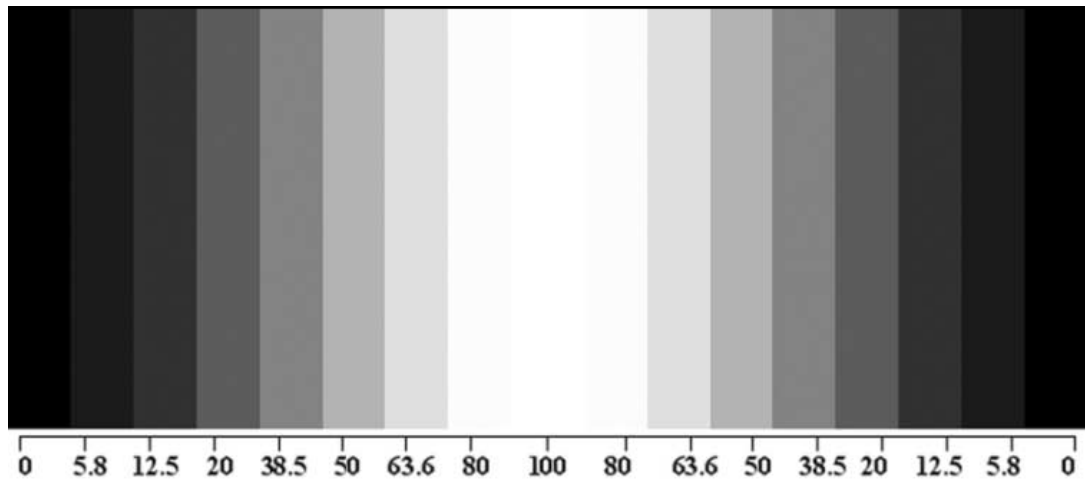
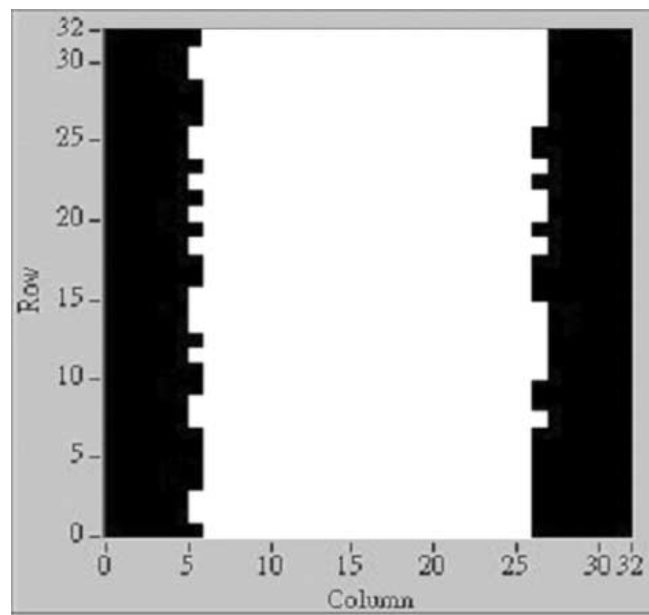


Fig. 3.3. 11. Measurement results normalized with fluorescent light at wavelength of $550 \mu\text{m}$ (13.8 lux) of different illuminations for character “B” at (a) 0.02, at (b) 0.04, at (c) 0.54, at (d) 0.87, at (e) 2.65, and at (f) 5.3.



(a)



(b)

Fig. 3.3. 12. (a) Static-graded image pattern with different contrasts (%) incident upon the retinal sensor. (b) The measurement results for enhanced edges with the minimum acceptable contrast of 20%.

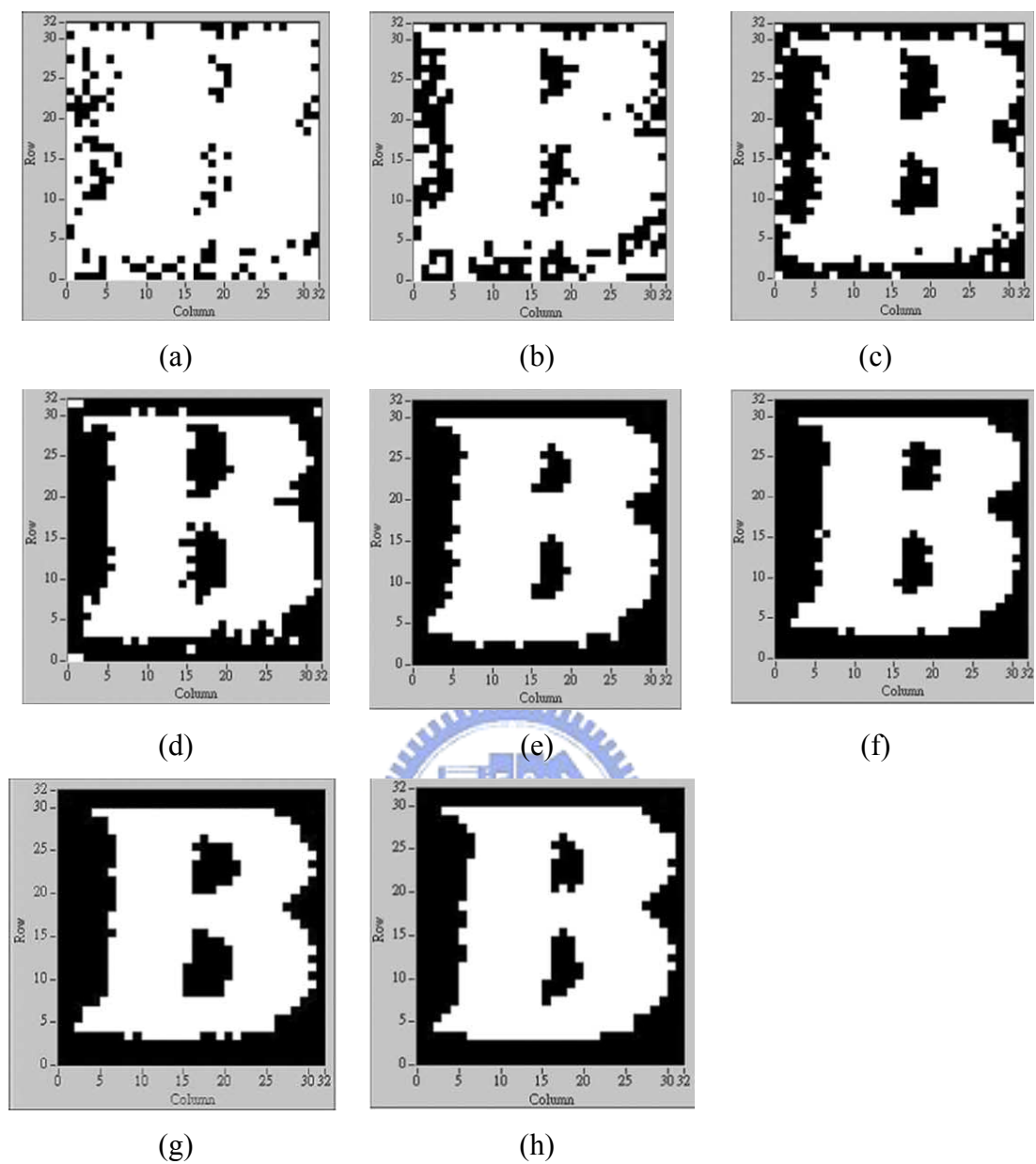


Fig. 3.3. 13. Measurement results of the smoothing function for noise removal at different control voltage for character “B” at (a) $V_F = 0.85$ V, at (b) $V_F = 0.9$ V, at (c) $V_F = 0.95$ V, at (d) $V_F = 1$ V, at (e) $V_F = 1.1$ V, at (f) $V_F = 1.2$ V, at (g) $V_F = 1.4$ V, at (h) $V_F = 1.5$ V.

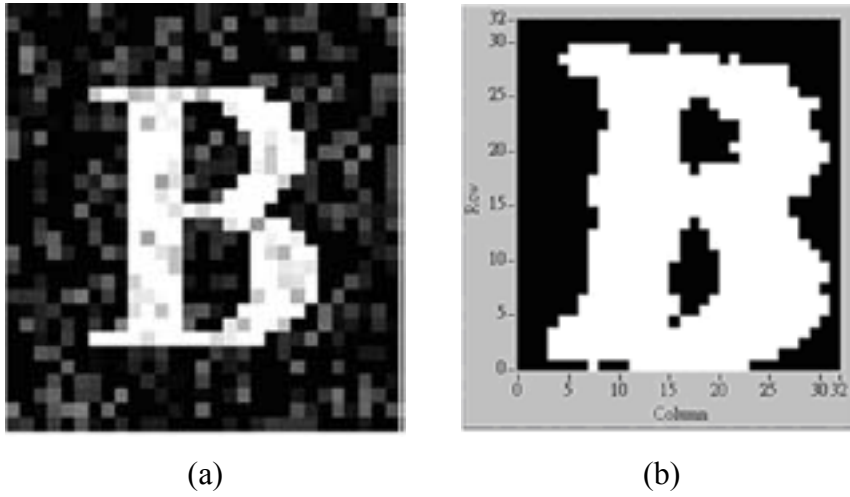


Fig. 3.3. 14. (a) Incident image with random distributed noise with a standard deviation of 50%. (b) The measurement result at $V_F = 1.5$ V.

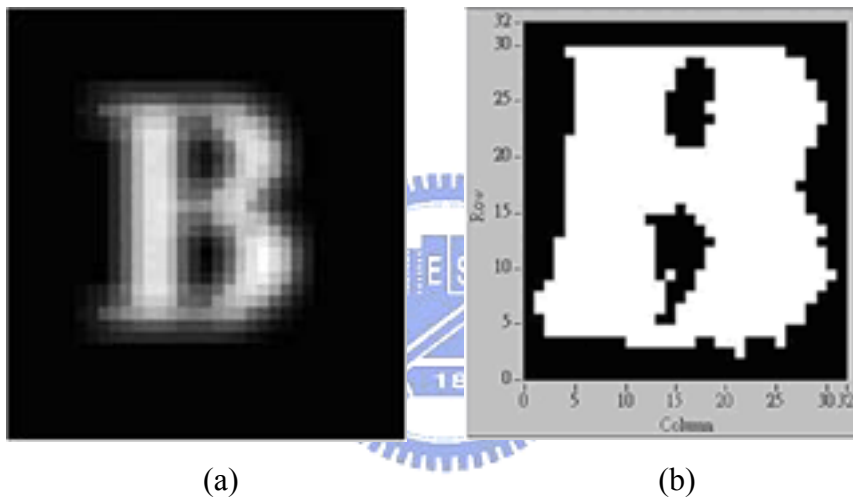


Fig. 3.3. 15. (a) Incident image blurred. (b) The measurement result at $V_F = 1.5$ V.

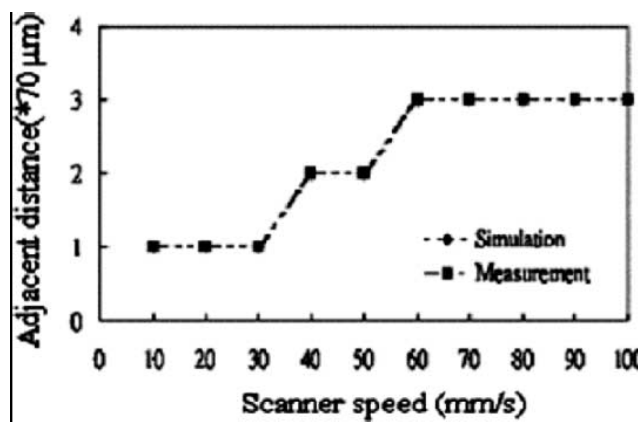


Fig. 3.3. 16. Scanner speed and minimum adjacent distance.

CHAPTER 4

THE BJT-BASED SILICON RETINA CHIPS

(II) –THE MOTION SENSORS

Motion provides rich cues in understanding the environment, and is therefore crucial for many applications including robot control, vehicle navigation and surveillance systems. Much effort has been devoted to realizing detection functions through hardware or software implementation. Typically, hardware implementation is more feasible than software implementation in achieving real-time processing under a critical speed requirement. Parallel and pixel-level computation is required to detect motion in real-time [127]. Many hardware-implemented motion detectors have recently been elucidated [9], [10], [12]-[14], [17], [108], [113], [115], [128]-[132]. Their adopted algorithms for motion detection can be separated into three categories - gradient-based [108], energy-based [9], [129], and correlation-based algorithms [10], [12]-[14], [17], [113], [115], [130]-[132]. The intensity-based algorithm, which is based upon the mapping of mathematical techniques, usually requires high-precision temporal and spatial derivatives. Therefore, it is not suitable for an analog hardware implementation. The correlation-based algorithm, which is inspired by a biological model [123], has the benefits of robustness and compactness, and it is thus the most practical algorithm for VLSI implementation. Comprehensive comparisons of these two algorithms and their implementations can be found in [119]-[122].

Besides, appropriate image acquisition and preprocessing is needed to locate accurately the edges of a moving object in the presence of noise and under varying illumination, to ensure the robustness of the motion detector. Recently, much research effort has been devoted to focal-plane motion sensors, which integrate photo sensing and signal processing into a single chip [133]. Focal-plane motion sensors are superior in size, processing time, cost and power consumption than conventional image processing systems, which includes cameras and processors. Many focal-plane motion sensors adopt the correlation-based algorithm to detect motion [10], [12]-[14], [17], [18], [131].

The required function of image acquisition and preprocessing in a motion sensor can be performed by using the retinal processing circuit. The retinal processing circuit mimics parts of functions of the cells in the outer plexiform layer of the real

retina. As in the real retina, the retinal processing circuit has similar advantages of high dynamic range, edge enhancement, and noise immunity. Of the proposed structures for retinal function [1], [7], [13], [14], [17], [46], the BJT-based retinal structure [7], [17], [46] is very compact and suitable for VLSI implementation.

In this chapter, four retinal motion sensors are presented. In section 4.1, a 2-D velocity- and direction-selective sensor with BJT-based silicon retina and temporal zero-crossing detector was introduced. This is the first motion sensor designed with the BJT-based silicon retina. In section 4.2, a CMOS focal-plane motion sensor with BJT-based retinal smoothing network and modified correlation-based algorithm is proposed. This design improved the correlation mechanism of the design of section 4.1. Thus precise motion direction and velocity can be calculated. In section 4.3, the design of a CMOS angular velocity- and direction-selective rotation sensor with retinal processing circuit is presented. In this design, the motion detection algorithm and architecture are the same with those of section 4.2 while the sensor array is arranged radially. Thus the direction (clockwise/counterclockwise) and angular velocity can be precisely detected. Moreover, special characteristics of circular motion detection are analyzed in this chapter. Finally in section 4.4, a CMOS focal-plane retinal sensor designed for shear motion detection is proposed. The motion detection algorithm and architecture are used to detect shear motion. Summary of these four works are shown in Table 4. 1.

4.1 A 2-D VELOCITY- AND DIRECTION-SELECTIVE SENSOR WITH BJT-BASED SILICON RETINA AND TEMPORAL ZERO-CROSSING DETECTOR

4.1.1 Introduction

A BJT-based silicon-retina sensory system for velocity- and direction-selective sensing is proposed. In this system, a token-based delay-and-correlate motion computation algorithm inspired by biological retinal processing is adopted, which uses edges as image tokens and correlates them with binary pulses. One of the two significant features of the proposed sensory system is that the circuitry of current-input edge extractor is simple and robust, which makes VLSI implementation feasible. The other is that the binary pulse correlation [113]-[115] is used to increase the accuracy of velocity- and direction-selective sensing. Using the proposed architecture, an experimental 32×32 motion measurement chip has been fabricated by

using a 0.6 μ m CMOS technology. The operations are also verified through measurements.

4.1.2 Motion Computation Algorithm

The token-based delay-and-correlate motion computation algorithm which is similar to the Reichardt algorithm [123], is adopted in the sensor design. The conceptual structure of the algorithm is shown in Fig. 4.1. 1. The elements R perform the functions of photoreceptors and horizontal cells in the retinas. The photoreceptors transduce light into electrical signals, whereas the horizontal cells perform the spatial smoothing on signals from photoreceptors. The edge extractors E perform the functions of the bipolar cells in the retinas, which process the signals from both photoreceptor and horizontal cell to generate a signal that contains spatial edge information of the incident image. Meanwhile, the edge extractors E identify both turn-ON and turn-OFF edges of the moving image from the signals generated by bipolar cells and generate edge pulses to perform a similar function as the action potential responses observed in transient amacrine cells of the retinas. The elements M are the correlators that correlate the edge pulse from E with the delayed edge pulse generated from the previous cell using the delay elements D. The correlator fires a pulse only when the object moves in the preferred direction and the difference between the traveling time of the object edge crossing the two cells and the selected delay time of the elements D is smaller than the width of edge pulse. The combination of M and D is used to mimic the direction-sensitive responses of ganglion cells in the retinas.

4.1.3 Hardware Implementation

A. The BJT-Based Silicon Retina

Fig. 4.1. 2 (a) shows the structure of BJT-based silicon retina [7], [124] which is used to realize the function of the elements R in Fig. 4.1. 1. In this BJT-based silicon retina, each cell has two BJTs, called smoothing BJT and isolated BJT, which are implemented using the parasitic BJT structure in a standard CMOS process. The base region of one smoothing BJT is connected with the base regions of the smoothing BJTs in its four neighbor cells via nMOSFETs to form a BJT smoothing network which is used to implement the equivalent function of the horizontal cells in the retina. The isolated BJT is used to realize the photoreceptor in the retina. The outputs are the emitter currents of the BJTs.

The response of the bipolar cell in the retina is realized by subtracting the emitter

current of the BJT in the smoothing network from that of the isolated BJT in the same cell. Fig. 4.1. 2(b) shows the measured responses [7] of a single cell in the BJT-based silicon retina with a moving light bar projected upon it. When the turn-ON edge and the turn-OFF edge of the moving light bar pass over the readout cell at t_1 and t_2 , respectively, the temporal averaging functions of the BJT smoothing network lead to the temporal zero-crossings in the emitter current difference of the photo-transistors. The appearance of temporal zero-crossings can be used to identify whether an edge of a moving object passes over the readout cell.

B. The Edge Extractor

To simultaneously realize the response of the bipolar cell and detect the temporal zero-crossings of the response as the edges of object image passing over the BJT-based silicon retina cell, an edge extractor is proposed as shown in Fig. 4.1. 3(a). In Fig. 4.1. 3(a), the transistors M_{lpi} , M_{ini} , M_{ni} , and M_{lps} , M_{ins} , M_{ns} are used to virtually bias the emitters of isolated BJT Q_{iso} and smoothing BJT Q_{smt} in the BJT-based silicon retina cell at the fixed voltage V_P and read out emitter currents I_{iso} and I_{smt} , respectively. This readout scheme, which has a common part as shown on the left, is proposed in [125] as the readout circuit for the infrared detector.

To detect the zero-crossing point without ambiguity even under noise and disturbance, a current-input Schmitt trigger [126] (M_s , M_{sr} , M_{ir} , M_i , M_F and M_{F1}) is used. The input current I_{smt} is applied to the drain of the M_s whereas the other input current I_{iso} is applied to the drain of M_i via a cascoded current mirror M_{p1} - M_{p4} . If the current through M_F and M_{F1} is ΔI , the edge signal at the output of the Schmitt trigger has a sudden change from VDD to GND when I_{iso} becomes greater than $\Delta I + I_{smt}$. This corresponds to the temporal zero-crossing point of the turn-ON edge at t_1 in Fig. 4.1. 2(b). In this case, the GND level of the edge signal turns off the NMOS M_F and ΔI is cut off from the drain of M_i . Only if I_{iso} is decreased to a value smaller than I_{smt} , will the edge signal at the output of the edge extractor change from GND to VDD. This corresponds to the temporal zero-crossing point of the turn-OFF edge at t_2 .

A temporal transition at the Edge-Signal output is further converted into an edge pulse by using the pulse conversion circuit also shown in Fig. 4.1. 3(a). It consists of two inverters used to shape the signal at the Edge-Signal node, a simple transient detection circuit used to perform the temporal differentiation, and an inverter used to produce a narrow pulse. The capacitor in the circuit is implemented using the PMOS transistor with its source and drain tied together as one plate and the gate as

the other plate of the capacitor. The discharge in the circuit is implemented by an NMOS transistor with an adjustable bias voltage V_{pulse} .

At the falling temporal transition of the input to the transient detector, the negative voltage due to the capacitance coupling makes the drain junction of the nMOSFET forward biased, which inhibits the generation of a large negative voltage pulse. Hence, another set of transient detector and inverter is used with an extra inverter at the input to invert the falling temporal transition and generate a positive voltage pulse. Then the outputs of two pulse-conversion circuits are connected to a NAND gate to form a single output. The circuit of Fig. 4.1. 3(a) realizes the function of the element E in Fig. 4.1. 1.

C. The Delay Element

Fig. 4.1. 3 (b) shows the circuit architecture used to realize the element D in Fig. 4.1. 1 for the generation of delayed edge pulse. There are four signal paths in this circuit architecture. The first two paths are used to generate delayed binary narrow pulses at the temporal transitions of signals from the edge extractor along the X direction whereas the last two paths to generate those along the Y direction. In each signal path, there are two transient detectors with the adjustable voltages V_{dX} , V_{dY} , and V_{pulse} . The first one with V_{dX} (V_{dY}) is used to generate specified delay time whereas the second one with V_{pulse} to generate narrow pulses.

D. The Correlator

Since the signals to be correlated are binary pulses, the correlators can easily, compactly, and robustly be implemented by simple NAND gates as shown in Fig. 4.1. 3(c). Motion is selectively detected by correlating the edge pulse at a pixel with the delayed edge pulse from a neighboring pixel. Only the preferred moving direction and velocity can enable the correlator to fire a pulse out. Four such correlators are used in each pixel to correlate the edge pulse with the delayed edge pulse from which four neighbors in four directions $\pm X$ and $\pm Y$ to extract 2-D velocity and direction. The outputs of all the correlators in the pixels along each direction are combined into one output terminal via a simple wired OR gate. Therefore, when the object moves with preferred velocity and direction, there are serial pulses to appear at the output terminal.

The detection of a particular velocity and direction can be realized by controlling the delay times of the delay paths along the X-axis and Y-axis with the tuning voltages

V_{dx} and V_{dy} . For example, if the selected direction of object motion is θ and the velocity is v , the selected delay times t_{dx} and t_{dy} along X-axis and Y-axis, respectively, can be written as

$$t_{dx} = d/|v \cos \theta| \quad (1)$$

$$t_{dy} = d/|v \sin \theta| \quad (2)$$

where d is the space between two adjacent BJT-based silicon retina cells. If $0^\circ \leq \theta < 90^\circ$ ($90^\circ \leq \theta < 180^\circ$), the outputs +X (-X) and +Y in Fig. 4.1. 3(c) have pulse outputs. If $180^\circ \leq \theta < 270^\circ$ ($270^\circ \leq \theta < 360^\circ$), -X (+X) and -Y have pulse outputs.

4.1.4 Measurement Results

An experimental chip was designed and fabricated in a $0.6\mu\text{m}$ N-well CMOS technology, which consists of a 32×32 array of the proposed motion detection cells. Fig. 4.1. 4(a) shows the layout diagram of the basic cell whereas Fig. 4.1. 4(b) shows the photography of the whole chip. Since both image acquisition elements and computation elements are integrated into one pixel, the wiring will not increase as the size of array increases. Thus if the die size can be freely increased, the size of array can be freely increased as well.

Fig. 4.1. 5 shows the measured waveforms in the various computational stages of one motion detection cell in the fabricated 2-D sensor array. The top traces show the measured emitter currents of isolated BJT and smoothing BJT in the fabricated BJT-based silicon retina cell, where the currents are measured by linearly converting them into voltages via the external circuits. The third trace shows the response at the Edge-Signal node in the current-mode edge extractor shown in Fig. 4.1. 3(a). As predicted, the response has sharp transitions when I_{iso} is greater than $I_{smt} + \Delta I$ or I_{iso} is smaller than I_{smt} . The fourth trace shows the edge pulse response of the current-input edge extractor shown in Fig. 4.1. 3(a). The last two traces show the X and Y delayed edge pulses from the delay element shown in Fig. 4.1. 3(b). In Fig. 4.1. 5, the delay time of the first X delayed edge pulse and that of the second X delayed edge pulse are respectively generated via the first two delay paths shown in Fig. 4.1. 3(b). The component mismatches between these two delay paths induce the mismatch between these two delay times even under the same V_{dx} . Fig. 4.1. 6 shows the measured output waveforms at the four output terminals of the fabricated chip when a bright spot moves in the 45° direction with the preferred speed 1m/sec , where only the outputs +X and +Y have serial pulses as expected.

The inter-pixel variance of the delay times is one of important factors that determine the selectivity of the sensor chip. Generally, the inter-pixel variance of the pulse width and the delay time which caused by process variations has a Gaussian distribution with mean value and standard deviation. Through the adjustment of V_{dX} (V_{dY}) and V_{pulse} , the mean value of the delay time can be set to the desired delay time whereas the mean value of the pulse width is equal to the standard deviation of the delay time. Then one can obtain around 61% of the overall output pulses with some pulses missing. In this case, the velocity and the direction of the moving objects still can be detected with good selectivity. However, the minimum pulse width has a lower limit equal to the standard deviation of the delay-time. Fig. 4.1. 7 shows the measured maximum variance of the delay time of one pixel among 8 fabricated chips where the variance percentage is around 16%. The variance is dependent on the mean value of the delay time. Using half of the delay time variances as the pulse widths to detect the preferred speeds respectively, the measured selectivity tolerance is around 8 % for all preferred speeds with some output pulses missing.

To verify the direction-selective function, a bright spot moving in different directions with same speed is projected on the chip and the inter-pulse delay time of the serial pulses at the four output terminals is measured. The required delay times along the X-axis and Y-axis for the preferred direction are set according to (1) and (2), which are equal to the inter-pulse delay times of the same direction. Fig. 4.1. 8 shows the measured inter-pulse delay times where the negative delay times represent those along the -X or -Y direction. As may be seen from Fig. 4.1. 8, the motion directions with any angles from 0° to 360° at a fixed speed of 0.5 m/sec can be detected by specifying the suitable delay times from $100 \mu s$ to $300 \mu s$ in the four directions via the tuning voltages V_{dX} and V_{dY} . If the specified delay time is infinity, the tuning voltage is set to zero to turn off the nMOSFET.

Table I shows the summary on the characteristics of the fabricated motion-selective detection chip. From the measurement results, the correct operations of the proposed visual motion detection system which is realized in CMOS technology, have been successfully verified.

4.1.5 Conclusion

A 2-D velocity- and direction-selective visual motion sensor with BJT-based silicon-retina and temporal zero-crossing detector has been proposed, analyzed, and experimentally verified. In this sensor, a token-based delay-and-correlated

computational algorithm is adopted and the motion-selective detection is achieved by correlating two binary edge pulses. Both image acquisition elements and computation elements are integrated into one cell and complicated inter-cell wiring is avoided. Moreover, the robust edge detection in the basic detection cell of the sensor is achieved using the compact structure of the BJT-based silicon retina with the current-input edge extractor which identifies the temporal zero-crossing points. The operations of the proposed motion sensor have been verified by the measurements on a 32×32 CMOS experimental chip. It has been shown that the proposed hardware architecture of the visual motion sensor provides an efficient solution for implementing a dense and robust 2-D visual chip with little power consumption and real-time processing capability.

4.2 A CMOS FOCAL-PLANE MOTION SENSOR WITH BJT-BASED RETINAL SMOOTHING NETWORK AND MODIFIED CORRELATION-BASED ALGORITHM

4.2.1 Introduction

In the previous designs [10], [12], [17], the delay element is realized by RC circuits. The resistor is typically implemented by a MOSFET resistor or a transconductance amplifier, to control the time constant. In such designs, the delay time cannot be accurately controlled. Moreover, the tunable range of the delay time is also somewhat limited. Furthermore, in conventional correlation-based computation of motion, either the temporal or the spatial edge detector is adopted for computing motion [12], [17], [113], [115], [130], [132]. However, both spatial and temporal edge detectors may occupy a large area of silicon, so that the pixel area is large.

The adopted motion computation method here is based on the correlation-based algorithm, with some modifications. It should be noted that the proposed motion sensor is intended to calculate the global velocity and direction and the terms, “velocity” and “direction” hereafter mean the global velocity and the global direction. The motion computation method is firstly to sample two image frames at a frame sampling period of 100 clock cycles. Subsequently, the previously sampled image frame is shifted to four positions along $\pm x$ and $\pm y$ directions. Then, correlation between the shifted previous frame and the current frame is computed. The

correlation results are averaged over 16 frame sampling periods. The averaged correlation results are used to calculate displacement and direction. Notably, the motion computation method is digital, and thus robust.

The delay time of the proposed motion sensor is governed by the sampling period. Consequently, the delay time is accurately controlled via adjusting the clock rate. The tunable range of the clock rate is thus high. The proposed design greatly reduces the pattern-related deviations in calculating the displacement and direction by averaging the correlation results. Averaging over longer time generally corresponds to more accurately calculated velocity and direction.

In the proposed motion sensor, the BJT-based retinal smoothing network is used to obtain the smooth signal [46], which is subtracted from the photoreceptor signal. The difference after subtraction is amplified by the current-input Schmitt trigger [126], which enhances noise immunity and eliminates ambiguity [17]. The outputs are further amplified to digital levels by two inverters. The image contrast is thereby enhanced. This structure is very suitable for motion detection applications.

The experimental chip of the proposed motion sensor is designed and fabricated by the 0.5 μ m double-ploy-triple-metal (2P3M) CMOS process. Experimental results confirmed the correct functioning of this chip. This 2-D motion sensor is suitable for the applications of image stabilization, ego motion detection and optical mouse.

Section 4.2.2 discusses the motion computation method. Section 4.2.3 describes the architecture and circuit. Section 4.2.4 gives experimental results. A concluding section ends the paper.

4.2.2 Motion Computation Method

The modified correlation-based algorithm is adopted in the proposed motion sensor. Fig. 4.2. 1 depicts the conceptual structure of the adopted motion computation method. The incident image is acquired and processed by the retinal processing circuit, R . The retinal processing circuit includes the retinal smoothing network, photoreceptor, current-input Schmitt trigger and two inverters. The incident image is processed by R to yield a contrast-enhanced, bi-level black-and-white image. The outputs of R are binary signals which are sampled and stored in two registers CF and PF , which store the current and previous sampled outputs of R , respectively. The output of PF is then shifted to the nearest neighbors, along the preferred direction, to correlate with the output of CF . All the outputs of the correlator, C , along the preferred direction, are accumulated by the accumulator throughout the array, to

determine the correlation output. The correlation output is used to calculate the displacement in a sampling period. The term, "displacement" hereafter refers to the displacement in a sampling period, except where specified. In the proposed motion sensor, the output of PF is shifted to the four nearest neighbors in $+x$, $-x$, $+y$ and $-y$ directions so that the displacement along these four directions can be determined. The corresponding correlation outputs are $C(+x)$, $C(-x)$, $C(+y)$ and $C(-y)$, respectively. The correlation output between the output of PF without shift and the output of CF as defined by $C(no)$, is also determined and is used to calculate the displacement.

The five kinds of correlation outputs are averaged over 16 sampling periods and are defined as $C_a(+x)$, $C_a(-x)$, $C_a(+y)$, $C_a(-y)$ and $C_a(no)$, corresponding to $C(+x)$, $C(-x)$, $C(+y)$, $C(-y)$ and $C(no)$, respectively. The calculated displacement, Δx , in the $+x$ or $-x$ direction normalized to the distance between two adjacent photo sensors, P , can be expressed by the averaged correlation outputs as

$$\frac{\Delta x}{P} = \frac{A - B}{2 * [C_a(no) - B]} \quad (1)$$

$$A \equiv \max\{C_a(+x), C_a(-x)\}$$

$$B \equiv \min\{C_a(+x), C_a(-x)\}$$

The introduction of A and B is used to obtain the absolute value of the difference between $C_a(+x)$ and $C_a(-x)$ and to decide whether the image is moving along $+x$ or $-x$. Similarly, the displacement, Δy , in the $+y$ or $-y$ direction can be expressed as,

$$\frac{\Delta y}{P} = \frac{G - H}{2 * [C_a(no) - H]} \quad (2)$$

$$G \equiv \max\{C_a(+y), C_a(-y)\}$$

$$H \equiv \min\{C_a(+y), C_a(-y)\}$$

The physical interpretation is discussed later. The direction of motion can be determined by comparing the amplitude of $C_a(+x)$ with that of $C_a(-x)$ as well as $C_a(+y)$ with that of $C_a(-y)$. For example, if $C_a(+x)$ exceeds $C_a(-x)$ and $C_a(+y)$ exceeds $C_a(-y)$, then the image is moving in the $(+x, +y)$ direction. The directional angle, θ , is given by,

$$\tan \theta = \frac{\Delta y}{\Delta x} = \frac{G - H}{A - B} \quad (3)$$

If the displacement and direction of motion is calculated without using the

averaged correlation outputs, the pattern-related deviations are significant. A variable, d , is defined as the distance from the edge of the incident image patterns to the center of the front pixel, in the direction of motion, as shown in Fig. 4.2. 2. The value of d is between 0 and P . Assume that the edges must move over the center of a pixel, to be detected by that pixel. The influence of the pattern on the deviation of the calculated displacement is illustrated by the example presented in Fig. 4.2. 2, in which the image pattern of a vertical stripe with a width of $4P$ is used. If the displacement within a sampling period equals P , then the detected image will move to the right by exact one pixel. If the displacement of motion is calculated without using the averaged correlation outputs, the calculated displacement will become P , according to (1) with $C_a(+x)$, $C_a(-x)$ and $C_a(no)$ replaced by $C(+x)$, $C(-x)$ and $C(no)$, respectively. If the displacement within a sampling period is less than P , d will gradually decline over successive sampling periods since the edge is approaching the center of the front pixel in the direction of motion. The calculated displacement is 0 in these sampling periods. Finally, the edge will cross the center of the front pixel in the direction of motion and the calculated displacement will become P in that sampling period. In the example of Fig. 4.2. 2, it is found that the calculated displacement is either 0 or P . Neither value, however, is the actual displacement. As can be found in the example of Fig. 4.2. 2, the calculated displacement depends on the number pixels crossed by the edge within a sampling period. The number of pixels crossed by the edge within a sampling period is determined by the distribution of the value of d for all edges, which is a property related with the pattern of the incident image. The phenomena discussed above, indicates that the deviation in the displacement and direction calculation is large and dependent on input patterns. This problem can be solved by using the averaged correlation outputs in the proposed design.

To illustrate why it is advantageous to average the correlation outputs, an example is analyzed below. Assume that the displacement is $0.2P$ and d is P , so the calculated displacements, without using the average correlation outputs, in the five subsequent sampling periods are $\{0,0,0,0,P\}$ according to (1), with $C_a(+x)$, $C_a(-x)$ and $C_a(no)$ replaced by $C(+x)$, $C(-x)$ and $C(no)$, respectively, in each sampling period. An average of correlation outputs is taken to calculate the displacement so that the deviation between calculated and actual displacement can be eliminated. Using (1) with an average over five sampling periods, yields a calculated displacement of 0.2, which is exactly the displacement normalized to P . A more generally analysis on how accuracy

is improved by averaging the correlation results is discussed below.

Assume that a rectangular pattern moves in the +x direction. $C(+x)-C(-x)$ equals the number of pixels crossed by the edges as they move to the right. $C(no)-C(-x)$ equals half the number of the pixels at the vertical edges. For example, in Fig. 4.2. 2, when the edges do not cross any pixels, then $C(+x)-C(-x)$ is zero. When the edges cross the pixels, $C(+x)-C(-x)$ is ten, which is exactly the number of pixels crossed by the edges. $C(no)-C(-x)$ is fixed at five in every sampling period, which is half the number of the pixels at the vertical edges. The ratio of $C(+x)-C(-x)$ to twice $C(no)-C(-x)$ is equal to the number of pixels crossed by edges divided by the total number of pixels at the vertical edges, which is the displacement normalized to P in the +x direction [132].

Assume that $C_a(+x)$, $C_a(-x)$, $C_a(+y)$, $C_a(-y)$ and $C_a(no)$ are the average correlation outputs over N sampling periods and E_t is defined as the total number of the pixels at the vertical edges, which is equal to $2*[C(no)-C(-x)]$. If the boundary condition is ignored, then (1) can be rewritten as,

$$\begin{aligned}
\frac{\Delta x}{P} &= \frac{C_a(+x) - C_a(-x)}{2 * [C_a(no) - C_a(-x)]} \\
&= \frac{\frac{1}{N} \sum_{i=1}^N C(+x)_i - \frac{1}{N} \sum_{i=1}^N C(-x)_i}{2 * [\frac{1}{N} \sum_{i=1}^N C(no)_i - \frac{1}{N} \sum_{i=1}^N C(-x)_i]} \\
&= \frac{\sum_{i=1}^N [C(+x)_i - C(-x)_i]}{N * E_t} \tag{4}
\end{aligned}$$

where $C(+x)_i$, $C(-x)_i$ and $C(no)_i$ are the correlation outputs at the i^{th} sampling period.

If the velocity is P/m , the number of pixels that are crossed by the edges in every m sampling periods will equal to E_t . It is because that the vertical edges move to the right by exact one pixel in every m sampling periods so that the number of the pixels at the vertical edges will equal to the total number of pixels that are crossed by the edges in every m sampling periods. Thus, the number of pixels that are crossed by the edges within N sampling periods can be expressed by,

$$\sum_{i=1}^N [C(+x)_i - C(-x)_i]$$

$$\begin{aligned}
&= \sum_{i=1}^{qm} [C(+x)_i - C(-x)_i] + \sum_{i=qm+1}^N [C(+x)_i - C(-x)_i] \\
&= q * E_t + \sum_{i=qm+1}^N [C(+x)_i - C(-x)_i] \tag{5}
\end{aligned}$$

$$N = qm + r$$

where q is the quotient of N/m and r is the residue of N/m . Substituting (5) into (4) yields,

$$\begin{aligned}
\frac{\Delta x}{P} &= \frac{q * E_t + \sum_{i=qm+1}^N [C(+x)_i - C(-x)_i]}{N * E_t} \\
&= \frac{1}{m} - \frac{r}{m * N} + \frac{\sum_{i=qm+1}^N [C(+x)_i - C(-x)_i]}{N * E_t} \tag{6}
\end{aligned}$$

$1/m$ is the displacement normalized to the P , and the other terms in (6) are deviations. From the above derivation, it is shown that the accuracy is improved by using the averaged the correlation results and a larger N corresponds to more accurately calculated displacement. The above analysis is more complex for arbitrary patterns. However, $C(+x)-C(-x)$ remains a function of the number of pixels crossed by the edges and $C(no)-C(-x)$ remains a function of half the number of the pixels at the vertical edges. Hence, the conclusion that the deviation can be reduced by averaging the correlation outputs still holds.

Notably, determining the correlation is complicated by the boundary condition because of the shifting of the previous image frame. This boundary is fixed at zero for simplicity. Therefore, the correlation at the boundary yields errors in calculating $C(+x)$, $C(-x)$, $C(+y)$ and $C(-y)$. However, the boundary condition does not influence the calculation of $C(no)$ because the previous image frame is not shifted when $C(no)$ is calculated. Two boundary factors are added in (1) and (2) to calibrate the effect due to boundary conditions and thus solve this problem in calculating displacement. Equations (1) and (2) are modified to,

$$\frac{\Delta x}{P} = \frac{A - B + b_1}{2 * [C_a(no) - B - b_2]} \tag{7}$$

$$\frac{\Delta y}{P} = \frac{G - H + b_1}{2 * [C_a(no) - H - b_2]} \quad (8)$$

where b_1 and b_2 are the calibrating factors. The value of b_1 is chosen as half of the numbers of the pixels at one side of the boundary while b_2 is the half of b_1 . Since the size of the pixel array is 32x32, b_1 and b_2 are chosen as 16 and 8, respectively.

The maximum detectable displacement is P because the output of PF is shifted only to the nearest neighbors. The minimum detectable displacement depends on the accuracy of the calculation. The sampling period can be adjusted to fit the desired range of velocity, according to the detectable range of displacement. In practice, the sampling period may be fixed or automatically adjusted according to application.

4.2.3 Architecture and Circuit

Fig. 4.2. 3 illustrates the architecture of the proposed focal-plane motion sensor, which includes the 32x32 pixel array and the peripheral circuits, including five sets of 6-bit accumulators for each row, and five sets of 11-bit accumulators. The data in the five 11-bit accumulators are read out as $C(+x)$, $C(-x)$, $C(+y)$, $C(-y)$ and $C(no)$, respectively. The average, displacement, and direction are calculated off-chip by software.

Each pixel of the 32x32 array includes the BJT-based retinal processing circuit, two registers, five correlators, and five shift registers, as depicted in Fig. 4.2. 4.

In the implementation of the BJT-based retinal processing circuit, as shown in Fig. 4.2. 5, an isolated photo-BJT is used as the photoreceptor, a smoothing photo-BJT with adjustable N-channel MOSFET resistors is used to form the retinal smoothing network, and a current-input CMOS Schmitt trigger [17], [126] and two inverters are included. The base of the smoothing photo-BJT Q_1 is connected to the photo-BJT Q_1 's four nearest neighbors, via the N-channel MOSFET resistors, M_{srd} and M_{srr} , whose resistance is controlled by the gate voltage, V_{smooth} , forming the smoothing network. The transistors, M_{ins} , M_{ips} , M_n and M_{ipi} , M_{ini} , M_p , are used to virtually bias the emitters of Q_1 and Q_2 at V_{bias1} . M_{ip} , M_{in} and M_c are common to all pixels. The current-input CMOS Schmitt trigger comprises of M_s , M_{sr} , M_i , M_{ir} , M_{f1} and M_{f2} transistors. The voltage, V_f is used to adjust the threshold level. The transistors, M_{p1} , M_{p2} , M_{p3} and M_{p4} are used to mirror the emitter current of Q_2 to the current-input CMOS Schmitt trigger. The inverters, A and B, amplify the output of the current-input CMOS Schmitt trigger to VDD or VSS so that the signal is converted from analog to binary.

The output of the retinal processing circuit is then sent to *CF*, which memorizes the current frame, as depicted in Fig. 4.2. 4. The *PF* in Fig. 4.2. 4 stores the previous frame, and sends its output to the four nearest neighboring pixels in the $+x$, $-x$, $-y$ and $+y$ directions. The sample signal in Fig. 4.2. 4 causes *CF* and *PF* to sample their inputs every 100 clock cycles. The output of *CF* is then correlated with the output of *PF* and the outputs of *PF* from its neighbors. The outputs of the correlators are stored in five shift registers and then shifted to the 6-bit accumulators in each row. The motion computation method precisely controls the sampling period by controlling the clock rate and the velocity can be calculated as the displacement divided by the frame sampling period. Moreover, the tunable range of the clock rate exceeds that of the RC delay circuits, so the detectable range of the velocity is greatly increased.

NAND rather than XOR is used in the correlator because the former is less likely to have errors. If a noise exists in the signal path, then the inputs of the correlator have a probability, g , of error. The probability of error in the output of the correlator is $2*(g-g^2)$ for XOR and $g-g^2$ for NAND. The probability of error for XOR is clearly double that for NAND.

The outputs of the correlator stored in five shift registers are shifted to the 6-bit accumulators in each row to be accumulated. This chip includes five sets of 11-bit accumulators. The outputs of the 6-bit accumulators are shifted to the 11-bit accumulators, which accumulate the outputs of the 6-bit accumulators. The data in the 11-bit accumulators are sent out of chip serially as the correlation outputs, $C(+x)$, $C(-x)$, $C(+y)$, $C(-y)$ and $C(no)$. It takes totally 100 clock cycles to sample the image, shift the outputs of the correlators to the 6-bit accumulators, shift the data in the 6-bit accumulators to 11-bit accumulators, send the data out of chip and wait for the next sampling period. The software calculates the average of the correlation outputs, displacement and direction.

Fig. 4.2. 6 presents the results of the HSPICE simulation. As shown in Fig. 4.2. 6, a pattern, “H”, is incident on the motion chip under various conditions, to confirm the advantages of high dynamic range, contrast enhancement and noise immunity. In Fig. 4.2. 6(a), the photocurrents of the dark and bright regions are $0.66I_b$ and I_b , respectively, where I_b is defined as the photocurrent generated by the light source. Assuming that the illumination of the light source varies, the simulation result of HSPICE indicates that the outputs of retinal processing circuit are constant as I_b varies from $0.1 \mu\text{A}$ to 1 nA . As can be calculated from Fig. 4.2. 6(a), the minimum

acceptable contrast of input image is about 20%. Fig. 4.2. 6(b) offers another example of contrast enhancement. The pattern is the same but the image is blurred. The simulation result shows that the contrast can be enhanced. The location of the edge is governed by the resistance of the MOSFETs in the smoothing network. Fig. 4.2. 6(c) depicts a situation in which the pattern is disturbed by noise. The noise immunity is enhanced by the current-input CMOS Schmitt trigger, which is controlled by V_f . A normally distributed noise is added to the original image with a standard deviation of 0.04 nA and V_f is set at 0.4 V. The simulation result indicates that the outputs of retinal processing circuit are not affected by this noise level. The retinal processing circuit can work with the standard deviation of noise greater than 0.04 nA, if V_f is greater than 0.4 V. The simulation results confirm the advantages of the retinal processing circuit. Firstly, the output of the retinal processing circuit can adapt to the background illumination, so that a high dynamic range can be obtained. Secondly, the error in the computation of motion can be reduced since the contrast of image is enhanced with the minimum acceptable contrast of 20%. Finally, the retinal processing circuit is immune to noise and the noise immunity is enhanced by the current-input CMOS Schmitt trigger.

4.2.4 Experimental Results

An experimental focal-plane motion sensor chip is designed and fabricated by the 0.5 μm single-poly-triple-metal CMOS process. Fig. 4.2. 7(a) presents a photograph of the fabricated chip and Fig. 4.2. 7(b) displays the photograph of a single pixel. The area of this chip is $4200 \times 4000 \mu\text{m}^2$ and that of a single pixel is $100 \times 100 \mu\text{m}^2$ with a fill factor of 11.6%. The dc power dissipation is 120 mW at 5 V in the dark.

The emitter and the collector were biased at 3.5 V and 0 V, respectively, and the base was floating, to investigate the photo response of a photo-BJT. The intensity of the incident light on the photo-BJT was then varied and the collector current, corresponding to various illuminations, was recorded. The generated photo current is expressed as, $I_{ph} = I_c / (\beta + 1)$, where β is the current gain of BJT and I_c is the collector current. The current gain is measured as 48 and the photo current is evaluated as in Fig. 4.2. 8. The illumination for all the following experiments is set at 36 lux at wavelength of 550 μm .

Fig. 4.2. 9 shows four patterns used to test the motion sensor, to show that the proposed design can work on the different patterns. The four patterns are chosen for

their different characteristics. Fig. 4.2. 9(a) shows a striped pattern. The stripes are equally spaced so that d is a constant, as in the example in Fig. 4.2. 2. Fig. 4.2. 9(b) depicts the pattern formed by the circles. This pattern has a more uniform distribution of d than does the stripes because the edge of the circles is round. Both the stripes and the circles are spatially periodic. The third pattern presented in Fig. 4.2. 9(c) is, "soccer". The third pattern involves a rather random distribution of d and is spatially aperiodic, unlike the stripes and the circles. The fourth pattern is Lena and is used to test the motion sensor to determine whether the displacement can be calculated for a gray-scale image with a randomly distributed d . The contrast is 80% for all test patterns except Lena. Only a part of image pattern is incident on the chip since the size of the four patterns exceeds that of the motion sensor chip.

Fig. 4.2. 10 shows the calculated velocity and the deviation ratio. The displacement is calculated from (7) and (8) and the velocity is the ratio of the displacement to the frame sampling period. The deviation ratio is defined,

$$\text{deviation ratio (\%)} = \frac{(V_e - V_a)}{V_a} * 100 \quad (9)$$

where V_e is the calculated velocity and V_a is the actual velocity. The sampling rate is 10 Hz. The correlation results are averaged over 16 frame sampling periods in all experiments. The image moves in the $-x$ direction with the velocity varying from 1 pixel/sec to 10 pixels/sec; only the calculated result for the x direction is shown, since the calculated displacement in the y direction is zero. According to Fig. 4.2. 10, the four curves rather closely resemble each other and the deviation is within $\pm 20\%$. Experimental results confirm that the proposed design can work for different patterns. Only the striped pattern is used in the following experiment because the choice of pattern will not affect accuracy.

Fig. 4.2. 11 shows the detectable range of the velocity. The velocity of the moving image decreases one decade from 140,000 pixels/sec and 1 pixel/sec along the $-y$ direction, and the sampling rate is 140K Hz and 1 Hz, respectively. As shown in Fig. 4.2. 11, the proposed design could work with a sampling rate that varied by six decades and a velocity deviation within $\pm 20\%$.

The minimum detectable velocity depends on the number of the frame sampling periods over which the correlation results are averaged. The correlation outputs are averaged over 16 sampling periods in the proposed motion sensor. In commercial optical mouse systems, the maximum detectable velocity is around 12 inch/sec (304.8

mm/sec). If the effect of the lens is ignored, then the on-chip velocity will be 304.8 mm/sec. According to this velocity, the sampling rate is set to 3,050 Hz. As shown in Fig. 4.2. 12, the proposed design can calculate a velocity of 152.5 pixels/sec, that is, a displacement of 5 μm within a sampling period.

Fig. 4.2. 13 illustrates the accuracy of the calculation of direction. The sampling rate is 75kHz. Two velocities are tested. The selected test velocity is fixed and the direction of motion is varied from 0 to 360 degrees. Since the striped pattern is used, the stripes are rotated to be perpendicular to the direction of motion so that the aperture problem is avoided. Experimental results indicate that the proposed design can determine the direction of motion with an angular deviation less than 4 degrees while the velocity varies.

4.2.5 Conclusion

This work presents a real-time CMOS focal-plane motion sensor that uses the BJT-based retinal processing circuit and a modified correlation-based algorithm. The correlation-based algorithm is modified and applied to calculate the velocity and direction and the BJT-based retinal processing circuit is used to acquire images and enhance contrast. The presented motion sensor greatly reduces the deviation of the calculated displacement and direction for different image pattern by averaging correlation results over 16 frame sampling periods. Consequently, the proposed design can work for different incident images. Furthermore, the velocity ranging from 1 pixel/sec to 140,000 pixels/sec can be calculated by the proposed design via adjusting the clock signal, without reducing accuracy. The smallest displacement that can be calculated within a sampling period is 5 μm . The direction can be calculated correctly between 0 and 360 degrees with an angular deviation less than 4 degrees. The proposed motion sensor is comprised of a 32 \times 32 pixel array and peripheral circuits. The area of a pixel is 100 \times 100 μm^2 with a fill factor of 11.6%, and the total chip area is 4200 \times 4000 μm^2 . The supply voltage is 5 V and the dc power consumption is 120 mW. The average, velocity, and direction are calculated off-chip by software. In the future, the functionality of the software will be further integrated into the chip and the sampling rate will be adaptively adjusted according to desired applications.

4.3 ANALYSIS AND DESIGN OF A CMOS ANGULAR VELOCITY- AND DIRECTION-SELECTIVE ROTATION SENSOR WITH RETINAL PROCESSING CIRCUIT

4.3.1 Introduction

The correlation-based algorithm is adopted by the proposed rotation sensor to detect the local motion vectors, whereas the retinal processing circuit [7][18][46], which mimics some of the functions of the cells in the outer plexiform layer of the real retina, is used to sense and preprocess the incident images. The output of the retinal processing circuit can adapt to the background illumination so that a high optical dynamic range can be obtained.

In previously proposed focal-plane motion sensors, the spatial distribution of the pixels is typically regular and periodic because these sensors are intended to detect invariants in Cartesian coordinates. For these sensors, a mapping from Cartesian to polar coordinates is required to detect rotation. However, if the pixels are placed in a polar arrangement, rotation can be detected by shifting the images in the θ direction so complex mapping can be avoided.

The pixels of the proposed rotation sensor here are placed in a circular arrangement to detect the global rotation direction and velocity of the rotating images. There are totally 104 pixels, which form five concentric circles. The numbers of pixels in the circles are 8, 16, 16, 32 and 32 in order from the center. Every pixel is correlated with clockwise and counterclockwise pixels that are 45° apart. Local motion vectors are detected by the correlators in each pixel. The outputs of all correlators in a single circle are aggregated to determine the velocity and direction of the global rotation. The proposed rotation sensor is selective to the angular direction and velocity of rotating images. The selected angular velocity is controlled by the frequency of an external clock signal. The angular velocity-selectivity is enhanced by placing more than one pixel between two correlated pixels and correlating with the pixel that is 45° apart. The angular velocity-selectivity is analyzed and equations are derived to describe the angular velocity-selectivity. If the incident image has multiple edges, then the angular velocity-selectivity is related to both the number and the positions of the edges and the angular velocity-selectivity is expressed by a set of inequalities.

The advantageous characteristics of the proposed rotation sensor include a high optical dynamic range, real-time image processing, and a wide range of detectable angular velocity. The proposed rotation sensor is appropriate for applications like the real-time and remote detection of the rotation of automobile engines and wheels,

motors, microscopic rotating images, etc.

An experimental chip was designed and fabricated by a 0.6 μm single-poly-triple-metal CMOS process. The total chip area was 1812 \times 1825 μm^2 . The area of a single pixel was 91 \times 84 μm^2 with a fill factor of 20%. The dc power consumption was 10 mW at 5 V in the dark. The experimental results of the fabricated chip confirmed that both the clockwise and counterclockwise directions can be accurately detected. The angular velocity-selectivity was also verified at angular velocities from 2.5×10^{-3} π/sec to 40 π/sec . By sweeping the clock rate, the proposed rotation sensor can be used to detect a range of angular velocities from 2×10^{-2} π/sec to 206 π/sec . The optical dynamic range at a contrast of 80% was 52 dB, from 0.91 lux to 366 lux.

Section 4.3.2 analyzes the method of detecting rotation. Section 4.3.3 shows the architecture of the proposed rotation sensor. Section 4.3.4 presents the experimental results and, finally, conclusion is presented.

4.3.2 Rotation Detection Method

In most correlation-based motion sensors, the pixels are regularly distributed in a rectangular pattern and each pixel is correlated with the delayed photo-inputs of the adjacent pixels to determine the local motion vectors. However, if the incident image is rotated, the tangential velocity is proportional to the radius. For the motion sensors with regularly and rectangularly distributed pixels, the delay time, which determines the local velocity to be detected, must be adjusted according to the radius in order to detect the tangential velocity. A motion sensor cannot easily adjust all the local delay times of each pixel to detect rotation. Moreover, even if all the local delay times could be generated, mapping must be performed from Cartesian coordinates to polar coordinates to detect angular velocities and directions. The pixels in the proposed rotation sensor are arranged in a polar structure to detect the rotation, and thus resolve these problems. Instead of generating the desired delay times for each pixel, the pixels are placed on a circle, with an equal angular spacing, so that the distance between two adjacent pixels is proportional to the radius of rotation, and the delay time is thus the same for all pixels.

The conceptual structure of the adopted correlation-based algorithm for detecting rotation is shown in Fig. 4.3. 1, where there are K pixels in a circle. A single pixel consists of both photo sensing and signal processing units, to form a focal-plane

motion sensor. The retinal processing circuit PH includes the retinal smoothing network [7], [18], [46], a photoreceptor, a current-input Schmitt trigger [126] and an inverter. The retinal smoothing network is used to extract the local spatial and temporal averages of the input images. The photoreceptor senses the input images. The output currents of the retinal smoothing network and the photoreceptor are sent to the current-input Schmitt trigger, which amplifies the difference between the two input currents with hysteresis. The output of the current-input Schmitt trigger is a voltage signal and is further amplified to VDD and VSS by the inverter. The output image of PH is a black-and-white image. In the black region, the output voltage of the retinal processing circuit will be VSS, which is logic zero, whereas in the white region, the output voltage will be VDD, which is logic one. The output voltage of PH is sampled at the rising edge of the clock signal and is stored in the register CF . The data in CF is shifted to the register PF after a clock period. The two registers CF and PF are used to store current and previous image frames. The output of PF is then sent to the correlator C of the pixel in the preferred direction. The delay time is determined by the period of the clock signal, which can be precisely adjusted to detect wide range of angular velocities, independent of the process variation [18]. If the clock period equals the time for which the incident image moves from one pixel to the next pixel, then the two inputs of the correlator will be the same and the output of the correlator will be at logic one. The appearance of logic one indicates that a selected local motion vector is detected. MLE is used to aggregate the outputs of all correlators in a single circle, to determine the velocity and direction of the global rotation. MLE is implemented using a NAND gate, so the output of MLE is logical zero if the outputs of all correlators are at logic one.

A. Analysis of Angular Velocity-selectivity for a Single-edged Image

The angular velocity-selectivity of a single-edged image is initially analyzed and generalized to the image with more than one edge. A single edge is rotated clockwise from the $(i-1)^{\text{th}}$ pixel P_{i-1} to the i^{th} pixel P_i within n_0 clock cycles, as shown in Fig. 4.3. 2(a), where P_{i-1} and P_i are the two adjacent and correlated pixels in the same circle and θ_s is the angle between the two correlated pixels. The region behind the edge is black as shown in Fig. 4.3. 2(a). In Fig. 4.3. 2(a), the edge is rotated clockwise by an angle of ωT in a clock cycle, where ω is the angular velocity and T is the clock period. In computing the output of MLE at any clock cycle, only the two correlated pixels that

are next to the edge, i.e. P_{i-1} and P_i in Fig. 4.3. 2(a), are significant in determining the output of MLE during any clock cycle because the pixels that are not next to the edge are either in the black or the white region, so the data stored in CF and PF of these pixels are the same, and the correlation results for these pixels are always at logic one. Thus, the correlation results for these pixels do not influence the output of MLE .

If ωT does not exceed θ_s , this edge is approaching to P_i by an angle of ωT in a clock cycle. During these clock cycles, the output of the correlator of P_{i-1} is maintained at logic one while the output of the correlator of P_i is at logic zero. The output of the correlator of P_i becomes logic one at $t=n_0T$ when the edge moves over P_i . The output of MLE becomes logic zero at $t=n_0T$. Since the angle between P_{i-1} and P_i is θ_s and the edge approaches P_i by an angle ωT in a clock cycle, the period for which the MLE outputs logic zero is $n_0=\theta_s/\omega T$ clock cycles. For example, if the edge moves from P_{i-1} with an angular velocity of $\theta_s/5T$, the outputs of the correlators of P_{i-1} and P_i in five successive clock cycles are $\{1,1,1,1,1\}$ and $\{0,0,0,0,1\}$. The output of MLE is $\{1,1,1,1,0\}$ and the period n_0 is five.

If the angular velocity of the rotating image exceeds θ_s/T , the edge will move over P_i in every clock cycle. However, this edge approaches P_{i+1} by an angle of $\omega T-\theta_s$ in every clock cycle. Once this edge reaches P_{i+1} , a correlation result of logic zero is generated at P_{i+1} and the output of MLE is at logic one. The period during which the MLE outputs logic one is $n_1=\theta_s/(\omega T-\theta_s)$ clock cycles. For example, if ωT is $6\theta_s/5$, then the correlation outputs of P_{i-1} , P_i , and P_{i+1} in five successive clock cycles are $\{1,1,1,1,1\}$, $\{1,1,1,1,1\}$ and $\{1,1,1,1,0\}$, respectively. The output of MLE is $\{0,0,0,0,1\}$ so n_1 is five.

The ratio R is defined as the ratio of the number of times for which the output of MLE is at logic zero during N clock cycles to N . If ωT does not exceed θ_s , since the period for which the MLE outputs logic zero is $n_0=\theta_s/\omega T$ clock cycles, q_0 MLE outputs of logic zero occur within N clock cycles, where q_0 is the quotient N/n_0 . If r_0 is the remainder of N/n_0 , $N=q_0n_0+r_0$. According to the definition of R , R can be expressed by

$$R(\%) \cong \frac{100q_0}{N} = \frac{100(N-r_0)}{n_0N} = 100\left(\frac{1}{n_0} - \frac{r_0}{n_0N}\right) \quad 0 \leq \omega \leq \frac{\theta_s}{T} \quad (1)$$

If N is large, the ratio R can be approximated as,

$$R(\%) \cong \frac{100}{n_0} = \frac{100\omega T}{\theta_s} \quad 0 \leq \omega \leq \frac{\theta_s}{T} \quad (2)$$

If ωT is greater than θ_s , then the period for which the *MLE* output is logic one is $n_1 = \theta_s / (\omega T - \theta_s)$ clock cycles. Thus, q_1 *MLE* outputs of logic one occur within N clock cycles, where q_1 is the quotient of N/n_1 . If r_1 is the remainder of N/n_1 , $N = q_1 n_1 + r_1$. According to the definition, R can be expressed by,

$$R(\%) \equiv 100 \frac{N - q_1}{N} = 100 \left(1 - \frac{N - r_1}{n_1 N}\right) = 100 \left(1 - \frac{1}{n_1} + \frac{r_1}{n_1 N}\right) \quad \frac{\theta_s}{T} \leq \omega \leq \frac{2\theta_s}{T} \quad (3)$$

If N is large, the ratio R can be approximated as,

$$R(\%) \cong 100 \left(1 - \frac{1}{n_1}\right) = 100 \left(1 - \frac{\omega T - \theta_s}{\theta_s}\right) \quad \frac{\theta_s}{T} \leq \omega \leq \frac{2\theta_s}{T} \quad (4)$$

Fig. 4.3. 2 (b) plots the relationship between R and angular velocity. R is maximum at θ_s/T , which can be controlled by the period, T , of the clock signal. Notably, R is also maximum at $\omega = \theta_s/T + b(2\pi/T)$, where b is a arbitrary integer, due to the aliasing effect.

B. Analysis of Angular Velocity-selectivity for Multiple-edged Image

The above analysis concerns a single edge. In practice, the incident image always has more than one edge. Angular velocity-selectivity is influenced by the number and positions of the edges. The following analysis is based on the assumption that there is no more than one edge existing between two adjacent pixels. If the image has several edges, every edge has to move across the pixel that lies in front of the edge, for example P_i in Fig. 4.3. 2(a), in a single clock cycle to yield a logic zero at the *MLE* output. If the angular velocity is θ_s/T , then R equals 100%. However, if the edges are not exactly rotated by θ_s in a clock cycle, the time taken by an edge to move across its own front pixel is different for different edge since the initial positions of the edges are different.

Fig. 4.3. 3 illustrates how the initial positions of the edges affect the time taken by an edge to move across its own front pixel. There are eight pixels, P_0 to P_7 , in a circle. The image has four edges E_1, E_2, E_3 and E_4 and the initial angles θ_{ep} between these edges and their own front pixels are $\theta_s, 3\theta_s/4, \theta_s/2$ and $\theta_s/4$, respectively. If the angular velocity is $3\theta_s/4T$, the front pixel of E_1 is P_1, P_1, P_2 and P_3 for the first, second, third and fourth clock cycles, respectively. Thus, the pattern of correlation outputs at the front pixels of E_1 in the first four clock cycles is $\{0,1,1,1\}$. For E_2, E_3 , and E_4 , the patterns of correlation outputs at their front pixels during the first four clock cycles are $\{1,0,1,1\}$, $\{1,1,0,1\}$ and $\{1,1,1,0\}$, respectively. Each set of correlation output

patterns periodically repeats. This example indicates that the different values of θ_{ep} result in a time difference between the occurrences of logic zero in the correlation output patterns of the front pixels. The resultant *MLE* outputs during the first four clock cycles are $\{1,1,1,1\}$ and R is zero. If θ_{ep} is the same for every edge, then the time taken by every edge to move across its own front pixel is the same, so it is similar with the single-edged case. Thus, the correlation output patterns are the same for every edge and are one of $\{0,1,1,1\}$, $\{1,0,1,1\}$, $\{1,1,0,1\}$ and $\{1,1,1,0\}$. The output of *MLE* is $\{1,0,0,0\}$, $\{0,1,0,0\}$, $\{0,0,1,0\}$ or $\{0,0,0,1\}$ and R is 75%, which is the value derived from Eq. (2) with $\omega=3\theta_s/4T$.

If we consider a single edge, the number of times for which correlation output is at logic one during N clock cycles is the same as that for which the *MLE* output is at logic zero during N clock cycles, which can be calculated from Eq. (2) as $N\omega T/\theta_s$, if ω is less than θ_s/T . In the multiple-edged case, every edge generates $N\omega T/\theta_s$ times of logic one at the correlation output of its front pixels within N clock cycles. For example, if $N=4$, E_1 generates logic one at the output of correlator $4(3\theta_s/4T)T/\theta_s=3$ times. The same number can be also calculated from the correlation output pattern of E_1 $\{0,1,1,1\}$ as three. Thus, for each edge, there are $N-N\omega T/\theta_s$ times of logic zero at the correlation output of its front pixels during N clock cycles. The above example of Fig. 4.3. 3 shows that the different values of θ_{ep} cause the logic zero of correlation output of the front pixels to occur at different time. If the image has L edges and the values θ_{ep} for all of the edges are equally distributed within θ_s , as in the above example of Fig. 4.3. 3, logic zero appears at the correlation outputs of the front pixel for L edges in turn. The output of *MLE* is logic one if one of the outputs of the correlators is at logic zero. Thus, the number of times for which the output of *MLE* is logic one during N clock cycles is $L(N-N\omega T/\theta_s)$. According to the definition of R , R is given by,

$$R(\%) = 100 \frac{[N - L(N - N\omega T/\theta_s)]}{N} = \frac{100L(\omega T - \frac{L-1}{L}\theta_s)}{\theta_s} \quad \frac{(L-1)\theta_s}{LT} \leq \omega \leq \frac{\theta_s}{T} \quad (5)$$

According to Eq. (5), R is decreased to zero at $\omega=\theta_s(L-1)/LT$ and increased to 100% at $\omega=\theta_s/T$. If ω exceeds θ_s/T , a similar analysis can be performed to obtain the relationship between R and ω as

$$R(\%) = 100 \left[1 - \frac{L(\omega T - \theta_s)}{\theta_s} \right] \quad \frac{\theta_s}{T} \leq \omega \leq \frac{(L+1)\theta_s}{LT} \quad (6)$$

R falls to zero at $\omega = \theta_s(L+1)/LT$ and increases to 100% at $\omega = \theta_s/T$.

If θ_{ep} is the same for every edge, the time when every edge moves across its own front pixel is the same, so the relationship between R and ω is the same as in the single-edged case. The relationship between R and ω is given by Eqs. (2) and (4).

The above two extreme cases of θ_{ep} set the maximum and minimum values of R at every ω . Fig. 4.3. 4(a) presents the relationship between R and ω for arbitrary position of the edges. R is confined to the shaded region, defined by Eqs. (2), (4), (5), and (6).

MATLAB simulations were performed by rotating the image clockwise, and the outputs of MLE were recorded over 100 successive clock cycles, such that $N=100$, to compute R . ω was swept from 0 to $2\theta_s/T$ to obtain the curve of R versus ω . Simulations were performed with various numbers of edges in various positions. Fig. 4.3. 4(b) and 4(c) show the simulation results for $L=2$ and $L=4$, respectively, where L is the number of edges. The angles θ_{ep} for every edge are the same for curve 1 in Fig. 4.3. 4(b) and (c). As can be seen from Fig. 4.3. 4(b) and (c), the relationship between R and ω depicted by curve 1 is consistent with Eqs. (2) and (4). For curve 2 in Fig. 4.3. 4(b), θ_{ep} is set to θ_s and $\theta_s/2$ and for curve 2 in Fig. 4.3. 4(c), it is set to θ_s , $3\theta_s/4$, $\theta_s/2$ and $\theta_s/4$. The relationship between R and ω represented by curves 2 in Fig. 4.3. 4(b) and (c) are consistent with Eqs. (5) and (6) with $L=2$ and $L=4$, respectively. Curves 3 and 4 in Fig. 4.3. 4(b) and (c) plot the simulation results with random θ_{ep} for every edge. These figures show that curves 3 and 4 are confined by curves 1 and 2, while there are some peaks in curves 3 and 4, because R is not linearly proportional to ω for certain θ_{ep} values. The nonlinearity arises because the operation of MLE , which is the logical operation of NAND, is not linear. However, in the above two extreme cases, the corresponding θ_{ep} does not cause peaks. The simulation was performed 160,000 kinds of θ_{ep} values and all 160,000 curves were verified to be confined within curves 1 and 2.

C. Analysis of Angular Velocity-selectivity with a Modified Structure

Equations (2) and (4) imply that MLE output of logic zero is generated only if the images are rotated with the angular velocities ranging between 0 and $2\theta_s/T$. To

further enhance the angular velocity-selectivity, the range of angular velocities that generate the logic zero at *MLE* outputs should be confined to be narrower than $2\theta_s/T$. Fig. 4.3. 5(a) shows a modified structure intended to enhance the angular velocity-selectivity. The modified structure includes a pixels rather than one pixel within θ_s while the correlation is still performed on the two pixels that are θ_s apart. The number of pixels in a circle is thus increased by a factor of a . In the original structure in Fig. 4.3. 2(a), the correlation result of P_i has to be at logic one in order to obtain an *MLE* output of logic zero. In the modified structure, the correlation results of all the a pixels from P_1 to P_a within θ_s must be at logic one to yield an *MLE* output of logic zero, where P_0 is defined as the pixel that is just behind the edge at the beginning of every clock cycle. Consequently, the edge has to move across a pixels from P_1 to P_a in a clock cycle to ensure all a pixels have a correlation result of logic zero. If ωT is less than $(a-1)\theta_s/a\pi\omega$, then the number of pixels crossed by the edge during a clock cycle is always less than a , so the output of *MLE* is always logic one. If ωT is greater than $(a-1)\theta_s/a$, then *MLE* begins to output logic zero.

Fig. 4.3. 5 (b) presents an example in which the angular velocity-selectivity is analyzed. Since ωT is greater than $(a-1)\theta_s/a$, then the edge can cross $a-1$ pixels from P_1 to P_{a-1} in each clock cycle and exceed P_{a-1} by an angle of $\omega T-(a-1)\theta_s/a$ in every clock cycle. The exceeding angle is accumulated during successive clock cycles until the edge crosses P_a . An *MLE* output of logic zero is generated whenever the edge crosses a pixels from P_1 to P_a in a clock cycle. Since the angle between P_{a-1} and P_a is θ_s/a , the period for which an *MLE* output of logic zero appears is $n_0=(\theta_s/a)/(\omega T-(a-1)\theta_s/a)$ clock cycles. As in the derivations of Eqs. (1) and (2), R can be approximated by $100/n_0=100(\omega T-(a-1)\theta_s/a)/(\theta_s/a)$ if N is large. A similar analysis can be also performed for the case in which ωT is greater than θ_s and less than $(a+1)\theta_s/a$. In such a case, R can be derived as $100(1-a(\omega T-\theta_s)/\theta_s)$ if N is large. The relationship between R and angular velocity for the modified structure can be summarized as,

$$R(\%) = \begin{cases} \frac{100a(\omega T - \frac{a-1}{a}\theta_s)}{\theta_s} & \frac{(a-1)\theta_s}{aT} \leq \omega \leq \frac{\theta_s}{T} \\ 100 \left[1 - \frac{a(\omega T - \theta_s)}{\theta_s} \right] & \frac{\theta_s}{T} \leq \omega \leq \frac{(a+1)\theta_s}{aT} \end{cases} \quad (7)$$

Fig. 4.3. 5 (c) plots R versus ω from Eq. (7). Fig. 4.3. 5(c) indicates that the range of the angular velocities that generate logic zero at MLE output is confined to only $2\theta_s/aT$ so the angular velocity-selectivity is enhanced.

If the images have more than one edge, an analysis similar to that in Section 4.3.2-B can be performed. The relationship between R and ω is given by,


$$\begin{aligned}
0 \leq R(\%) &\leq \frac{100a(\omega T - \frac{a-1}{a}\theta_s)}{\theta_s} \\
\frac{100aL(\omega T - \frac{aL-1}{aL}\theta_s)}{\theta_s} &\leq R(\%) \leq \frac{100a(\omega T - \frac{a-1}{a}\theta_s)}{\theta_s} \\
100 \left[1 - \frac{aL(\omega T - \theta_s)}{\theta_s} \right] &\leq R(\%) \leq 100 \left(1 - \frac{a(\omega T - \theta_s)}{\theta_s} \right) \\
0 \leq R(\%) &\leq 100 \left(1 - \frac{a(\omega T - \theta_s)}{\theta_s} \right) \\
\frac{(a-1)\theta_s}{aT} \leq \omega &\leq \frac{(aL-1)\theta_s}{aLT} \\
\frac{(aL-1)\theta_s}{aLT} \leq \omega &\leq \frac{\theta_s}{T} \\
\frac{\theta_s}{T} \leq \omega &\leq \frac{(aL+1)\theta_s}{aLT} \\
\frac{(aL+1)\theta_s}{aLT} \leq \omega &\leq \frac{(a+1)\theta_s}{aT}
\end{aligned} \tag{8}$$


Fig. 4.3. 6(a) plots R against ω , according to Eq. (8). R is confined to the shaded region. Equation (8) implies that a alone determines the maximum value of R at every ω whereas both a and L determine the minimum value of R at every ω . Fig. 4.3. 6(b) shows the MATLAB simulation results with $a=2$ and $L=16$. The angles θ_{ep} for every edge are the same for curve 1 in Fig. 4.3. 6(b). As can be seen from Fig. 4.3. 6(b), the relationship between R and ω depicted by curve 1 is given by Eqs. (2) and (4). The θ_{ep} values are $m\theta_s/32T$, $m=1,2,\dots,16$, for curve 2, which describes the extreme case in which R is set to a minimum value at every ω . Curves 3 and 4 plot the simulation results with random θ_{ep} values for every edge. Fig. 4.3. 6(b) indicates that curves 3 and 4 are confined within curves 1 and 2.

D. Analysis of Misalignment Effect

The angular velocity-selectivity is degraded if the center of the rotating image is not precisely aligned to the center of the circle of the pixels. Fig. 4.3. 7 shows the

angular velocity under the condition that the center of rotation is shifted in the 0° direction with r_n values of 0, 0.4 and 0.8, where r_n is the ratio of the shifted distance, r_s , to the radius of the circle of the pixels, r . The angular velocity of rotation is fixed at 62.8 deg/sec. As can be seen in Fig. 4.3. 7, the deviation in angular velocity from 62.8 deg/sec increases with r_n . This misalignment degrades the angular velocity-selectivity. When the image is rotated with an angular velocity of θ_s/T , the theoretical maximum R is 100%. However, due to the misalignment effect, the angular velocity deviates from θ_s/T so that the maximum R falls as r_n increases. On the other hand, if the angular velocity is greater than $(a+1)\theta_s/(aT)$, then the theoretical value of R should be zero, as shown in Fig. 4.3. 6(a). However, since the angular velocity is decreased at part of the circle of the pixels, the MLE output may be logic zero when the edges move across this part. The angular velocity-selectivity is thus degraded. If r_s is fixed, then the misalignment effect can be reduced by increasing r .

4.3.3 Architecture and Circuit

The pixels are placed in a circular arrangement to detect rotation. Fig. 4.3. 8 presents the architecture of the proposed rotation sensor, which is comprised of 104 pixels, which form five concentric circles. The radii of the circles are 127.4 μm , 254.55 μm , 387.55 μm , 523.5 μm and 671.9 μm in order from the center. The numbers of pixels in the five circles are 8, 16, 16, 32, and 32 and the angles between the adjacent pixels are fixed at 45° , 22.5° , 22.5° , 11.25° and 11.25° , respectively. Every pixel is correlated with the clockwise and counterclockwise pixels that are 45° apart; that is, $\theta_s=45^\circ$. The clockwise or the counterclockwise correlation results of all the pixels in the same circle are sent to MLE . MLE is implemented using a NAND gate. Two sets of $MLEs$ are involved, corresponding to clockwise and counterclockwise rotation, for a single circle. CW1, CW2, CW3, CW4, and CW5 in Fig. 4.3. 8 are the clockwise outputs of the $MLEs$ of the first, second, third, fourth, and fifth circles while CCW1, CCW2, CCW3, CCW4, and CCW5 are the counterclockwise outputs of the $MLEs$ of the first, second, third, fourth, and fifth circles, respectively. The proposed rotation sensor includes a total of ten sets of $MLEs$.

Fig. 4.3. 9 shows the structure of a single pixel. Each pixel consists of a retinal processing circuit, two registers, two correlators and two P-channel MOSFETs, which are parts of the NAND gates that form MLE . The dimensions of the transistor M_{nxc} , M_{nxc} , M_{pxcc} , M_{pxc} , M_{mlecc} , and M_{mlec} are $W/L=1.5/0.6$ (μm). Fig. 4.3. 10 depicts the

retinal processing circuit, which includes an isolated photo-BJT Q_2 used as a photoreceptor, a smoothing photo-BJT Q_1 with adjustable N-channel MOSFET resistors used as the retinal smoothing network, a current-input CMOS Schmitt trigger and an inverter. The base of the smoothing photo-BJT Q_1 is connected to the bases of the smoothing photo-BJT in the four nearest neighbors, in both θ and r directions, via the N-channel MOSFET resistors M_{sc} and M_{si} , whose resistance is controlled by the gate voltage V_{smooth} . The transistors M_{ins} , M_{ips} , M_{ini} , M_{ipi} , M_n , M_p , M_{ip} , M_{in} , and M_c are used to virtually bias the emitters of Q_1 and Q_2 at V_{bias1} . The current-input CMOS Schmitt trigger comprises of M_s , M_{sr} , M_i , M_{ir} , M_{f1} , and M_{f2} transistors. The voltage V_f is used to adjust the threshold level of the current-input CMOS Schmitt trigger. The transistors M_{p1} , M_{p2} , M_{p3} , and M_{p4} are used to mirror the emitter current of Q_2 to the current-input CMOS Schmitt trigger. The inverter A amplifies the output of the current-input CMOS Schmitt trigger to VDD or VSS. The size of the transistors of the retinal processing circuit is summarized in Table 4.3. 1.

As shown in Fig. 4.3. 9, two registers are used to store the output of the retinal processing circuit at the current and the previous clock cycles. The register CF samples and stores the output of the retinal processing circuit at the rising edge of every clock cycle. The data stored in the register CF is shifted to the register PF after a clock cycle. The output of register CF is sent to the correlators of the pixel itself, whereas the output of register PF is sent to the correlators of the two correlated pixels, which are 45° apart in clockwise and the counterclockwise directions. The output of register CF is correlated with the outputs of register PF of the two pixels, which are 45° apart in the clockwise and counterclockwise directions. The two correlators correspond to detect clockwise and counterclockwise rotations, respectively. The correlators are implemented using XNOR gates. If the two inputs of the correlators are the same, then the correlation output is at logic one.

Fig. 4.3. 11 shows the structure of MLE , which is implemented by a NAND gate with a fan-in number equal to the number of pixels in a circle. The P-channel MOSFETs of the NAND gate are located inside each pixel, which are the MOSFETs M_{mlecc} and M_{mlec} in Fig. 4.3. 9. The outputs of the correlators in each pixel are sent to the gates of M_{mlecc} and M_{mlec} , as shown in Fig. 4.3. 9. The drains of M_{mlecc} (M_{mlec}) of every pixel in a single circle are connected together to the diode-connected N-channel MOSFET M_{nload} , which acts as the load to generate the counterclockwise (clockwise)

MLE output. The dimension of the transistor M_{load} is $W/L=1/15$ (μm). If one of the outputs of the correlators is at logic zero, then the output of *MLE* is at logic one. If the outputs of the correlators of every pixel in a single circle are at logic one, the output of *MLE* is at logic zero.

4.3.4 Experimental Results

An experimental focal-plane rotation sensor chip was fabricated in a $0.6 \mu\text{m}$ single-poly-triple-metal CMOS process. The resultant chip area was $1812 \times 1825 \mu\text{m}^2$ and the area of a single pixel was $91 \times 84 \mu\text{m}^2$, with a fill factor of 20%. The dc power consumption was 10 mW at 5V in the dark. Fig. 4.3. 12 shows photographs of the whole chip and a single pixel.

A pattern shown in Fig. 4.3. 13(a) was used to verify the direction-selectivity. The contrast of the pattern was 99% and the light source was a 5-mW LASER, which was used in all of the following experiments, except where specified. The contrast is computed as $(I_{\text{white}} - I_{\text{black}}) / (I_{\text{white}} + I_{\text{black}})$, where I_{black} and I_{white} are the induced photocurrents at the black and white regions, respectively. A lens was used to focus the image on the area that covers the three inner circles for good alignment. The clock frequency was 10 Hz and the angular velocity was $2.5 \pi/\text{sec}$. Fig. 4.3. 13(b) and (c) show the output waveforms, measured by a logic analyzer. The image was rotated clockwise in Fig. 4.3. 13(b) and counterclockwise in Fig. 4.3. 13(c). The waveforms at the nodes CW2, CW3, CW4, CW5, CCW2, CCW3, CCW4 and CCW5 in Fig. 4.3. 8 were recorded. Since the image was focused on the area of the three inner circles, the *MLE* outputs of the fourth and fifth circles were kept at logic one. As can be seen in Fig. 4.3. 13(b) (Fig. 4.3. 13(c)), when the image was rotated clockwise (counterclockwise), CCW2 and CCW3 (CW2 and CW3) was kept at logic one and logic zero appear at CW2 and CW3 (CCW2 and CCW3). Thus, the direction of rotation was correctly detected.

Although the angular velocity was tuned to maximize R to 100%, CW2 and CW3 in Fig. 4.3. 13(b) as well as CCW2 and CCW3 in Fig. 4.3. 13(c) were not always at logic zero in each clock cycle. R measured with $N=80$ was 50% and 66% for CW2 and CW3 in Fig. 4.3. 13(b) and 52% and 70% for CCW2 and CCW3 in Fig. 4.3. 13(c). The lowered R is caused by the misalignment effect described in Section 4.3.2-D. As discussed in Section 4.3.2-D, the maximum R decreases as r_n increases. Since the radius r of the third circle is larger than that of the second circle while r_s is the same

for both circles, the number of times for which *MLE* outputs logic zero at the second circle was less than that for which *MLE* outputs logic zero at the third circle, as can be seen in Fig. 4.3. 13(b) and (c).

Fig. 4.3. 14 (d) plots the measured values of *R* versus angular velocity at CCW3 for the four patterns of Fig. 4.3. 13(a), and Fig. 4.3. 14(a), (b) and (c). For the pattern in Fig. 4.3. 14(a), θ_{ep} are 11.25° and 22.5° . For the pattern in Fig. 4.3. 14(b), θ_{ep} for each edge are 0° , 5.125° , 11.25° , and 16.375° . The test image was rotated counterclockwise and the output at CCW3 was recorded to calculate *R*. The clock rate was 8 Hz so the theoretical ω at which *R* was 100% was $2\pi/\text{sec}$. As can be seen in Fig. 4.3. 14(d), all four curves had a maximum *R* at an angular velocity equal to $2\pi/\text{sec}$. However, due to the imperfection of alignment, *R* did not reach 100% at that angular velocity. The imperfect alignment also degraded the angular velocity-selectivity. According to the analysis in Section 4.3.2-C, the theoretical angular velocities at which *R* goes to 0 are 1 and $3\pi/\text{sec}$ for the pattern in Fig. 4.3. 13(a), 1.5 and $2.5\pi/\text{sec}$ for the pattern in Fig. 4.3. 14(a), and 1.75 and $2.25\pi/\text{sec}$ for the pattern in Fig. 4.3. 14(b). The pattern in Fig. 4.3. 14(c) has many edges but the number and positions of the edges are too complicated to be analyzed. However, the maximum *R* at every ω is determined for the pattern in Fig. 4.3. 14(c) since *a* equals two for the third circles. Thus, for this pattern, the theoretical values of angular velocity at which *R* is 0 should be greater than $1\pi/\text{sec}$ and less than $3\pi/\text{sec}$, according to the analysis in Section 4.3.2-C with *a*=2. The measured angular velocities at which *R* goes to 0 were 1 and $3.2\pi/\text{sec}$ for the pattern in Fig. 4.3. 13(a), 1.3 and $2.7\pi/\text{sec}$ for the pattern in Fig. 4.3. 14(a), 1.5 and $2.4\pi/\text{sec}$ for the pattern in Fig. 4.3. 14(b), and 1.2 and $2.7\pi/\text{sec}$ for the pattern in Fig. 4.3. 14(c). Although the angular velocities at which *R* goes to 0 were disturbed by the misalignment effect, the effect of θ_{ep} on the angular velocity-selectivity were consistent with the analysis in Section 4.3.2. The angular velocity-selectivity for the pattern in Fig. 4.3. 14(b) is the best while the angular velocity-selectivity for the pattern in Fig. 4.3. 13(a) is the worst.

Fig. 4.3. 15 presents the angular velocity-selectivity at different clock rates. The angular velocity with maximum *R* can be controlled by the clock rate. The pattern in Fig. 4.3. 13(a) was rotated counterclockwise and CCW3 was recorded to compute *R*. The CW3 was kept at logic one and was therefore not shown in Fig. 4.3. 15. The clock rate was set to 0.01, 0.1, 1, 10, and 160 Hz. The angular velocities with

maximum R were correctly the theoretical values, 0.0025, 0.025, 0.25, 2.5 and 40 π /sec, respectively. The imperfection of the alignment prevented R from being 100%. As shown in Fig. 4.3. 15, the angular velocity-selectivity was verified at the clock rate that changed through four orders of magnitude from 0.01 to 160 Hz. Furthermore, the delay time can be as large as 100 seconds, which is impossible to be realized in a conventional RC circuit in integrated circuits technology.

On the other hand, if the image is rotated with a constant angular velocity, this rotation sensor can be used to measure the angular velocity by sweeping the clock rate and checking the occurrence of the maximum R as shown in Fig. 4.3. 16. The pattern in Fig. 4.3. 13(a) was rotated counterclockwise and CCW3 was recorded. The CW3 was kept at logic one and was therefore not shown in Fig. 4.3. 16. The angular velocity of the rotating image was set to 0.02, 0.2, 2, 50, and 206 π /sec. The clock rates that maximize R were correctly the theoretical values, 0.08, 0.8, 8, 200 and 824 Hz, respectively. The misalignment caused R to be less than 100%. The detectable range of angular velocity was at least four orders of magnitude, as shown in Fig. 4.3. 16. The upper limit comes from the limited angular velocity of the motor in the measurement equipment. The lowest available clock rate of the clock signal generator imposes the lower limit on the detectable range.

Fig. 4.3. 17 plots the angular velocity-selectivity at the illumination of 0.91 and 366 lux at a wavelength of 550 nm. The pattern in Fig. 4.3. 13(a) with a contrast of 80% was used. The image was rotated counterclockwise and CCW3 was recorded. The light source was a white light source. The clock rate was set to 10 Hz. Fig. 4.3. 17 indicates that the angular velocity-selectivity is only slightly degraded by the low illumination. The power dissipation at the illumination of 366 lux is 95 mW.

4.3.5 Conclusion

A CMOS focal-plane rotation sensor, which uses a retinal processing circuit and a correlation-based algorithm, is implemented and analyzed. The proposed rotation sensor has a polar structure and is selective to the angular velocity and direction (clockwise and counterclockwise) of rotating images. The selected angular velocity is controlled by the period of a clock signal. The relationship between R and ω is derived to describe the angular velocity-selectivity. The maximum R is 100% when the image is rotated by $\omega = \theta_s/T$. R is decreased if the angular velocity deviates from θ_s/T .

More than one pixel is placed between two correlated pixels, 45° apart, to enhance the angular velocity-selectivity. The structure with more than one pixel between two correlated pixels is analyzed. The angular velocity at which R is decreased to zero is given by $\theta_s/T \pm \theta_s/aT$. Thus, the angular velocity-selectivity is enhanced by increasing a .

If the incident image has multiple edges, then the angular velocity-selectivity is related to both the number and positions of the edges and the value of R is confined in a range described by a set of inequalities. The upper bound of the range is reached if θ_{ep} are the same for every edge. The lower bound of the range is reached when θ_{ep} for every edge are equally distributed between 0 and θ_s/a .

An experimental rotation sensor chip was fabricated using the $0.6 \mu\text{m}$ single-poly-triple-metal CMOS process. The rotation sensor is comprised 104 pixels, which form five concentric circles. The numbers of pixels in the circles are 8, 16, 16, 32 and 32 in order from the center. The area of a single pixel is $91 \times 84 \mu\text{m}^2$, with a fill factor of 20%. The chip area is $1812 \times 1825 \mu\text{m}^2$. The dc power consumption was 10 mW at 5 V in the dark while that at the illumination of 366 lux is 95 mW. The experimental results concerning the fabricated chip verified that both the clockwise and the counterclockwise directions could be correctly detected. The angular velocity-selectivity was also verified at a clock rate from 0.01 to 160 Hz. The proposed rotation sensor can be used to detect the angular velocity ranging from 2×10^{-2} to $206 \pi/\text{sec}$ by sweeping the clock rate. The optical dynamic range at a contrast of 80% was 52 dB from 0.91 lux to 366 lux. It is found from the experimental results that the angular velocity selectivity is degraded by the misalignment effect. A practical method to solve this problem is to read out the sensed image and find the center of the rotating image. Then, precise motors can be used to adjust the position of the chip and align the center of the rotating image to the center of the circle of the pixels so that the error caused by misalignment effect can be reduced.

4.4 A CMOS FOCAL-PLANE RETINAL SENSOR DESIGNED FOR SHEAR MOTION DETECTION

4.4.1 Introduction

Mathematically, optical flows can be decomposed locally into div (or contraction/expansion), curl (or rotation), and def (or shear), up to a translation [132]. Rotation, expansion (or contraction) and shear (or deformation) are called

Elementary Flow Components (EFCs) as shown in Fig. 4.4. 1. These invariants can be used to describe the relative motion between an observer and his surroundings, and also the 3D structure of the surroundings. On the other hand, some electrophysiological recordings of the cortical neuron of the monkey have revealed that some neurons in Medial Superior Temporal (MST) area of the visual cortex are selective to rotation, expansion/contraction, combinations of these stimuli, and translation in a given direction. It has been observed that another group of neurons in the fundus of superior temporal sulcus visual area (FST) of visual cortex is sensitive to shear. While rotation and expansion determine the relative motion between the observer and his surroundings, shear depends only on 3D structure of the environment.

In conventional focal-plane motion sensors, the arrangement of the pixels is regular and forms a rectangular pattern. Also, the correlation is performed between the four immediate neighbors to obtain the local motion vectors. These sensors are designed for translation [18] but not suitable for EFCs detection because of their special motion model. In [19], the pixels are placed in a polar structure to overcome the difficulty of extracting the information of rotation in conventional sensors. In order to fit shear motion model, the pixels of this proposed shear sensor are placed in a shear-motion-like structure to ensure the detection of shear-motion. Every pixel is correlated with the shear and reversed-shear pixels that are neighbored apart in the same path. Based on the proposed computation method, shear motion can be detected and other motions can be dismissed. Displacement and velocity are determined by off-chip computation of summations of all correlation outputs.

In the proposed shear sensor, the function of image acquisition and preprocessing can be performed by using the pseudo-BJT-based retinal processing circuit with an adaptive current-input Schmitt trigger [107]. It has the advantages of pseudo-BJT as well as the robust noise immunity, high dynamic range and contrast-enhanced. The proposed shear motion sensor are designed and fabricated by 0.35 μm 2P4M CMOS process. The sensor contains 92 pixels and form four shear-motion detection pairs. Each pair is composed of four sets of pixels placed in symmetric manner to correspond to the shear motion. The area of a single pixel is 52.96 x 55.07 μm^2 with a fill factor of 16% whereas the chip area is 1100 x 1100 μm^2 .

This paper is organized as follows. In Section 4.4.2, the architecture and circuit of the proposed shear sensor is presented. Section 4.4.3 shows the experimental results.

Finally conclusions are drawn in Section 4.4.4.

4.4.2 Circuit Implementation

To detect shear motion, it is necessary to arrange the positions of pixel along the shear-motion paths. First of all, find several primary paths according to the optical flow of shear motion. In this design, four symmetry pairs of path are found and furthermore each pixel is placed along these selected primary paths. It is also important to keep the tangential distance between two pixels in the same path equal. If not, it is difficult to extract the information of displacement or velocity of shear motion. Fig. 4.4. 2 shows the architecture of the proposed shear sensor, which consists of 92 pixels and form four shear-motion detection pairs. The arrangement of pixels is depicted from this figure. Every pixel is correlated with itself and the shear and reversed-shear pixels that are neighbored apart. The shear, reversed-shear and self correlation results of all the pixels are serially read out. The three primary outputs, *ashear*, *arshear*, and *aself*, of the sensor are thus accumulated to obtain three correlation outputs which are used to determine the displacement per frame. Followed the motion computation method of [134], the displacement of shear motion can be obtained by

$$\frac{\Delta P}{P} = \frac{M - m + b_1}{2 * \left[\sum C(self) - m - b_2 \right]}$$

$$M \equiv \text{MAX} \left\{ \sum C(\text{shear}), \sum C(\text{rshear}) \right\}$$

$$m \equiv \text{min} \left\{ \sum C(\text{shear}), \sum C(\text{rshear}) \right\}$$
(1)

where $\sum C(\text{shear})$, $\sum C(\text{rshear})$ and $\sum C(\text{self})$ represent the sum of *ashear*, *arshear* and *aself* which are generated sequentially by the whole pixel array. During shifting of the previous image frame to compute $\sum C(\text{shear})$ and $\sum C(\text{rshear})$, the boundary pixels are fixed at zero for simplicity. The boundary condition, however, does not influence $\sum C(\text{self})$ because of no shifting needed in the calculation of $\sum C(\text{self})$.

To calibrate this boundary condition, two factors b_1 and b_2 are added to calculate displacement during measurement. The value of b_1 is chosen to be half the number of pixels at one side of the boundary while b_2 is half of b_1 . In this design, b_1 is 8 and b_2 is 4. If the motion under detection is shear, for example, $\sum C(\text{shear})$ is greater than $\sum C(\text{rshear})$, $\sum C(\text{shear})$, and $\sum C(\text{rshear})$ are equal when the motion is neither shear nor reversed shear. Therefore, the formula gives both the information of direction and displacement.

Fig. 4.4. 3 shows the structure of a single pixel. Each pixel consists of a retinal processing circuit, two registers, three correlators, three shift registers. The register CF samples and stores the output of the retinal processing circuit and shift the stored data to the register PF after a clock cycle. The output of register CF is then sent to the correlators of the same pixel to be correlated with the output of PF and the outputs of PF from its adjacent pixels, which are belong to the same set along shear and the reversed-shear direction. Two of the correlators are corresponding to the detection of shear and reversed-shear motions and the other is used to adjuvant the computation of displacement. These outputs of the correlators are sent out for further computation mentioned above.

The retinal processing circuit is detailed in Fig. 4.4. 4 [107], in which an isolated PNP pseudo-BJT is used as a photoreceptor, a smoothing NPN pseudo-BJT with adjustable N-channel MOS resistors is used as the retinal smoothing network, an adaptive current-input CMOS Schmitt trigger and an inverter are included. It mimics parts of functions of the cells in the outer plexiform layer of the real retina. The retinal processing circuit converts incident images to bi-level images and therefore has properties of high dynamic range and contrast-enhanced. With aid of adaptive current Schmitt trigger, the ability of noise immunity is adjustable adaptively according to the value of induced photocurrent. The purpose of additional output, *image_out*, is used to monitor the image captured.

4.4.3 Experimental Results

The area of the experimental shear motion sensor is $1100\ \mu\text{m} \times 1100\ \mu\text{m}$ as shown in Fig. 4.4. 5 (a) where the area of a single pixel is $52.96\ \mu\text{m} \times 55.07\ \mu\text{m}$ with a fill factor of 16%. Fig. 4.4. 5 (b) is a single pixel. The pixel arrangement of the core circuit is along shear motion paths as seen in Fig. 4.4. 5 (a). In Fig. 4.4. 5 (b), the left upper corner of the pixel is photodiode and metal four covers the other pixel circuits in order to prevent leakage current when light is incident. The DC power dissipation of the sensor, except the off-chip counter used to control the decoder in the core circuit, is 3mW at 3V in the dark.

The testing chip is attached on a holder and placed behind the lens. The test patterns are controlled by the software in a computer and projected on the chip by a projector. The outputs of chip are recorded by a logic analyzer for further analysis. Lens is used in the setup of measurement to focus the test patterns onto the chip. The velocity of test pattern is controlled by the software in the computer but it is not the

actual velocity on the chip. The ratio of the object velocity to the image velocity is obviously equal to the ratio of the object height to the image height. According to the theory of geometric optics [136], the lateral magnification of a thin lens is defined as the ratio of image height to object height and can be obtained by the image distance over the object distance. In the case of measurement, the object distance is about 83 cm and the image distance is 16 cm. The magnification is approximately 5.1.

Fig. 4.4. 6 and Fig. 4.4. 7 illustrates calculated velocities when shear and reversed-shear motion pattern is incident to the sensor, respectively. The testing velocities are 0.06 mm/sec, 0.09 mm/sec and 0.18 mm/sec. From the measurement results, it shows the deviations between calculated and actual velocities are within $\pm 10\%$. The deviations are obtained from

$$deviation(\%) = \frac{V_{cal} - V_{act}}{V_{act}} \times 100 \quad (2)$$

,where V_{cal} and V_{act} represents calculated and actual velocities, respectively. The shear and reversed-shear patterns are 0.25 cm^2 and each includes 11×11 pixels. Fig. 4.4. 8 (a) to (k) depicts successive 11 frames of shear motion test patterns. Reverse the order of the 11 frames shown in Fig. 4.4. 8, that is, (k) to (a) is reversed-shear patterns.

Fig. 4.4. 9 shows three patterns used to test the proposed shear motion sensor can dismiss translation. Fig. 4.4. 10 (a) is measurement results when the test pattern, an edge, which is shown in Fig. 4.4. 9 (a) translates at different velocities. The calculated velocities are obtained after the image sampled 11 frames. In this figure, it is the fact that each calculated velocity is much smaller than the actual velocity image translates. In other words, this means the sensor did not detect the shear motion. Fig. 4.4. 10 (b) displays the trend that the calculated velocity decrease as the image sampled frames increase. The calculated velocity does not have much difference from the actual velocity at initial frames since translation is similar with shear motion in the first instance. When the sampled images increase, the difference between shear motion and translation enlarges and thus the calculated velocity decreases. In the same way, Fig. 4.4. 11 and Fig. 4.4. 12 show how the proposed shear motion sensor dismisses translation of test patterns in Fig. 4.4. 9 (b) and (c). Each test pattern is 0.35 cm^2 and includes 11×11 pixels. Calculated velocity is obtained from correlation outputs accumulated over 11 frames. This is because patterns make positive contributions to shear motion when they translate from the left side of chip to the center, and make negative contributions when translating from center to the right side. The chip is 11

pixels wide from the left side to the right and thus every computation and simulation is done over 11 frames. Measurement results of Fig. 4.4. 9 (b) to Fig. 4.4. 11 (b) ensure this idea. A summary of the fabricated chip is given in Table 4.4. 1.

4.4.4 Conclusion

A first shear motion sensor has been proposed, designed and tested successfully. In the proposed shear sensor, it uses the pseudo-BJT-based retinal processing circuit with adaptive current Schmitt trigger to achieve image acquisition and thus has advantages of high dynamic range, edge enhancement, and robust noise immunity. The correlation-based algorithm with modification which is inspired by a biological model has the benefits of robustness and compactness and is adopted to calculate the velocity. With the specific pixel arrangement along with the modified correlation-based algorithm, the shear motion can be detected and other motions are dismissed. The experimental shear motion sensor was fabricated in a 0.35 μm double-poly-quadruple-metal CMOS process. The chip area is 1100 x 1100 μm^2 where the area of a single pixel is 52.96 x 55.07 μm^2 with a fill factor of 16%. Using this chip along with off-chip computation, shear motion is tested under 0.06 mm/sec, 0.09 mm/sec and 0.18 mm/sec and the velocity deviations are less than $\pm 10\%$. The shear motion sensor is also tested by three translating patterns and the shear motion selectivity is thus verified. The DC power dissipation is 3mW at 3V in the dark.

To make the shear motion sensor more completely, the off-chip computation has to be combined with the proposed circuits on the next chip. Moreover, the detection of translation, rotation, and expansion may be integrated with this shear motion sensor to moreover analyze the 3D motion in the future.

Table 4. 1 Summary of the results of CHAPTER 4

Section	4.1 [17]	4.2 [18]	4.3 [19]	4.4 [47]
Published year	1999	2002	2004	2004
Technology	0.6 μ m 1P3M	0.5 μ m 1P3M	0.6 μ m 1P3M	0.35 μ m 2P4M
Sampling geometry	linear	linear	circular	shear
Resolution	32 x 32	32 x 32	104 pixels 5 circles	92 pixels 5 paths
Pixel size	100 μ m \times 100 μ m	100 μ m \times 100 μ m	91 μ m \times 84 μ m	53 μ m \times 55 μ m
Chip size	3.6mm x 3.6mm	4.2mm x 4mm	1.812mm x 1.825mm	1.1 mm x 1.1mm
Power supply	5V	5V	5V	3.3V
DC Power dissipation in dark	20mW	120 mW	10mW	3 mW
The measured range of selectively detected speed	56 mm/sec ~ 5 m/sec	1 pixel/sec ~ 1.4 \times 10 ⁵ pixels/sec	2 \times 10 ⁻² π /sec ~ 206 π /sec	

Table 4.1. 1. The summary on the characteristics of the fabricated motion-selective detection chip

Technology	0.6 μ m N-well CMOS
Resolution	32 \times 32
Chip size	3.6mm \times 3.6mm
Cell size	100 μ m \times 100 μ m
Fill factor	20 %
Space between two adjacent silicon retina cells	50 μ m
Power supply	5 V
The measured power dissipation	20 mW
The measured capacitance of PMOS in the transient detector (W/L=6 μ m/6 μ m)	0.072 pF
The measured range of selectively detected speed (on-chip speed)	56 mm/sec ~ 5 m/sec (Pulse width: 195 μ sec ~ 1.2 μ sec)
The measured range of selectively detected direction (On-chip direction)	0 $^{\circ}$ ~ 360 $^{\circ}$

Table 4.3. 1. The size of the transistors of the retinal processing circuits

	W (μm)	L (μm)
M_c	1.5	1.2
$M_{ip}=M_{ips}=M_{ipi}$	1.5	1.2
$M_{in}=M_{ins}=M_{ini}$	3	1.2
$M_p=M_n$	1.5	0.6
$M_s=M_{sr}=M_i=M_{ir}$	4.5	2.4
$M_{f1}=M_{f2}$	1.5	0.6
$M_{p1}=M_{p2}=M_{p3}=M_{p4}$	9	3
$M_{sc}=M_{si}$	1.5	0.6
M_{invp}	1.5	0.6
M_{invn}	1.5	0.6

Table 4.4. 1 The summary on the characteristics of the fabricated chip of shear

motion sensor

Technology	0.35 μm CMOS 2P4M
Sampling geometry	Shear motion
Pixel number	92 pixels
Pixel size	52.96 μm x 55.07 μm
Fill factor	16%
Chip size	1100 μm \times 1100 μm
Clock rate	490Hz
Frame rate	3Hz
Testing velocities	0.06 mm/sec, 0.09 mm/sec and 0.18 mm/sec
Deviation of testing velocity	< \pm 10%
Power dissipation @ 3V	~ 3 mW in dark (except the off-chip counter used to control the decoder)

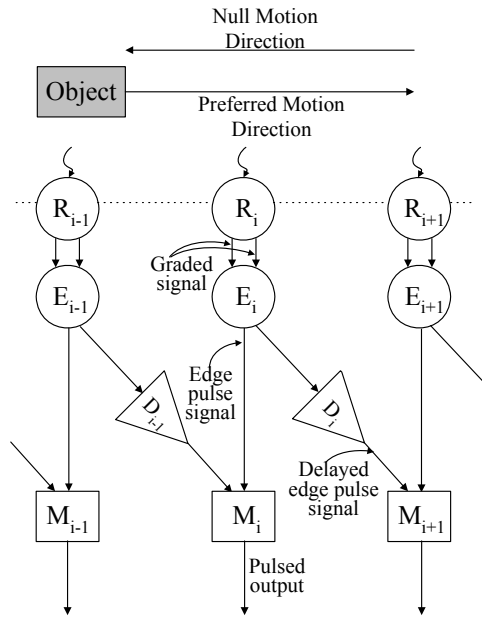
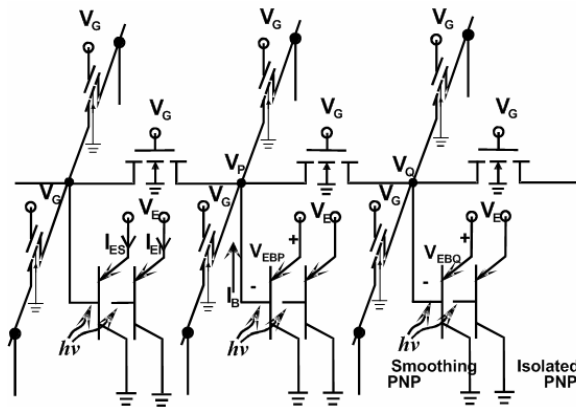
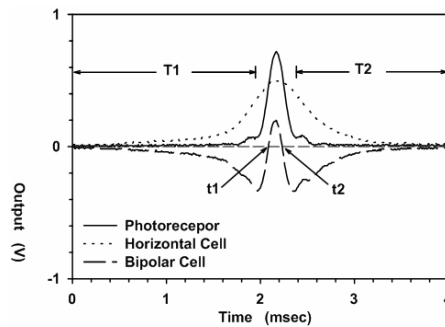


Fig. 4.1. 1. The adopted token-based delay-and-correlate motion computation algorithm.

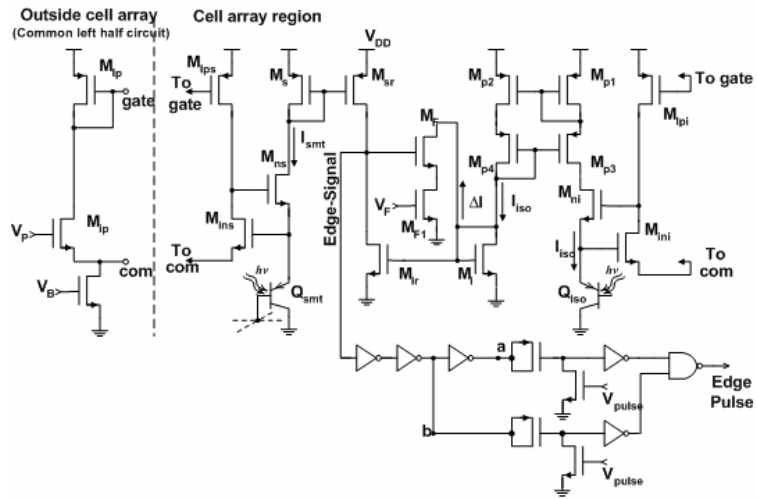


(a)

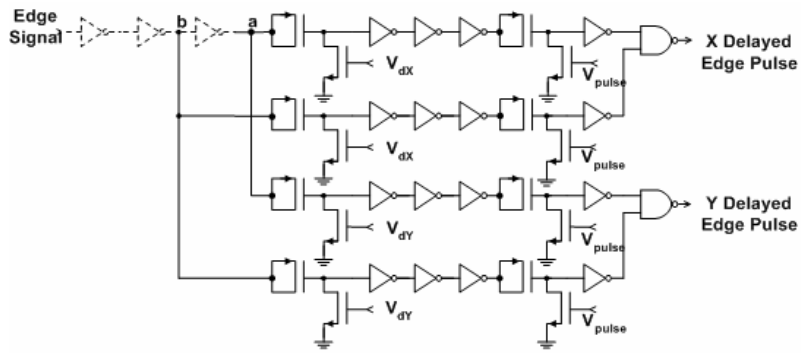


(b)

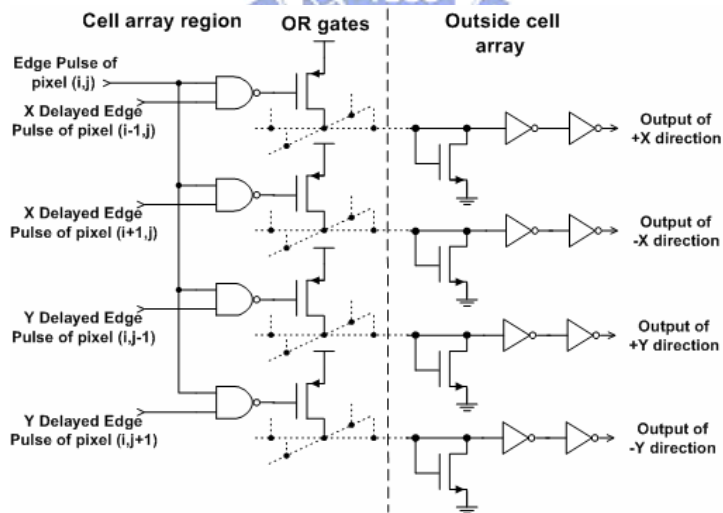
Fig. 4.1. 2. (a) The structure of BJT-based silicon retina with tunable image smoothing capability which is proposed in [7], [124]. (b) The measured responses of the emitter current difference of a single cell in the BJT-based silicon retina [7] with a moving light bar incident upon the chip.



(a)

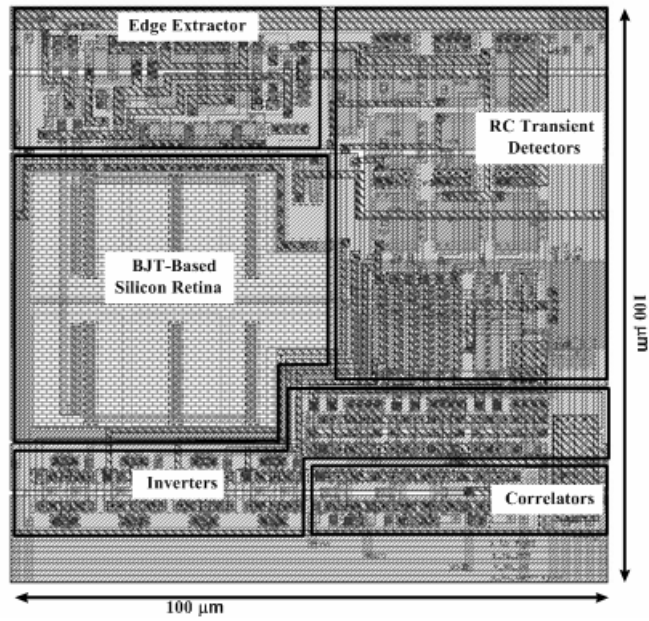


(b)

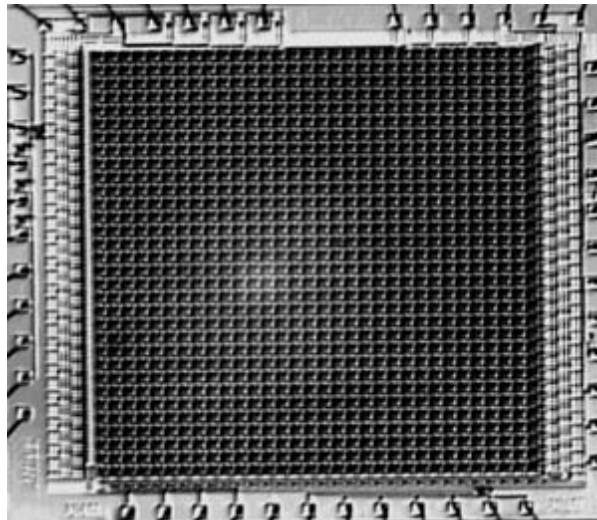


(c)

Fig. 4.1. 3. (a) The edge extractor which detects the temporal zero-crossings from the edge signals given by the BJT-based silicon retina and generate the edge pulse. (b) The circuit architecture which is used to realize the element D in Fig. 4.1. 1 for the generation of delayed edge pulse signals. (c) The circuit architecture of the correlators.



(a)



(b)

Fig. 4.1. 4. (a) The layout diagram of the basic detection cell, and (b) the photography of the 32×32 2-D velocity- and direction-selective sensing chip which is fabricated by using 0.6 μm N-well CMOS technology.

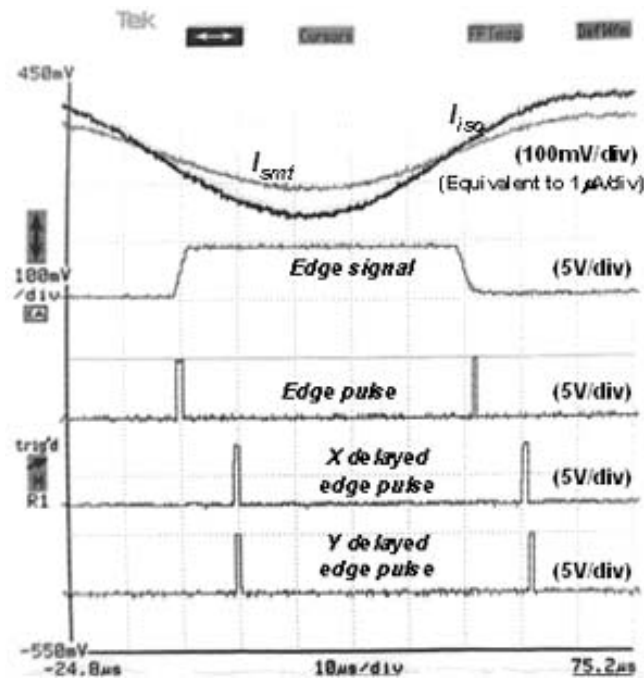


Fig. 4.1. 5. The oscilloscope traces of the various computational stages of one motion detection cell in the 2-D array. The emitter currents of the BJTs are read out by using off-array OP AMPs circuits with negative-feedback resistors to linearly convert them into voltages. The bias voltages are: $V_G=3V$, $V_B=1.2V$, $V_P=2V$, $V_F=0V$, $V_{pulse}=0.9V$, and $V_{dx}=V_{dy}=0.7V$.

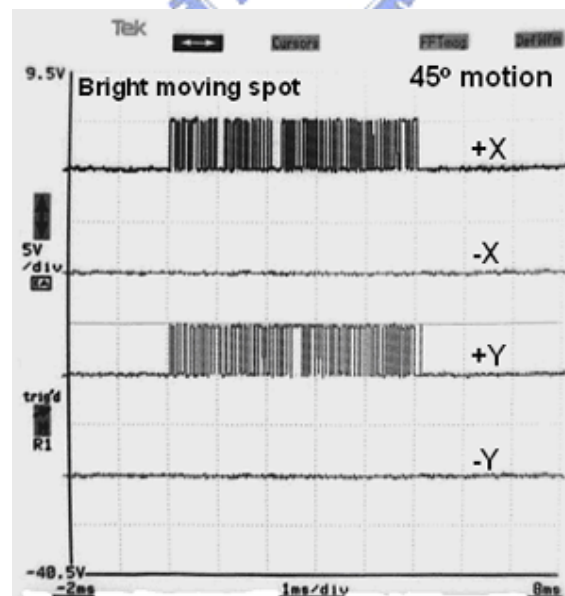


Fig. 4.1. 6. The measured output waveforms at the four output terminals of the fabricated sensor chip when a bright spot moves in the 45° direction with the preferred speed. The bias voltages are: $V_G=3V$, $V_B=1.2V$, $V_P=2V$, $V_F=0.3V$, pulse width= $10\mu s$, and delay time= $71\mu s$.

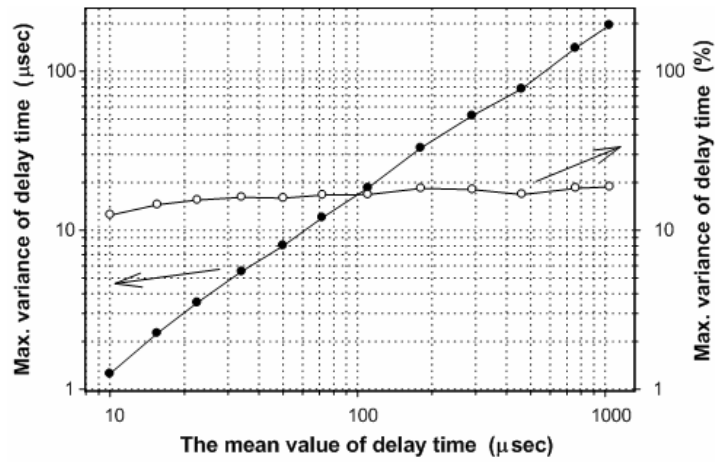


Fig. 4.1. 7. The measured maximum variance of the delay time of one pixel among 8 fabricated chips.

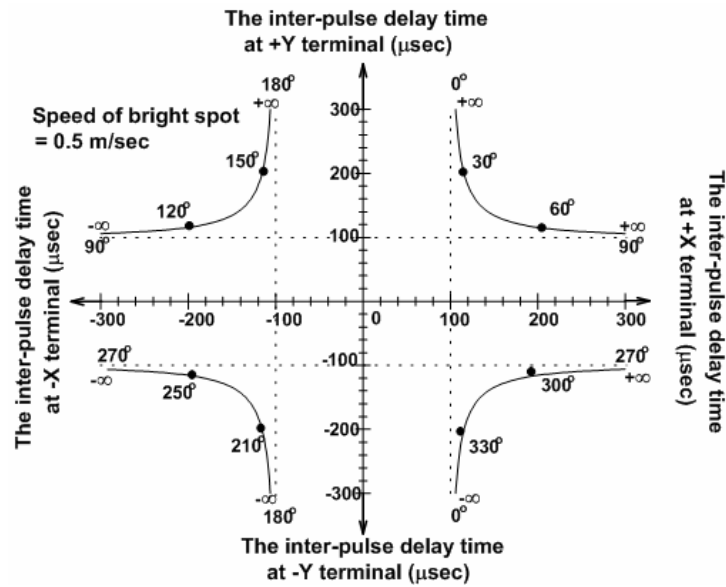


Fig. 4.1. 8. The measurement of the direction-selective function of the fabricated sensor chip where the inter-pulse delay time at the four terminals are measured and plotted for different directional angles. The bias voltages in the measurement are $V_G=3V$, $V_B=1.2V$, $V_P=2V$, $V_F=0.3V$, and pulse width= $25\mu s$.

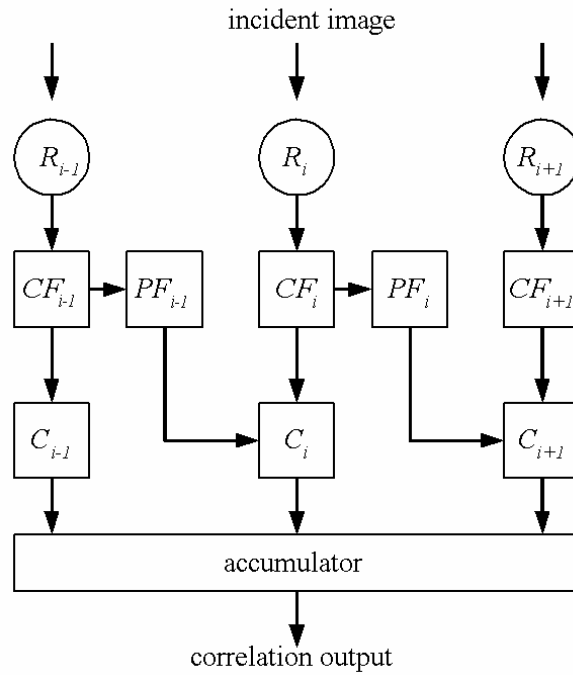


Fig. 4.2. 1. Conceptual structure of the motion computation method. R is the retinal processing circuit; CF and PF are registers used to store the current and previous sampled outputs of R , and C is the correlator. All the outputs of C are summed by the accumulator to obtain the correlation output.

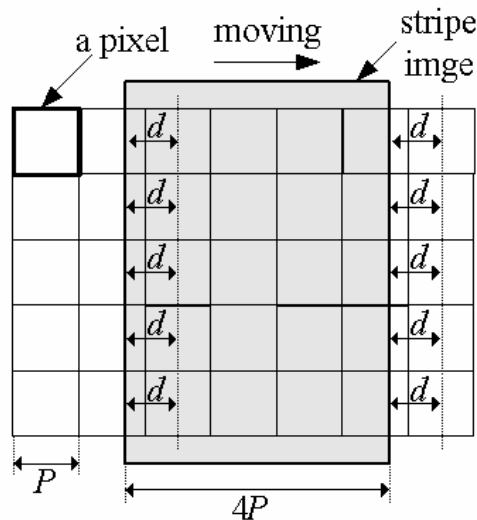


Fig. 4.2. 2. The pattern of a stripe with a width of $4P$, moving to the right. d is the distance from an edge to the center of the nearest pixel in the direction of motion. P is the distance between two adjacent photo sensors in two adjacent pixels, or the length of each pixel.

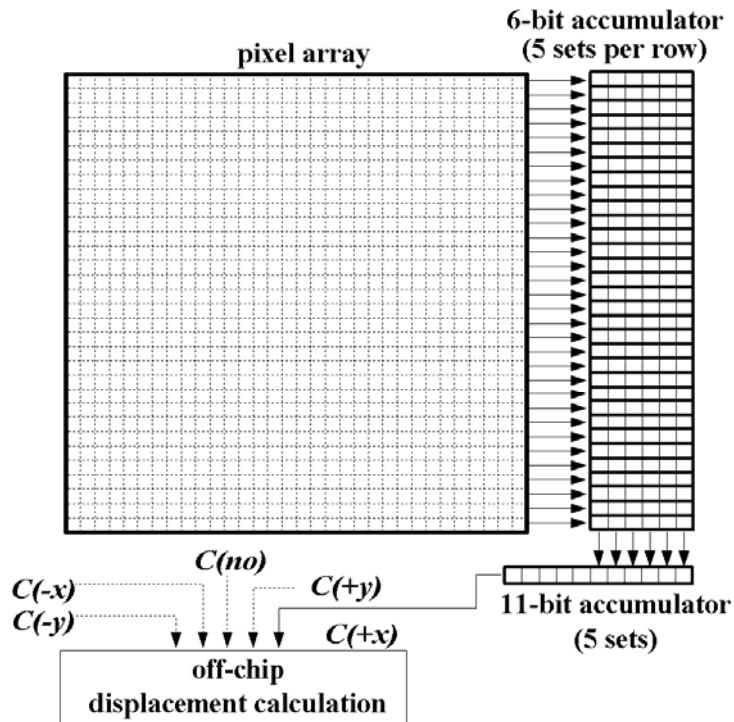


Fig. 4.2. 3. Architecture of the proposed focal-plane motion sensor.

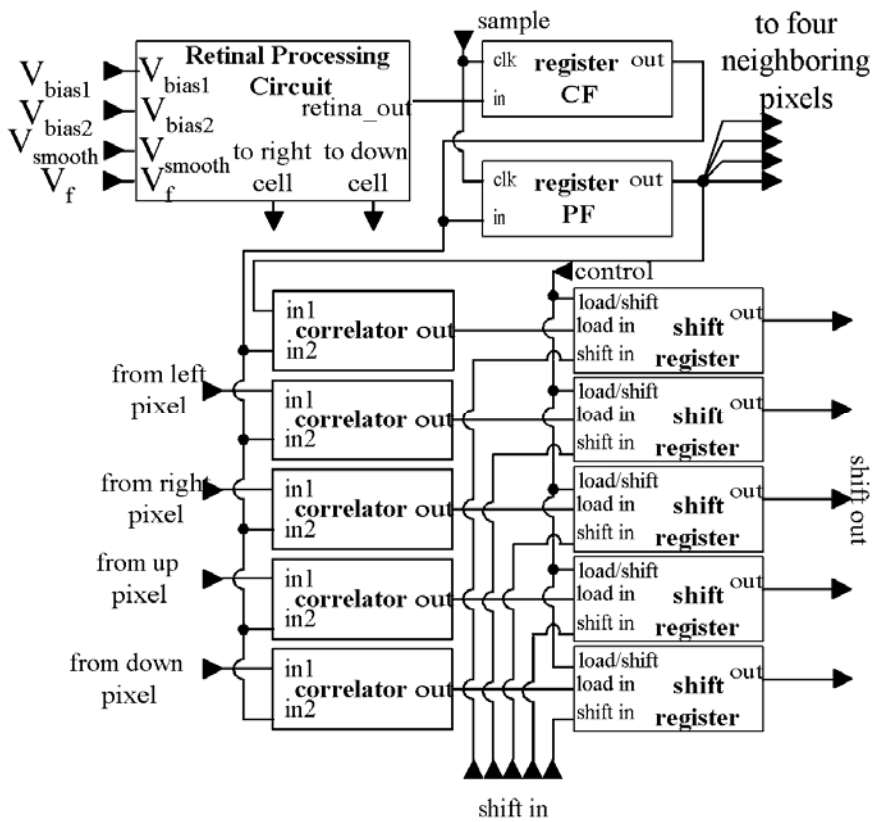


Fig. 4.2. 4. Structure of a single pixel.

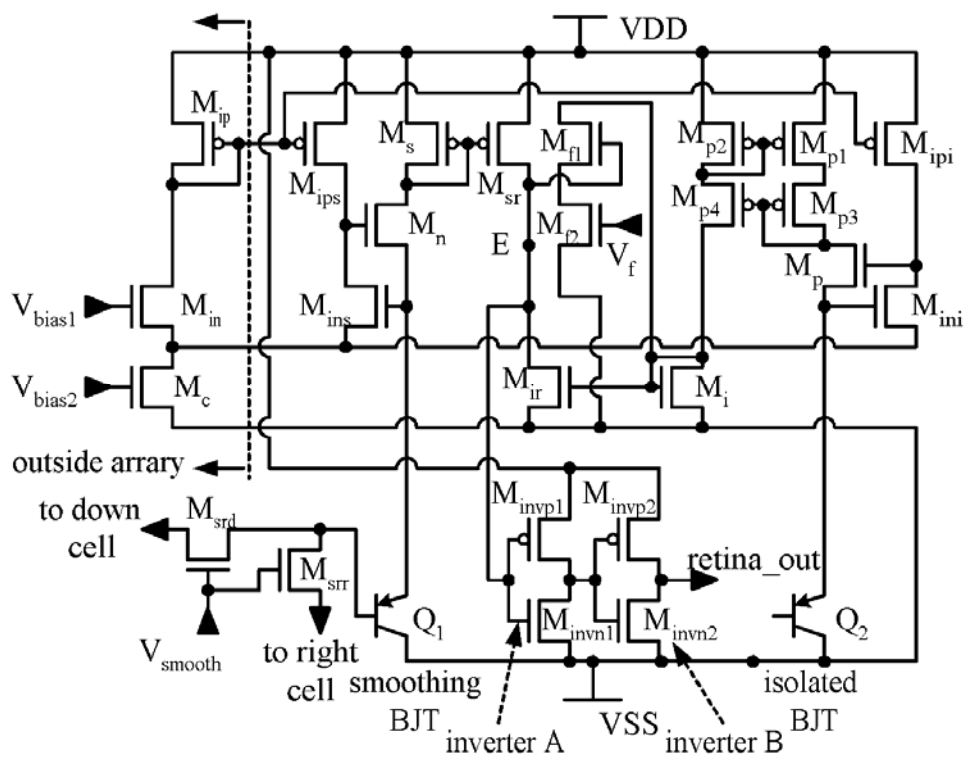
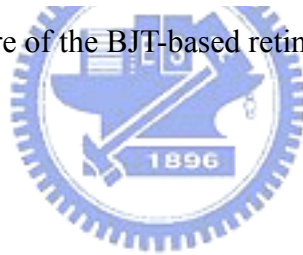
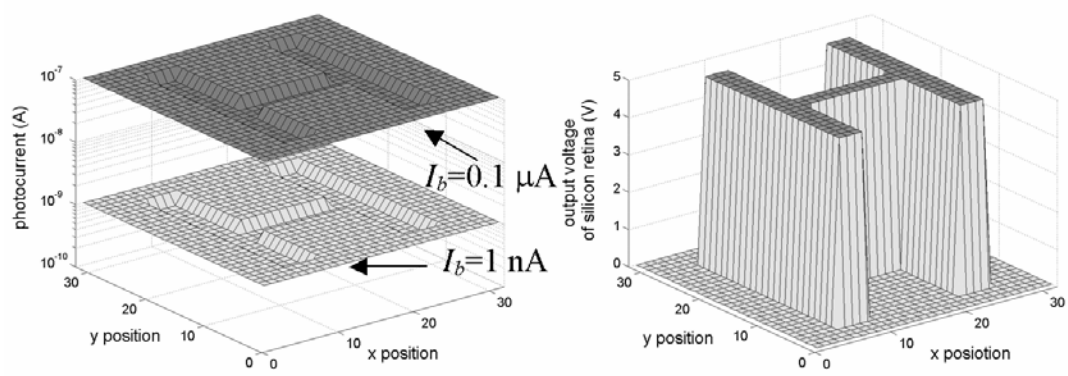
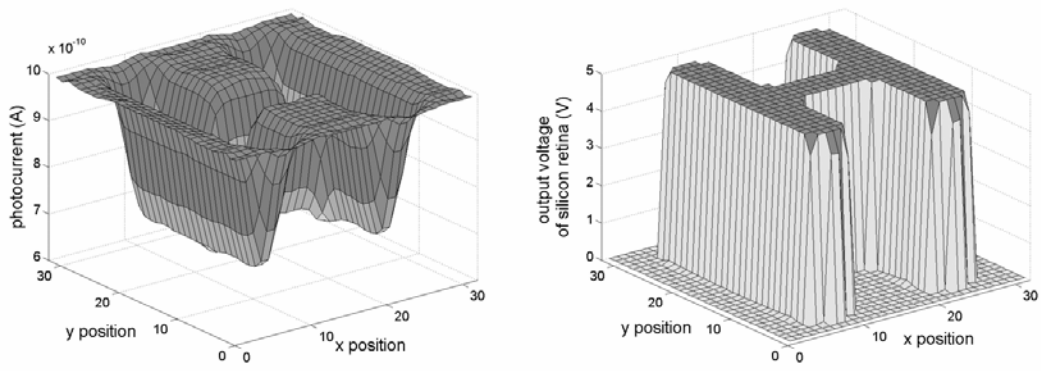


Fig. 4.2. 5. Structure of the BJT-based retinal processing circuit.

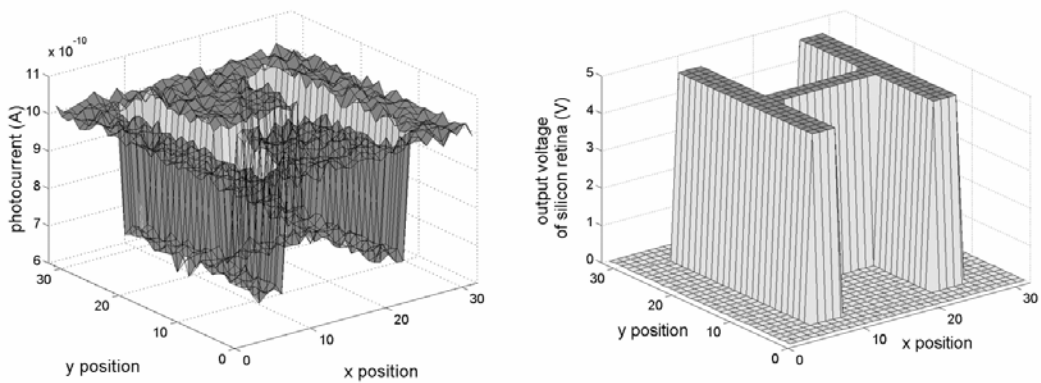




(a)



(b)



(c)

Fig. 4.2. 6. HSPICE simulation results, illustrating the output of the retinal processing circuit (a) with the background photocurrent's varying from 1 nA to 0.1 μ A; (b) with the image blurred, and (c) with normally distributed noise, with a standard deviation of 0.04 nA.

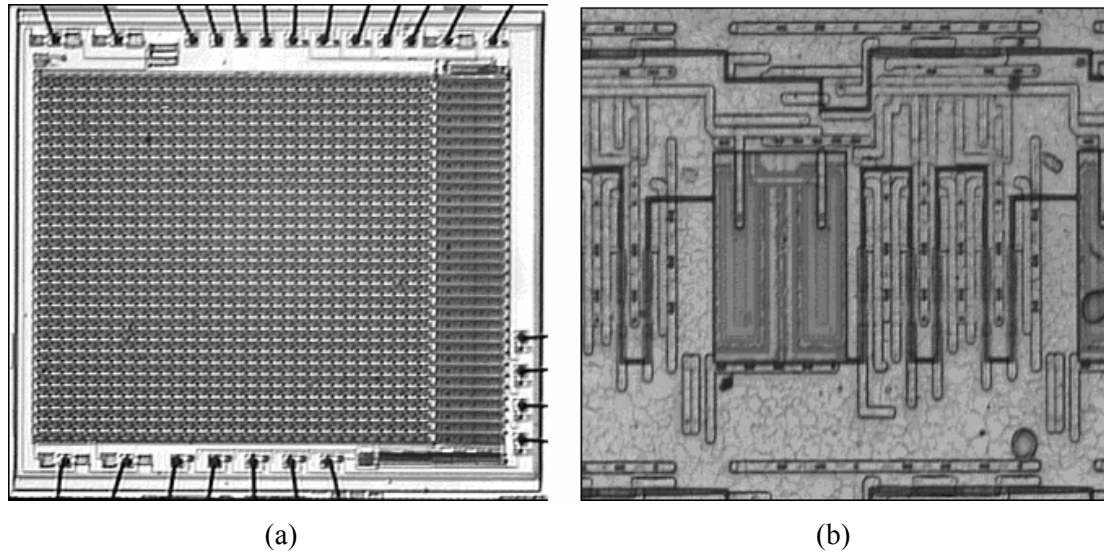


Fig. 4.2. 7. Photographs of the proposed motion sensor for (a) the whole fabricated chip and (b) a single pixel.

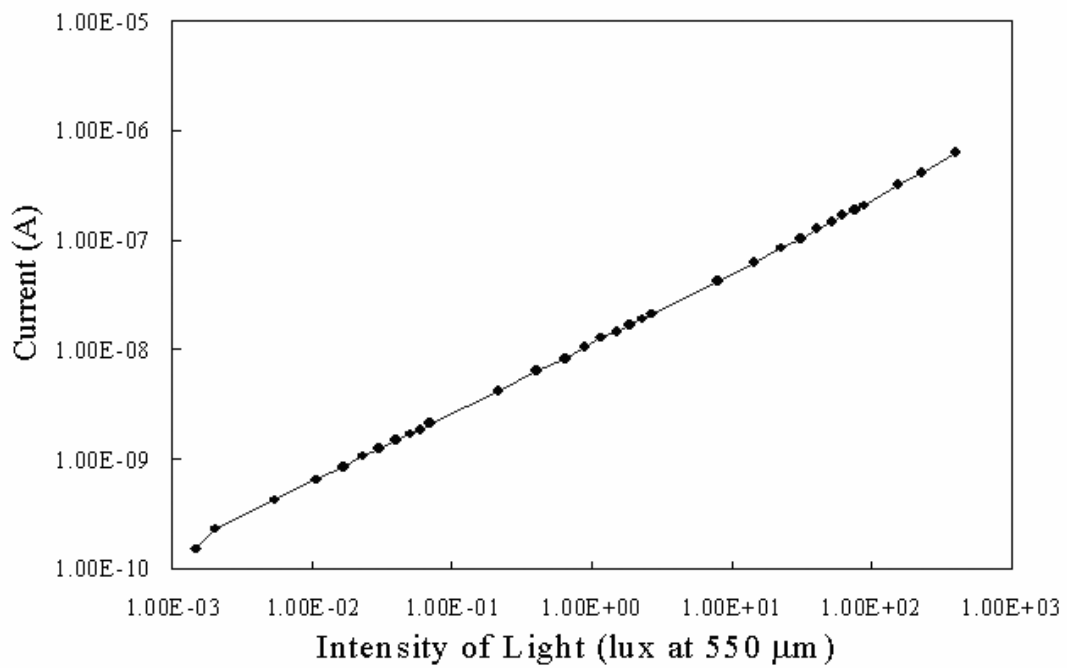


Fig. 4.2. 8. Photo response of the photo-BJT.

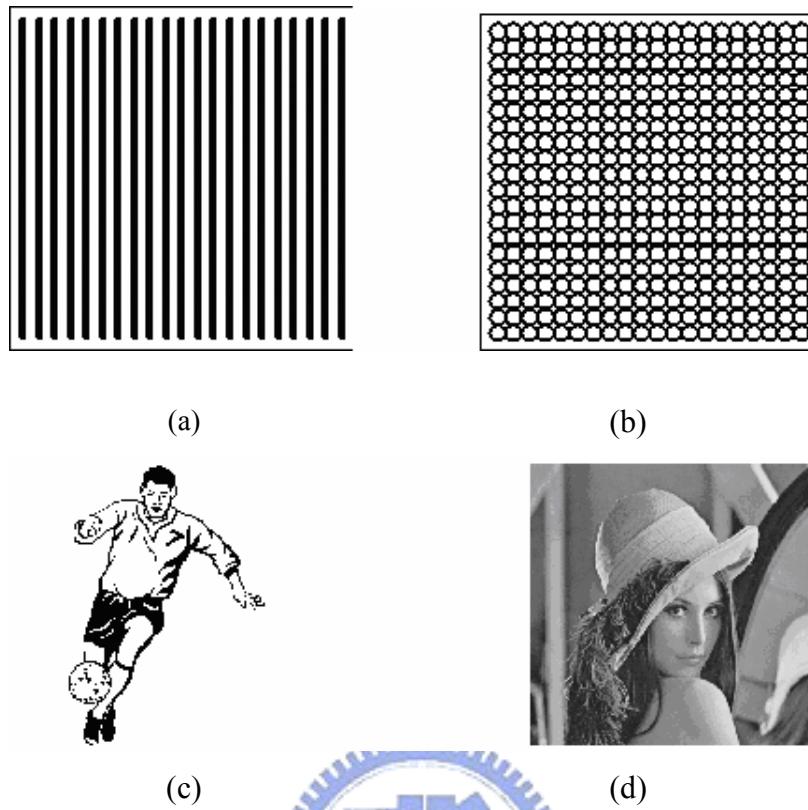


Fig. 4.2. 9. Four test patterns; (a) stripes (b) circles (c) soccer (d) Lena.

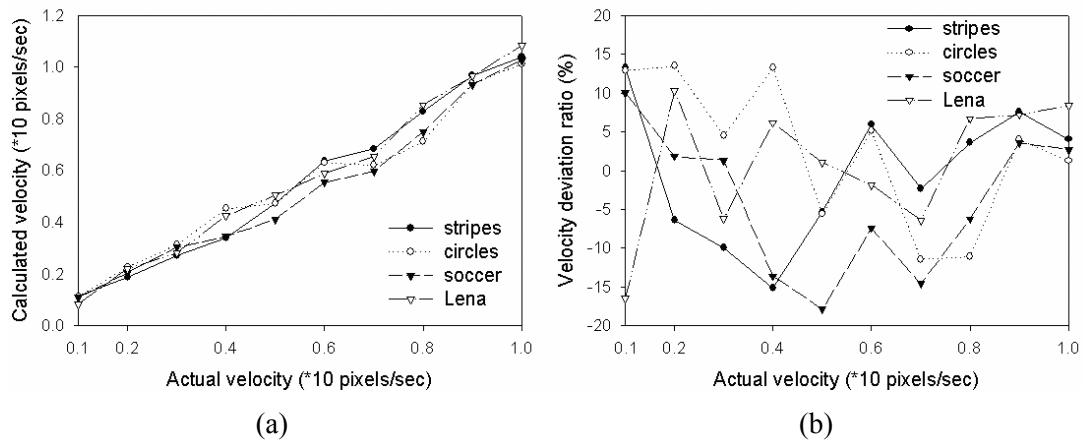


Fig. 4.2. 10. Calculated velocity for the four kinds of patterns; (a) calculated velocity; (b) velocity deviation ratio. The velocity of the moving image varies from 1 pixel/sec to 10 pixels/sec in the $-x$ direction; the sampling rate is 10 Hz.

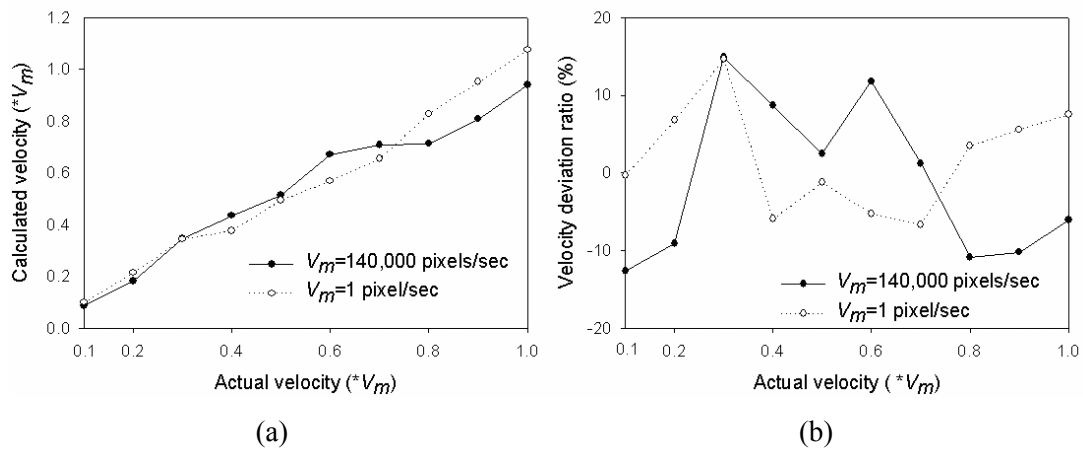


Fig. 4.2. 11. Calculated velocity at different sampling rates; (a) calculated velocity; (b) velocity deviation ratio. The sampling rate is 140K Hz for $V_m=140,000$ pixels/sec and 1 Hz for $V_m=1$ pixel/sec. Motion is in the $-y$ direction.

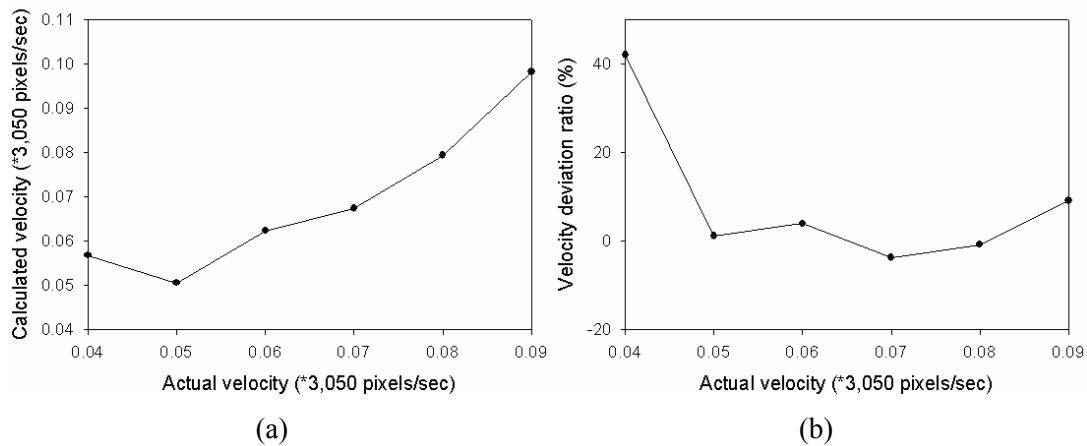


Fig. 4.2. 12. Minimum detectable velocity; (a) calculated velocity; (b) velocity deviation ratio. The velocity of the moving image varies from 274.5 to 122 pixels/sec in the $-x$ direction; the sampling rate is 3.05K Hz.

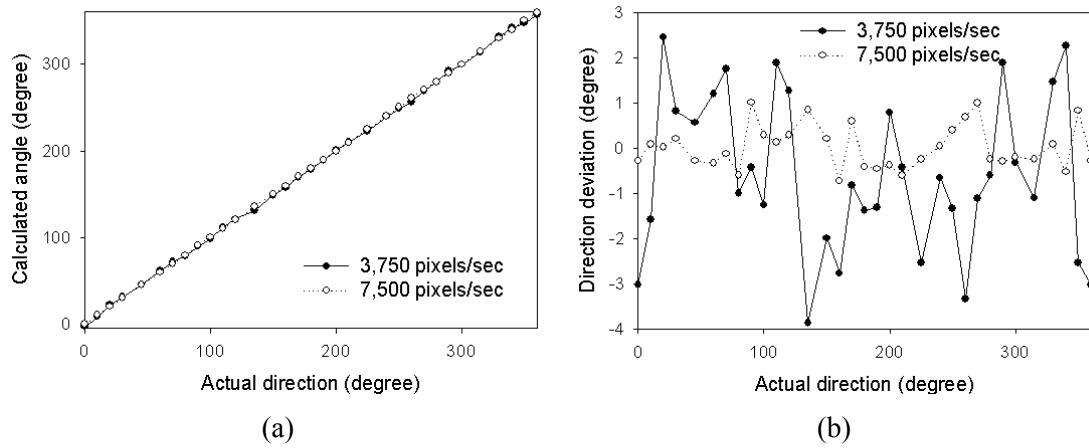


Fig. 4.2. 13. Calculated direction as the image moves at two different velocities; (a) calculated direction; (b) direction deviation. The velocities of the moving image are 3,750 and 7,500 pixels/sec, respectively. The sampling rate is 75K Hz for both curves.



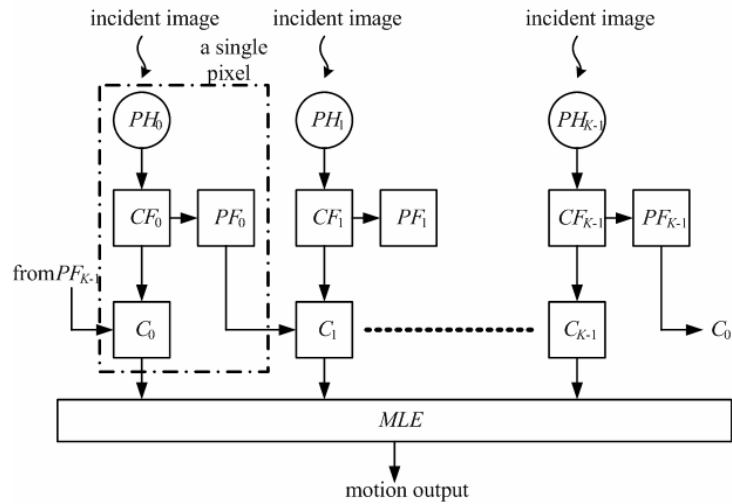


Fig. 4.3. 1. Conceptual structure of the adopted correlation-based algorithm for rotation detection. Each pixel is comprised of a retinal processing circuit PH , registers CF and PF , and correlator C . MLE aggregates the output of all correlators in a single circle to determine the global rotation.

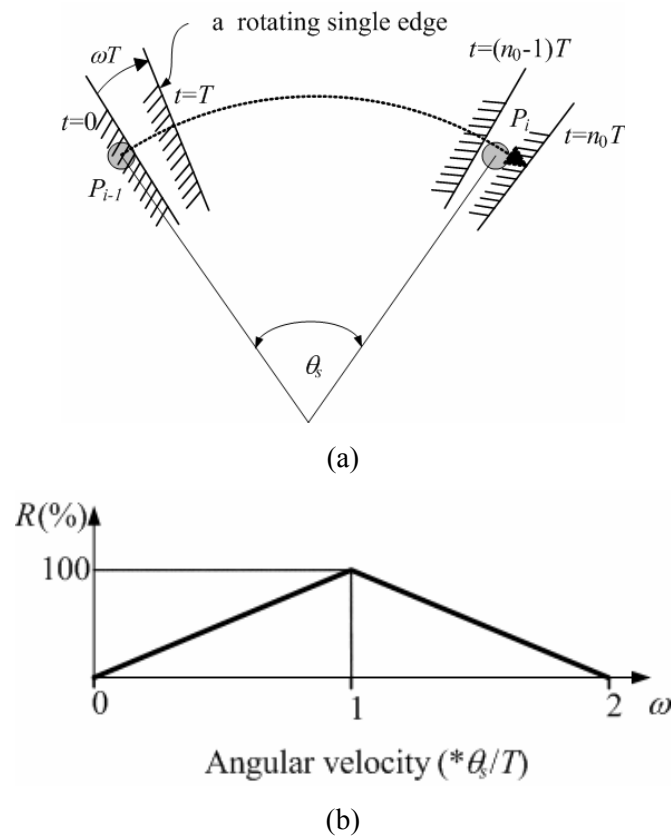


Fig. 4.3. 2. (a) An edge, rotating from the $(i-1)^{\text{th}}$ pixel P_{i-1} to the i^{th} P_i pixels within n_0 clock cycles. θ_s is the angle between two correlated pixels. ω is the angular velocity and T is the clock period. (b) The relationship between R and ω , where R is defined as the ratio of the number of times when the output of MLE is at logic 0 in N clock cycles, to N .

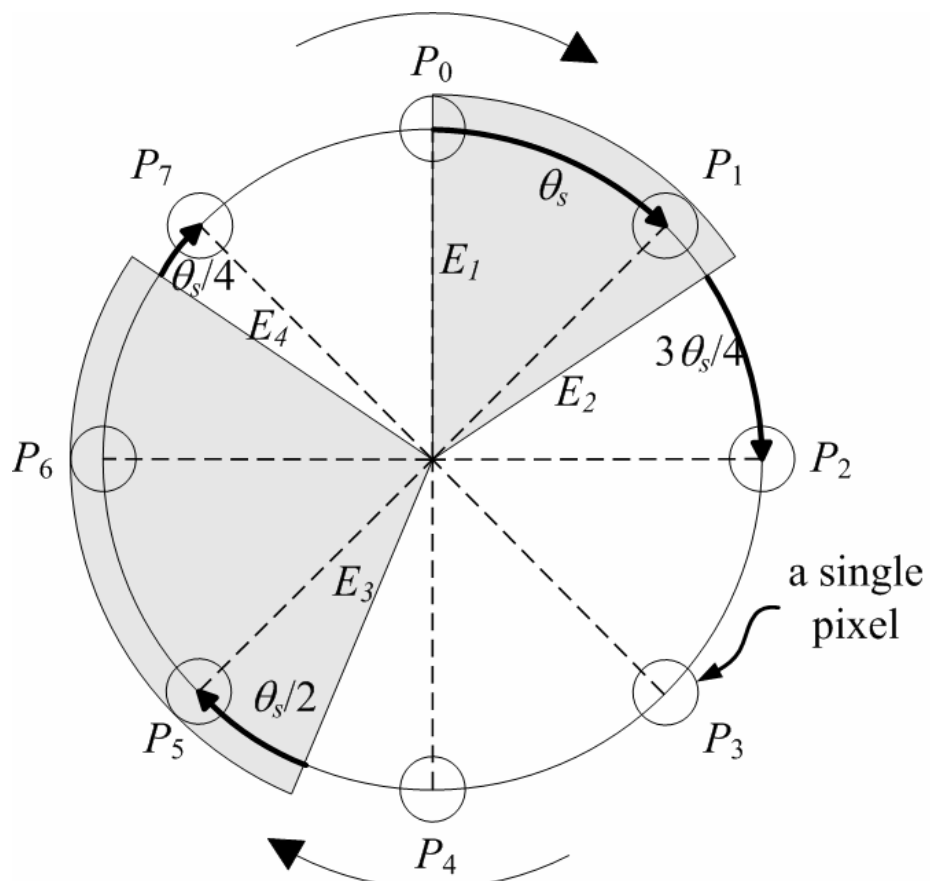


Fig. 4.3. 3. Example of an image with four edges located in various positions, rotating clockwise. There are eight pixels, P_0 to P_7 . The image has four edges E_1 , E_2 , E_3 , and E_4 and the initial angles between these edges and their own front pixels are θ_s , $3\theta_s/4$, $\theta_s/2$ and $\theta_s/4$, respectively.

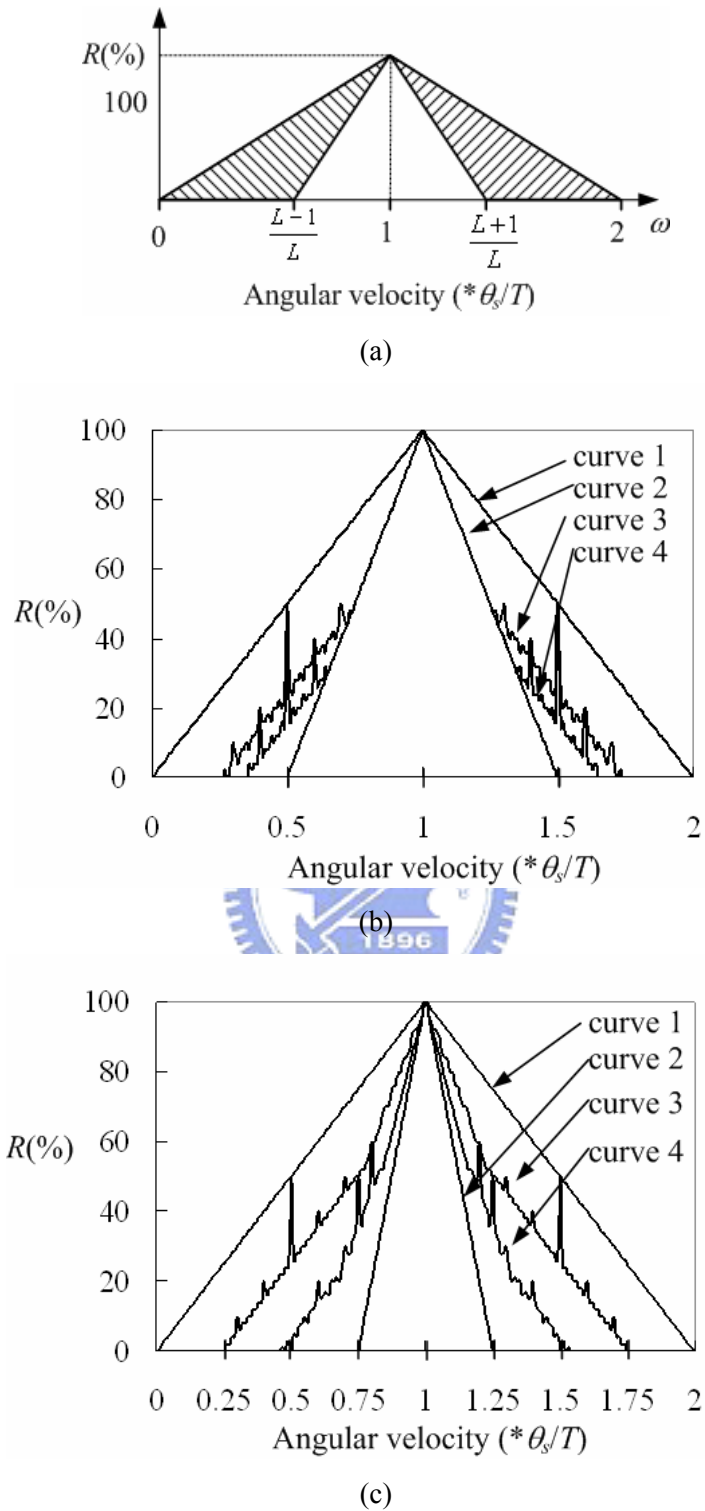


Fig. 4.3. 4. (a) Relationship between R and ω for an image with L edges located at various positions. (b) MATLAB simulation results with $L=2$. (c) MATLAB simulation results with $L=4$. Curves 1 and 2 refer to the extreme cases in which R is maximum and minimum at every ω , respectively. Curves 3 and 4 refer to the simulation results with random θ_{ep} for every edge.

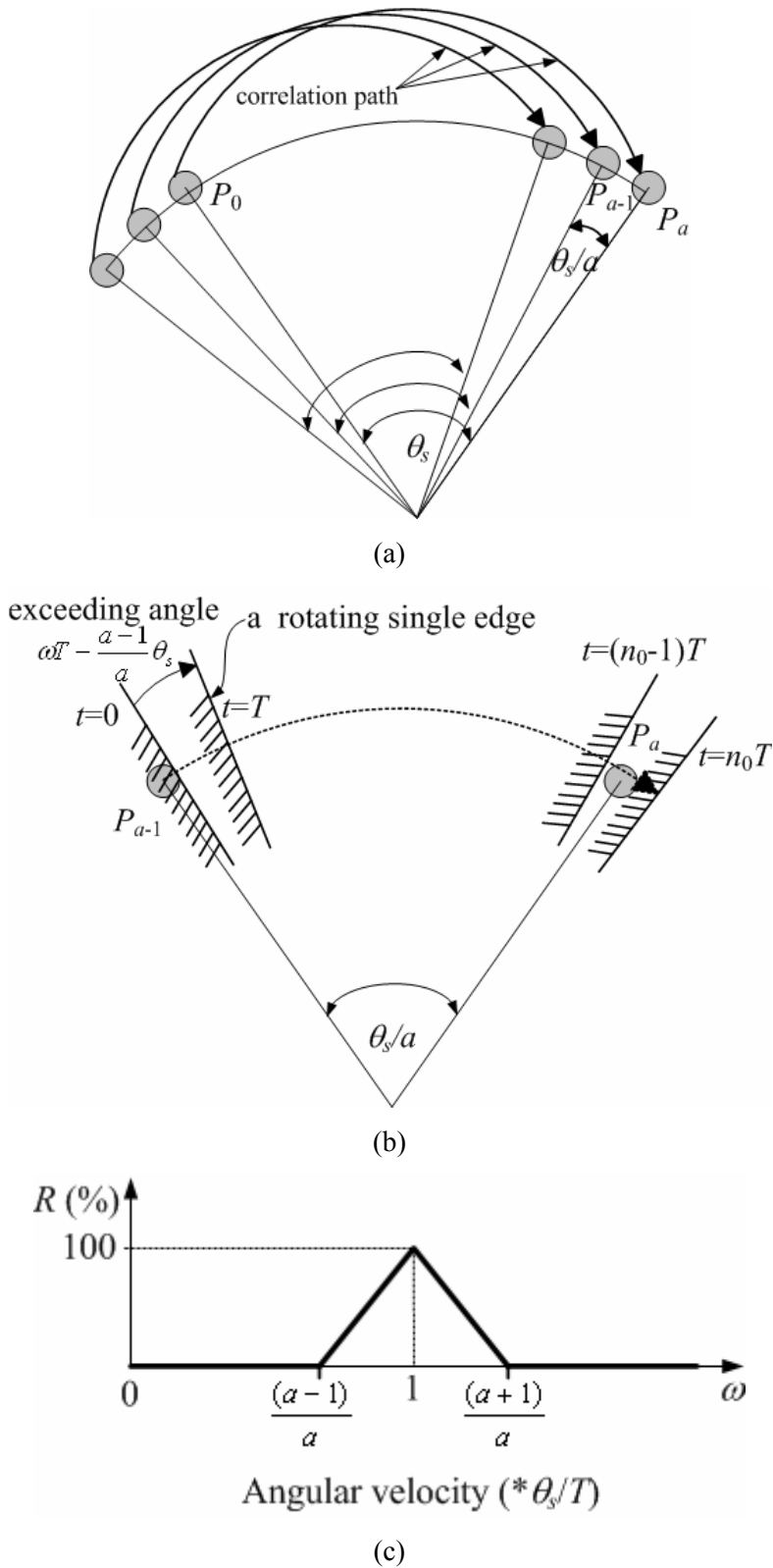
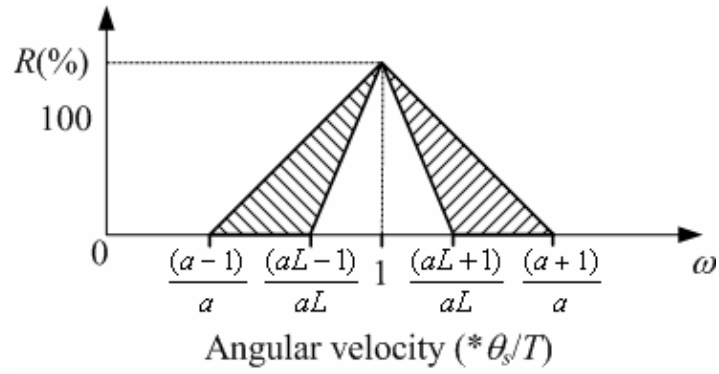
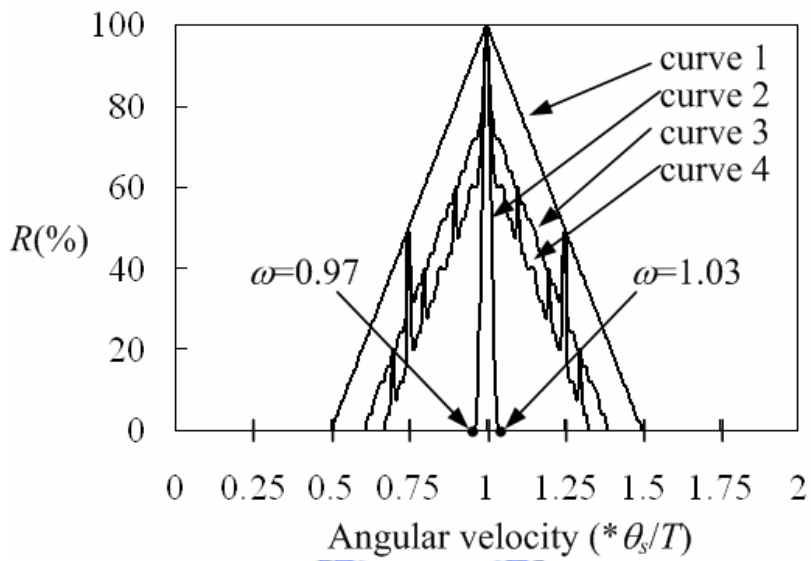


Fig. 4.3. 5. (a) Structure modified to enhance the angular velocity-selectivity. A total of a pixels are placed within θ_s while the two pixels separated by θ_s are correlated. (b) Example of an edge's approaching the a^{th} pixel P_a . The edge crosses P_a at the n_0^{th} clock cycle. (c) Relationship between ω and R for the modified structure.



(a)



(b)

Fig. 4.3. 6. (a) Relationship between R and ω for the modified structure when the image has L edges at arbitrary positions. (b) MATLAB simulation results with $a=2$ and $L=16$. Curves 1 and 2 are the extreme cases in which R is maximum and minimum at every ω , respectively. Curves 3 and 4 are the simulation results with random θ_{ep} for every edge.

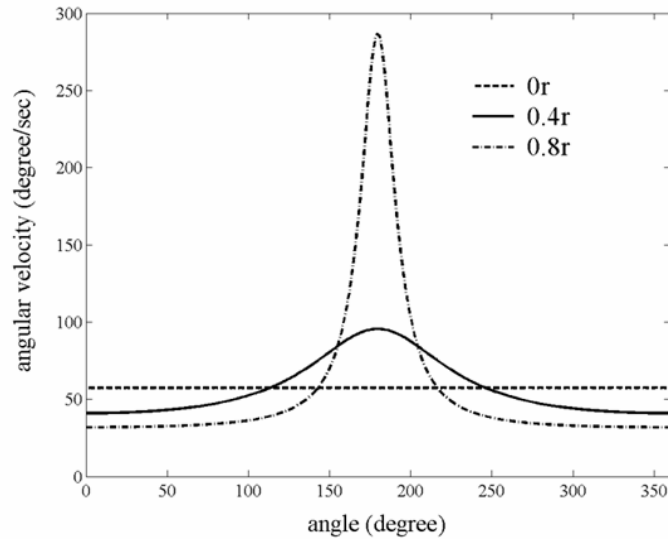


Fig. 4.3. 7. Angular velocity versus angle with the center of rotation shifted in the 0° direction by 0 , $0.4r$, and $0.8r$, where r is the radius of the circle of pixels.

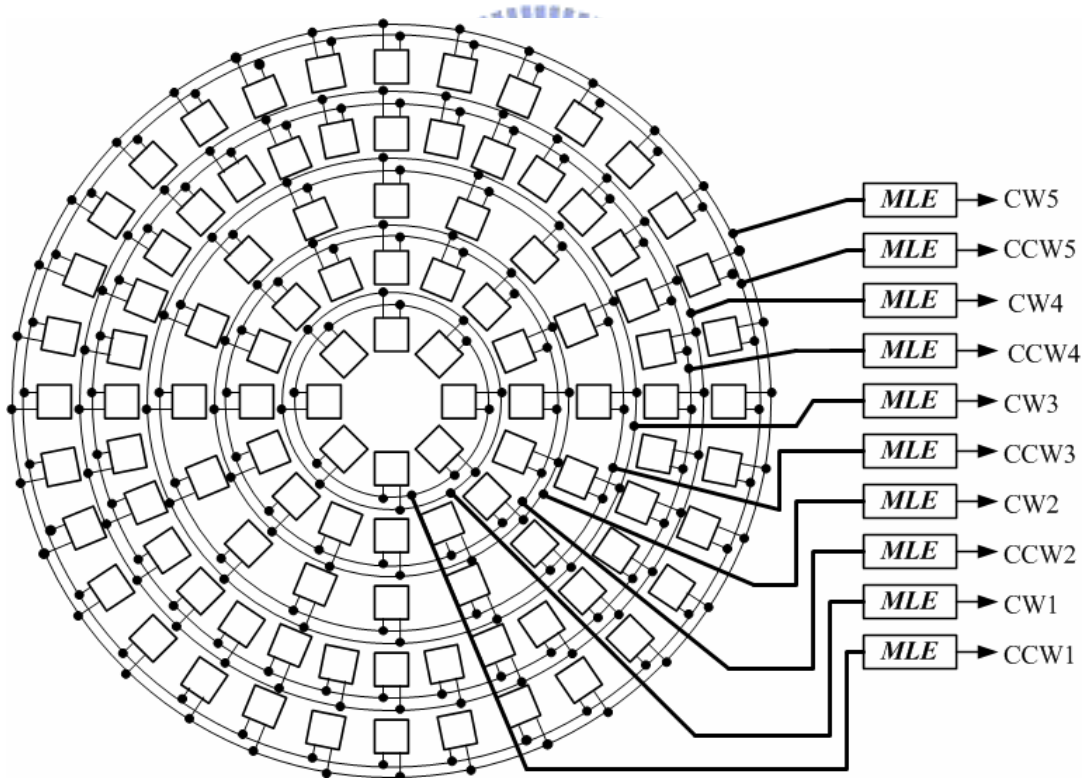


Fig. 4.3. 8. Architecture of the proposed rotation sensor, which includes 104 pixels in five concentric circles. The clockwise and the counterclockwise correlation results of all the pixels in a single circle are sent to *MLE*.

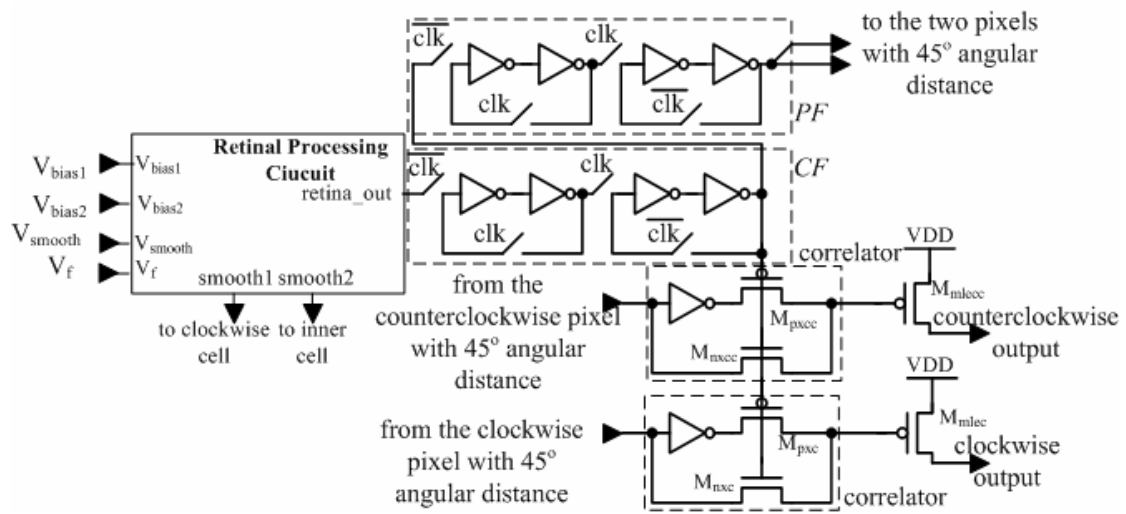


Fig. 4.3. 9. Pixel structure of the rotation sensor. Each pixel consists of a retinal processing circuit, two registers CF and PF , two correlators, and two P-channel MOSFETs M_{mlecc} and M_{mlec} , which are parts of MLE , implemented by NAND gates.

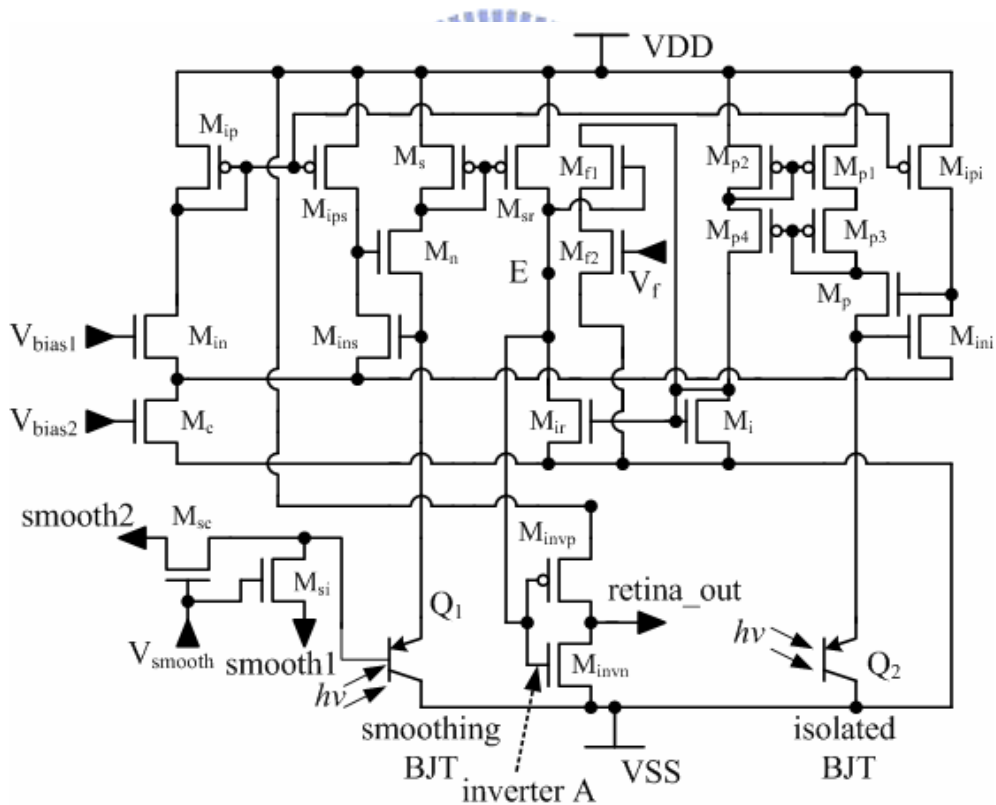


Fig. 4.3. 10. Structure of the retinal processing circuit. The retinal processing circuit includes an isolated photo-BJT Q_2 , a smoothing photo-BJT Q_1 , a current-input CMOS Schmitt trigger and an inverter.

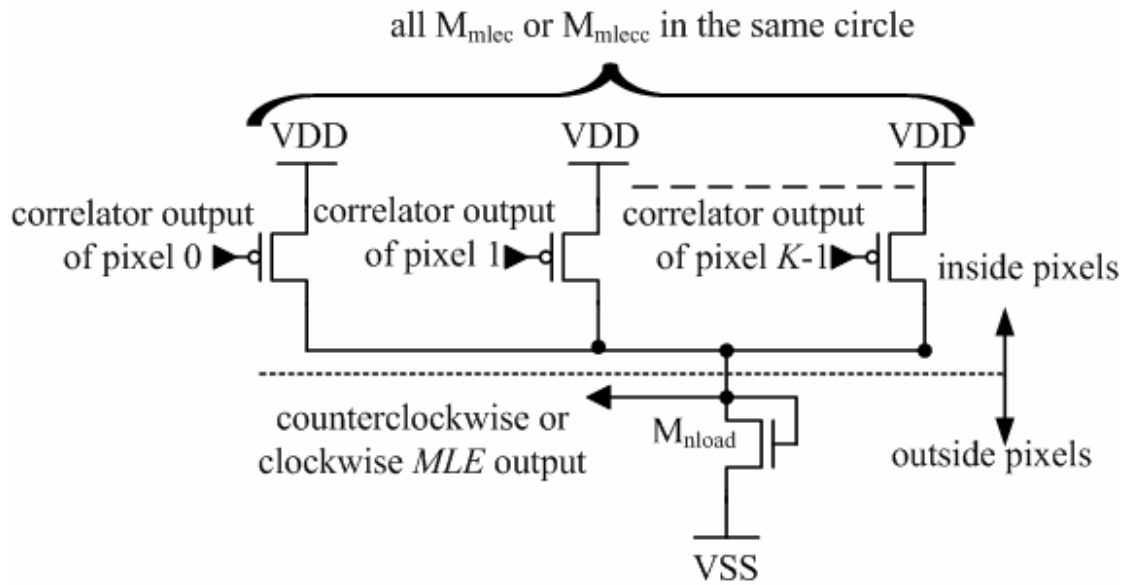


Fig. 4.3. 11. Structure of *MLE*, which is implemented by a NAND gate with a fan-in number equal to the number of pixels in a circle.

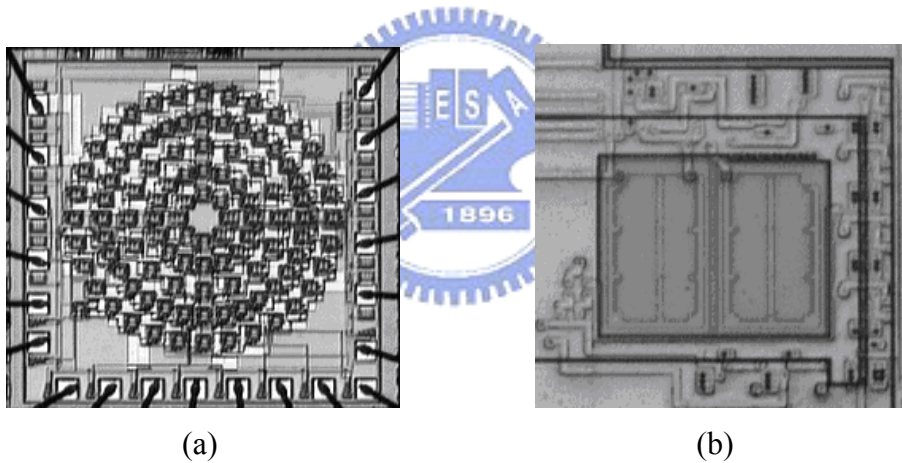
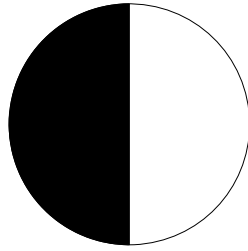
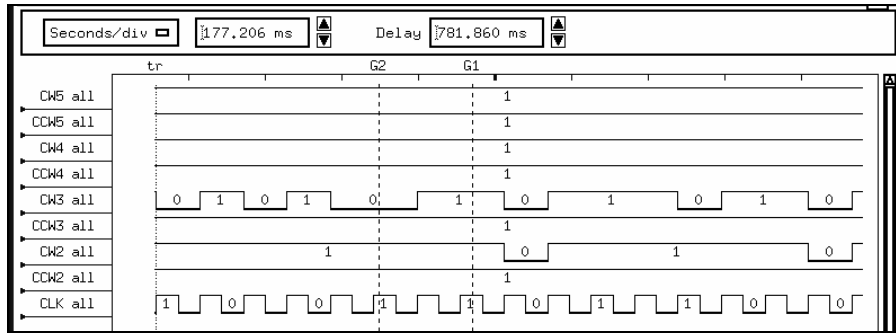


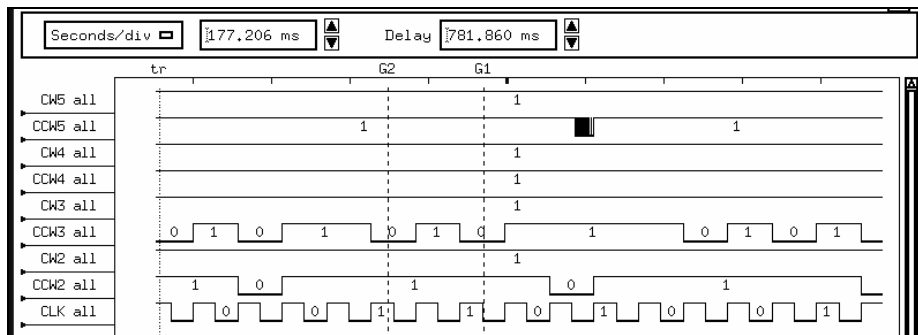
Fig. 4.3. 12. Photograph of (a) the whole chip and (b) a single pixel, of the rotation sensor.



(a)



(b)



(c)

Fig. 4.3. 13. (a) Pattern used to test rotation direction-selectivity. (b) Waveforms measured by the logic analyzer with the image rotated clockwise. (c) Waveforms measured by the logic analyzer with the image rotated counterclockwise. The waveforms, CW2 (CCW2), CW3 (CCW3), CW4 (CCW4) and CW5 (CCW5) are the clockwise (counterclockwise) outputs of *MLE* of second, third, fourth and fifth circles. The contrast of the pattern is 99% and the light source is a 5mW LASER. The clock rate is 10 Hz and the angular velocity is $2.5 \pi/\text{sec}$.

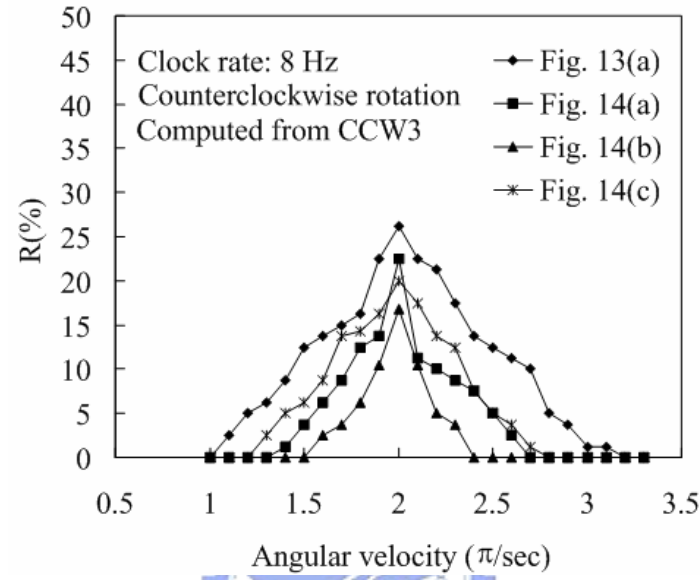
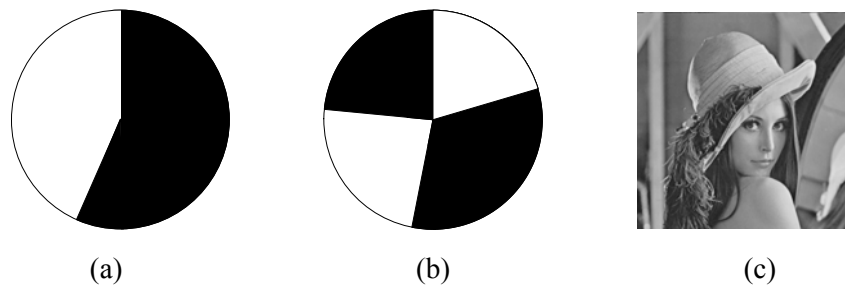


Fig. 4.3. 14. (a) Test pattern with θ_{ep} of 11.25° and 22.5° . (b) Test pattern with θ_{ep} of 0° , 5.125° , 11.25° and 16.375° (c) Test pattern, Lena. (d) Angular velocity-selectivity with the four patterns in Figs. 13(a), 14(a), 14(b) and 14(c).

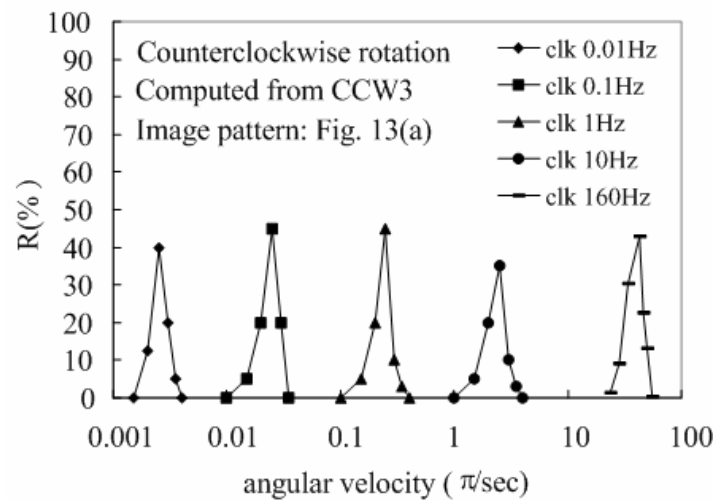


Fig. 4.3. 15. Relationship between R and ω at clock rates of 0.01, 0.1, 1, 10, and 160 Hz. Angular velocities when R is maximum are at 0.0025, 0.025, 0.25, 2.5 and 40 π/sec .

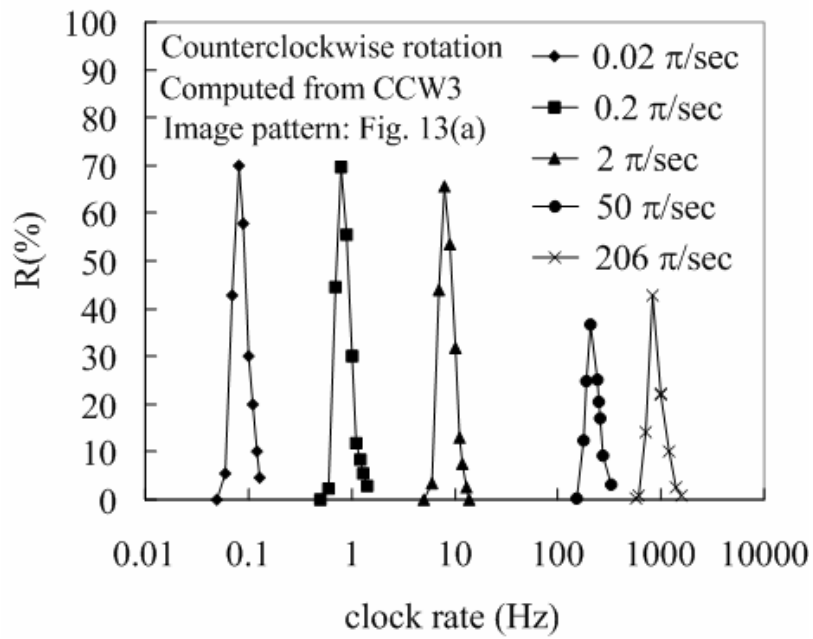


Fig. 4.3. 16. Relationship between R and clock rate at angular velocities of 0.02, 0.2, 50 and 206 π/sec . Clock rates when R is maximum at are 0.08, 0.8, 8, 200 and 824 Hz.

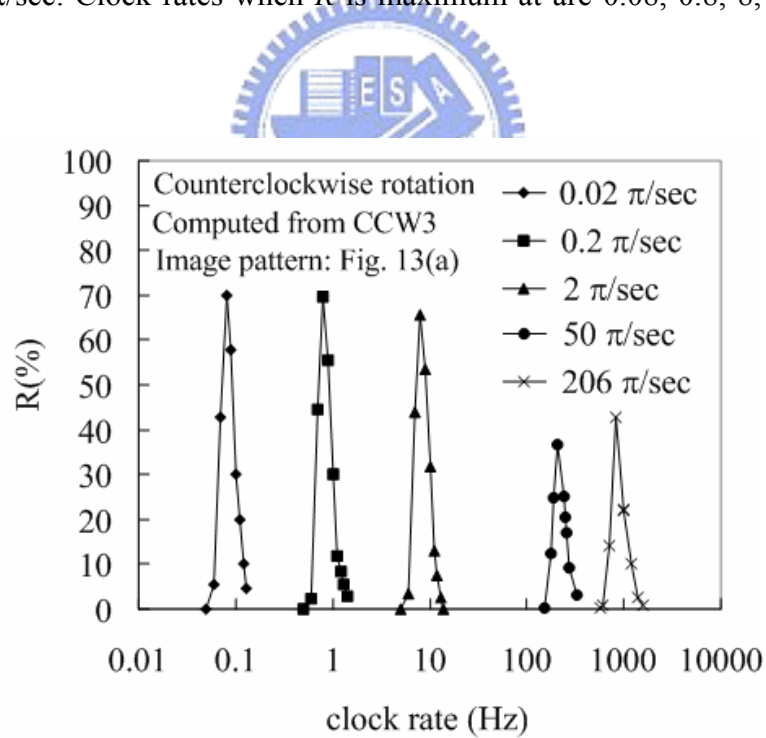


Fig. 4.3. 17. Angular velocity-selectivity under an illumination of 0.91 and 366 lux at a wavelength of 550 nm.

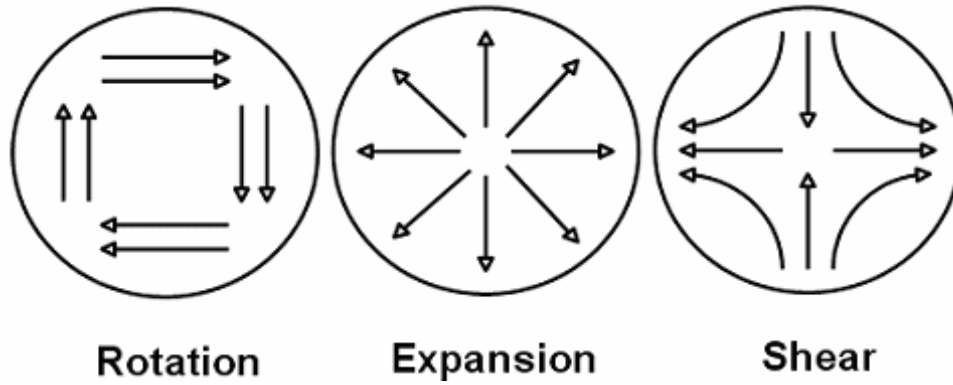


Fig. 4.4. 1. Elementary flow components (EFCs).

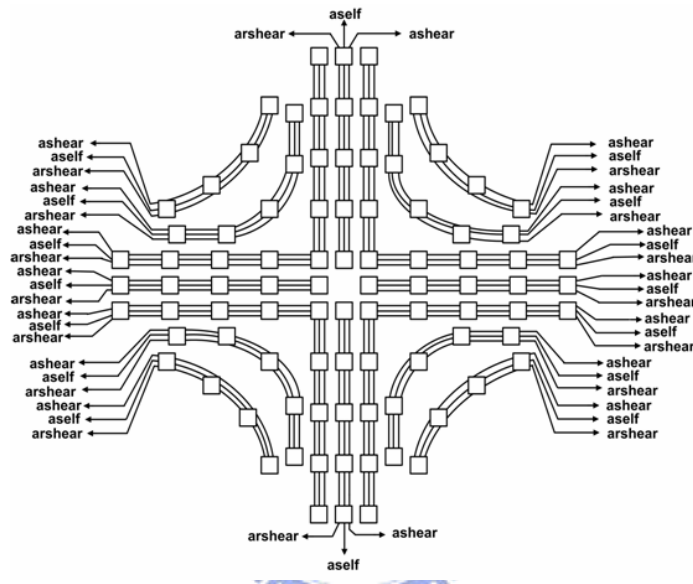


Fig. 4.4. 2. The architecture of the proposed shear sensor.

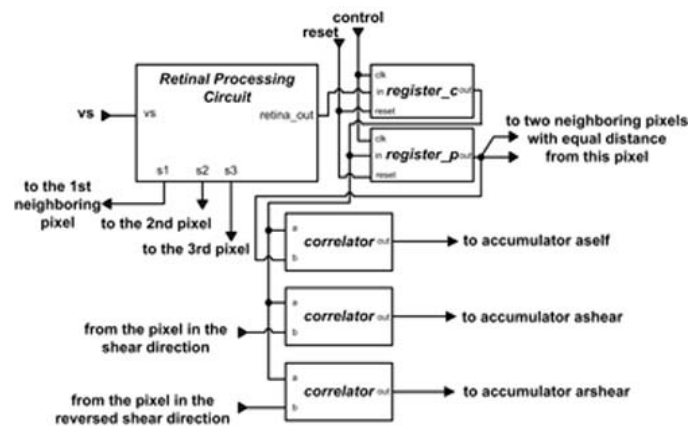


Fig. 4.4. 3. The pixel structure of the shear sensor.

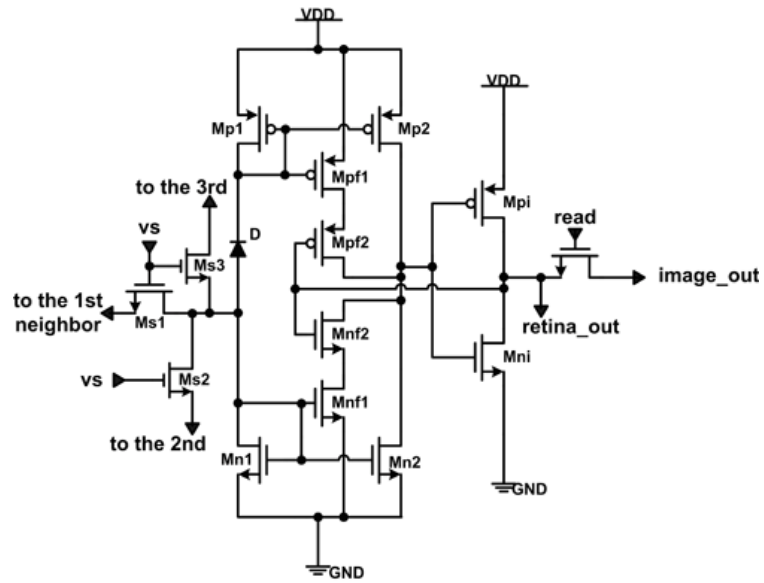


Fig. 4.4. 4. The schematic of the retinal processing circuit.

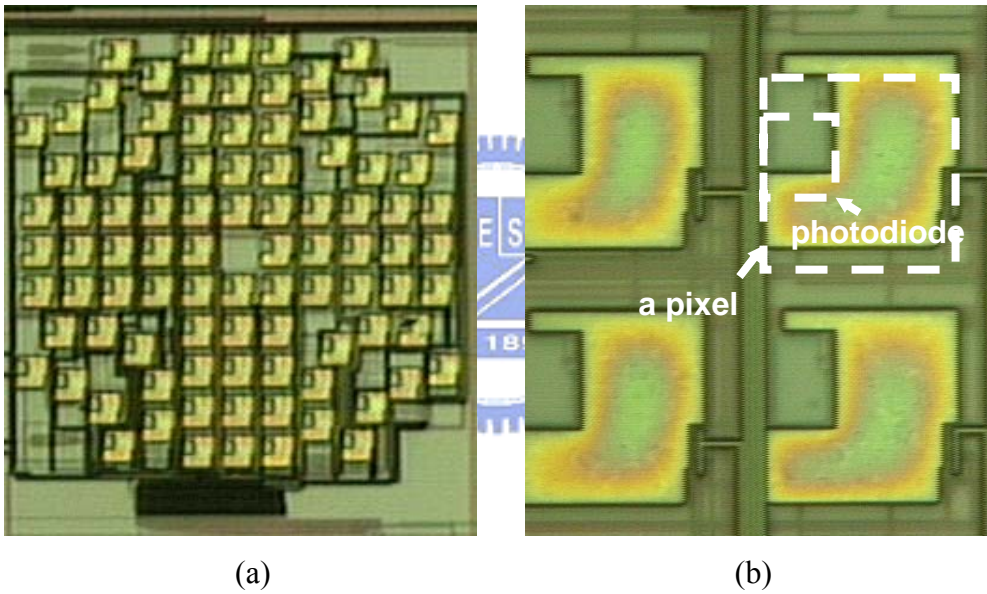


Fig. 4.4. 5. Photograph of (a) the whole chip, and (b) a single pixel, of the shear motion sensor.

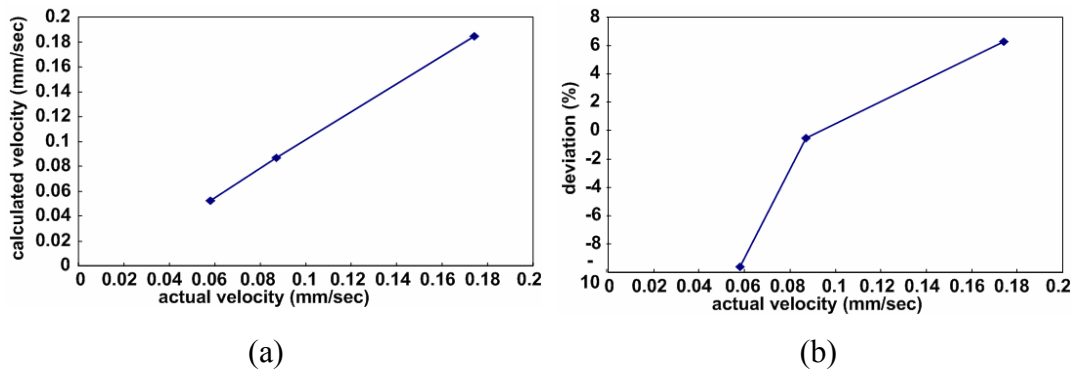


Fig. 4.4. 6. (a) Calculated velocities over 11 frames when the shear pattern moves at 0.06 mm/sec, 0.09 mm/sec and 0.18 mm/sec; (b) Deviations between calculated and actual velocities. The sampling rate is 3 Hz.

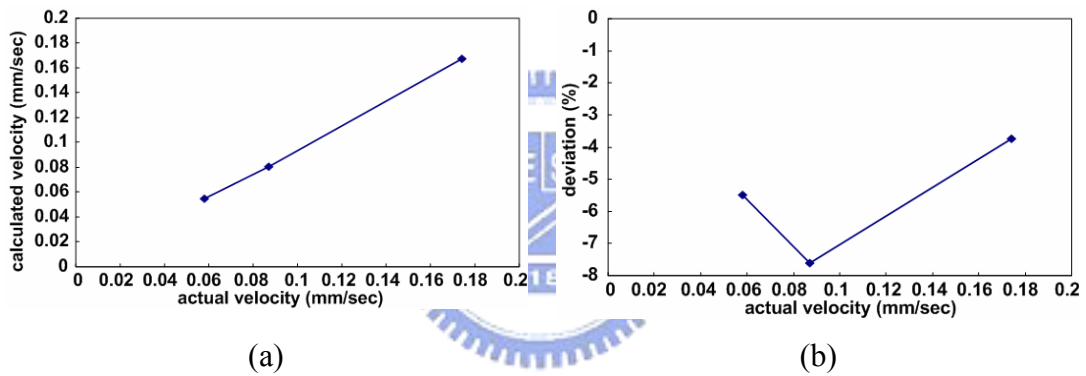


Fig. 4.4. 7. (a) Calculated velocities over 11 frames when the reversed-shear pattern moves at 0.06 mm/sec, 0.09 mm/sec and 0.18 mm/sec; (b) Deviations between calculated and actual velocities. The sampling rate is 3 Hz.

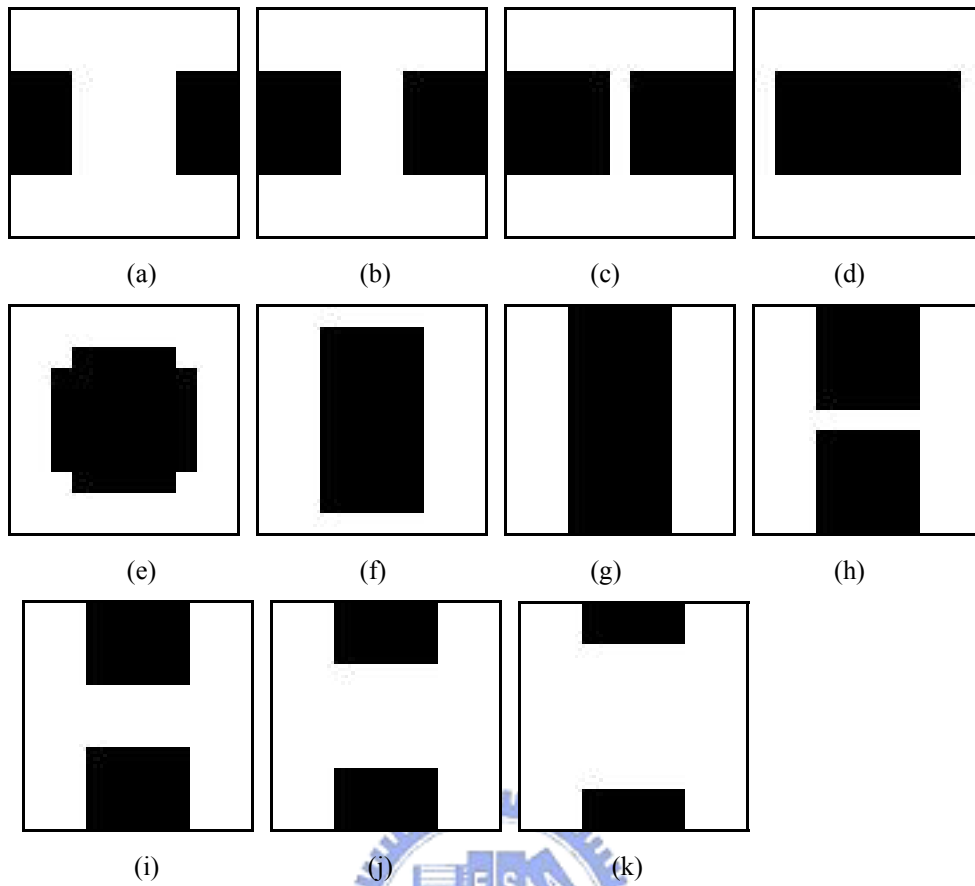


Fig. 4.4. 8. From (a) to (k) represents eleven frames of shear motion test patterns, while (k) to (a) represents reversed-shear test patterns.

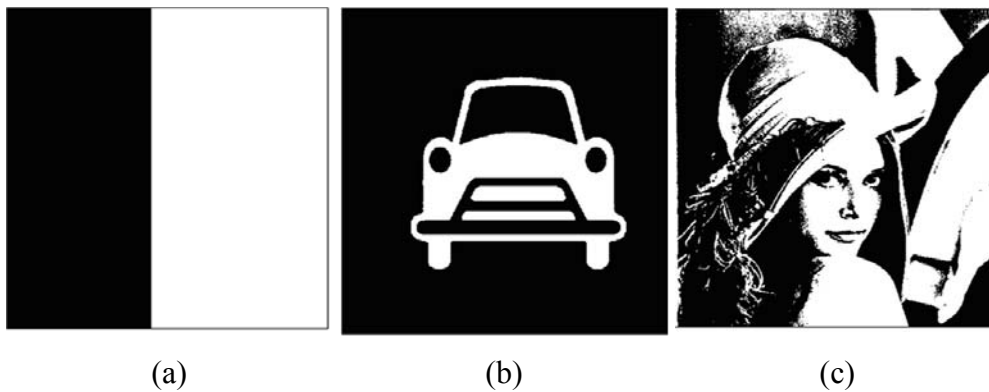


Fig. 4.4. 9. Three patterns used to test if the translation is dismissed: (a) an edge (b) a car and (c) Lenna

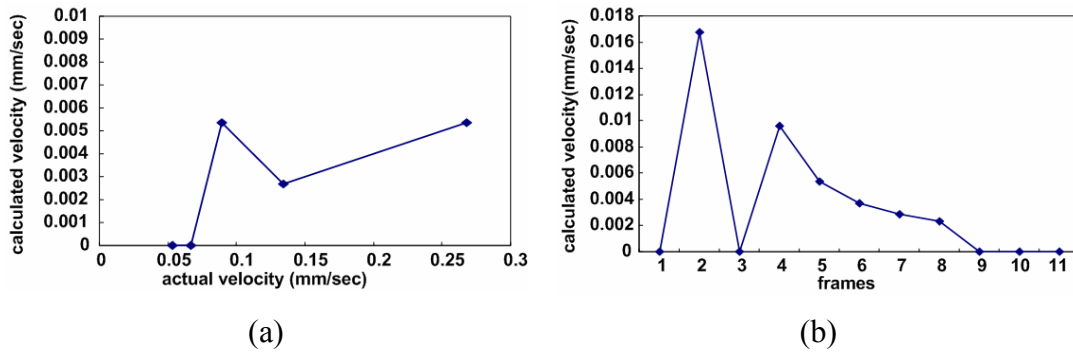


Fig. 4.4. 10 (a) Calculated velocities when the test pattern shown in Fig. 4.4. 8 (a), an edge, moving to the right at different velocities; (b) Calculated velocity decrease to nearly zero as sampling frames increase. The image translates to the right at 0.27 mm/sec. The sampling rate is 3 Hz.

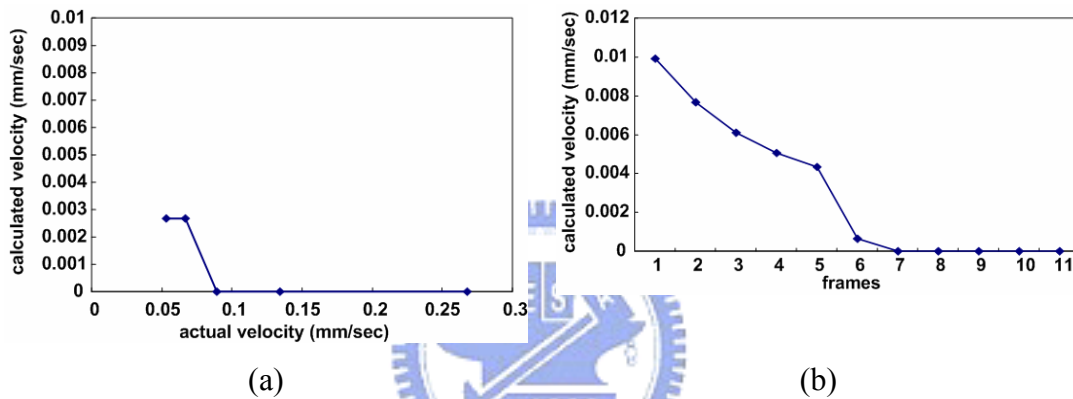


Fig. 4.4. 11. (a) Calculated velocities when the test pattern shown in Fig. 4.4. 8 (b), a car, moving to the right at different velocities; (b) Calculated velocity decrease to nearly zero as sampling frames increase. The image translates to the right at 0.27 mm/sec. The sampling rate is 3 Hz.

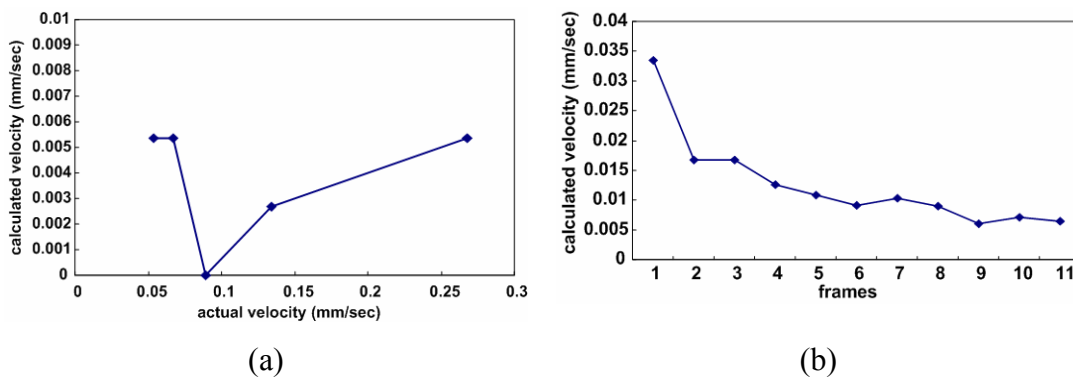


Fig. 4.4. 12. (a) Calculated velocities when the test pattern shown in Fig. 4.4. 8 (c), Lenna, moving to the right at different velocities; (b) Calculated velocity decrease to nearly zero as sampling frames increase. The image translates to the right at 0.27 mm/sec. The sampling rate is 3 Hz.

CHAPTER 5

A NEUROMORPHIC CHIP THAT IMITATES THE ON BRISK TRANSIENT GANGLION CELL SET IN THE RETINAS OF RABBITS

5.1 INTRODUCTION

The retina is a unique organ common to all organisms with the faculty of sight and is used to communicate with the visual world. It has superior performance in such areas as visual perception image detection and preprocessing: for example, in covering a wide range (10^{10}) of light intensities; in responding to very low levels of contrast ($\sim 1\%$); and in integrating for short periods of times (~ 0.04 second) [25]. As a consequence, much research has been devoted to implementations of retinal functions on silicon chips, such as the partial functions of photoreceptors and horizontal cells with part of knowledge of bipolar cells [7][46][68][74]. Various kinds of applications have also been developed using the designed chips, such as motion detection sensors [8]-[19], and high-performance image sensors [20]-[24]. Neuroscientists see the retina as a part of the brain that develops within the eye to provide neural processing for photoreceptor signals [25]. With the latest advances in neuroscience, it has been found that the mammalian visual system analyses the world through a set of separate spatio-temporal channels [25], [38]. These channels are constructed by different retinal cells, later by different cells of the lateral geniculate nucleus (LGN), and also the 36 retinotopic cortical channels. In the retina, the output ganglion cells can translate photoreceptor signals into neural spikes and send the spikes to the brain. Each channel extracts a unique spatiotemporal feature of the visual world. About half of the cerebral cortex is used to analyze the data from these channels [25], [49]. These features comprise the necessary visual information needed for the brain to analyze the visual world, thus they constitute visual language for the brain [39], [43]. This visual language is very complicated and much of it is still unknown or not understood by neuroscientists.

Our detailed view of the operation of the mammalian retina, however, changed dramatically by the discovery of the operation of the inner plexiform layer [38], [39]. This led to the understanding of the roles of different amacrine cells, as well as the

dual path in each channel. These channels have different responses to light input patterns from the visual world. Therefore, both the morphological and electrophysiological characteristics of the retina should be considered before designing a retinal chip in seeking to understand visual language. Moreover, the neuromorphic multilayer CNN model [44], [43] shed light to understand the role of different circuits and layer parameters.

It is important to duplicate successfully the retinal functions, channels, and visual language on silicon chips because of the key advantages this might provide. First, it could help neuroscientists to understand retinal functions and visual language. Since biological experiments can only be performed on a very limited number of cells, it is very difficult to see the global spatiotemporal features of retinal cells using this method alone. Second, it could provide valuable clues concerning neural activities in the visual cortex and thus move a few more steps toward the discovery of the visual processing of the brain. Third and finally, duplication could enable important applications in the areas of intelligent visual sensor systems and retinal prostheses.

To date some CMOS neuromorphic chips have been designed to imitate the retinal channels [26]-[30]. In these chips the retinal channels are simply divided into ON/OFF and transient/sustained channels. To implement these channels, a general circuit is used to generate the channel signals that are similar to the measurement results of retinal cells. Some of the functionalities have been implemented using programmable cellular visual microprocessors. After the major discovery in retinal operation mentioned above [38], the first real-time, programmable, multi-channel, neuromorphic physical implementation was constructed using the Bi-i camera computer [138].

In our research, a design methodology has been developed to implement specific retinal channel in CMOS technology. Since each retinal channel is represented by an array of the corresponding ganglion cell types, it is suitable to define the channel with the corresponding ganglion cell. In the proposed methodology, each kind of ganglion cell set is implemented in a compact CMOS circuit. Different kinds of ganglion cell sets can be implemented similarly and integrated together.

In this thesis, the ON brisk transient ganglion cell set of rabbits' retinas is adopted and implemented on a CMOS neuromorphic chip. The circuitry and cellular responses of this ganglion cell set has been completely revealed. Therefore, the design methodology can be verified well with the chosen ganglion cell set. The

neuromorphic model of the ON brisk transient ganglion cell set, which is directly derived from the biological measurements, is considered. The model-building approach is to incorporate the available knowledge concerning morphology, electro-physiology, and pharmacology and by only using elementary building blocks [44]. Then the model is transformed into a RC equivalent circuit which consists of gain blocks, resistors, and capacitors. Based on the RC equivalent circuit, a suitable macromodel is developed for CMOS circuit implementation. The resultant chip has been fabricated and measured, and its retinal functions have been verified successfully.

In Section II of this paper, the retinal model of the ON brisk transient ganglion cell set is presented. In Section III, the detailed CMOS circuits and the chip architecture are described. The experimental results are presented in Section IV, where the various spatial, temporal, and spatiotemporal characteristics of the neuromorphic model and the implemented chip are shown. Finally, the summary is given in Section V.

5.2 RETINA MODEL

5.2.1 Neuromorphic Model of the Retinal Cell Set

The block diagram of the neuromorphic model of the ON brisk transient ganglion cell set is shown in Fig. 5. 1(a), where each block has a specific name and is defined as the abstract neuron in [44]. An abstract neuron is a lowpass filter (LPF) with laterally diffusive capability. The parameter τ denotes the time constant in millisecond of the LPF. The parameter D denotes the space constant, which is defined by the laterally diffusing range in cell number in a 180-cell array. Its physical meaning is defined by the spatial range where the signals decrease to 10% of its highest value. The small block with the parameter G is the gain factor of each interconnection between two blocks. The black block denoted as R means the signals are positively rectified through it. Since biological cells don't work very precisely, relationships between both time and space constants affect the spatiotemporal features more than their absolute values. Even if scaling down these parameters by similar factors, similar spatiotemporal features are still obtained after normalization.

The space constants are obtained from morphological and electrophysiological data derived from living neural tissue, which may contain information concerning both cell sizes and lateral coupling between cells. However, it has been found that

there are only three levels of lateral inhibition mediated by the horizontal cell, the OFF bipolar cell, and the amacrine cell [37]. The lateral inhibitions compress the spatial representation of the stimulus, thus they have some key effects on the spatiotemporal characteristics of the ganglion cell channels. Therefore, only the space constants of the horizontal cell, the OFF bipolar cell, and the amacrine cell contain the information of lateral coupling between cells and, as a consequence, they play more important roles than the other space constants.

Corresponding to biological cells, the blocks PH1 and PH2 together comprise the photoreceptor, where PH1 performs the sensing function of a photoreceptor and PH2 performs the temporal function of the photoreceptor feedback. The photoreceptor receives photo stimuli and transduces them into electrical signals. The block H provides functions of a horizontal cell, which performs lateral wide-range diffusion operation on signals of the photoreceptor and sends inhibitory feedback to the photoreceptor. The feedbacks from both PH2 and H are subtracted from the photo-stimuli at the block PH1 and then sent to the bipolar cells. The PH1 signals are amplified to four times their existing level before they enter the bipolar cells.

There are two bipolar cells, namely the ON and OFF bipolar cells, in the proposed cell set and both the ON and OFF bipolar cells are of a transient type. The transient-type bipolar cell acts like a bandpass filter (BPF). Since the neuromorphic model is built by using LPF blocks, two LPF blocks are needed to realize the function of a bipolar cell. As can be seen in Fig. 5. 1(a), blocks HELP1 and ONBIP comprise the ON bipolar cell, whereas HELP2 and OFFBIP together comprise the OFF bipolar cell. Blocks HELP1 and HELP2 are not real neurons, but are assistant blocks to achieve the BPF function of the ON and OFF bipolar cells, respectively. Since the block ONBIP has a smaller time constant ($\tau=30\text{ms}$) than that of the block HELP1 ($\tau=250\text{ms}$), subtracting the output of HELP1 from that of ONBIP can generate BPF signals with the up 3dB frequency at 4Hz and the down 3dB frequency at 33.33Hz in the ON bipolar cell. The same principle can be applied to blocks HELP2 ($\tau=80\text{ms}$) and OFFBIP ($\tau=20\text{ms}$). The up and down 3dB frequencies of the BPF are 5Hz and 12.5Hz respectively in the OFF bipolar cell. Moreover, the OFF bipolar cell performs a very narrow lateral diffusion while the ON bipolar cell lacks this function. Subsequently, the ON and OFF bipolar cell signals are positively rectified before they enter the amacrine and ganglion cells.

The block named Ama provides the functions of an amacrine cell in the proposed

cell set. The amacrine cell receives positively rectified signals from the ON and OFF bipolar cells with different gain factors: 0.2 and 1 respectively. It performs a lateral diffusion in a small range and then sends inhibitory signals to the ganglion cell. The block named GC performs the functions of the ganglion cell. It receives the positively rectified signal from the ON bipolar cell with a gain factor of 2 and the signal from the amacrine cell with a gain factor of -2.2. Finally, the GC signal is positively rectified to achieve the complete function of the ganglion cell before generating spikes. This signal can be used to generate neural spikes necessary to communicate with the brain.

The actual RC equivalent circuit of the electrical model is shown in Fig. 5. 1(b), where τ is realized by a RC LPF and D is realized by a 2-D laterally resistive network. To understand the behavior and spatiotemporal pattern of every cell, the RC equivalent circuit is simulated and analyzed. The simulated results are presented in Section 5.4. Since the neuromorphic model is based on the available neuroscientific knowledge of the retina, the simulated spatiotemporal patterns of the RC equivalent circuit are similar to the biologically measured results.

5.2.2 Macromodel for Chip Implementation

To facilitate the integrated circuit implementation, the neuromorphic model in Fig. 5. 1(a) is transformed into the macromodel in Fig. 5.2. This macromodel is used to integrate the cell set into a single pixel. A sensory chip containing 32x32 pixels is employed to verify the function of the macromodel. The macromodel consists of a photoreceptor (PH1 and PH2), a horizontal cell (H), an ON and OFF bipolar cells (ONBIP and OFFBIP), an amacrine cell (Ama), and a ganglion cell (GC). Block R ensures that the signals are positively rectified as they pass through it. The + and - signs within a circle indicate the signals which are added and subtracted, respectively, at that node. Due to the variations of biological cells, the constants in space and time for each cell have their varying degrees of tolerance. This allows inevitable process variations in CMOS circuit realization of these space and time constants.

There were some modifications when constructing the macromodel from the neuromorphic model of Fig. 5. 1(a). First, a gain stage with a value -8 was added in front of the pixel circuit. This is used to enlarge the input photocurrent to facilitate the tracking of the circuit operations. Second, space constants of PH1, ONBIP, and GC were removed. Only the space constants of the horizontal cell, the OFF bipolar cell, and the amacrine cell are considered in order to simplify the complex interconnection

while retaining the functions of the three levels of lateral inhibition. Furthermore, since the pixel array shrinks from 180x180 to 32x32, the space constants of the horizontal cell, OFF bipolar cell, and amacrine cell are proportionally scaled down to 27, 2, and 6, respectively. Third, there are better methods to implement a BPF with CMOS circuit rather than subtracting a LPF from the other LPF. Therefore, at the ON bipolar cell, the two blocks HELP1 and ONBIP are merged into the one block ONBIP in the macromodel, as can be seen in Fig. 5.2. The time constants of HELP1 and ONBIP are also merged into a single time constant, τ_{BPF} . The two values in τ_{BPF} denote the up and down 3dB time constants. Similarly, the blocks HELP2 and OFFBIP are merged into the block OFFBIP. Fourth, the time constants of the blocks PH1 and H are modified to τ_{L} and that of block PH2 is modified to $4\tau_{\text{L}}$ to facilitate chip implementation. For the same reason, the down 3dB time constants of blocks ONBIP and OFFBIP are changed to $4\tau_{\text{L}}$, and the up 3dB time constants of blocks ONBIP and OFFBIP are changed to $3.2\tau_{\text{H}}$ and τ_{H} , respectively. Finally, since the time constants of the amacrine cell and the ganglion cell are smaller than those of the ON and OFF bipolar cells, their neglect had no effect on the signal flow. Therefore, the time constants of the blocks Ama and GC were removed in the macromodel.

5.3 CIRCUIT AND CHIP ARCHITECTURE

Fig. 5.3 is the block diagram corresponding to the macromodel in Fig. 5.2. A vertically parasitic p+-n-well-p-substrate BJT Q_{PHO} with a floating base is used as a photo-BJT. The photo-BJT traduces light stimuli into electrical currents. Then the photocurrent is read out, inversed, amplified by eight times, and sent to the block PH1. The PH1 signal is sent to PH2 and H to perform temporal delay and spatial diffusion, respectively. Then the signals from PH2 and H are again sent to PH1. Since the input of this circuit is a photocurrent, all signals in PH1, PH2, and H are in current-mode.

The output current I_{OPL} of PH1 directly enters the OFF bipolar cell (OFFBIP). On the other hand, an additional cascode current mirror (denoted by sub-block CM) is used to inverse it and send it to the ON bipolar cell (ONBIP) in order to achieve the inverse band-pass-filtering function. Since very low frequency BPFs (denoted by sub-block BPF) operating in voltage-mode are needed for the bipolar cells, the current-mode signals from PH1 and CM are converted into voltage-mode signals by R_{m} amplifiers (denoted by the sub-block R_{m} Amp.) before entering the BPF sub-blocks. The output signals of the sub-blocks BPF are converted to current-mode

signals again using the sub-blocks named V-I converter.

The absolute-value circuits (denoted by the sub-block ABS) are used to rectify the bipolar cell signals. At the amacrine cell (Ama), the positively rectified signals of both ONBIP and OFFBIP are summed with different gain factors. The ganglion cell (GC) subtracts the Ama signal from the positively rectified ONBIP signal. Another sub-block ABS is used to rectify the GC signal to realize the function of the ON brisk transient ganglion cell set.

There are three space constants in blocks H, OFFBIP, and Ama. The space constants are realized by using tunable NMOSFET smoothing networks [7]. Such a technique can adjust the space constants by controlling the gate biases of the NMOSFETs, thus allowing greater flexibility in designing the space constants. Moreover, since the horizontal cell has a relatively large space constant compared with the other cells, the NMOSFETs used in its smoothing network have a larger W/L ratio than the other two cells. The detailed transistor-level circuit of a pixel is shown in Fig. 5.4(a)-(c), and the transistor sizes are listed in Table 5. 1.

5.3.1 Photoreceptor and Horizontal Cell

Fig. 5.4(a) represents the circuit of the photoreceptor (PH1 and PH2) and horizontal cell (H). Because the light-induced photocurrent is around one hundred-pA to several hundred-nA, it can benefit from the good linearity of cascode current mirrors. Moreover, since the photocurrent might flow in or out of the circuit, complementary current mirrors are used to enable both current directions. The transistors M_1 - M_6 are used to bias the emitter of Q_{PHO} at V_{B1} and to direct the photocurrent into the circuit. The transistors M_7 - M_{18} provide a current gain of -8, as described in Fig. 5.3.

The CMOS transmission gates composed of transistors M_{LP1} - M_{LP8} and M_{LP9} - M_{LP16} in Fig. 5.4(a) and (b) are used as resistors. Their resistances are controlled by V_{NLP} and V_{PLP} for NMOSFET and PMOSFET, respectively. The resistances and the gate capacitances compose the LPF time constants of the blocks PH1, PH2, H, ONBIP, and OFFBIP. The unit LPF time constant τ_L can be controlled by V_{NLP} and V_{PLP} simultaneously. On the other hand, the ratios of time constants can be set by designing the MOSFET's sizes to get the suitable gate capacitances.

The current mirror composed of transistors M_{PH11} - M_{PH14} and M_{H1} - M_{H4} is designed to have a current gain of four times. Thus the current of block PH1 is enlarged to enter block H. The enlarged current is spread by a diffusion network

controlled by V_{CH} , and then it is sent to the block PH1 by transistors M_{H5} - M_{H12} . On the other hand, the current of the block PH1 is directly repeated to enter the block PH2 via transistors M_{PH11} - M_{PH14} and M_{PH21} - M_{PH24} . Transistors M_{PH25} - M_{PH212} are used to perform the temporal delay and to send feedback to the block PH1. Therefore, the channel length and width of transistors M_{PH26} , M_{PH28} , M_{PH210} , and M_{PH212} , are both twice as large as those of M_{PH25} , M_{PH27} , M_{PH29} , and M_{PH211} . Thus, the current gain is kept as unity because the W/L ratio doesn't change. However, the time constant of the block PH2 is four times larger than that of the block PH1 because the gate capacitances of M_{PH26} and M_{PH210} are four times larger than those of M_{H1} and M_{H3} .

The output current of block PH1 is enlarged four times by two current mirror slaves composed of transistors M_{PH15} - M_{PH18} and M_{PH19} - M_{PH112} while transistors M_{PH11} - M_{PH14} serving as the current mirror master. Transistors M_{PH19} - M_{PH112} generate I_{OPL} , which is sent to the block OFFBIP. The drain current of transistors M_{PH110} and M_{PH112} is inversed using a complementary current mirror (CM) to generate I_{OPLB} , which is sent to the block ONBIP.

At the output stage, the transistors M_{O1} and M_{O2} , M_{O3} and M_{O4} , and M_{O5} and M_{O6} are used to repeat the output currents of the blocks PH1, H, and PH2, respectively, to enable chip measurement. Since there are external biases applied to measure the chip, simple structure instead of the cascode type slaves are used to save the pixel area.

5.3.2 ON and OFF Bipolar Cells

The circuit of the bipolar cell stage is shown in Fig. 5.4(b). The circuit can be divided into two parallel paths including blocks ONBIP and OFFBIP, separately. At the OFFBIP path, an R_m amplifier composed of transistors M_{RM5} - M_{RM8} is used to transduce the current I_{OPL} into voltage-mode. Afterward, a poly capacitor C_{OFF} and a CMOS transmission gate, including transistors M_{HP3} and M_{HP4} , are used to form a highpass filter (HPF). This HPF and the LPF composed of M_{LP6} , M_{LP8} , and M_{VI10} form the sub-block BPF. The bandwidth of the HPF, which is also the up 3dB time constant of the BPF τ_H , can be tuned by the biases V_{NHP} and V_{PHP} at gates of M_{HP3} and M_{HP4} , respectively. The transmission gate is connected to the reference bias V_{ref} , which is set to a half of the supply voltage to balance both upward and downward signal swings.

The voltage-mode signal of the sub-block BPF is transduced into the current-mode signal again by using a V-I converter composed of transistors M_{VI8} -

M_{VI14} [137]. The V-I converter is a differential amplifier. Its positive input node connects to the output of the sub-block BPF, and its negative input node connects to the reference bias V_{ref} . Its output current is passed to a modified absolute value circuit (ABS) composed of the transistors M_{OFF1} - M_{OFF6} . Transistors M_{OFF1} - M_{OFF4} form a simple current mirror, and transistors M_{OFF5} and M_{OFF6} play the roles of adjustable switches that are controlled by V_{absN} and V_{absP} , respectively. When M_{ON5} M_{ON6} are biased suitably, the output of sub-block BPF, which is smaller than V_{ref} , will be converted into current-mode and mirrored only by M_{OFF1} , M_{OFF2} ; and M_{OFF7} , while that larger than V_{ref} will be converted and mirrored only by M_{OFF3} and M_{OFF4} . The transistors M_{OFF2} and M_{OFF4} repeat the complete signal of the block OFFBIP and send it out of the chip as I_{OFFBIP} . In the mean time, the transistor M_{OFF7} sends the positively rectified signal of the block OFFBIP to the block Ama as I_{OFF_A} .

At the ONBIP path, the circuit operations are mostly the same as at the OFFBIP path. The main differences of the ONBIP path from the OFFBIP path are as follows: First, the ONBIP path receives the inversed signal from the block PH1 as I_{OPLB} [Fig. 5.4(a) and (b)]. Second, C_{ON} is designed to be 1pF and C_{OFF} is designed to be 312.5fF in order to achieve the ratio of time constants of the blocks ONBIP and OFFBIP. Third, there is a smoothing network at the output node of the V-I converter of the OFFBIP path to perform the lateral diffusion, but this is lack at the ONBIP path. Finally, the transistors M_{ON7} and M_{ON8} repeat the signal of the block ONBIP when the output of the sub-block BPF is smaller than V_{ref} , and send it to blocks Ama and GC as I_{ON_A} and I_{ON_GC} , respectively.

5.3.3 Amacrine and Ganglion Cells

The circuit of the amacrine and the ganglion cell is shown in Fig. 5.4(c). The block Ama is constructed using transistors M_{A1} - M_{A10} . The transistor M_{A3} receives the summation of I_{ON_A} and I_{OFF_A} , shown in Fig. 5.4(b), and transistors M_{A1} - M_{A4} repeat the summed current. The repeated current is laterally diffused by a smoothing network at the drain node of transistors M_{A4} and M_{A7} . Then this diffused current is inversely repeated by transistors M_{A5} - M_{A8} and is sent out of the chip via M_{A11} as I_{Ama} . At the same time, this current is inversely repeated again to enter the block GC by the cascode current mirror composed of transistors M_{A9} , M_{A10} , M_{G1} , and M_{G2} . This current mirror is also designed to implement the gain block after the block Ama, as shown in Fig. 5.2. The block GC receives I_{ON_G} as shown in Fig. 5.4(b) and subtracts it from the current mirrored using transistors M_{A9} , M_{A10} , M_{G1} , and M_{G2} . The

subtracted current is sent to the sub-block ABS composed of the transistors M_{G3} - M_{G9} to be positively rectified. Thus, only the signal on the positive side is repeated and sent out of the chip by M_{G9} as I_{GC} .

5.3.4 Whole Chip Architecture

The architecture of the fabricated chip is shown in Fig. 5.5(a). The pixel circuit mentioned above is arranged in a 32x32 array. A row decoder and a column decoder are used to select the pixel that is to be observed. Every time there is only one pixel that can be observed with seven observable signals: I_{PH1} , I_{PH2} , I_H , I_{ONBIP} , I_{OFFBIP} , I_{Ama} , and I_{GC} as shown in Fig. 5.4(a)-(c). Using this method, the behavior of each pixel, as well as that of the whole array, can be observed by setting different controlling strategies using the row and column decoders.

The technique to implement the smoothing networks should be mentioned next. Since there are three lateral diffusion layers at the horizontal cell, the OFF bipolar cell, and the amacrine cell, three diffusion networks are needed in the designed chip. As can be seen in Fig. 5.5(b), there are three NMOSFETs which connect two neighboring pixels. These NMOSFETs correspond to the smoothing networks in Fig. 5.3 and Fig. 5.4. On average, each pixel has six NMOSFETs to perform the lateral diffusion. Thus three two-dimensional smoothing networks are achieved.

5.4 EXPERIMENTAL RESULTS

5.4.1 Neuromorphic Model Simulation

The RC equivalent circuit in Fig. 5.1(b) is used to construct a 32x32 array which is simulated by HSPICE. Since the array size differs from the original definition of the space constants D , all the space constants in the simulation are shrunk with the same factor, 32/180. The simulation results are shown in Fig. 5.6. In this simulation, a voltage pulse is applied to the 6x6 cells in the center of the array to imitate the 1Hz flashing light stimulus and the spatiotemporal patterns of the 17th row are observed. In Fig. 5.6, the x-axis is time and the y-axis is the pixel location which denotes space. The black and white bars denote the spatial and temporal region of the input stimulus. The stimulus is applied to the 15th to the 20th pixel from 1001 msec to 2000 msec. The waveform at the right of each pattern is the spatial domain waveform(s) obtained at the time marked by the vertical arrow(s). The waveform at the bottom of each pattern is the temporal domain waveform obtained at the location marked by the horizontal arrow.

Fig. 5.6(a) and (b) represent the spatiotemporal patterns of the photoreceptor and horizontal cell, respectively. It can be seen from Fig. 5.6(a) that the photoreceptor's signal level drops when there is a stimulus, and it returns to its original level when the stimulus disappears. Slight undershooting and overshooting in temporal domain can be expected in the periphery as it reacts to the stimulus directly. In the spatial domain, there is strong contrast at the edge of the stimulus. At the edge pixels inside the stimulus, the signal level is higher than the other stimulated pixels. Contrarily, at the edge pixels where the stimulus is just absent, the signal level is higher than the other silent pixels. Therefore, the spatial range of the stimulus can be well defined. In the temporal domain, the horizontal cell has a similar reaction to the photoreceptor, as can be seen in Fig. 5.6(b). However, since the horizontal cell performs lateral diffusion in space, its spatial domain waveform spreads wider than that of the photoreceptor.

Fig. 5.6(c) and (d) represent the spatiotemporal patterns of the ON and OFF bipolar cells, respectively. The OFF bipolar cell performs bandpass-filtering on the signals from the photoreceptor, whereas the ON bipolar cell performs bandpass-filtering on the same signals but with an opposite polarization. In the amacrine cell, the rectified signals from both bipolar cells are added with different gain factors, as shown in Fig. 5.6(e). Moreover, the response to the appearance of the stimulus is weaker than the response to the disappearance of the stimulus. Thus the amacrine cell provides a strong inhibition to the ganglion cell when the stimulus disappears in time. Therefore, the ganglion cell exhibits clear turned-ON reaction, as can be seen in Fig. 5.6 (f).

5.4.2 The Experimental Chip and Setup

The chip is designed using the TSMC 0.35 μ m double-poly-quadruple-metal standard CMOS technology. The photograph of the whole chip is shown in Fig. 5.7(a) and that of a single cell is shown in Fig. 5.7(b). The whole chip area is 4.3mm x 4.41mm, and the cell pitch is 105 μ m. There is a photo-BJT in the center to transduce light stimuli into photocurrents as shown in Fig. 5.7(b). The fill factor of the photo-BJT is 7.44%. It can be seen from Fig. 5.7(a) that the pixel array occupies most of the chip area. The row decoder and column decoder are on the left and top of the chip. The ESD pads are used to protect the chip from electrostatic damages.

Since the designed chip sends pixel signals in current format, external current-to-voltage converters are needed to facilitate measurements. The read-out circuit of each output is shown in Fig. 5.8. Since there are seven output signals

generated by this chip, as shown in Fig. 5.5(a), there are seven similar read-out circuits. The circuit contains one operational amplifier (OP), a resistor, and a LPF composed of a resistor and a capacitor. The operational amplifier with a negative feedback provides a virtual bias at the negative input node, which is connected to the chip's output node. The value of the virtual bias is determined by V_B . The resistor R_{OUT} converts the current into voltage. Therefore, the current flowing out from the chip I_{OUT} will be transduced into V_{OUT} through the readout circuit. Assuming the voltage gain of the operational amplifier A is infinite. The relationship between I_{OUT} and V_{OUT} is:

$$V_{out} = \left(\frac{A}{A+1}\right)(-I_{out}R_{out} + V_B) \quad (1)$$

The voltage-mode signal V_{OUT} is actually observed and recorded.

The measured data are presented and analyzed below. Considering the different signal swings of the output currents, the R_{OUT} for I_{PH1} , I_{PH2} , I_{Ama} , and I_{GC} are set as $3M\Omega$, while the R_{OUT} for I_H , I_{ONBIP} , and I_{OFFBIP} are set as $1M\Omega$ to optimize experimental conditions. The optimization of the experimental condition will yield the largest but unsaturated signal levels.

A white light LED is used to generate flashing light to stimulate the test chip. The LED is controlled by a function generator, so that the amplitude and frequency of the incidental light can be monitored. However, the input stimuli are always repetitive because of the inherent nature of the function generator. An optical lens is used to concentrate the light from the LED onto the test chip, thus only a small part (around 5×5 pixels) of the chip is stimulated while the other part remains relatively dark. The biases are controlled by a group of regulators adjusted with precisely variable resistors.

5.4.3 The Measured Spatiotemporal Patterns

The bias condition for measuring the spatiotemporal patterns is listed in Table 5.2(a). The normalized spatiotemporal patterns are shown in Fig. 5.9. The light stimulated region is from the 19th pixel to the 23rd pixel in space, and from the 1001 point to the 2000 point in time. At the bottom of each pattern is the temporal domain waveform recorded at the 21st pixel, and at the right is the spatial domain waveform(s) recorded at the time point(s) marked by the vertical arrow(s). In Fig. 5.9(a) and (b), the spatial domain waveforms are recorded at the time point 1500. In Fig. 5.9(c), (d) and (e), the spatial domain waveforms are recorded at the time points 1020 and 2020.

In Fig. 5.9(f), the spatial domain waveforms are recorded at the time point 1020. The effects of the spatial diffusions can be seen in Fig. 5.9(b), (d) and (e).

Fig. 5.9(a) illustrates the spatiotemporal pattern of the photoreceptor. The pattern is not as perfect as that in Fig. 5.6(a) because of the inter-pixel variation and imperfection of the light stimulus. However, the spatial edge of light stimulus still can be recognized by the contrast between grey and white rows. The spatiotemporal pattern of the horizontal cell in Fig. 5.9(b) covers a wide area of space. The phenomenon can be seen clearly from its spatial waveform represented at the right of Fig. 5.9(b). Because of this phenomenon, the effects of inter-pixel variation and imperfection of the light stimulus are not as strong as those presented in Fig. 5.9(a).

The spatiotemporal patterns of the ON and OFF bipolar cells are shown in Fig. 5.9(c) and (d). The two patterns are roughly complementary, except that the pattern of the OFF bipolar cells is narrower in time but wider in space than the pattern of the ON bipolar cells. The pattern of the ON bipolar cell is noisier than the pattern of the OFF bipolar cell. Both cells are affected by the photoreceptor, but the lateral diffusion of the OFF bipolar cell reduces the effects of inter-pixel variation and imperfection of the light stimulus. The pattern of the amacrine cell, as shown in Fig. 5.9(e), also covers a wide area of space. It responds to both appearance and disappearance of the light stimulus in time, as can be seen at the bottom of Fig. 5.9(e). It can be seen from Fig. 5.9(b) and (e) that their temporal domain waveforms are noisier than the other cells because the wide-range lateral diffusion introduces noise into the cells. This phenomenon is not very obvious in Fig. 5.9(d) because the range of lateral diffusion of the OFF bipolar cell is very narrow. The spatiotemporal pattern of the ganglion cell in Fig. 5.9(f) only responds to the appearance of the light stimulus in time, and has a sharp edge in space.

Through this experiment, it is found that the cells without lateral diffusion have good immunity to temporal noise, but have bad immunity to spatial noise. Contrarily, the cells with lateral diffusion have bad immunity to temporal noise, but have good immunity to spatial noise. Thus a good spatiotemporal filter can be implemented through combining two kinds of cells described above.

5.4.4 Temporal Domain Analyses

In order to demonstrate the degree of coincidence between the neuromorphic model and the measured results, the normalized waveforms of the neuromorphic model and measurements are grouped together and represented in Fig. 5.10. Since the

ON bipolar cell, OFF bipolar cell, amacrine cell, and ganglion cell are the key components of the cell set, only the waveforms of the four cells are shown in Fig. 5.10 (a)-(d), respectively. The temporal domain waveforms of the neuromorphic model (dissected line) are obtained by setting the bias condition as listed in Table 5.2(b). The waveforms of measurements (solid line) are the temporal domain waveforms of Fig. 5.9(c)–(f). The light stimulus starts at the time point 1001, and ends at the time point 2000. It can be seen from Fig. 5.10 (a)-(d) that the shape of each waveform in the same comparison is similar. The slight deviations are caused by process and inter-pixel variations. However, this level of variation is acceptable because biological cells also have inter-cell variations.

The variation of time constants is shown in Fig. 5.11. In Fig. 5.11(a), the relationship between τ_H and V_{PHP} and V_{NHP} is presented, and Fig. 5.11(b) is the relationship between τ_L and V_{PLP} and V_{NLP} . In this experiment, a parameter ΔV is used to represent the x-axis. In Fig. 5.11(a), the bias voltage V_{PHP} is equal to ΔV , and bias voltage V_{NHP} is equal to $V_{dd}-\Delta V$. Thus, while increasing ΔV , V_{PHP} is increased while V_{NHP} is decreased. An assumption is applied that the two biases V_{PHP} and V_{NHP} affect the equivalent resistance of the transmission gate symmetrically. Similarly, the bias voltage V_{PLP} is set to ΔV , and bias voltage V_{NLP} is set to $V_{dd}-\Delta V$ for finding the relationship between τ_L and V_{PLP} and V_{NLP} . The maximum value of ΔV is 0.85V in Fig. 5.11 (a), and is 0.9V in Fig. 5.11 (b). The functions of the corresponding HPF and LPF are completely distorted if ΔV exceeding these values. This experiment provides the available range of time constants of the HPF, LPF, and BPF used in the circuit.

5.5 SUMMARY

A neuromorphic chip that imitates the ON brisk transient ganglion cell set of rabbits' retinas was implemented and observed. Most parts of the chip deal with current-mode signals. The chip contains 32x32 pixels where each pixel imitates one cell set of the ON brisk transient ganglion cell. The total power consumption is 1.675W under 0.45mW light stimuli. The power consumption can be further reduced by simplifying the cell circuit according to specific applications. The measured results under flashing lights have the same spatiotemporal characteristics as those from biological measurements obtained using similar stimuli. Such consistency strongly suggests that the chip, in extracting the features of the visual world, behaves in a way which is similar to that of real retinal cells. Therefore, this study provides the

experimental evidence needed by neuroscientists to understand the performance of all other retinal cells.

Furthermore, the verifications of the implemented chip establish the success of the proposed design methodology. Thus, every kind of ganglion cell sets can be implemented and integrated in the same way. With the development of biological circuitries and spatiotemporal features, the implementation of this design methodology should make possible the realization and analysis of complete visual language. Moreover, since some of the spatial and temporal parameters can be altered, part of the circuit can be shared to save chip area when integrating multi cell sets. By revealing and understanding the image processing technique of the retina, various applications in the areas of intelligent sensors and retinal prostheses are possible.



Table 5. 1 The transistors' sizes of circuits in Fig. 5.4(a)-(c)

Transistor numbers	W/L ($\mu\text{m}/\mu\text{m}$)	Transistor numbers	W/L ($\mu\text{m}/\mu\text{m}$)
M_1, M_2	1.5/0.8	M_{HP2}, M_{HP4}	2.25/10
M_3, M_4, M_5	2/0.8	$M_{LP1} \sim M_{LP8}$	0.4/10
$M_8, M_{10}, M_{12}, M_{14}, M_{15} \sim M_{18}$	4/0.4	$M_{LP9} \sim M_{LP16}$	1.2/10
M_{11}, M_{13}	1/0.4	$M_{VI1}, M_{VI2}, M_{VI8}, M_{VI9}$	4/2
M_7, M_9	2/0.4	$M_{VI3}, M_{VI4}, M_{VI10}, M_{VI11}$	0.8/4
$M_{PH11} \sim M_{PH14}, M_{H5} \sim M_{H12},$ $M_{PH21} \sim M_{PH24}, M_{PH25}, M_{PH27},$ $M_{PH29}, M_{PH211}, M_{O1} \sim M_{O4},$ $M_{CM1} \sim M_{CM8}$	1/0.8	$M_{ON1}, M_{ON2}, M_{ON8}, M_{OFF1},$ $M_{OFF2}, M_{OFF7}, M_{A1} \sim M_{A4},$ $M_{A5}, M_{A7}, M_{A9}, M_{A10},$ $M_{G1} \sim M_{G3}, M_{G8}, M_{G9}$	2/2
$M_{H1} \sim M_{H4}, M_{PH15} \sim M_{PH112}$	4/0.8	M_{VI7}, M_{VI14}	3/2
$M_{PH26}, M_{PH28}, M_{PH210}, M_{PH212},$ M_{O5}, M_{O6}	2/1.6	$M_{ON3}, M_{ON4}, M_{OFF3}, M_{OFF4},$ M_{G6}, M_{G7}	2/4
$M_{RM1}, M_{RM5},$	3/0.4	$M_{ON5}, M_{OFF5}, M_{G4}$	3/1
M_{RM2}, M_{RM6}	1/0.4	$M_{ON6}, M_{OFF6}, M_{G5}$	6/1
M_{RM3}, M_{RM7}	2.25/1	$M_{VI5}, M_{VI6}, M_{VI12}, M_{VI13}$	0.8/3
M_{RM4}, M_{RM8}	0.7/1	M_{ON7}	0.6/2
M_{HP1}, M_{HP3}	0.7/10	M_{A6}, M_{A8}	4.4/2
M_{SH}	1/1	CON	1pF
M_{sOFF}, M_{sA}	1/4	COFF	312.5fF

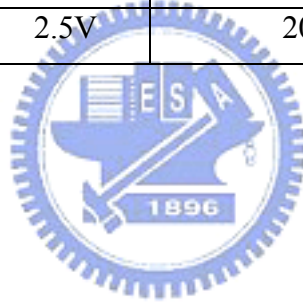
Table 5. 2

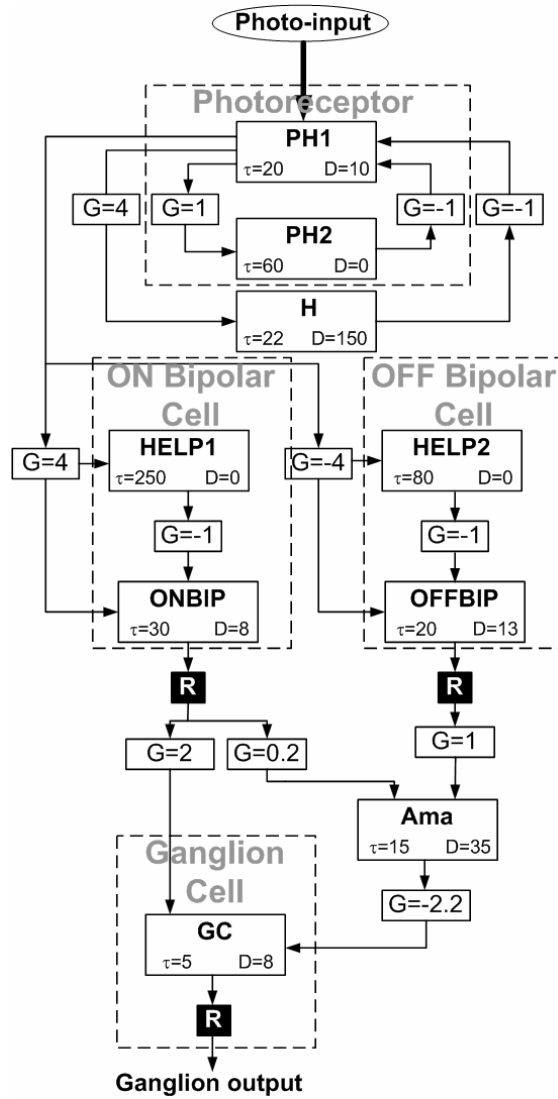
(a) The bias condition to measure the spatiotemporal patterns of Fig. 5.9

V_{dd}	V_{ref}	V_{B1}	V_{B2}	V_{absP}	V_{absN}
2.5V	1.255V	0.326V	0.244V	0.5V	2.13V
V_{cH}	V_{cOFF}	V_{cAma}	V_{prm}	V_{nrm}	V_{PHP}
2.502V	2.33V	2.17V	0.27V	1.91V	0.67V
V_{NHP}	V_{PLP}	V_{NLP}	Flashing Frequency		LED Power
1.67V	0V	2.5V	20Hz		0.45mW

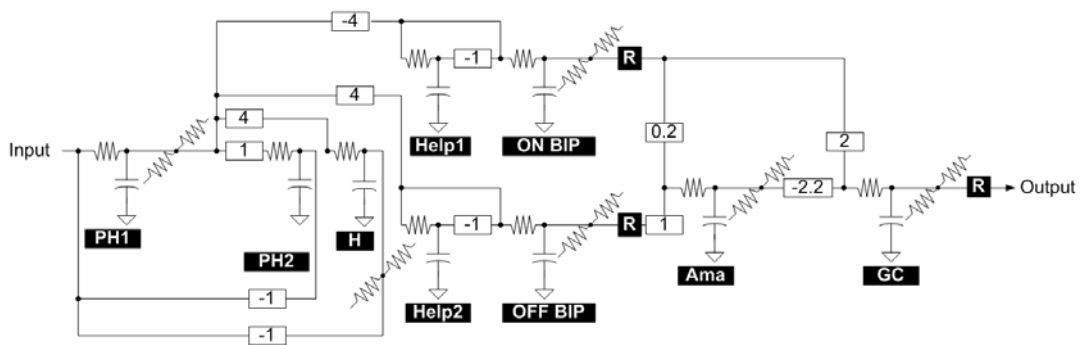
(b) The bias condition to measure the temporal domain waveforms of Fig. 5.10

V_{dd}	V_{ref}	V_{B1}	V_{B2}	V_{absP}	V_{absN}
2.5V	1.255V	0.326V	0.244V	0.973V	0.202V
V_{cH}	V_{cOFF}	V_{cAma}	V_{prm}	V_{nrm}	V_{PHP}
2.502V	2.468V	1.082V	0.27V	1.91V	0.67V
V_{NHP}	V_{PLP}	V_{NLP}	Flashing Frequency		LED Power
1.67V	0V	2.5V	20Hz		0.45mW





(a)



(b)

Fig. 5. 1. (a) The neuromorphic model and (b) the RC equivalent circuit of the ON brisk transient ganglion cell set of rabbits' retinas. The parameter τ denotes the time constant in millisecond of the LPF. The parameter D denotes the space constant, which is defined by the laterally diffusing range in cell number in a 180-cell array.

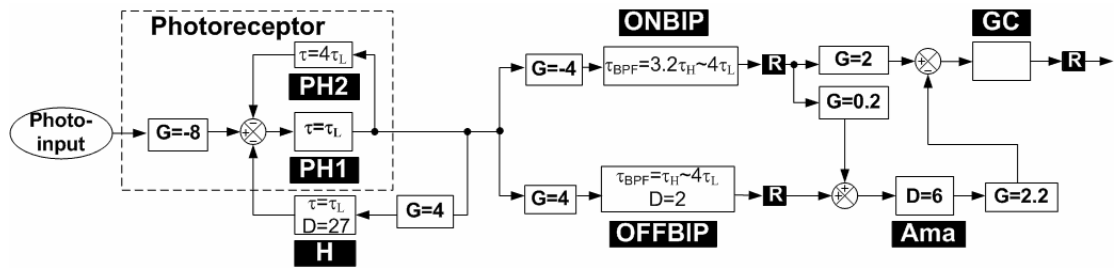


Fig. 5.2. The macromodel of a single pixel of the implemented chip.

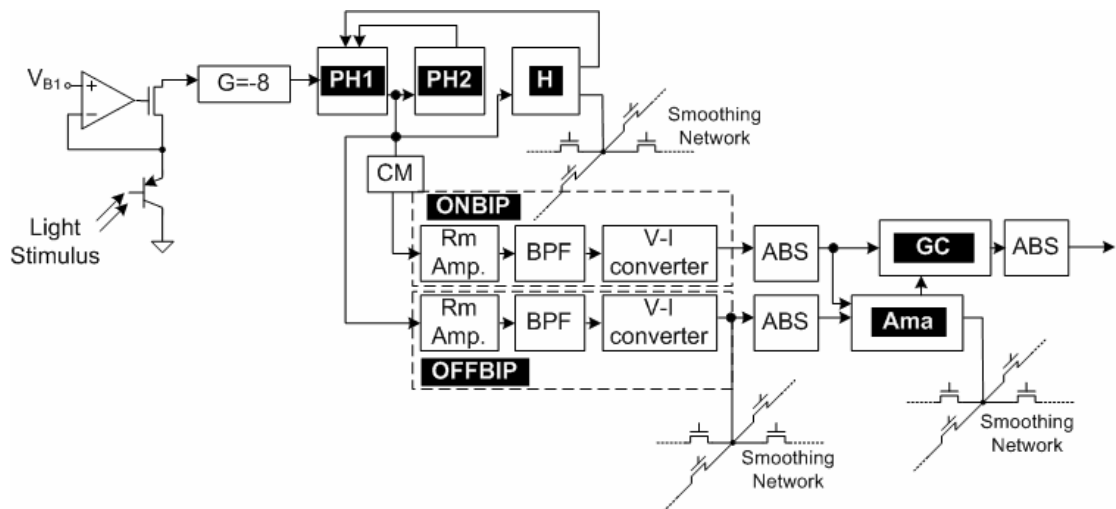
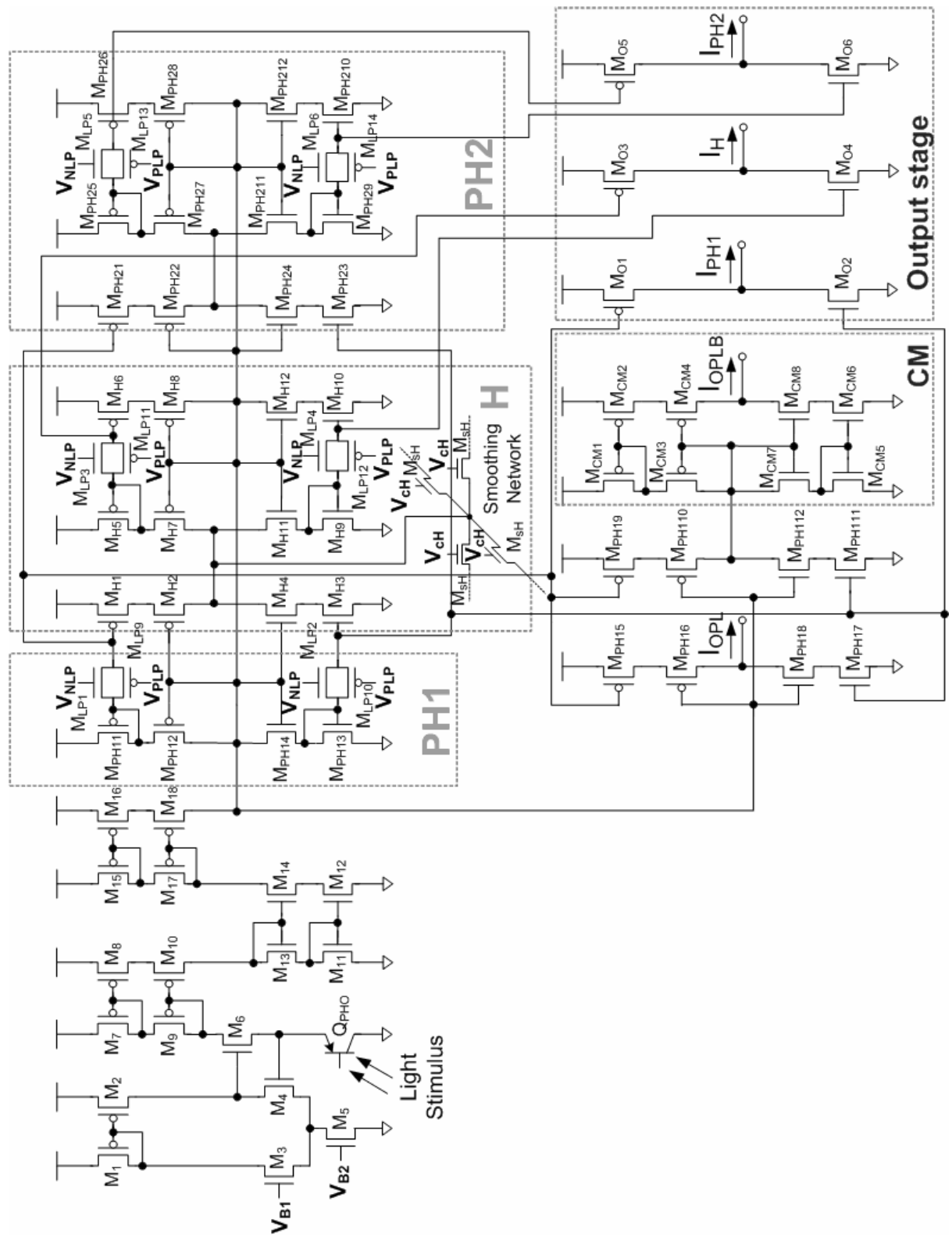


Fig. 5.3. The block diagram of a single pixel.



(a)

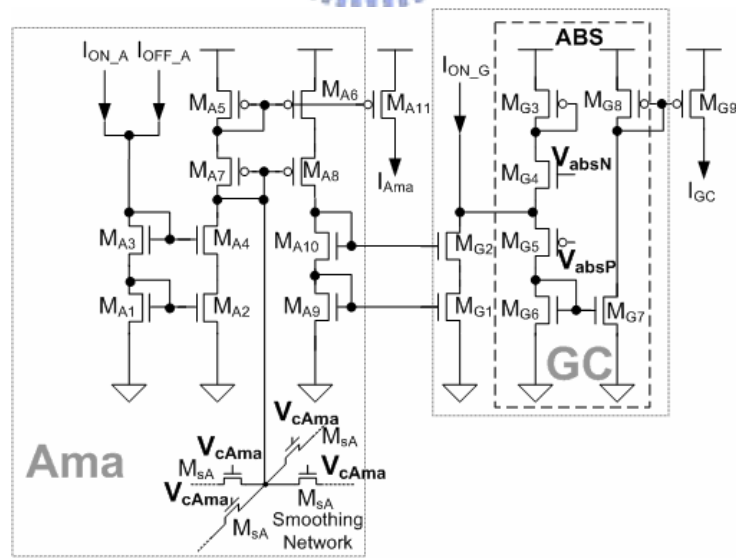
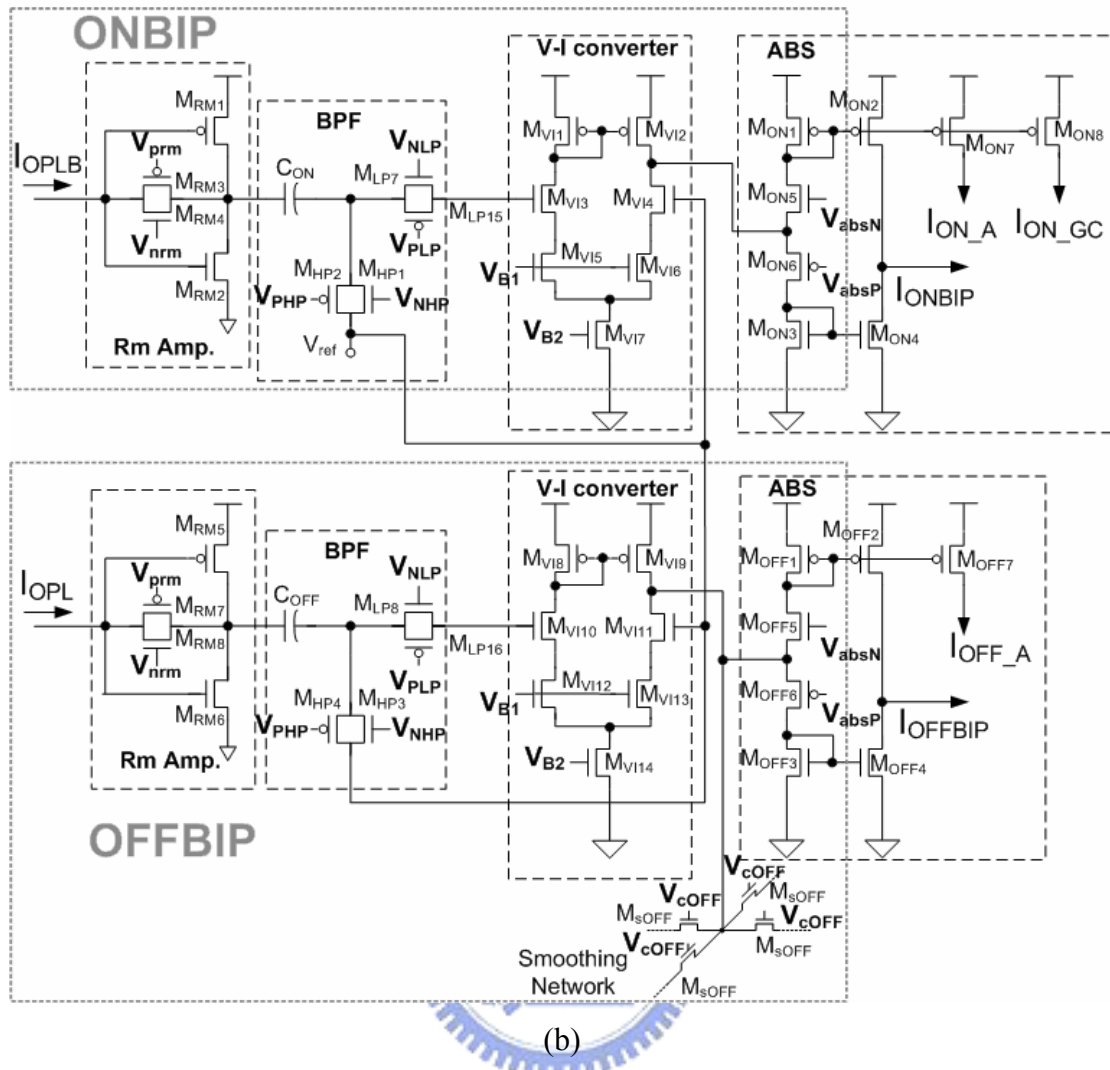
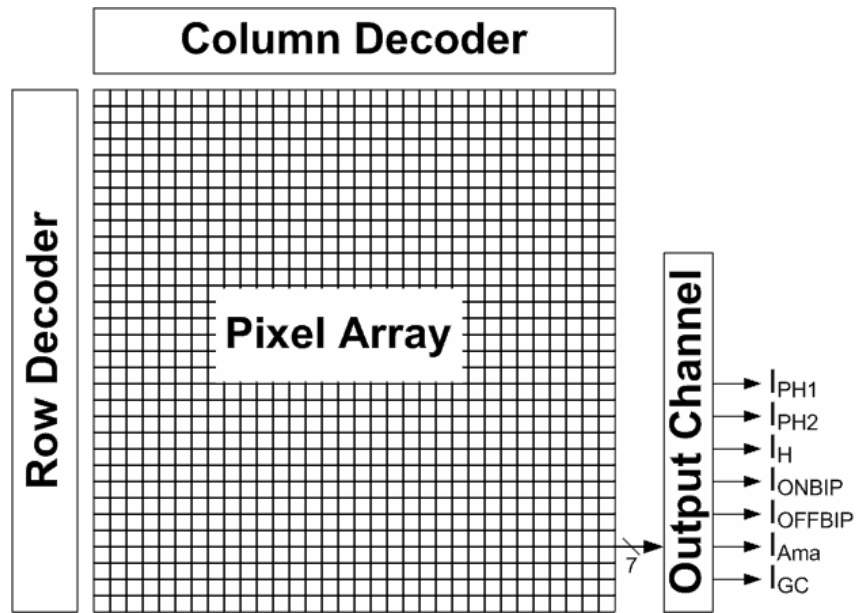
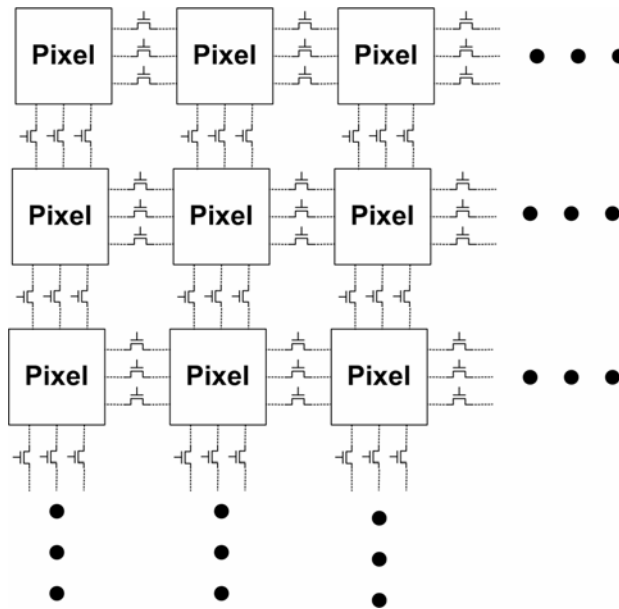


Fig. 5.4. (a) The circuit of the photoreceptor and horizontal cell (PH1, PH2, H); (b) The circuit of ON and OFF bipolar cells (ONBIP, OFFBIP); (c) The circuit of amacrine and ganglion cells (Ama, GC).



(a)



(b)

Fig. 5.5. (a) The whole chip architecture of the implemented chip, and (b) the implementation of smoothing networks.

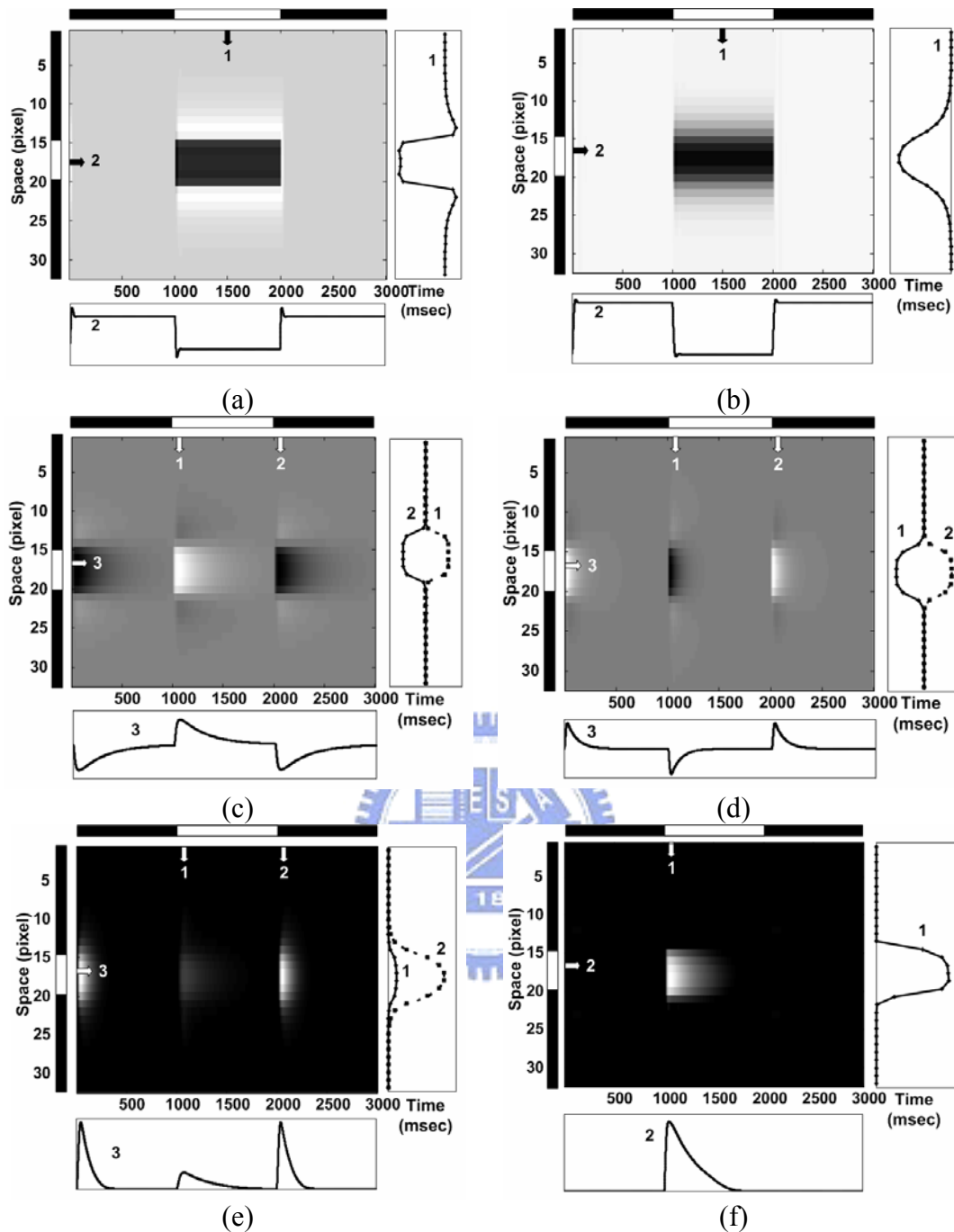


Fig. 5.6. The HSPICE simulated spatiotemporal patterns of the neuromorphic model of the ON brisk transient cell set in a 32x32 array for (a) photoreceptor, (b) horizontal cell, (c) ON bipolar cell, (d) OFF bipolar cell, (e) amacrine cell, and (f) ganglion cell. These patterns are recorded from the 17th row of the array. The x-axis is normalized time and the y-axis is the pixel location which denotes space. The stimulus is applied to the 15th to the 20th pixel at time point 1001 to 2000. The waveform at the right of each pattern is the spatial domain waveform(s) obtained at the time marked by the vertical arrow(s). The waveform at the bottom of each pattern is the temporal domain waveform obtained at the location marked by the horizontal arrow.

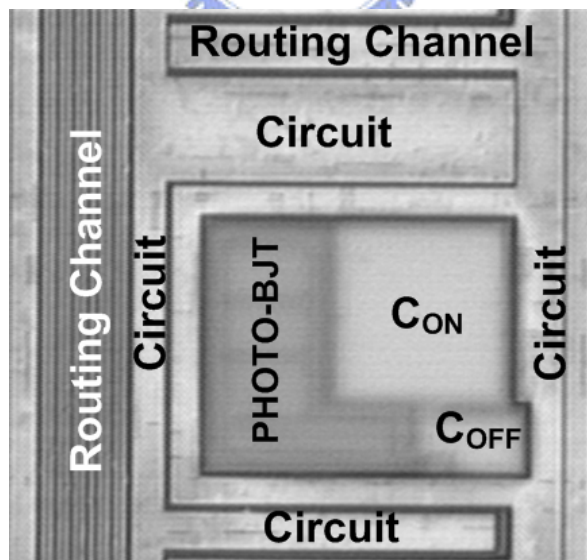
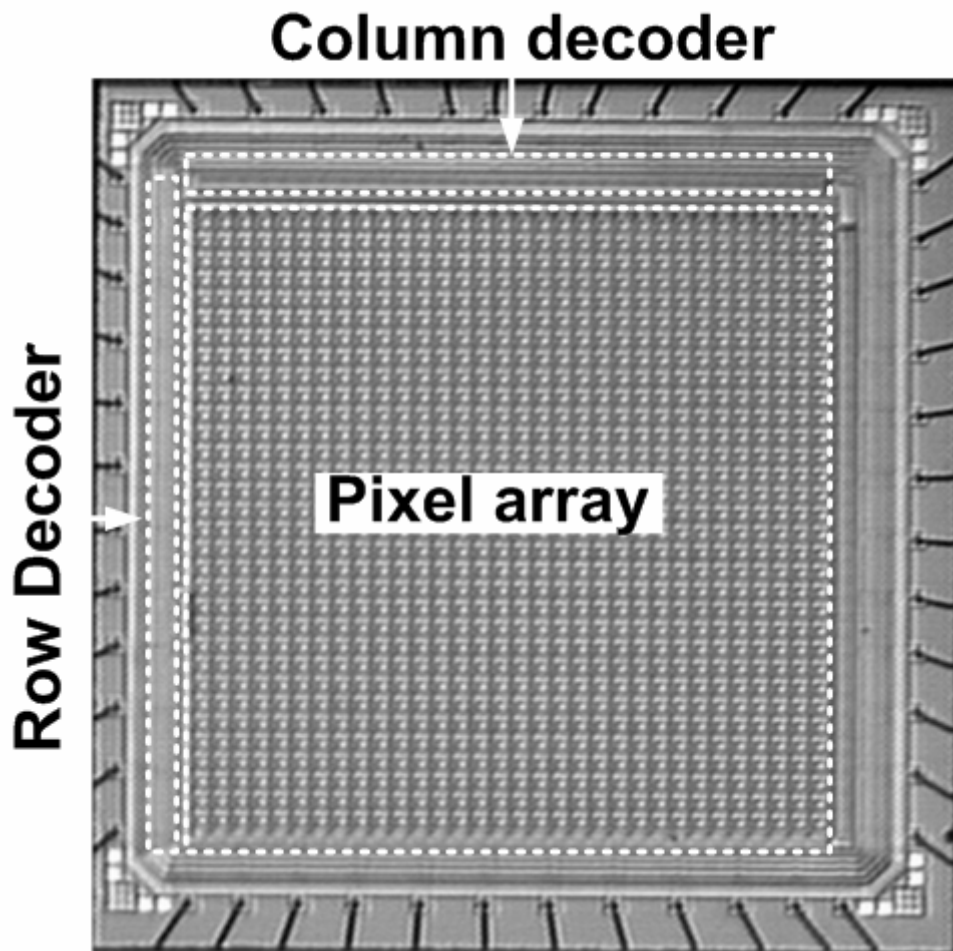


Fig. 5.7. Photographs of (a) the whole chip and (b) a single cell.

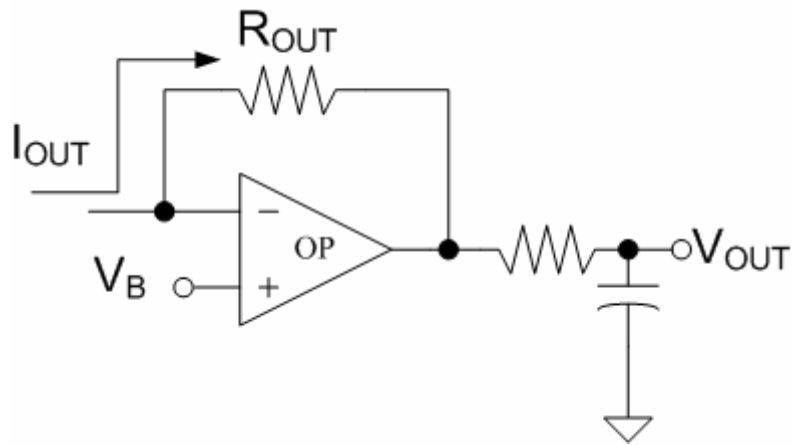


Fig. 5.8. The read-out circuit to translate the output current into voltage.



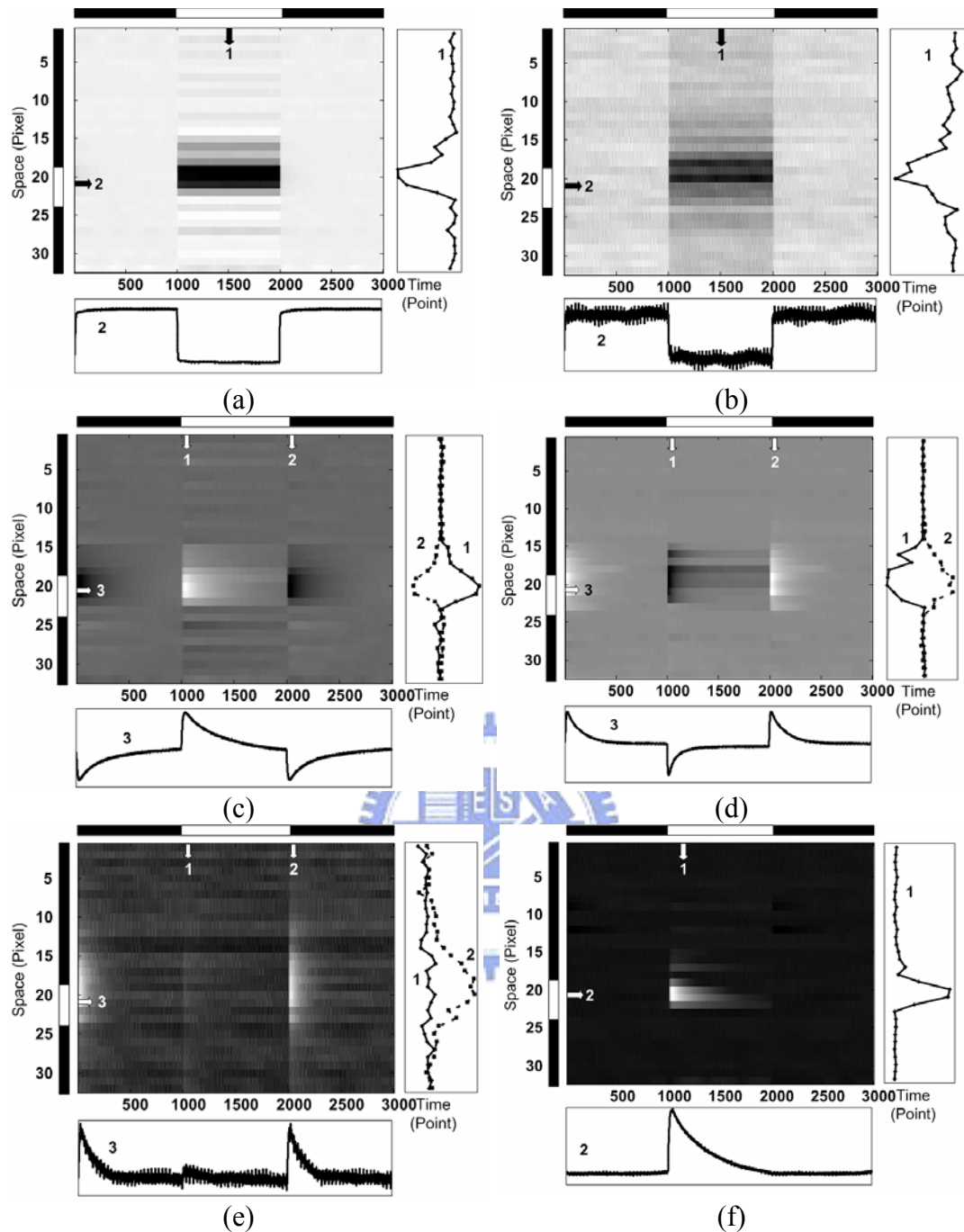


Fig. 5.9. The measured spatiotemporal patterns for (a) photoreceptor, (b) horizontal cell, (c) ON bipolar cell, (d) OFF bipolar cell, (e) amacrine cell, and (f) ganglion cell. These patterns are recorded from the 17th row of the array. The x-axis is normalized time and the y-axis is the pixel location which denotes space. The stimulus is applied to the 19th to the 23rd pixel at time point 1001 to 2000. The waveform at the right of each pattern is the spatial domain waveform(s) obtained at the time marked by the vertical arrow(s). The waveform at the bottom of each pattern is the temporal domain waveform obtained at the location marked by the horizontal arrow.

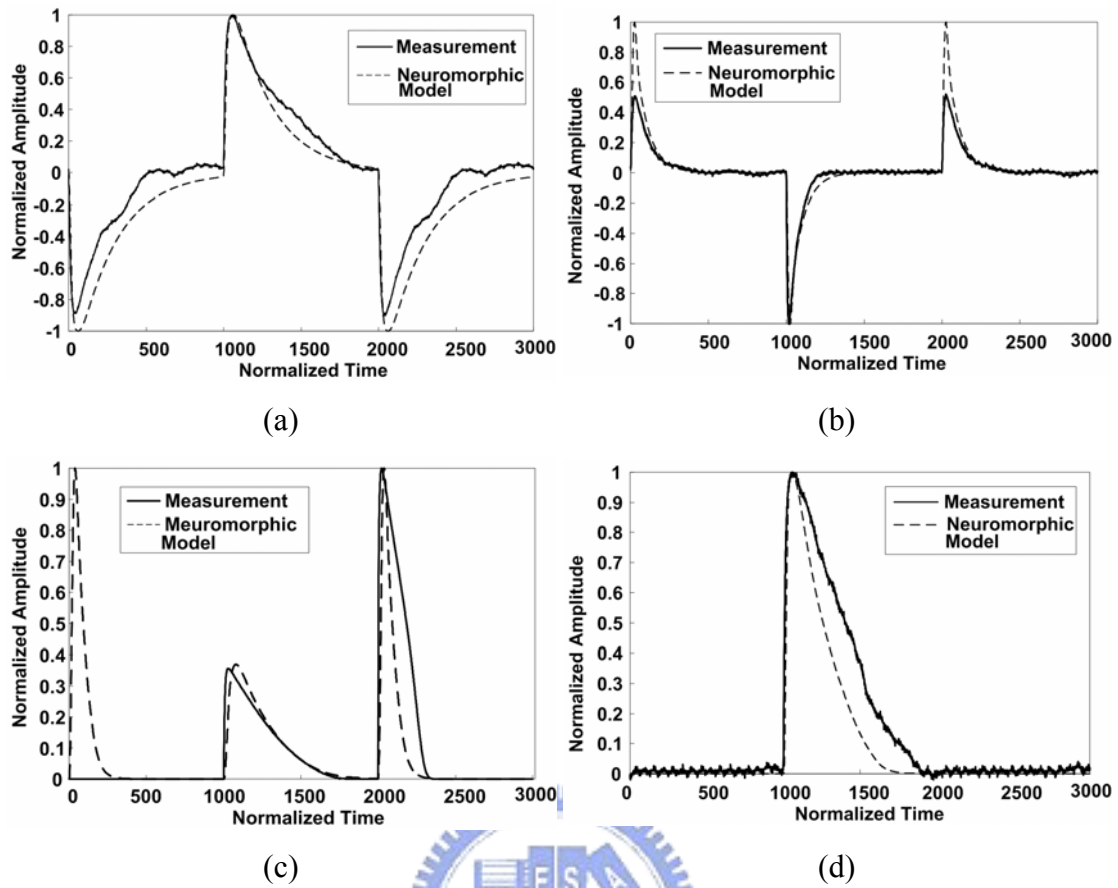
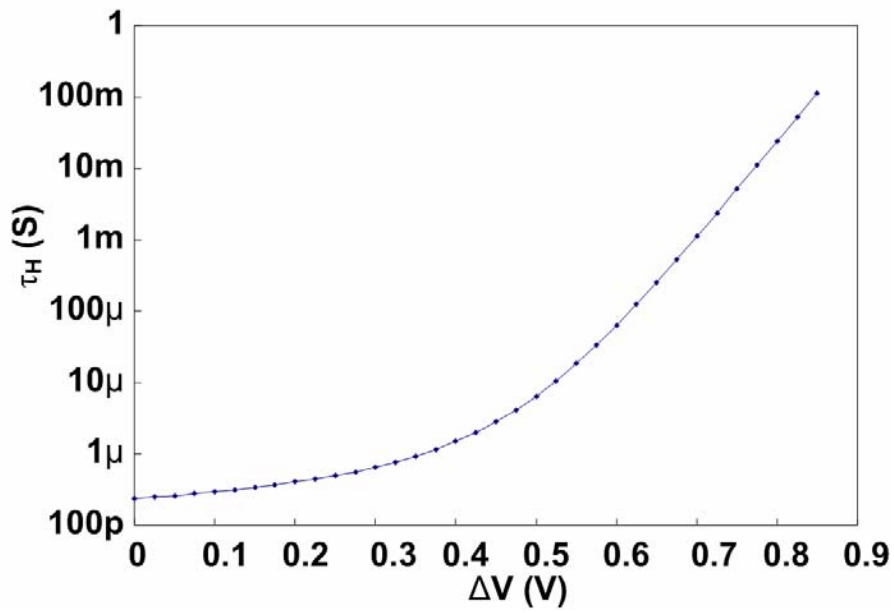
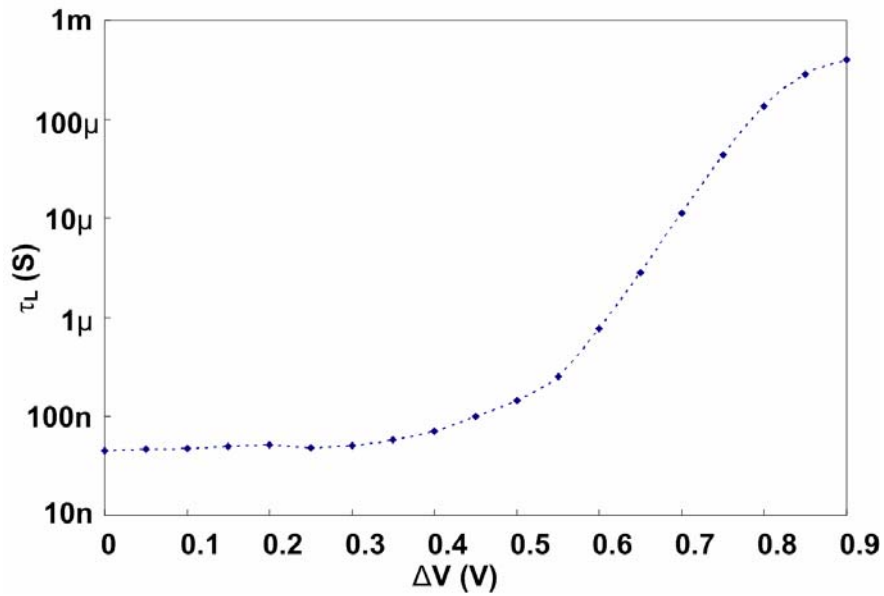


Fig. 5.10. The normalized waveforms of the electrical model and chip measurements of (a) the ON bipolar cell, (b) the OFF bipolar cell, (c) the amacrine cell, and (d) the ganglion cell. The light stimulus starts at time point 1001, and ends at time point 2000.



(a)



(b)

Fig. 5.11. (a) The relationship between the time constant τ_H and the controlling biases. The bias V_{NHP} is set as $V_{dd}-\Delta V$ and V_{PHP} is set as ΔV . (b) The relationship between the time constant τ_L and the controlling biases. The bias V_{NLP} is set as $V_{dd}-\Delta V$ and V_{PLP} is set as ΔV . The relationships are obtained by varying the value of ΔV .

CHAPTER 6

CONCLUSIONS AND FUTURE WORKS

6.1 MAIN RESULTS OF THIS THESIS

In this thesis, the BJT-based silicon retinas and their applications are reviewed as a milestone of the research on neuromorphic vision chips. Then a new design methodology to design retinal ganglion cell sets to realize the visual language is proposed to start a new direction on retinomorphic chip design.

In the past several years, the BJT-based silicon retina was first proposed using the parasitic BJT of the standard CMOS technology served as the phototransistor. The smoothing function of the horizontal cell in the retina is efficiently achieved by the diffusion and redistribution of the photogenerated excess carriers in the common base region of the phototransistors. Thus, the structure of the new silicon retina is very simple and compact. Then the smoothing function is further implemented by placing enhancement n-channel MOSFET's among the bases of parasitic BJT's such that the smoothing range became tunable. Based on the BJT-based silicon retina with tunable smoothing capability, many applications are proposed:

- (1) A new structure of low-photocurrent CMOS retinal focal-plane sensor adaptive current Schmitt trigger is proposed to be applied in scanner systems.
- (2) A 2-D velocity- and direction-selective visual motion sensor temporal zero-crossing detector is proposed to detect straight-line motion.
- (3) A CMOS real-time focal-plane motion sensor with modified correlation-based algorithm is proposed to detect the global motion.
- (4) A CMOS angular velocity- and direction-selective rotation sensor is proposed to detect the rotation motion.
- (5) A CMOS focal-plane shear motion sensor is proposed to detect deformation-like motion.

Now in this thesis, a new design methodology is proposed to implement CMOS neuromorphic chips. The model-building approach of the design methodology is to incorporate the available knowledge concerning morphology, electro-physiology, and pharmacology and by only using elementary building blocks. By designing the

parameters and circuitries of the building blocks, which are directly derived from the biological measurements, all kinds of ganglion cell sets can be implemented. An experimental chip which imitate the ON brisk transient ganglion cell set of rabbits' retinas is fabricated and measured to verify the design methodology. Most parts of the chip deal with current-mode signals. The chip contains 32x32 pixels where each pixel imitates one cell set of the ON brisk transient ganglion cell. The total power consumption is 1.675W under 0.45mW light stimuli. The measured results under flashing lights have the same spatiotemporal characteristics as those from biological measurements obtained using similar stimuli. Such consistency strongly suggests that the chip, in extracting the features of the visual world, behaves in a way which is similar to that of real retinal cells. Therefore, the verifications of the implemented chip establish the success of the proposed design methodology. Thus, every kind of ganglion cell sets can be implemented and integrated in the same way.

6.2 FUTURE WORKS

The design methodology proposed in this thesis has been successfully proved. Thus the research on retinomorphic chips can progress with neuroscientific developments on the retina. At the same time, learning from the nature does inspire new ideas for engineering design. The research on several aspects of advanced sensor design can be investigated in the future, including

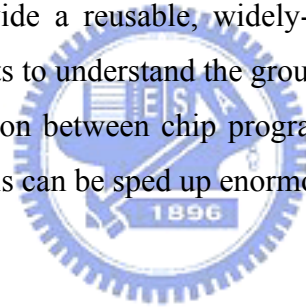
(1) Improvement of the experimental chip:

The designed chip provides neuroscientists clues to understand group behaviors of the ON brisk transient ganglion cells. Its responses to various kinds of images such as complex images, moving images, low-contrast images, etc. should be observed. The results help neuroscientists to design test patterns and experimental flows while discovering rest parts of retinal cells. On the other hand, the experimental chip can be applied to precisely detect light-ON. Thus further reducing the chip size and power consumption of the designed chip leads to an applicable chip using on flashing light detection.

(2) The directionally selective cell: While researching the ganglion cell types of the retina, the ON-OFF and ON directionally selective ganglion cells (DSGC) attracts our eyes. The DSGCs are special GCs that send the directional information to the brain. Many assumptions of the DSGC circuitry have been proposed, and the model proposed in [139] is especially attractive. In this model, the synaptic

connections are simple, but the resultant outputs reflect optical flows faithfully. Even though the circuitry of DSGC is not finalized, its operational principle has been very inspirational for technical applications.

- (3) The retinal prostheses: Research on retinal prostheses is like wildfire. Many researchers devoted into the problem how to help the blind to restore vision. There are mainly two methods considered: intraocular and extraocular. For the extraocular method, the ganglion cells are stimulated by neural spiking to provide visual information for the brain. However, the actual ganglion cell activities have never been taken into account. The design methodology proposed in this thesis can faithfully implement the actual ganglion cell activities. Then it is only a simple step to translate the ganglion cell activities into neural spikings. Thus the design methodology should be a good candidate to realize retinal prostheses.
- (4) The neuroscientific research: Nowadays neurophysiological research to find retinal cell behaviors can observe very limited cells. The chips implemented with the design methodology provide a reusable, widely-observable, and programmable platform for neuroscientists to understand the group behaviors of specific ganglion cell types. With the iteration between chip programming and cell measurements, the discovery of retinal cells can be sped up enormously.



- [1] CA. Mead, *Analog VLSI and Neural Systems*, Reading, MA, Addison-Wesley, 1989.
- [2] C. A. Mead, "Neuromorphic Electronic Systems," in *Proc. of IEEE*, vol. 78, pp. 1629-1636, 1990.
- [3] C. A. Mead, "Adaptive Retina," *Analog VLSI Implementations and Neural Systems*, pp. 239-246, 1989.
- [4] A.C. Andreou, "Analog VLSI Neuromorphic Systems," in *Proc. IEEE Int. Symp. Circuits and Systems*, pp. 1471-1474, 1993.
- [5] P.-F. Ruedi, "Motion detection silicon retina based on event correlation," in *Proceedings of the Fifth International Conference on Microelectronics for Neural, Fuzzy and Bio-Inspired Systems*, pp. 23-29, 1996.
- [6] A. G. Andreou and K. A. Boahen, "A 48,000 pixel, 590,000 transistor silicon retina in current-mode subthreshold CMOS," in *Proceedings of the 37th Midwest Symposium on Circuits and Systems*, vol. 1, pp. 97-102, 1994.
- [7] C.Y. Wu and H.C. Jiang, "An improved BJT-based silicon retina with tunable image smoothing capability," *IEEE Transactions on VLSI Systems*, vol. 7, no. 2, pp 241-248, June 1999.
- [8] T. Delbruck and C. A. Mead, "Analog VLSI Phototransduction by Continuous-Time, Adaptive, Logarithmic Photoreceptor Circuits," *Computation and Neural Systems Program*, Memo, no. 30, California Institute of Technology, July 1994.
- [9] A. B. Torralba and J. Hérault, "An efficient neuromorphic analog network for motion estimation," *IEEE Trans. Circuits and Systems I*, Vol. 46, no. 2, pp. 269-280, February 1999.
- [10] T. Delbruck, "Silicon retina with correlation-based velocity-tuned pixels," *IEEE Tran. Neural Networks*, Vol. 4, pp. 529-541, May 1993.
- [11] R. Benson and T. Delbruck, "Direction selective silicon retina that uses null inhibition," *Advances in Neural Information Processing Systems*, J. Moody, S. Hanson and R. Lippmann Ed., Vol. 4, pp. 756-763, San Mateo, CA: Morgan Kaufman, 1992.
- [12] S. C. Liu, "A neuromorphic aVLSI model of global motion processing in the fly," *IEEE Tran. Circuits and Systems II*, Vol. 47, no. 12, pp. 1458-1467, December 2000.
- [13] R. C. Meitzler, K. Strohbehn and A. G. Andreou, "A silicon retina for 2-D

- position and motion computation,” in *Proc. of 1995 IEEE Int. Symp. Circuits and Systems*, Vol. 3, pp. 2096-2099, 1995.
- [14] A. G. Andreou, K. Strohbehn and R.E. Jenkins,” Silicon retina for motion computation,” in *Proc. of 1991 IEEE Int. Symp. Circuits and Systems, Singapore*, pp. 1373-1376, June 1991.
- [15] P.-F. Ruedi, “Motion detection silicon retina based on event correlation,” in *Proc. of the Fifth Int. Conference on Microelectronics for Neural, Fuzzy and Bio-Inspired Systems*, pp. 23-29, 1996.
- [16] R. Etienne-Cummings, J. Van der Spiegel P. Mueller and M.-Z. Zhang, “A foveated silicon retina for two-dimensional tracking,” *IEEE Trans. Circuits and Systems II*, Vol. 47, no. 6, pp. 504-516, June 2000.
- [17] H.C. Jiang and C.Y. Wu, “A 2-D velocity- and direction-selective sensor with BJT-based silicon retina and temporal zero-crossing detector,” *IEEE J. Solid-State Circuits*, Vol. 34, no. 2, pp. 241-247, February 1999.
- [18] C. Y. Wu and K. H. Huang, “A CMOS focal-plane motion sensor with BJT-based retinal smoothing network and modified correlation-based algorithm,” *IEEE Sensors Journal*, Vol. 2, no. 6, pp. 549-558, December 2002.
- [19] K. H. Huang, L. J. Lin, and C. Y. Wu, “Analysis and design of a CMOS angular velocity- and directional-selective rotation sensor with retinal processing circuit,” *IEEE Sensors Journal*, Vol. 4, no. 6, pp. 845-856, December 2004.
- [20] K. A. Boahen and A. G. Andreou, “A contrast sensitive silicon retina with reciprocal synapse,” *Neural Information Processing Syst.*, Vol. 4, pp. 764-772, 1992.
- [21] A. G. Andreou and K. A. Boahen, “A 48,000 pixel, 590,000 transistor silicon retina in current-mode subthreshold CMOS,” in *Proc. of the 37th Midwest Symp. Circuits and Systems*, Vol. 1, pp. 97-102, 1994.
- [22] A. G. Andreou, K. A. Boahen, P. O. Pouliquen, A. Pavasovic, R. E. Jenkins and K. Strohbehn, “Current-mode subthreshold MOS circuits for analog VLSI neural systems,” *IEEE Trans. Neural Network*, Vol. 2, no. 2, pp. 205-213, 1991.
- [23] C.Y. Wu and C.T. Chiang, “A low-photocurrent CMOS retinal focal-plane sensor with a pseudo-BJT smoothing network and an adaptive current Schmitt trigger for scanner applications,” *IEEE Sensors Journal*, Vol. 4, no. 4, pp. 410-418, August 2004.
- [24] A. G. Andreou, “Low Power Analog VLSI Systems for Sensory Information

- Processing,” in *Microsystems Technology for Multimedia Applications*, IEEE Press, edited by Sheu, Ismail, Sanchez, and Wu, Ch. 7.5, 1995.
- [25] P. Sterling, “How retinal circuits optimize the transfer of visual information,” in *The Visual Neurosciences*, Vol. 1, L. M. Chalupa and J. S. Werner, Ed. Cambridge, MA: The MIT Press, pp. 234-278, 2003.
- [26] K. A. Boahen, “A retinomorph vision system,” *IEEE Micro*, Vol.16, no. 5, pp. 30-39, October 1996.
- [27] K. Boahen, “Retinomorph chips that see quadruple images,” in *Proc. MicroNeuro*, pp. 12-20, 1999.
- [28] K.A. Zaghloul and K. Boahen, “Optic nerve signals in a neuromorphic chip I: Outer and inner retina models,” *IEEE Trans. Biomedical Engineering*, Vol. 51, no. 4, pp. 657-666, April 2004.
- [29] K.A. Zaghloul and K. Boahen, “Optic nerve signals in a neuromorphic chip II: Testing and results,” *IEEE Trans. Biomedical Engineering*, Vol. 51, no. 4, pp. 667-675, April 2004.
- [30] S. Kameda, and T. Yagi, “An analog VLSI chip emulating sustained and transient response channels of the vertebrate retina,” *IEEE Trans. Neural Networks*, Vol. 14, no. 5, pp.1405-1412, September 2003.
- [31] C. Enroth-Cugell and J. G. Robson, “The contrast sensitivity of retinalganglion cells of the cat,” *J. Physiol.*, vol. 187, pp. 517–552, 1966.
- [32] B. G. Cleland, M.W. Dubin, and W. R. Levick, “Sustained and transient neurons in the cat’s retina and lateral geniculate nucleus,” *J. Physiol.*, vol. 213, pp. 473–496, 1971.
- [33] S.W. Kuffler, "Discharge patterns and functional organization of mammalian retina," *J. Neurophysiol.*, vol. 16, pp.37-68, 1953.
- [34] H. Kolb and R. Nelson, “Functional neurocircuitry of amacrine cells in the cat retina,” in *Neurocircuitry of the Retina: A Cajal Memorial*, A. Gallego and P. Gouras, Eds. New York: Elsevier, 1985.
- [35] G. Maguire and P. Lukasiewicz, “Amacrine cell interactions underlying the response to change in tiger salamander retina,” *J. Neurosci.*, vol. 9, pp. 726–35, 1989.
- [36] P. Sterling, Retina, and G. M. Shepherd, Eds., *The Synaptic Organization of the Brain*, fourth ed. New York: Oxford Univ. Press, 1998.
- [37] B. Roska, E. Nemeth, L. Orzo, FS. Werblin, “Three levels of lateral inhibition: A

- space-time study of the retina of the tiger salamander,” *J. Neuroscience*, Vol. 20(5), pp. 1941-1951, March 2000.
- [38] B. Roska and F. Werblin, “Vertical interactions across ten parallel, stacked representations in the mammalian retina,” *Nature*, Vol. 410, pp. 583-587, March 2001.
- [39] F. Werblin and B. Roska, “The Movies in Our Eyes,” *Scientific American*, pp. 73-79, April, 2007.
- [40] F. Werblin and B. Roska, “Parallel visual processing: a tutorial of retinal function,” *Int. J. Bifurcation and Chaos*, Vol. 14, No. 2, pp. 843-852, 2004.
- [41] H. Wässle,” Parallel processing in the mammalian retina,” *Nature Reviews Neuroscience*, Vol. 5, pp. 1-11, October 2004.
- [42] R. L. Rockhill, F. J. Daly, M. A. MacNeil, S. P. Brown, and R. H. Masland, “The Diversity of Ganglion Cells in a Mammalian Retina,” *J. Neuroscience*, Vol. 22(9), pp. 3831–3843, May 2002.
- [43] F. Werblin, B. Roska, D. Balya, C. Rekeczky, and T. Roska, “Implementing a retinal visual language in CNN: a neuromorphic study,” in *Proc. IEEE Int. Symp. Circuits and Systems*, Vol. 2, pp. 333-336, 2001.
- [44] D. Bálya, B. Roska, T. Roska, and F. S. Werblin, “A CNN framework for modeling parallel processing in a mammalian retina,” *Int. J. Circuit Theory and Applications*, Vol. 30, pp. 363-393, 2002.
- [45] D. Bálya, I. Petrás and T. Roska, “Implementing the multilayer retinal model on the complex-cell CNN-UM chip prototype,” *Int. J. Bifurcation and Chaos*, Vol. 14, No. 2, pp. 427-451, 2004.
- [46] C.Y. Wu and C.F. Chiu, “A new structure of 2-D silicon retina,” *IEEE J. Solid-State Circuits*, Vol. 30, no. 8, pp. 890-897, August 1995.
- [47] C.Y. Wu, W.C. Hsieh, and C.T. Chiang, “A CMOS focal-plane retinal sensor designed for shear motion detection,” in *Proc. of ICECS*, pp. 141-144, December, 2004.
- [48] H. A. Basler, A. A. Brewer, L. T. Sharpe, A.B. Moreland, H. Jagle, and B.A. Wandell, “Reorganization of human cortical maps caused by inherited photoreceptor abnormalities,” *Nature Neuroscience*, Vol. 5, pp. 364-370, 2002.
- [49] D. C. van Essen, C. H. Anderson, and D. J. Felleman, “Information processing in the primate visual system: an integrated systems perspective,” *Science*, Vol. 255, pp. 419-423, 1992.

- [50] M. A. MacNeil, and R. H. Masland, “Extreme diversity amongamacrine cells: implications for function,” *Neuron*, Vol. 20, pp. 971–982, 1998.
- [51] R. H. Masland, “Neuronal diversity in the retina,” *Curr. Opin. Neurobiol.*, Vol. 11, 431–436 (2001).
- [52] S. Hombach, et al., “Functional expression of connexin 57 in horizontal cells of the mouse retina,” *Eur. J. Neurosci.*, Vol. 19, pp. 2633–2640, 2004.
- [53] K. Nakatani, T. Tamura, and K.W. Yau, “Light adaptation in retinal rods of the rabbit and two other nonprimate mammals,” *J. Gen. Physiol.*, Vol. 97, pp.413-435, 1991.
- [54] Pugh, E. N. Jr., and T. D. Lamb, “Amplification and kinetics of the activation steps in phototransduction,” *Biochim. Biophys. Acta*, Vol. 1141, pp. 111-149, 1993.
- [55] J. L. Schnapf, B. J. Nunn, M. Meister, and D. A. Baylor, “Visual transduction in cones of the monkey *Macaca fascicularis*,” *J. Physiol.*, Vol. 427, pp.681-713, 1990.
- [56] K. K. Ghosh, S. Bujan, , S. Haverkamp, A. Feigenspan, and H. Wässle, “Types of bipolar cells in the mouse retina,” *J. Comp. Neurol.*, Vol. 469, pp. 70–82, 2004.
- [57] M. A. MacNeil, J. K. Heussy, R. F. Dacheux, E. Raviola, and R. H. Masland, “The population of bipolar cells in the rabbit retina,” *J. Comp. Neurol.*, Vol. 472, pp. 73–86, 2004.
- [58] G. B. Awatramani, and M. M. laughter, “Origin of transient and sustained responses in ganglion cells of the retina,” *J. Neurosci.*, Vol. 20, pp. 7087–7095, 2000.
- [59] S. M. Wu, F. Gao, and B. R. Maple, “Functional architecture of synapses in the inner retina: segregation of visual signals by stratification of bipolar cell axon terminals,” *J. Neurosci.*, Vol. 20, pp. 4462–4470, 2000.
- [60] R. H. Masland, “The fundamental plan of the retina,” *Nature Neuroscience*, Vol. 4 no, 9, september 2001.
- [61] D. M. Dacey and O. S. Packer, “Colour coding in the primate retina: diverse cell types and cone-specific circuitry,” *Curr. Opin. Neurobiol.*, Vol. 13, pp. 421–427 2003.
- [62] F. R. Amthor, E. S. Takahashi, and C. W. Oyster, “Morphologies of rabbit retinal ganglion cells with concentric receptive fields,” *J. Comp. Neurol.*, Vol. 280, pp.

72-96, 1989.

- [63] F. R. Amthor, E. S. Takahashi, and C. W. Oyster, "Morphologies of rabbit retinal ganglion cells with complex receptive fields," *J. Comp. Neurol.*, Vol. 280, pp97-121, 1989.
- [64] P. A. Ruetz and R. W. Brodersen, "Architectures and design techniques for real time image processing ICs," *IEEE J. Solid-State Circuits*, vol. SC-22, pp. 233-250. Apr. 1987.
- [65] M. Maruyama, H. Nakatiira, T. Araki, S. Sakiyama, Y. Kitao, K. Aono, and H. Yamada, "An image signal multiprocessor on a single chip," *IEEE J. Solid-State Circuits*, vol. 25. pp. 1476-143, Apr. 1990.
- [66] J. Dowling, *The Retina: An Approachable Part of the Brain*. Cambridge, MA: Harvard University Press, 1987.
- [67] D. Mart. *Vision*. San Francisco, CA: W. H. Freeman, 1982.
- [68] C. A. Mead and M. A. Mahowald. "A silicon model of early visual processing," *Neural Networks*, vol. 1, pp. 91-97. 1988.
- [69] H. Kobayashi, J. L. White, and A. A. Abidi, "An active resistor network for Gaussian filtering of images," *IEEE J. Solid-State Circuits*, vol. 26. pp. 738-748. May 1991.
- [70] P. C. Yu. S. J. Decker, H. S. Lee, C. G. Sodini, and J. L Wyatt. "CMOS resistive fuses for image smoothing and segmentation," *IEEE J. Solid-State Circuits*, vol. 27, pp. 545-553. Apr. 1992.
- [71] C. P. Chong, C. Andre. T. Salaina, and K. C. Smith, "Image-motion detection using analog VLSI," *IEEE J. Solid-Stare Circuits*, vol. 27, pp. 93-96, Jan. 1992.
- [72] A. Moini, A. Bouzerdoum, A. Yakovieff, D. Abbott, O. Kim, K. Eshraghian, and R. E. Bogner, "An analog implementation of early visual processing in insects," in 1993 *VLSITSA*, pp. 283-287.
- [73] T. I. Kamins and G. T. Fong, "Phowsensing arrays with improved spatial resolution," *IEEE J. Solid-State Circuits*, vol. SC-13, pp. 8-85, Apr. 1978.
- [74] C. Y. Wu and C. F. Chiu, "A new structure for the silicon retina," in *IEDM Tech. Dig.*, Dec. 1992, pp. 439-442.
- [75] P. H. Lu, C. Y. Wu, and M. K. Tsai, "VHF handpass filter design using CMOS transresistance amplifiers." in *Proc. IEEE Inmt. Symp. Circuits Syst.*, May 1993, pp. 990-993.
- [76] J. E. Dowling, "The Retina: An Approachable Part of the Brain," Cambridge,

- MA: Belknap Press of Harvard University Press, 1987.
- [77] R. W. Rodieck, "The Vertebrate Retina: Principles of Structure and Function," San Francisco, CA: W. H. Freeman, 1973.
- [78] F. S. Werblin,, "Control of Retinal Sensitivity Lateral Interactions at the Outer Plexiform Layer," *Journal of General Physiology*, 63:62, 1974.
- [79] Y. P. Tsividis, "Analog MOS Integrated Circuits - Certain New Ideas, Trends, and Obstacles," *IEEE Journal of Solid-State Circuits*, vol. 22, pp. 317-321, June, 1987.
- [80] E. A. Vittoz, "Future of Analog in the VLSI Environment," *Proc. IEEE Int'l Symp. Circuits and Systems*, vol. 22, pp. 1372-1375, 1990.
- [81] B. J. Hosticka, "Performance Comparison of Analog and Digital Circuits," *Proc. IEEE*, vol. 73, pp. 25-29, 1985
- [82] R. F. Lyon, "Cost, Power and Parallelism in Speech Signal Processing," *Proc. IEEE Custom Integrated Circuits Conf.*, pp. 15.1.1-9, 1993.
- [83] H. Kobayashi, J. L. White, A. A. Abidi, "An Active Resistor Network for Gaussian Filtering of Images," *IEEE J. Solid-State Circuits*, vol. SC-26, pp. 738-748, May 1991.
- [84] C. Y. Wu and C. F. Chiu, "A New Structure of the 2-Dimensional Silicon Retina," *IEEE J. Solid-State Circuits*, vol. SC-30, pp. 890-897, Aug. 1995.
- [85] N. H. Fletcher, "Some Aspects of the Design of Power Transistors," *PROCEEDINGS OF THE IRE*, vol. 43, pp. 551-559, May 1955.
- [86] J. R. Hauser, "The Effects of Distributed Base Potential on Emitter-Current Injection Density and Effective Base Resistance for Strip Transistor Geometries," *IEEE Trans. on Electron Devices*, vol. ED-11, pp. 238-242, May 1964.
- [87] C. Y. Wu and H. C. Jiang, "The Modeling and Design of the BJT-based Silicon Retina for Image Smoothing and Edge Detection," *The Third Australian and New Zealand Conference on Intelligent Information Systems*, vol. 1, pp. 232-235, Perth, 27 Nov. 1995.
- [88] P. Perona and J. Malik, "Scale-Space and Edge Detection Using Anisotropic Diffusion," *IEEE Trans. on Pattern Analysis and Machine Intelligence*, vol. 12, No. 7, pp. 629-639, July, 1990.
- [89] A. Rosenfeld and M. Thurston, "Edge and Curve detection for visual scene analysis," *IEEE Trans. Comput.*, vol. C-20, pp. 562-569, May, 1971.

- [90] A. Witkin, "Scale-Space Filtering," in *Int. Joint Conf. Artificial Intelligence*, Karlsruhe, West Germany, pp. 1019-1021, 1983.
- [91] A. Yuille and T. Poggio, "Scaling Theorems for Zero Crossings," *IEEE Trans. Pattern Anal. Machine Intell.*, vol. PAMI-8, Jan., 1986.
- [92] A Hummel, "Representations Based on Zero-Crossings in Scale-Space," in *Proc. IEEE Computer Vision and Pattern Recognition Conf.*, pp. 204-209, June, 1986.
- [93] E. Vittoz and J. Fellrath, "CMOS Analog Integrated Circuits Based on Weak Inversion Operation," *IEEE J. Solid-State Circuits*, vol. sc-12, No. 3, pp.231-244, June, 1977.
- [94] D. Marr, "Vision," San Francisco, CA: W. H. Freeman, 1982.
- [95] H. C. Jiang and C. Y. Wu, "The BJT-Based Silicon-Retina Sensory System for Direction- and Velocity-Selective Sensing," to be presented in *1998 IEEE International Symposium on Circuits and Systems*, June, 1998.
- [96] W. Bair and C. Koch, "An Analog VLSI Chip for Finding Edges from Zero-Crossings," *Neural Information Processing System*, Vol. 3, pp. 339-405, 1991.
- [97] E. Funatsu, Y. Nitta, Y. Miyake, T. Toyoda, J. Ohta, and K. Kyuma, "An artificial retina chip with current-mode focal plane image processing functions," *IEEE Trans. Electron Devices*, vol. 44, pp. 1777-1781, Oct. 1997.
- [98] R. A. Panicacci, S. E. Kemeny, P. D. Jones, C. Staller, and E. R. Fossum, "128 Mb/s multiport CMOS binary active-pixel image sensor," in *ISSCC Dig. Tech. Papers*, 1996, pp. 100-101.
- [99] C. Y. Wu, H. C. Huang, L. J. Lin, and K. H. Huang, "A new Pseudo-Bipolar-Junction-Transistor (PBJT) and its application in the design of retinal smoothing network," in *Proc. IEEE Int. Symp. Circuits and Systems*, vol. 4, July 2002, pp. 125-128.
- [100] P. Y. Burgi and F. Heitger, "A fast 100x100 pixel silicon retina for edge extraction with application in OCR," in *Proc. IEEE Int. Symp. Signal Processing and Its Applications*, vol. 37, 2001, pp. 288-291.
- [101] G. Liang and W. C. Miller, "A novel photo BJT array for intelligent imaging," in *Proc. IEEE Int. Symp. Circuits and System Systems*, vol. 2, Aug. 1993, pp. 1056-1059.
- [102] M. D. Rowley and J. G. Harris, "An edge enhancement technique for analog VLSI early vision applications," in *Proc. IEEE Int. Symp. Neural Networks*, vol.

- 2, June 1996, pp. 874–879.
- [103] Mhani, G. Sicard, and G. Bouvier, “Analog vision chip for sensing edges contrasts and motion,” in *Proc. IEEE Int. Symp. Circuits and Systems*, vol. 4, Aug. 1997, pp. 2769–2772.
- [104] R. E. Cummings, J. V. der Spiegel, P. Mueller, and M. Z. Zhang, “A foveated silicon retina for two-dimensional tracking,” *IEEE Trans. Circuits Syst. II*, vol. 47, pp. 504–517, June 2000.
- [105] J. H. Huang, Z. H. Liu, M. C. Jeng, K. Hui, M. Chan, P. K. Ko, and C. Hu, BSIM3 Version 3.2.2 MOSFET Model User’s Manual, 1999.
- [106] R. A. Boie and W. Turin, “Noise-limited reading of bar codes,” *IEEE Trans. Ind. Electron.*, vol. 44, no. 6, pp. 816–824, Dec. 1997.
- [107] C. Y. Wu and C. T. Chiang, “A low-photocurrent CMOS retinal focal plane sensor with pseudo-BJT smoothing network and adaptive current Schmitt trigger for scanner applications,” in *Proc. IEEE 2nd Int. Conf. Sensors*, vol. 2, Oct. 2003, pp. 1147–1152.
- [108] J. Tanner and C. Mead, “An Integrated analog optical motion sensor,” in *VLSI Signal Processing II*, S.-Y. Kung, R. Owen, and J. Nash, Eds. New York: IEEE Press, 1986, pp. 59-76.
- [109] J. Hutchinson, C. Koch, J. Luo, and C. Mead, “Computing Motion Using Analog and Binary Resistive Networks,” *IEEE Trans. Comput.*, vol. 21, pp. 52-64, 1988.
- [110] A. G. Andreou and K. Strohhahn, “Analog VLSI Implementation of the Hassenstein-Reichardt-Poggio Models for Vision Computation,” in *Proc. 1990 IEEE Symp. Syst., Man Cybern*, 1990, pp. 707-710.
- [111] T. Horiuchi, J. Lazzaro, A. Moore, and C. Koch, “A Delay line Based Motion Detection Chip,” in *Advances in Neural Information Processing Systems 3*, R. Lippman, J. Moody, and D. Touretzky, Eds. San Mateo, CA: Morgan Kaufman, 1991, pp. 406-412.
- [112] J. Kramer, “Compact Integrated Motion Sensor with Three-Pixel Interaction,” *IEEE Tran. Pattern Analysis and Machine Intelligence*, vol. 18, no. 4, pp. 455-460, Apr. 1996.
- [113] J. Kramer, R. Sarpeshkar, and C. Koch, “Pulse-Based Analog VLSI Velocity Sensors,” *IEEE Trans. Circuits and Systems II*, vol. 44, no. 2, pp. 86-101, Feb. 1997.

- [114]R. Sarpeshkar, W. Bair, and C. Koch, "Visual Motion Computation in Analog VLSI Using Pulses," *Advances in Neural Information Processing Systems*, vol. 5, pp. 781-788, 1993.
- [115]R. Etienne-Cummings, J. Van der Spiegel, and P. Mueller, "A Focal Plane Visual Motion Measurement Sensor," *IEEE Tran. Circuits and Systems I*, vol. 44, no. 1, pp. 55-66, Jan. 1997.
- [116]C. F. Chiu and C. Y. Wu, "Design of CMOS Elementary-Motion-Flow-Selective Image Detector Using the BJT-Based Silicon Retina," in *Proc. 1997 IEEE. Int. Symp. Circuits and Systems*, Hong Kong, June 1997, pp. 717-720.
- [117]G. Indiveri, J. Kramer, and C. Hoch, "Analog VLSI Architecture for Computing Heading Direction," in *Proc. International Vehicles Symposium*, 1995, pp. 24-29.
- [118]R. C. Meitzler, A. G. Andreou, K. Strohhahn, and R. E. Jenkins, "A Sampled-Data Motion Chip," in *Proc. Midwest Symposium on Circuits and Systems*, Vol. 1, pp. 288-291, 1995.
- [119]T. Poggio, W. Yang, and V. Torre, "Optical Flow: Computational Properties and Networks, Biological and Analog," in *The Computing Neuron*, R. Durbin, C. Mial, and G. Mitchison, Eds. Wokingham, U. K.: Addison-Wesley, 1989, pp. 355-370.
- [120]E. C. Hildreth and C. Koch, "The Analysis of Visual Motion: From Computational Theory to Neuronal Mechanisms," *Ann. Rev. Neurosci.*, vol. 10, pp. 477-533, 1987.
- [121]R. Sarpeshkar, J. Kramer, G. Indiveri, and C. Koch, "Analog VLSI Architectures for Motion Processing: From Fundamental Limits to System Applications," in *Proc. IEEE*, vol. 84, no. 7, pp. 969-987, Jul. 1996.
- [122]T. Horiuchi, W. Bair, B. Bishofberger, A. Moore, C. Koch, and J. Lazzaro, "Computing Motion Using Analog VLSI Vision Chips: An Experimental Comparison Among Different Approaches," *Int. J. Computer Vision*, vol. 8, pp. 203-216, 1992.
- [123]B. Hassenstein and W. Reichardt, "Systemtheoretische analyse der zeit-, reihenfolgen- und vorzeichenbewertung bei der bewegungsperzeption des rasselkafers chlorophanus," *Z. Naturforsch.*, vol. 11b, pp. 513-524, 1956.
- [124]C. Y. Wu and H. C. Jiang, "A High-Density 2-Dimensional BJT-Based Silicon Retina with Tunable Image Smoothing Capability," in *Proc. ICECS'97*, Dec. 1997.

- [125]C. C. Hsieh, C. Y. Wu, and T. P. Sun, "A New Cryogenic CMOS Readout Structure for Infrared Focal Plane Array," *IEEE J. Solid-State Circuits*, Vol. 32, No. 8, pp. 1192-1199, Aug. 1997.
- [126]Z. Wang and W. Guggenbuhl, "Novel CMOS Current Schmitt Trigger," *Electronics Letters*, Vol. 24, No. 24, pp. 1514-1516, Nov. 1988.
- [127]A. Moini, *Vision Chips*, Kluwer, 1999, chapter 4.
- [128]A. Moini, A. Bouzerdoun, K. Eshraghian, A. Yakovleff, X.T. Nguyen, A. Blanksby, R. Beare, D. Abbott, and R.E. Bogner, "An insect vision-based detection chip," *IEEE Journal of Solid-State Circuits*, vol. 32, no. 2, pp. 279-284, February 1997.
- [129]R. Etienne-Cummings, J. Van der Spiegel and P. Mueller, "Hardware Implementation of a visual-motion pixel using oriented spatiotemporal neural filters," *IEEE Transactions on Circuits and Systems II*, vol. 46, no. 9, pp. 1121-1136, September 1999.
- [130]C.M. Higgins, R.A. Deutschmann and C. Koch, "Pulse-based 2-D motion sensors," *IEEE Transactions on Circuits and Systems II*, vol. 46, no. 6, pp. 677-687, June 1999.
- [131]J. Tanner and C.A. Mead, "Correlation optical motion detector," U.S. Patent 4631400, Dec. 23, 1986.
- [132]X. Arreguit, F. Andre van Schaik, F. V. Bauduin, M. Bidiville, and E. Raeber, "A CMOS motion detector system for pointing devices," *IEEE Journal of Solid-State Circuits*, vol. 31, no. 12, pp. 1916-1921, December 1996.
- [133]E. R. Fossum, "Architectures for focal-plane image processing," *Optical Engineering*, vol. 28, no. 8, pp. 866-871, 1989.
- [134]G. A. Orban and H. -H Nagel (eds.), *Artificial and Biological Vision Systems*, Berlin: Springer-Verlag, 1992.
- [135]J. Konoderink, "Optical flow," *Vision Research*, no. 26, pp. 161-180, 1986.
- [136]Raymond A. Serway, *Physics for Scientists & Engineers with Modern Physics*, Saunders College Publishing, 1996.
- [137]C.-Y. Wu and C.-H. Cheng, "A learnable cellular neural network structure with ratio memory for image processing," *IEEE Trans. Circuits and Systems I*, Vol. 49, no. 12, pp. 1713-1723, December 2002.
- [138]D. Bálya and B. Roska, "Retina model with real-time implementation," in *Proc. IEEE Int. Symp. Circuits and Systems*, Kobe, pp. 5222-5225(Special Session C3LC),

2005.

- [139]S. I. Fried, T. A. Münch, and F. S.Werblin, “Mechanisms and circuitry underlying directional selectivity in the retina,” *Nature*, Vol. 420, pp. 411–414, 2002.

